Simulating the sorption dynamics of
Complex Metal Hydrides

J. G. O. Ojwang'

Simulating the sorption dynamics of
Complex Metal Hydrides

PROEFSCHRIFT

ter verkrijging van de graad van doctor
aan de Technische Universiteit Eindhoven,
op gezag van de Rector Magnificus,
prof.dr.ir. C.J. van Duijn,
voor een commissie aangewezen
door het College voor Promoties
in het openbaar te verdedigen
op maandag 25 mei 2009 om 16.00 uur

door

Julius Greenhamms Omondi Ojwang

geboren te Garissa, Kenia

iii

Dit proefschrift is goedgekeurd door de promotoren:

prof.dr. R.A. van Santen
en
prof.dr. G.J. Kramer

Samenstelling promotiecommissie:

Thesis Advisory Committee:
prof.dr. P.J. Lemstra	voorzitter
prof.dr. R.A. van Santen	Technische Universiteit Eindhoven, 1e promotor
prof.dr. G.J. Kramer	Technische Universiteit Eindhoven, 2e promotor
prof.dr. P.H. Notten	Technische Universiteit Eindhoven
prof.dr. G.J. Kroes	Universiteit Leiden
prof.dr. A.C.T. van Duin	Penn State University
prof.dr. A. Zuttel	ETH
dr. H.T.J.M. Hintzen	Technische Universiteit Eindhoven

To my grandmum Teresa (Nyodando). You are gone but not forgotten.

Contents

List of Figures

List of Tables

Part I

Background and Theoretical Techniques

Chapter 1

Paradigm Shift: Towards a Hydrogen Economy

> Yes, my friends, I believe that water will one day be employed as fuel, that hydrogen and oxygen which constitute it, used singly or together, will furnish an inexhaustible source of heat and light, of an intensity of which coal is not capable.
>
> JULES VERNE, *Mysterious Island*
> *- 1870*

1.1   Introduction

Hydrogen economy includes the design of fuel cells for converting hydrogen into electricity and the development of the requisite infrastructure like for instance "hydrogen filling stations" to refuel vehicles once the hydrogen is used up. The goal is to use hydrogen as an alternative to gasoline.[1–5] There is an interesting assessment on the possibility of paradigm shift (from fossil fuel economy to hydrogen economy) in the transport sector in Ref.[6] Figure 1.1 shows an example of a hydrogen based transport system in which the hydrogen storage device has to be removed from the vehicle for reprocessing/recharging. What the figure shows is the following. Fuel ($NaBH_4$)

3
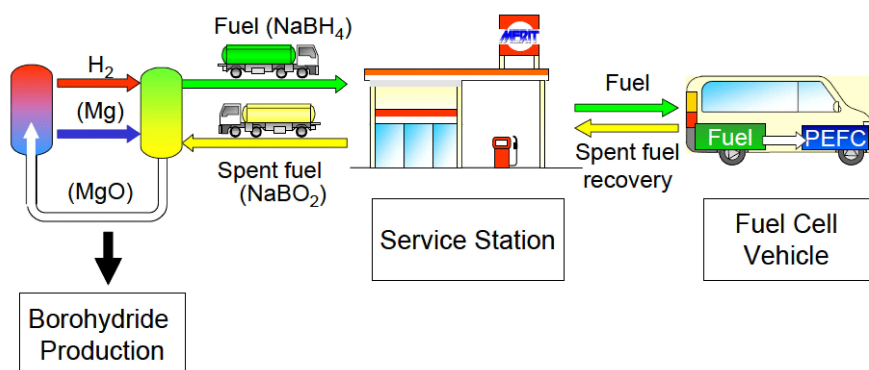
Fig. 1.1: Application of $NaBH_4$ for onboard hydrogen storage. (Reproduced from Ref. [7])

is delivered at the service station. A motorist drives to the station and picks up the fuel while leaving behind the spent fuel. The spent fuel is then taken to the central processing facility where it is recharged and then delivered back to the service station.

What makes a hydrogen economy tantalizing is that hydrogen is abundant in nature and also clean. The only product of its combustion is water, which is harmless. However, there are many hurdles that must be vaulted before hydrogen will be able to offer consumers a competitive alternative to gasoline. The most technically challenging hurdle to hydrogen economy is how to store hydrogen for onboard fuel application in vehicles. So daunting is the challenge that the quest to find an ideal hydrogen storage material has gone on for close to five decades with no solution in sight.[8–10] The main goal is to get a safe, light weight, compact and affordable means to store the hydrogen. The major problem beleaguering hydrogen storage is that although hydrogen has a good energy density per weight (120 MJ/kg for hydrogen compared to 44 MJ/kg for hydrocarbons), it also has poor energy density per volume vis-á-vis hydrocarbons (8 MJ/l for liquid hydrogen versus 32 MJ/l for hydrocarbons). Gaseous hydrogen requires a large tank to store. Under ambient conditions of temperature and pressure, the volume occupied by a kilogram of hydrogen gas is about 11 m^3. This means that to drive a car for a distance of 500 km using gaseous hydrogen at normal pressure would require a fuel tank with a size of approximately ten cars. The grand challenge therefore is to find a material that is capable of storing enough onboard hydrogen for a vehicle to cover over 500 km on a full tank without adding significant weight or volume to the present cars.

For a material to be considered as a potential hydrogen storage candidate for onboard fuels applications it must meet the following conditions: High gravimetric capacity, fast kinetics, favorable thermodynamics,[11–14] an operating temperature between 320 K - 470 K and dissociation pressure between 1-10 bars. Through more than 200 absorption/desorption cycles, the material should maintain more than 95% of hydrogen capacity. In addition, at the beginning of this decade, the United States' Department of Energy (DoE) set a minimum target of 6 wt% gravimetric and 45 g/l volumetric hydrogen by the year 2010 for economically practical storage of hydrogen in a solid state material for mobile applications. This is expected to shoot to 9 wt% gravimetric and 81 g/l volumetric hydrogen storage by 2015. As the clock ticks towards the year 2010, it is doubtful that there can be any revolutionary technological breakthrough to attain the 6 wt% of hydrogen storage target, either by theoretical simulations on in experiments, within the remaining time frame. Most likely, for the time being, storage of hydrogen in high pressure tanks and in liquid form by cryogenic cooling are the best alternative. In spite of this drawback to solid state storage solution, a lot of water has passed under the bridge in so far as studies of potential hydrogen storage candidates are concerned. Recently, the possibility of storing hydrogen in carbon nanotubes[15–20], clathrates, zeolites[21–23] and metal organic frameworks (MOFs)[24–26] has generated a lot of interest. In these materials, hydrogen is stored in a physisorbed form and therefore it is much easier to desorb it. The other advantage is that these materials are light, porous and robust. Therefore, they offer the possibility of achieving high reversible hydrogen storage with fast kinetics and stability over many cycles.

Figure 1.2 illustrates the various ways in which hydrogen can be compacted into a smaller volume with respect to the size of a car. The first method is to store the gas under high pressure (200 bars). The gas is densely packed to a smaller volume by intense pressurization. However, pressurization of the gas will still require a large volume, which is undesirable. The second method is to liquefy the gas. Liquid hydrogen needs to be stored under cryogenic conditions and boils at around 20 K (-253 °C).[28] The advantage of liquefaction is that more hydrogen can be stored in a liquid form compared to gaseous form in a given volume. The drawback to liquefaction process is that it costs enormous energy loss, far more than in producing compressed hydrogen. To the myriad of woes bedevilling cryogenic cooling of hydrogen as an alternative, add the costs incurred in insulating the tank to prevent boil-off and the susceptibility of the tank to corrosion and explosion.[29] Simply put, at the moment liquefaction of hydrogen is only viable in the case of space shuttle launch but not for normal commercial purposes. However, if "failsafe" methods can be developed to reduce the cost of liquefaction and make it more energy efficient then it offers an exciting mode of hydrogen storage. Until such a "failsafe" method is developed, a better alternative to compressing hydrogen into a tank or cooling it to cryogenic temperatures is to soak it up in a metallic sponge, like in metal hydrides and chemical hydrides such as $LaNi_5H_6$ and $MgNiH_4$.
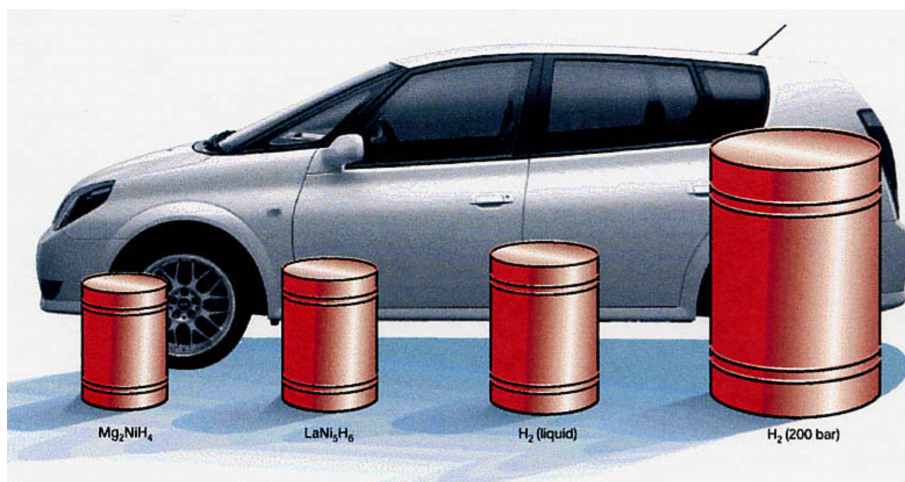
Fig. 1.2: Volume of 4 kg of hydrogen compacted in different ways, with size relative to the size of a car. (Reprinted with permission from Ref. [27])

When this project started (2004), NaAlH$_4$ was considered the ideal hydrogen storage material since it has favorable thermodynamics, and most important, it desorbs hydrogen reversibly. However, about a year later (2005) the DoE set a target of 6 wt% of hydrogen by the year 2010 for any potential hydrogen storage candidate. Theoretically, the maximum reversible capacity of hydrogen in NaAlH$_4$ is 5.6 wt% H$_2$, which is below the DoE target. As a result of this NaAlH$_4$ is no longer considered a potential hydrogen storage candidate. Figure 1.3 shows the gravimetric contents of some complex metal hydrides. From the figure, NaAlH$_4$ has a high gravimetric content of 7.8 wt% H$_2$ but its theoretical reversible capacity is 5.6 wt% H$_2$ due to the fact that the process

$$2\text{NaH} \rightarrow 2\text{Na} + \text{H}_2 \tag{1.1}$$

is never considered since it occurs at a relatively high temperature of more than 400°C. This high temperature is not practical for onboard storage purposes.

In spite of the failure of NaAlH$_4$ to meet the DoE's target, as will be explained later in the next section, NaAlH$_4$ remains an interesting material since it is one of the few solid state materials that can desorb hydrogen reversibly. Therefore the continued study of this compound will provide a fundamental understanding of the reversibility process within the hydrogen storage materials. We now present a more rigorous discussion of sodium aluminum hydride.
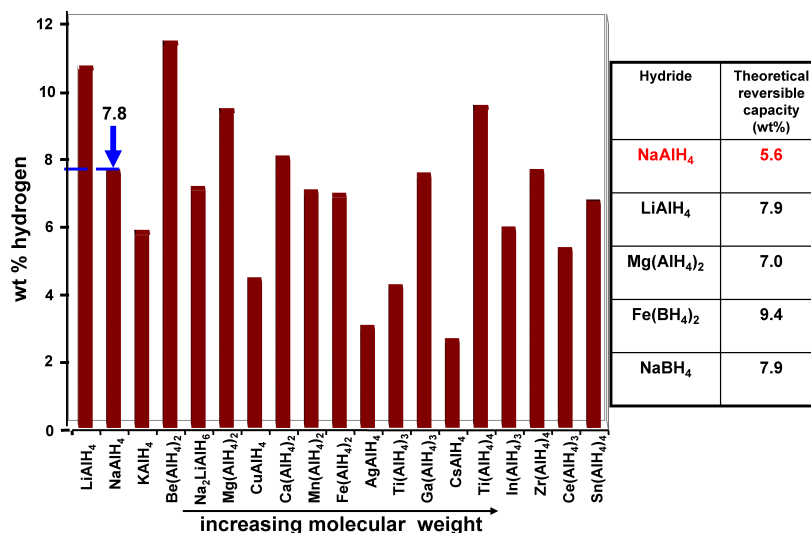
Fig. 1.3: Gravimetric contents of selected complex hydrides.

1.2   Hydrogen storage in sodium aluminum hydride

In the complex metal hydrides field, sodium alanate ($NaAlH_4$) is the most studied. This is due to its favorable thermodynamics and reversibility (when doped with titanium).[30–32] These favorable thermodynamics properties are illustrated in Fig. 1.4, which shows a van't Hoff plot of some technically interesting hydrogen storage materials. The van't Hoff plot is normally used to determine the sorption enthalpy. The dotted box shows the optimum temperature-pressure operational window for hydrogen fuel cell using a proton exchange membrane (PEM). As can be seen in the figure, $NaAlH_4$ falls within the requisite pressure-temperature region. In addition, Na_3AlH_6, which is an intermediate phase during the thermal decomposition of $NaAlH_4$, also falls within the optimum temperature-pressure window. This is one reason why $NaAlH_4$ generated a lot of interest as a potential hydrogen storage candidate at the beginning of this decade.

The goal of this project was to develop a force field for $NaAlH_4$ and use it to understand the dynamics governing the desorption of hydrogen in the material. To do this, it is important to understand the nature of chemical bonding and other subtle aspects of bonding in $NaAlH_4$. These little details are of paramount importance since a proper understanding of the complexities in chemical bonding of a system of interest, in this case $NaAlH_4$, is absolutely key in developing a well
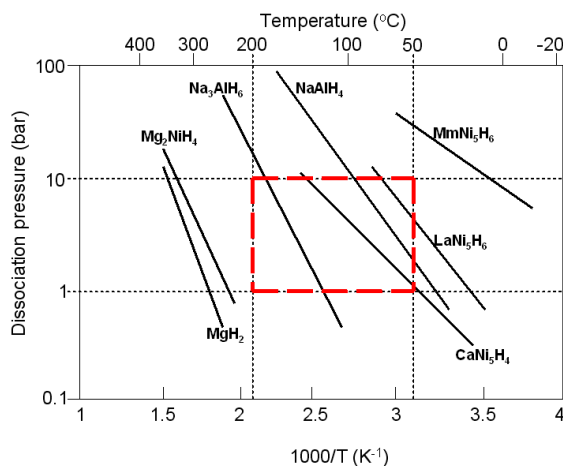
Fig. 1.4: van't Hoff plots of some alanates.

parameterized force field for the system. In the remaining part of this section we take a look at the crystal structure of $NaAlH_4$.

Crystallographically, under ambient conditions, $NaAlH_4$ crystallizes in the body centered tetragonal (space group: $I4_1/a$) with four formula units per unit cell (Z = 4). The Wyckoff positions of the atoms are as follows: Na is in 4a (0, 1/4, 1/8), Al in 4b (0, 1/4, 5/8) and H in 16f (x, y, z). Experimentally, its lattice constants were determined by Bel'skii et al.[33] to be $a = 5.021$ Å and $c = 11.346$ Å, while Lauher et al.[34] found $a = 5.020$ Å and $c = 11.330$ Å, using neutron diffraction. Works by Hauback et al.,[35] using neutron measurements on $NaAlD_4$, confirmed the space group, although with different H positions and lower lattice constants ($a = 5.0119$ Å, $c = 11.3147$ Å). α-Na_3AlH_6 has a monoclininc crystal structure (space group: $P2_1/n$) with lattice constants $a = 5.390$ Å, $b = 5.514$ Å, $c = 7.725$ Å and $\beta = 89.86°$.[36] Table 1.1 gives a summary of the lattice parameters of $NaAlH_4$ and Na_3AlH_6 as computed from experiments and as calculated by theory.

Figure 1.5(a) shows the crystal structure of $NaAlH_4$ while Fig. 1.5(b) shows the crystal structure of Na_3AlH_6. There are two chemical units per primitive cell for both $NaAlH_4$ and Na_3AlH_6. The aluminum atoms in $NaAlH_4$ are coordinated to four hydrogen atoms to form a tetrahedral moiety. The Al-H-Al angle within the tetrahedral complex is 107.5°. The Al-H distance, d_{Al-H}, is 1.638 Å. In α-Na_3AlH_6 aluminum atoms are octahedrally coordinated to hydrogen atoms. In this case the octahedral is slightly distorted and tilted. The average Al-H distance is 1.769 Å. Both $NaAlH_4$ and α-Na_3AlH_6 have four formula units per

Tab. 1.1: Lattice parameters for $NaAlH_4$ and Na_3AlH_6.

Na-Al-H phase	a(Å)	b(Å)	c(Å)	β angle	Symmetry	c/a
$NaAlH_4$						
Calc.[a]	4.995	4.995	11.008		$I4_1/a$	2.204
Calc.[37]	5.008	5.008	11.123		$I4_1/a$	2.221
Exp.[33]	5.021	5.021	11.346		$I4_1/a$	2.260
Exp.[38]	5.024	5.024	11.335		$I4_1/a$	2.256
Exp.[39]	5.027	5.027	11.371		$I4_1/a$	2.262
Exp.[35b]	5.012	5.012	11.315		$I4_1/a$	2.258
Exp.[35c]	4.980	4.980	11.148		$I4_1/a$	2.239
α-Na_3AlH_6						
Calc.[a]	5.378	5.570	7.762	89.91	$P2_1/n$	1.443
Calc.[37]	5.357	5.548	7.712	89.93	$P2_1/n$	1.440
Exp.[36]	5.408	5.538	7.757	89.83	$P2_1/n$	1.434
Exp.[40]	5.460	5.610	7.780	90.18	$P2_1/n$	1.425

[a] This work

[b] 295 K

[c] 8 K

unit cell.

Fig. 1.6 shows the AlH_4^- moiety and the calculated charges. The calculations were done at the B3LYP level of theory in CRYSTAL06.[41,42] The calculated charges in the case of aluminum (+2.118) and hydrogen (-0.773) are less than the nominal charges of +3 and -1 for aluminum and hydrogen, respectively. This implies that the bonding is not completely ionic since there is incomplete charge transfer from aluminum to hydrogen. Peles et al.[43] convincingly showed that this is due to the presence of polar-covalent interactions in the system. The bonding is largely ionic but there is also a strong covalent bonding influence. Even more interesting, is the work of Hauback et al.[35] in which they showed that there is anomalous lattice expansion when $NaAlD_4$ is heated up from 8 K to 295 K as shown in Tab. 1.1. They showed that when $NaAlD_4$ is cooled from 295 K to 8 K there is shrinkage of the tetragonal unit cell. The shrinkage is largest along the crystallographic c-axis, $\frac{\Delta c}{c}$ = -1.5% whereas, $\frac{\Delta a}{a}$ = -0.6%. This shows that the bonding along c-axis is weaker than along the a-b plane.

The other interesting detail is the effect of doping of $NaAlH_4$ with titanium. In 1997, Bogdanović, in a breakthrough discovery, showed that $NaAlH_4$ could desorb hydrogen reversibly by doping with titanium.[30] Later, Jensen and co-
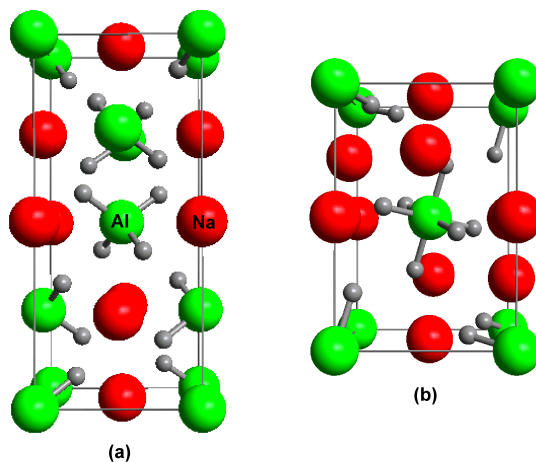
Fig. 1.5: Crystal structure of (a) $NaAlH_4$ (space group: $I4_1/a$) and (b) α-Na_3AlH_6 (space group: $P2_1/n$).

Na	+0.976
Al	+2.118
H	-0.773

Mulliken charges:

B3LYP Level of Theory –
CRYSTAL06
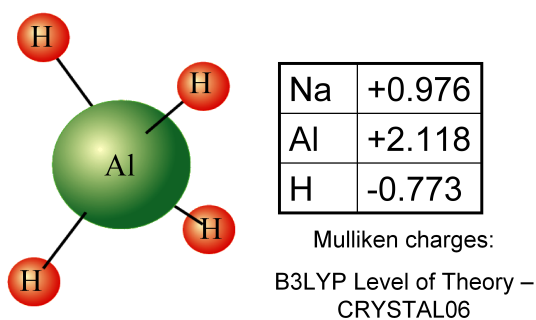
Fig. 1.6: Polar-covalent interaction in AlH_4^- moiety. The sodium ion is not included in the picture but the calculated charge (+0.976) is given. Sodium ion provides the electrostatic stabilization of the lattice.

workers found that kinetic enhancement was attainable by using alternative catalysts and doping methods.[31,32] However, in spite of the remarkable research progress, it seems as if we are still at the teething stage in so far as understanding the reversible sorption process in $NaAlH_4$ is concerned. What is known is that doping $NaAlH_4$ with titanium accelerates, renders reversible and lowers the release temperature of hydrogen. What is not known is the mechanism by which Ti promotes the cycling kinetics of hydrogen. In addition, the exact location of the titanium atoms[44,45] during the desorption process is unknown. Pertinent

questions in the sorption process includes the baffling issue on how is hydrogen desorbed and re-absorbed back into the host matrix. Is titanium a catalyst or a dopant? How does titanium aid the desorption and re-absorption process? Where exactly does titanium resides in during the desorption-reabsorption process? Is it located in the bulk or on the surface? Of sodium and aluminum, which one does titanium substitute for during the thermal decomposition process of NaAlH$_4$.

Some workers say that titanium resides in the bulk sodium site.[46–51] Others posit that titanium prefers to reside on the surface.[30,52] Experimentally, it has been shown that Ti combines with Al to form TiAl$_3$, which segregates to the zone boundary.[53,54] Løvvik and Opalka[55] showed that Ti prefers to substitute for Al whereas Íniguez and Yildrim[56] found that Ti prefers to occupy the Na site. Whereas in Ref.[47,49,50] the isolated atoms were used as the reference energies, in Ref.[56] the bulk cohesive energies of Ti, Al and Na were used as the reference energies. With this in mind, Araújo et al.[57] showed that in both cases the energy needed to remove a hydrogen atom is lower than in the case of undoped NaAlH$_4$, regardless of whether Ti occupied the Na or Al site. Clearly, there is still more work to be done by both theorists and experimentalists in trying to solve the mystery of the role of titanium in the (de)sorption process of NaAlH$_4$.

The goal of this research project was to have a clear picture of the detailed thermal decomposition mechanism of NaAlH$_4$ at the atomistic/molecular level. In particular we set out to understand the mechanism of mass transport of aluminum atoms during the thermal decomposition of NaAlH$_4$. Although there is an ongoing extension of this research work on the role of titanium during the thermal decomposition process of NaAlH$_4$ but this is outside the scope of this thesis. The following subsection (1.2.1) highlights the key objectives of the various chapters in this thesis.

1.2.1 Goals and scope of this thesis

This thesis investigates the dynamics of hydrogen desorption during the thermal decomposition of NaAlH$_4$ based on a reactive force field (ReaxFF). ReaxFF is parameterized using density functional theory (DFT) derived data. To parameterize the reactive force field, the DFT data (equations of state, partial charges and heats of formation) of the relevant condensed phase structures and molecular systems are computed and fit into the training set of ReaxFF. A number of simulations are carried out to ascertain that the force field is properly parameterized. These include comparing ReaxFF's equations of state and heats of reaction to the DFT input. Once properly parameterized, ReaxFF is used to do molecular dynamics simulations on small clusters of AlH$_3$, both in the gas phase and on Aluminum surfaces, with a view to understanding the dynamics

associated with the thermal decomposition of $NaAlH_4$.

This thesis is divided as follows:

- Chapter 1, this chapter, contains a general introduction to the thesis and discusses the research challenges. We discuss the issue of hydrogen economy. Why is hydrogen storage important and what are the criteria that materials must meet in order to be considered as viable hydrogen storage candidates? What kind of materials have been or are being considered as potential hydrogen storage materials? We zero in on sodium aluminum hydride, which is the main focus of this research work. Highlighted in the discussion on $NaAlH_4$ are the issue of mass transport of aluminum atoms and the role of titanium in cyclability process of $NAlH_4$ during its thermal decomposition.

- Chapter 2 dwells on the various theoretical techniques and tools deployed in this work. These include the density functional theory (DFT), Mulliken population analysis, the concept of force field and molecular dynamics.

- In chapter 3 parameterization of a reactive force field for NaH is discussed. The parameterized force field is then used to study the dynamics of hydrogen desorption in NaH cluster. During the abstraction process of molecular hydrogen from a cluster of NaH it is seen that charge transfer is correctly described by ReaxFF. In order to get a better understanding of the structural transformations during thermal decomposition of NaH, a heating run in a molecular dynamics simulation is performed. These runs exhibits a series of drops in potential energy, which are associated with cluster fragmentation and desorption of molecular hydrogen. This is found to be consistent with experimental works.

- In chapter 4 we delve into the energetics associated with possible intermediate structures during the thermal decomposition of $NaAlH_4$. The possible intermediate structures are Na_2AlH_5 and $Na_5Al_3H_{14}$. The conventional and experimentally observed intermediate phase in the thermal decomposition of $NaAlH_4$ is Na_3AlH_6. However, this pathway does not explain the mass transport of aluminum atoms. Using Na_2AlH_5 and $Na_5Al_3H_{14}$ as possible intermediate phases in the thermal decomposition process of $NaAlH_4$ it is shown that alane molecules are formed. The results are then used to show that alane might facilitate the mass transport of aluminum atoms. Alanes are now believed to be the facilitators of the mass transport of aluminum atoms during the thermal decomposition of $NaAlH_4$.

- Chapter 5 deals with the parameterization of a reactive force field for aluminum. Once parameterized, the force field is used to study the melting and crystallization of aluminum clusters. It is shown that this

force field gives results that are consistent with other force fields developed for aluminum systems. The aluminum force field forms the foundation for developing the reactive force field for aluminum hydride.

- Chapter 6 is devoted to the parameterizations and applications of a reactive force field for aluminum hydride (AlH_3). Most important the mechanism of mass transport of aluminum atoms using alane (AlH_3 molecules) as facilitators is explored. In the gas phase, alane and dialane (Al_2H_6) are very stable to decomposition. It is seen that if alanes were to facilitate the mass transport of aluminum atoms then the only way this situation can take place is if the alane molecules agglomerate. This thermodynamically driven spontaneous agglomeration followed by desorption of molecular hydrogen provides a mechanism on how mobile alane clusters can facilitate mass transport of aluminum atoms during the thermal decomposition of $NaAlH_4$. It is also shown that even on aluminum surface alanes oligomerize into larger clusters. The dynamical details of surface diffusion of alanes on Al(111) surface is also discussed. These results have been validated by the experimental works of Chabal et al.[58] and Go et al.[59] Finally, the issue of trapping of molecular hydrogen in solid AlH_3 is discussed. Using ReaxFF, we unambiguously identified a molecular hydrogen trapped in a cluster of AlH_3.

- Chapter 7 gives a comprehensive summary of this work. Based on our findings, a proposal is made on the possible thermal decomposition pathway of $NaAlH_4$.

References

[1] R. Coontz and R. Hanson. *in Towards a Hydrogen Economy*, volume 305, page 957. *special issue of Science*, 2004.

[2] D. W. Keith and A. E. Farrell. *Science*, 301:315–316, 2003.

[3] R. A. Pielke Jr., R. Klein, G. Maricle, and T. Chase. *Science*, 302:1329, 2003.

[4] D. M. Kammen and T. E. Lipman. *Science*, 302:226–229, 2003.

[5] T. K. Tromp, R. Shia, M. Allen, and Y. L. Eiler, J. M.and Yung. *Science*, 300:1740–1742, 2003.

[6] M. Balla and M. Wietschel. *Int. J. Hydrogen Energy*, 34:615–627, 2009.

[7] M. Dresselhaus et al. Basic research needs for the hydrogen economy. Report prepared by Argonne National Laboratory.

[8] C. E. Thomas, B.D. James, F. D. Lomax Jr., and I. F. Kuhn Jr. *Int. J. Hydrogen Energy*, 25:551–567, 2000.

[9] G. Nicoletti. *Int. J. Hydrogen Energy*, 20:759, 1995.

[10] J. W. Hanneken. *Int. J. Hydrogen Energy*, 24:1005–1026, 1999.

[11] W. Grochala and P. P. Edwards. *Chem. Rev.*, 104(1283-1315), 2004.

[12] F. Schüth, B. Bogdanović, and M. Felderhoff. *Chem. Commun.*, pages 2249–2258, 2004.

[13] A. M. Seayad and D. M. Antonelli. *Adv. Mater.*, 16:765–777, 2004.

[14] L. Schlapbach. *(Ed.) in Intermetallic Compounds I, Springer Series Topics in Applied Physics*, volume 63, page 10. Springer-Verlag, 1988.

[15] A. C. Dillon, K. M. Jones, T. A. Bekkedahl, C. H. Klang, D. S. Bethune, and M. J. Heben. *Nature*, 386:377–379, 1997.

[16] C. Liu, Y. Y. Fan, M. Liu, H. T. Cong, H. M. Cheng, and M. S. Dresselhaus. *Science*, 286:1127–1129, 1999.

[17] H. Dodziuk and G. Dolgonos. *Chem. Phys. Lett.*, 356:79–83, 2002.

[18] Y. S. Lee, E. C.and Kim, Y. G. Jin, and K. J. Chang. *Phys. Rev. B*, 66:73415, 2002.

[19] J. Li and S. Yip. *J. Phys. Chem. A*, 119(2376-2385), 2003.

[20] H. S. Cheng, A. C. Cooper, G. P. Pez, M. K. Kostov, P. Piotrowski, and S. J. Stuart. *J. Phys. Chem. B*, 109(3780-3786), 2005.

[21] X. M. Du and E. D. Wu. *Chin. J. Chem. Phys.*, 19:475, 2006.

[22] Z. Yang, Y. Xia, X. Sun, and R. Mokaya. *J. Phys. Chem. B*, 110:18424, 2006.

[23] Z. Yang, Y. Xia, and R. Mokaya. *J. Am. Chem. Soc.*, 129:1673, 2007.

[24] N. L. Rosi, J. Eckert, M. Eddaoudi, D. T. Vodak, J. Kim, M. O'Keeffe, and O. M. Yaghi. *Science*, 300:1127–1130, May 2003.

[25] O. M. Yaghi. *Nat. Mater.*, 6:92, 2007.

[26] J. L. C. Rowsell and O. M. Yaghi. *Angew. Chem. Int. Ed.*, 44:4670, 2005.

[27] L. Schlapbach and A. Züttel. *Nature*, 414:353–358, 2001.

[28] D. K. Ross. *Vacuum*, 80:1084–11089, 2006.

[29] F. Schüth. *Nature*, 434:712–713, 2005.

[30] B. Bogdanović and M. Schwickardi. *J. Alloys Compd.*, 253/254:1–9, May 1997.

[31] C. M. Jensen, R. A. Zidan, N. Mariels, A. G. Hee, and C. Hagen. *Int. J. Hydrogen Energy*, 24:461, 1999.

[32] R. A. Zidan, S. Takara, A. G. Hee, and C. M. Jensen. *J. Alloys Compd.*, 285:119, 1999.

[33] V. K. Bel'skii, B. M. Bulyshev, and A. V. Golubeva. *Russ. J. Inorg. Chem.*, 28:1528, 1983.

[34] J. W. Lauher, D. Dougherty, and P. J Herley. *Acta Cryst.*, page 1454, 1979.

[35] B. C. Hauback, H. W. Brinks, C. M. Jensen, K. Murphy, and A. J. Maeland. *J. Alloys Compd.*, 358:142–145, 2003.

[36] E. Rönnebro, D. Noreus, K. Kadir, A. Reiser, and Bogdanović B. *J. Alloys Compd.*, 299:101–106, 2000.

[37] S. M. Opalka and D. L. Anton. *J. Alloys Compds*, 356-357:486–489, 2003.

[38] J. P. Bastide, J. El Hajri, P. Claudy, and A. El Hajbi. *Synth. React. Inorg. Met. -Org. Chem.*, 25:1037, 1995.

[39] J. K. Gross, S. Guthrie, S. Takara, and G. Thomas. *J. Alloys Compd.*, 297: 270–281, 2000.

[40] J. P. Bastide, B. Bonnetot, J. M. Letoffe, and P. Claudy. *Mater. Res. Bull.*, 16:91, 1981.

[41] R. Dovesi, M. Causá, R. Orlando, C. Roetti, and V. R. Saunders. *J. Chem. Phys.*, 92:7402–7411, 1990.

[42] V. R. Saunders et al. *CRYSTAL2003 User's Manual, University of Torino.*

[43] A. Peles, J. A. Alford, Z. Ma, L. Yang, and M. Y. Chou. *Phys. Rev. B*, 70 (16):165105–+, October 2004.

[44] K. J. Gross, G. J. Thomas, and C. M. Jensen. *J. Alloys Compd.*, 330-332: 683, May 2002.

[45] T. Kiyobayashi, S. S. Srinivasan, D. Sun, and C. M. Jensen. *J. Phys. Chem. A*, 107(7671-7674), 2003.

[46] H. W. Brinks, C. M Jensen, S. S. Srinivasan, B. C. Hauback, D. Blanchard, and Murphy K. *J. Alloys Compd.*, 376:215, 2004.

[47] J. Iniguez, T. Yildirim, T. J. Udovic, M. Sulic, and C. M. Jensen. *Phys. Rev. B*, 70(6):060101–+, 2004.

[48] O. M. Løvvik and S. M. Opalka. *Phys. Rev. B*, 71(5):054103–+, February 2005.

[49] A. Marashdeh, R. Olsen, O. Løvvik, and G. Kroes. *Chem. Phys. Lett.*, 426: 180–186, July 2006.

[50] D. Sun, T. Kiyobayashi, H. T. Takeshita, N. Kuriyama, and C. M. Jensen. *J. Alloys Compd.*, 337:L8–L11, 2002.

[51] G. J. Thomas, K. J. Gross, N. Y. C. Yang, and C. Jensen. *J. Alloys Compd.*, 330-332:702, 2002.

[52] J. M. Bellosta von Colbe, B. Bogdanović, M. Felderhoff, A. Pommerin, and F. Schüth. *J. Alloys Compd.*, 370:104, 2004.

[53] E. H. Majzoub and K. J. Gross. *J. Alloys Compd.*, 356-357:363, 2003.

[54] V. Ozolins, E. H. Majzoub, and T. J. Udovic. *J. Alloys Compd.*, 375:1–10, 2004.

[55] O. M. Løvvik and S. M. Opalka. *Appl. Phys. Lett.*, 88:161917, 2006.

[56] J. Iniguez and Yildirim. *Appl. Phys. Lett.*, 86:103109, 2005.

[57] C. M. Araújo, S. Li, R. Ahuja, and P. Jena. *Phys. Rev. B*, 72(16), October 2005.

[58] S. Chaudhuri, S. Rangan, J. Veyan, J. T. Muckerman, and Y. J. Chabal. *J. Am. Chem Soc.*, 130:10576–10587, 2008.

[59] E. Go, K. Thuermer, and J. E. Reutt-Robey. *Surf. Sci.*, 437:377–385, September 1999.

Chapter 2

Theoretical Methods

"The electron does anything it likes," he said. "It just goes in any direction at any speed, forward or backward in time, however it likes, and then you add up the amplitudes and it gives you the wave-function." I said to him,"You're crazy." But he wasn't.

FREEMAN J. DYSON, *in reference to Richard Feynman*

Abstract

Many theoretical tools have been used in this work. Some of these are: density functional theory (DFT), molecular dynamics simulation, the concept of force field (in chemistry) or potential (physics), electron localization function, equation of state, electronegativity equalization method and Mulliken population analysis. In this chapter we take a brief rehash of these theoretical tools.

2.1   Density functional theory

Density functional theory (DFT) is nowadays the "standard model" for computational physicists, chemists and material scientists in the investigation of the properties of many-body systems. DFT has been shown to be quite accurate in predicting description of the groundstate (electronic structure, dynamical, structural, thermochemical stability and transport) properties of materials, in bulk, at surfaces and nanostructures.

The starting point for understanding DFT is to go back to the Thomas-Fermi (TF) model which was independently put forward by Enrico Fermi and L.H. Thomas.[1,2]

$$
E_{TF}[\rho] = A \int d^3\tilde{r} \rho(\tilde{r})^{5/3} + \int d^3\tilde{r} V_{ext}(\tilde{r})\rho(\tilde{r}) +
$$

$$
B \int d^3\tilde{r} \rho(\tilde{r})^{4/3} + \frac{1}{2} \int d^3\tilde{r} d^3\tilde{r}' \frac{\rho(\tilde{r})\rho(\tilde{r})'}{|\tilde{r} - \tilde{r}'|} \quad (2.1)
$$

where $A = \frac{3}{10}(3\pi^2)^{2/3}$, $B = -\frac{3}{4}(\frac{3}{\pi})^{1/3}$ and $V_{ext}(r) = -\sum_i \frac{Z_i}{|r-r_i|}$. The first term is the local approximation to the kinetic energy, the third term is the local exchange and the last term is the classical electrostatic Hartree energy. In 1928 Dirac added an exchange energy functional to the TF model in order to represent the exchange energy of the atom.

In 1964 Hohenberg and Kohn (HK)[3] laid the foundations of DFT with a view to systematically mapping out the many-body problem. Hohenberg and Kohn gave proofs of two key theorems of DFT:

1. The ground state electron density, ρ_0, of a many electron system in the presence of an external potential, V_{ext}, uniquely determines, except for a constant, the external potential, $V_{ext}(\tilde{r})$. This implies that all properties are functionals of the electron density.

   This theorem basically demonstrates the existence of a one-to-one mapping between the ground state electron density and the ground state wavefunction of a many-particle system, $v(\tilde{r}) \leftrightarrow \rho(\tilde{r})$.

2. The groundstate energy can be obtained variationally: the density that minimizes the total energy is the exact groundstate density ρ_0, i.e. $\mathcal{E}[\rho] \geq \mathcal{E}[\rho_0]$ for every trial electron density ρ.

The electron density, $\rho(\tilde{r})$, is given by

$$\rho(\tilde{r}) = N \int d^3r_2 \int d^3r_3 .... \int d^3r_N |\Psi(\tilde{r}, \tilde{r}_2, \tilde{r}_3 ....\tilde{r}_N)|^2 \qquad (2.2)$$

In 1965 Kohn and Sham (KS) gave a prescription for obtaining the energy of an N-electron density using a one-particle formalism. In this formalism the total ground state energy, the kinetic energy, the electron-electron interaction energy and the energy of the electrons in the external potential are all functionals of the electron density. KS considered a fictitious system of N non-interacting electrons which were subjected to a local potential $V_{KS}(\tilde{r})$, which was exactly mapped, density-wise, to a system of interacting electrons with a potential $V(\tilde{r})$. The total electronic energy in the KS formalism is

$$\begin{aligned} E[\rho] &= T_s[\rho] + V_{ext}[\rho] + U_{ee}[\rho] + E_{XC}[\rho] & (2.3) \\ &= \int dr V(\tilde{r})\rho(\tilde{r}) + \mathcal{F}[\rho] & (2.4) \end{aligned}$$

where

$$\mathcal{F}[\rho] = T[\rho] + \frac{1}{2} \int dr \int dr' \rho(\tilde{r})\rho'(\tilde{r}) \frac{e^2}{4\pi\epsilon_i |\tilde{r} - \tilde{r}'|} + E_{XC}[\rho] \qquad (2.5)$$

In equation (2.5), $T[\rho]$ is the kinetic energy of a non-interacting gas with density $\rho(\vec{r})$ and the second term is the classical electrostatic (Hartree) energy, $E_{XC}[\rho]$ is the exchange-correlation energy, which contains the non-classical electrostatic interaction energy and the difference between the kinetic energies of the non-interacting and interacting systems. Using equation (2.5) the variational problem of the HK density functional can be written as

$$\delta[\mathcal{F}[\rho] + \int dr V_{ext}(\tilde{r})\rho(\tilde{r}) - \mu(\int dr\rho(\tilde{r}) - N)] = 0 \qquad (2.6)$$

where μ is a Lagrange multiplier used to constrain the number of electrons to be N. Equation (2.6) can be rewritten as

$$\frac{\delta T_s[\rho]}{\delta\rho(\tilde{r})} + V_{ks}(\tilde{r}) = \mu \qquad (2.7)$$

where the KS potential $V_{KS}(\tilde{r})$ is given by

$$V_{KS}(\tilde{r}) = \int dr' \frac{\rho(\tilde{r}')}{|\tilde{r} - \tilde{r}'|} + V_{XC}(\tilde{r}) + V_{ext}(\tilde{r}) \qquad (2.8)$$

with

$$V_{XC}(\tilde{r}) = \frac{\delta E_{XC}[\rho]}{\delta\rho(\tilde{r})} \qquad (2.9)$$

The ground state density, ρ_0, for this non-interacting system can be obtained

by minimizing the KS energy functional:

$$\hat{H}_{KS}\psi_i(\tilde{r}) = [-\frac{1}{2}\nabla^2 + V_{KS}(\tilde{r})]\psi_i(\tilde{r}) = \mathcal{E}_i\psi_i(\tilde{r}) \tag{2.10}$$

The electron density is given as

$$\rho(\tilde{r}) = 2\sum_{i=1}^{N/2}|\psi_i(\tilde{r})|^2, \tag{2.11}$$

(the factor 2 accounts for the spin degeneracy).

The exact analytical form of the universal exchange-correlation energy, $E_{XC}[\rho]$, functional in DFT is not known. For this reason, it is approximated. One of the most widely used approximation is the local density approximation (LDA). The LDA substitutes the exchange-correlation functional of an inhomogeneous system with that of an electron gas computed at the local density i.e. it assumes that the exchange-correlation interactions between electrons in an atom, molecule, cluster or condensed phase can be approximated by the local interactions in an electron gas. The LDA's exchange-correlation energy is given by:

$$E_{XC}[\rho] = \int \epsilon_{XC}(\rho)\rho(\tilde{r})d^3r \tag{2.12}$$

where the exchange-energy per electron is that of the homogeneous gas

$$\epsilon_{XC}[\rho] = \epsilon_{XC}^{hom}(\rho)|_{\rho=\rho(\tilde{r})} \tag{2.13}$$

The exchange-correlation potential then takes the form

$$V_{XC}(\tilde{r}) = \frac{\delta E_{XC}[\rho]}{\delta\rho(\tilde{r})} = \epsilon_{XC}(\rho(\tilde{r})) + \rho(r)\frac{d\epsilon_{XC}}{d\rho}|_{\rho=\rho(\tilde{r})}$$

The values of exchange-correlation energy of homogeneous electron gases of varying densities have been calculated by Ceperley and Alder[4] using Monte Carlo methods. In the limit of slowly varying densities the LDA is exact. However, most physically interesting systems have rapidly varying densities thereby rendering the LDA to be a very crude approximation. Surprisingly, even in these cases the LDA gives very good results! Part of this success can be attributed to the fact that it obeys the sum rule for the exchange-correlation hole.[5] A spin polarized form of the LDA is the local spin density approximation (LSDA), which takes the electron spin into account as follows:

$$E_{XC}[\rho_\uparrow, \rho_\downarrow] = \int \epsilon_{XC}(\rho_\uparrow, \rho_\downarrow)\rho(\tilde{r})d^3r \tag{2.14}$$

An improvement of the LDA is the generalized gradient approximations (GGA),

which not only takes into account the local density but also includes the density fluctuations (inhomogeneities) via the gradient of the density at the same coordinate:

$$\mathrm{E_{XC}}[\rho] = \int \epsilon_{\mathrm{XC}}(\rho, \tilde{\nabla}_\rho)\rho(\tilde{r})\mathrm{d}^3\mathrm{r} \tag{2.15}$$

The GGA functional gives very good results for crystalline properties, ground state energies and molecular properties. Two of the most common analytic representation in use for $\epsilon_{\mathrm{XC}}^{\mathrm{hom}}$ are that of Perdew and Zunger [6] and that due to Perdew and Wang. [7] In this work we have mostly used the Perdew and Wang parameterization of the GGA (PW91).

In DFT computation, one makes an initial guess of the electron density, $\rho(\vec{r})$, (see Fig. 2.1). This electron density is used to calculate the effective potential
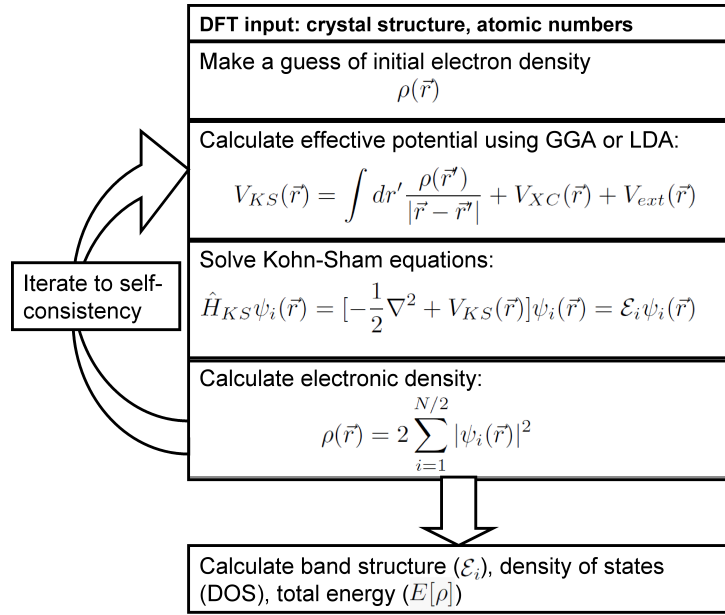
Fig. 2.1: The self-consistent iteration loop used in DFT computation.

using either the LDA or the GGA functional. The effective potential is then used to solve the KS equation after which the electronic density is computed. This process is repeated iteratively until self-consistency is achieved. Once the self-consistent loop is converged one can then calculate properties such as total energy, band structure and density of states (DOS).

Although the GGA has done much better than the LDA but there are cases

where the LDA has also given very good results. This is evident in the 5d transition metals[8] and in alumina structural predictions[9,10] where the LDA has scored favorably relative to the GGA. Well known deficiencies of LDA include overestimation of bulk modulus and cohesive energy, underestimation of lattice constant and thus cell volume. Thus, the LDA gives a lower bound to the pressure for a given volume. The GGA's shortcoming, on the other hand, include: underestimation of the bulk modulus and cohesive energy, overestimation of lattice constant and thus cell volume. It thus gives an upper bound to the pressure for a given volume.

An improvement of the GGA are the hybrid functionals. The hybrid functionals incorporate a portion of the exact exchange from Hartree-Fock with that from DFT's exchange-correlation form. For instance, the B3PW91 uses the Becke-3 exchange blended with the PW91 correlation. The B3LYP functional has a fraction of exact (Hatree-Fock) exchange and a correlation-energy functional from the LDA. It combines Becke's 3-parameter exchange functional[11] and the non-local correlation potential of Lee, Yang and Parr[12] as shown in equation (2.16).

$$E_{xc}^{B3LYP} = E_{xc}^{LDA} + a_0(E_x^{HF} - E_x^{LDA}) + a_x(E_x^{GGA} - E_x^{LDA}) + a_c(E_c^{GGA} - E_c^{LDA})$$
(2.16)

where the coefficients a_i are adjustable parameters, which are determined from a fit to atomization energies, ionization energies, atomic charges and proton affinities from a set of molecules. Their values are as follows: $a_0 = 0.20$, $a_x = 0.72$, and $a_c = 0.81$. E_x^{GGA} and E_c^{GGA} are the generalized gradient approximation formulation of the Becke 88 exchange functional[13] and the correlation functional of Lee, Yang and Parr,[12] and E_c^{LDA} is the Vosko, Wilk and Nusair (VWN) functional.[14] The B3LYP has done quite well in so far as estimating band gaps for a variety of materials are concerned.[15] For molecular systems, in this work, we have used the B3LYP as a benchmark for comparison with the PW91 functional.

The meta-GGA functionals, which are even more accurate than the GGA functionals, include a further term in the expansion. This term depends on the density, the gradient of the density and the Laplacian of the density.

Lastly, it is important to note that although DFT has been very successful in predicting properties of materials there are cases where it has spectacularly failed. An example is the strongly correlated materials e.g. the f-electron systems and transition metal oxides. This is due to the difficulty in dealing with the correlation effects between electrons. For instance, DFT predicts that FeO is metallic in spite of studies dating back to the 1980's that shows that it is an insulator. DFT predicts that hcp-Fe is antiferromagnetic[16,17] but detailed studies dating back to the 80s failed to find any magnetic ordering in hcp-Fe.[18–20]

2.2   Population analysis

Of great importance in force field modeling is the assignment of charges to the atoms in a system. There are many methods for calculating partial atomic charges. The most common method is Mulliken population analysis.[21] In Mulliken population analysis formalism, the overlap population is arbitrarily divided equally between two partner atoms. For a closed system where each electron molecular orbital is doubly occupied the integral over the electron density, equation (2.11), gives the total number of electrons:

$$N \quad = \quad \int \rho(\mathbf{r})d\mathbf{r} = 2 \sum_{i=1}^{N/2} \int \psi_i^*(\mathbf{r})\psi_i(\mathbf{r})d\mathbf{r} \tag{2.17}$$

$$= \quad 2 \sum_{i=1}^{N/2} \sum_{\alpha=1}^{M} \sum_{\beta=1}^{M} C_{\alpha i}^* C_{\beta i} \int b_\alpha^*(\mathbf{r})b_\beta(\mathbf{r})d\mathbf{r} \tag{2.18}$$

$$= \quad 2 \sum_{\alpha=1}^{M} \sum_{\beta=1}^{M} \sum_{i=1}^{N/2} C_{\alpha i}^* C_{\beta i} S_{\alpha\beta} \tag{2.19}$$

where $C_{\alpha i}$ are the coefficients of the basis functions in the molecular orbital for the α'th basis function in the i'th molecular orbital. $S_{\alpha\beta}$ is an overlap matrix of the basis function. Defining the density matrix as:

$$D_{\alpha\beta} = 2 \sum_{i=1}^{N/2} C_{\alpha i}^* C_{\beta i} \tag{2.20}$$

Then the number of electrons, equation (2.19), is given by

$$N = \sum_{\alpha=1}^{M} \sum_{\beta=1}^{M} D_{\alpha\beta} S_{\alpha\beta} = \sum_{\alpha=1}^{M} (\mathbf{DS})_{\alpha\alpha} = \mathrm{tr}(\mathbf{DS}) \tag{2.21}$$

where $(\mathbf{DS})_{\alpha\alpha}$ is the number of electrons associated with the basis function b_α. The net charge associated with an atom is defined as the difference in the number of electrons on the isolated free atom (i.e. the atomic number $\mathbf{Z_A}$) and the gross population of atoms:

$$\mathbf{q_A} = \mathbf{Z_A} - \sum_{\mu \in A} (\mathbf{DS})_{\alpha\alpha} \tag{2.22}$$

where $\mathbf{Z_A}$ is the charge of atomic nucleus A and the summation runs over only the basis functions that are centered at the atom with position $\mathbf{R}_A$.[22] Mulliken population analysis provides useful information on type of chemical bonding involved between atoms.[23]

2.3 Electronegativity Equalization Method

The concept of Electronegativity Equalization Method (EEM)[24,25] allows charge to move from an atom to its bonded neighbors such that the total charge remains the same. The principle of EEM was founded on the theory of DFT. To a second order, in a Taylor series, the energy needed to transfer an amount of charge between two sites can be approximated as

$$
\begin{aligned}
E(q_i) &\approx E(q_i)^0 + \left(\frac{\partial E(q_i)}{\partial q_i}\right) \cdot (q_i - q_0) + \frac{1}{2}\left(\frac{\partial^2 E(q_i)}{\partial^2 (q_i)}\right) \cdot (q_i - q_0)^2 + ... \\
&= E(q_i)^0 + \chi(q_i - q^0) + \eta(q_i - q^0)^2 \qquad (2.23)
\end{aligned}
$$

where

$$
\chi = -\mu = \left(\frac{\partial E(q_i)}{\partial q_i}\right) \text{ is related to the chemical potential} \qquad (2.24)
$$

$$
\eta = \frac{1}{2}\left(\frac{\partial^2 E(q_i)}{\partial^2 (q_i)}\right) = \frac{1}{2}\left(\frac{\partial \mu}{\partial q_i}\right) \qquad (2.25)
$$

are adjustable parameters referred to as electronegativity and hardness respectively. These parameters are unknown quantities in the EEM equations and can be calibrated by using a training set, which depends on the system being studied.

Considering a molecule with N atomic charges, the total electrostatic energy is the sum of the polarization term and the Coulomb interactions.

$$
E_{el} = \sum_i^N [E_i(q_i)^0 + \chi_i^0(q_i - q^0) + \eta_i^0(q_i - q^0)^2 + \sum_{j>i} \frac{q_i q_j}{R_{ij}}] \qquad (2.26)
$$

where χ_i^0 and η_i^0 are the electronegativity and hardness respectively of the isolated atom. q_i is the atomic charge on atom i and R_{ij} is the distance between atoms i and j. The Coulomb term in equation (2.26) accounts for the influence of surrounding atoms/molecules. However, for the total charge in the system to be kept constant a Lagrange multiplier is introduced into equation (2.26)

$$
L = \sum_i^N [E_i(q_i)^0 + \chi_i^0(q_i - q^0) + 2\eta_i^0(q_i - q^0)^2 + \sum_{j>i} \frac{q_i q_j}{R_{ij}}] - \lambda(\sum_i q_i - Q) \qquad (2.27)
$$

where

$$\sum_{i}^{N} q_i = Q, \text{ is the total charge of the system/molecule.} \qquad (2.28)$$

Minimizing equation (2.27) with respect to q_i yields

$$\chi_i = \frac{\partial E_{el}}{\partial q_i} = \chi_i^0 + 2\eta_i^0(q_i - q_i^0) + \sum_j \frac{q_j}{R_{ij}} = \lambda \qquad (2.29)$$

According to the principle of electronegativity equalization method,

$$\chi_i = \chi_1 = \chi_2 = \chi_3 = ... = \chi_N \qquad (2.30)$$

Equations (2.28) and (2.29) gives rise to N+1 linearly independent equations (EEM matrix).

$$
\begin{pmatrix}
2\eta_1^0 & \frac{1}{R_{12}} & ...... & \frac{1}{R_{1N}} & -1 \\
\frac{1}{R_{21}} & 2\eta_2^0 & ...... & \frac{1}{R_{2N}} & -1 \\
. & . & . & . & . \\
. & . & . & . & . \\
. & . & . & . & . \\
. & . & . & . & . \\
. & . & . & . & . \\
\frac{1}{R_{N1}} & \frac{1}{R_{N2}} & ...... & 2\eta_N^0 & -1 \\
1 & 1 & ...... & 1 & 0
\end{pmatrix}
\begin{pmatrix}
q_1 \\
q_2 \\
. \\
. \\
. \\
. \\
. \\
q_N \\
\chi_i
\end{pmatrix}
=
\begin{pmatrix}
-\chi_1 \\
-\chi_2 \\
. \\
. \\
. \\
. \\
. \\
-\chi_N \\
Q
\end{pmatrix}
$$

Solution of the EEM matrix gives the atomic charges.

2.4 Charge density

An important way of understanding chemical bonding is by studying charge distribution in real space. Charge density is an intrinsic property of the nature of chemical bonding in a structure and shows how charges are distributed within a given structure. Quantum mechanically, the electronic charge density is related to the wavefunction as shown in equation (2.11). An example of charge density plot is shown in Fig. 2.2(a), which shows the total charge density plotted along the $Na_5Al_3H_{14}$ (001) plane. The two types of AlH_6 octahedra in $Na_5Al_3H_{14}$ (see section (4.3.1)) can also be seen with the $Al(1)H_6^{3-}$ having four H neighbors on this plane and $Al(2)H_6^{3-}$ having two H neighbors. In the plot it is seen that charges are concentrated around H atoms with a slight directionality towards Al atoms while there are hardly any charges around Na. This shows that the bonding between $[AlH_6]^{3-}$ moiety and Na^+ is ionic. In the total charge

distribution it can be seen that the contours are not completely centered around hydrogen but rather are oblongated towards Al. This gives credence to the covalent-ionic interaction within complex metal hydrides.[26]

(a)   (b)
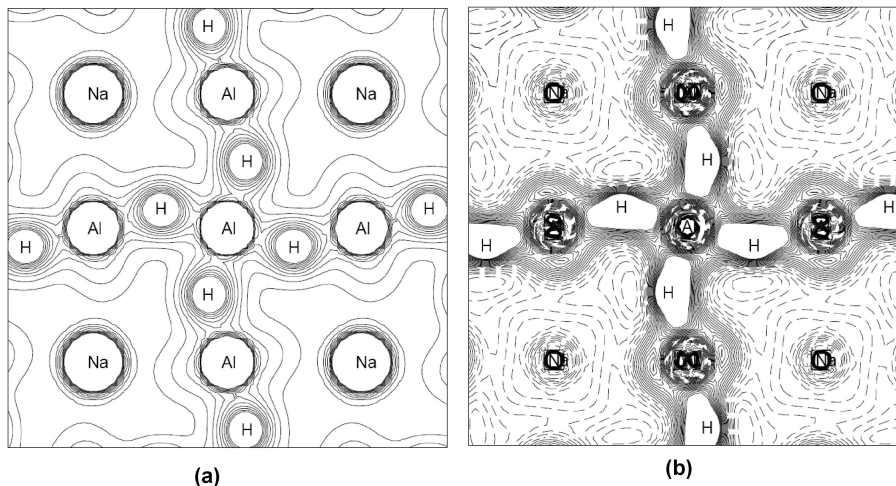
Fig. 2.2: (a) The total electron density map in the $Na_5Al_3H_{14}$ (001) plane containing Na, Al and H atoms. Most of the charge is concentrated in the region between H and Al while there is hardly any charge around Na. (b) The electron density difference map. The electron difference density gives the difference between the self-consistent electron density and the electron density obtained by a superposition of atomic charge distributions.

A better understanding of the chemical bonding within this structure ($Na_5Al_3H_{14}$) can be obtained by the charge density transfer, which is shown in Fig. 2.2(b). Charge density transfer is computed as the difference between the self-consistent electron density and a reference electron density obtained by a superposition of atomic charge distributions with the same spatial coordinates as in the solid under consideration, i.e.

$$\rho_d(r) = \rho(r) - \rho(r)_{superposition} \qquad (2.31)$$

The isolines in Fig. 2.2(b) are as follows: dashed lines-negative value, continuous lines-positive value and dot-dashed lines-zero value of the electronic density in electrons/bohr^3. In the total electron density map the range of the isolines is from -0.1 to 0.1 a.u. with a step of 0.01 while in the difference map the range is from -0.01 to 0.01 in steps of 0.001 a.u. A keen examination of the the $[AlH_6]^{3-}$ moiety shows that the positive contours are not centered on H but rather extended to Al. It is also evident in the charge transfer plot that most of the charge is concentrated around H while there is hardly any charge on Na.

The difference charge density plot essentially shows that charges are transferred from Al to H, leaving hydrogen negatively charged and Al positively charged.

2.5 Electron Localization Function

Another qualitative approach of understanding charge distribution is the concept of electron localization function (ELF), which was originally introduced by Becke and Edgecombe in the early 1990's. They defined it as a "simple measure of electron localization in atomic and molecular systems".[27] In DFT, the ELF is given by:

$$\text{ELF} = [1 + (\frac{\text{T}(\mathbf{r})}{\text{T}_\text{h}(\mathbf{r})})^2]^{-1} \tag{2.32}$$

The quantities in equation (2.32) are defined as follows:

1. Excess kinetic energy arising from Pauli exclusion principle, $\text{T}(\mathbf{r})$,

$$\text{T}(\mathbf{r}) = \frac{1}{2} \sum_i |\nabla \Psi_i(\mathbf{r})|^2 - \frac{1}{8} \frac{|\nabla \rho(\mathbf{r})|^2}{\rho(\mathbf{r})} \tag{2.33}$$

2. Thomas-Fermi kinetic energy density, $T_h(\mathbf{r})$,

$$\text{T}_\text{h}(\mathbf{r}) = 0.3(3\pi^2)^{2/3} \rho(\mathbf{r})^{5/3} \tag{2.34}$$

3. Local electronic density, $\rho(\mathbf{r})$,

$$\rho(\mathbf{r}) = \sum_i^n |\Psi_i(\mathbf{r})|^2 \tag{2.35}$$

By measuring electron localization in direct space, the ELF essentially discriminates the various types of chemical bonding within a system and is therefore a powerful too for visualizing chemical bonding in crystalline matrix as well as molecules.[28,29] By definition, ELF varies from 0 to 1.0, with a value close to 1.0 corresponding to a perfect localization of the electrons at that point. In homogeneous electron gas, which is used as a reference in definition of ELF, it takes a value of 0.5 and corresponds to perfect delocalization of electrons i.e. metallization of the system. In low electron density regions the ELF value is small. However, interpretations of values less than 0.5 should be justified. Figure 2.3 shows the ELF for $Na_5Al_3H_{14}$ plotted on the (100) plane. In the figure it can be seen that the region between Al and H has ELF values close to 1.0, suggesting that there is covalent interaction between Al and H. The almost negligible ELF between AlH_6^{3-} and Na^+ is a sign of ionic interaction.
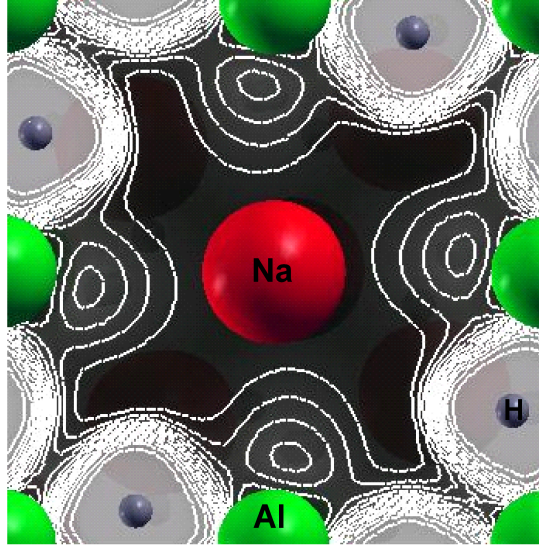
Fig. 2.3: Electron localization function for the valence electron density of the relaxed structure of $Na_5Al_3H_{14}$ plotted on the (100) plane. The contours are divided by intervals of 0.1.

2.6 Equation of state

In thermodynamics, an equation of state (EoS) is a thermodynamical equation which describes the mathematical relationship between two or more thermodynamical variables (such as volume, temperature, pressure and internal energy). Two of the most common EoS are the Murnaghan and Birch-Murnaghan equations of state.

2.6.1 Murnaghan equation of state

The energy-volume form of the Murnaghan EoS (F.D. Murnaghan[30]) is given as follows:

$$E(V) = \frac{BV_0}{B'} \left[\frac{1}{B'-1} \left(\frac{V_0}{V} \right)^{B'-1} + \frac{V}{V_0} - \frac{B'}{B'-1} \right] + E_0 \qquad (2.36)$$

The pressure is given by $P(V) = \frac{\partial E(V)}{\partial V}$, which gives

$$P(V) = \frac{B}{B'}\left[\left(\frac{V_0}{V}\right)^{B'} - 1\right] \tag{2.37}$$

from which we can calculate the bulk modulus:

$$B = -V\left(\frac{\partial P}{\partial V}\right)_T \tag{2.38}$$

The bulk modulus gives a measure of a material's resistance to uniform compression.

The pressure derivative of the bulk modulus is given by:

$$B' = \left(\frac{\partial B}{\partial P}\right)_T \tag{2.39}$$

A fitting to the Murnaghan equation of state, therefore, depends on four parameters: the equilibrium volume (V_0), the equilibrium energy (E_0), the bulk modulus (B) and its pressure derivative (B').

2.6.2 Birch-Murnaghan equation of state

This is an improvement of the Murnaghan's equation of state and was formulated by Francis Birch:[31]

$$P(V) = \frac{3B_0}{2}\left[\left(\frac{V_0}{V}\right)^{\frac{7}{3}} - \left(\frac{V_0}{V}\right)^{\frac{5}{3}}\right]\left[1 + \frac{3}{4}(B_0' - 4)\left\{\left(\frac{V_0}{V}\right)^{\frac{2}{3}} - 1\right\}\right] \tag{2.40}$$

and E(V) is given by:

$$E(V) = E_0 + \frac{9V_0 B_0}{16}\left\{\left[\left(\frac{V_0}{V}\right)^{\frac{2}{3}} - 1\right]^3 B_0' + \left[\left(\frac{V_0}{V}\right)^{\frac{2}{3}} - 1\right]^2\left[6 - 4\left(\frac{V_0}{V}\right)^{\frac{2}{3}}\right]\right\} \tag{2.41}$$

Figure 2.4 shows the equation of state of two different crystallographic modifications of NaH (the NaCl-type (B_1) and the CsCl-type (B_2)). Under ambient conditions of temperature and pressure, the B_1 phase is the most stable. The calculated bulk modulus for the stable NaCl-type phase is 23.7 GPa and the pressure derivative of the bulk modulus, B_0', is 3.8. This is in excellent match with the measured value of 19.4 ± 2.0 GPa[32] and the theoretical value of 22.8
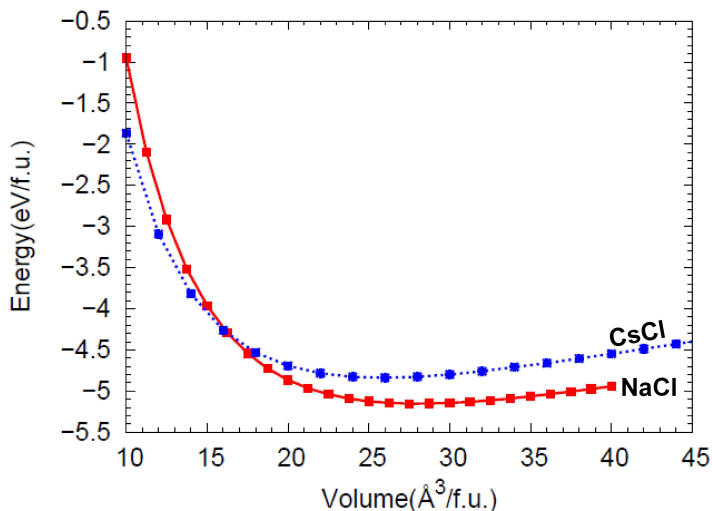
Fig. 2.4: Equation of state of NaH phases. Under ambient conditions of temperature and pressure the NaCl-type is the most stable.

GPa.[33] In all calculations in this work, we have used the Birch-Murnaghan EoS to compute the bulk modulus.

2.7   Molecular Modeling

Molecular modeling is a method used to calculate the conformational structures and energies of molecules based on the motion of the nucleus. Electrons are not considered explicitly, but rather it is assumed that they will find their optimum distribution once the positions of the nuclei are known. Therefore, a major assumption of molecular modeling is the validity of the Born-Oppenheimer approximation of the Schrödinger equation, which allows for the decoupling of electronic and nuclear motion. The Born-Oppenheimer approximation states that nuclei are much heavier than the electrons and therefore move much more slowly than electrons. Thus, nuclear motions, vibrations and rotations can be studied separately from electrons; the electrons are assumed to move fast enough to instantaneously adjust to any movement of the nuclei.

In general, processes involving large number of atoms (e.g. grain boundaries, disordered phases, interfaces, amorphous materials) and those involving large timescales (e.g. diffusion, condensation processes) are inaccessible in the

ab initio realm. And this is where molecular dynamics simulation methods have a cutting edge in calculating various chemical, thermodynamical and mechanical properties of these systems. In the heart of molecular dynamics simulations lies the interaction potentials (force fields) that forms the base of the calculations. Figure 2.5 shows the timescales and length scales of various computational techniques used in physics and chemistry. Quantum
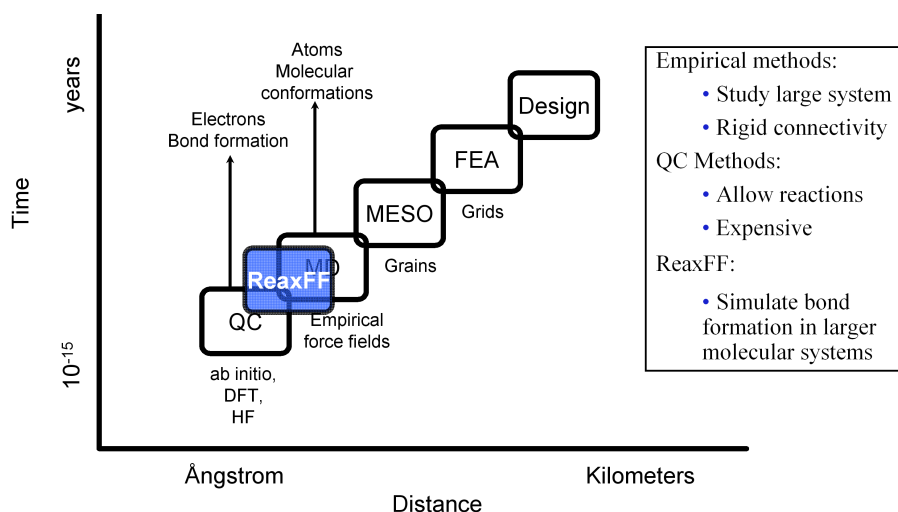
Fig. 2.5: Timescales and length scales of various computational techniques used in physics, chemistry and biology.

mechanics reigns in the femtosecond (fs) and angstrom regime. This is followed by molecular dynamics simulation in the pico/nanosecond and nanometer region. However, to do molecular dynamics one needs the right potential (force field) that aptly captures the chemical bonding in the system under investigation. So we can think of a force field as providing a link between quantum mechanical/experimetal data and molecular dynamics simulation. Once properly mathematically formulated (by including all the relevant chemical interactions), the force field can be parameterized using either experimental data or quantum mechanical (QM) data. Often QM is used because it provides information unavailable from experiment.

There are shortcomings of molecular modeling. These include: the results are pegged on the quality of the force field (junk in, junk out), size and time scales i.e. there is a length scale (few tens of angstroms) and timescale (few nanoseconds) limitation, conformational freedom of molecules might be enormous (grows exponentially with rotatable bonds), properties that are

dependant on electronic distribution such as photoemission cannot be computed using force fields.

2.8   Force Fields

A force field is a collection of the analytical forms and the parameter sets used to describe the nature of chemical bonding in a system of particles. The mathematical formulation of a force field depends on the complexity of bonding in the system. The basic idea of a force field is that when describing the bonding of a system from a classical point of view one looks at the various contributions to the chemical bond. The energy of the system is then apportioned into two parts: the bonding term and the non-bonded interactions as shown in Fig. 2.6.
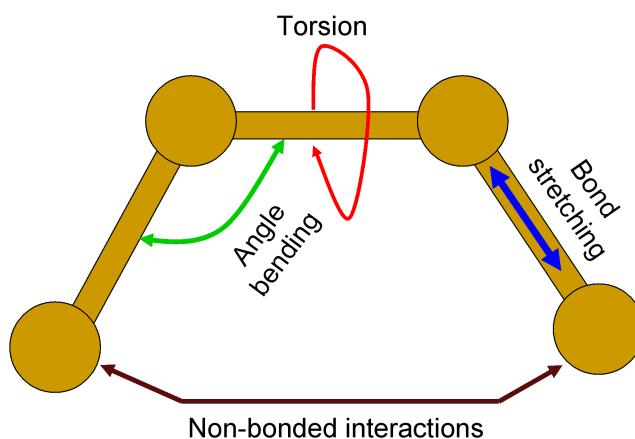
Fig. 2.6: The bonding and non-bonding terms.

In most chemical models the atoms are drawn as balls with rigid rods that connect them. In reality, the atoms vibrate about their equilibrium state. With this in mind, a better model is to use springs as bonds. In this model we can visualize the atoms as balls (connected by springs) which vibrate about their mean position. Figure 2.7 shows the various contributions to the chemical bonds using springs as connectors (bonds).

The energy of the various terms making up the system shown in Figs. 2.6 and
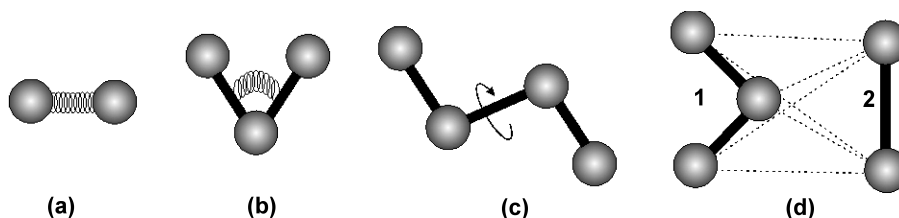
Fig. 2.7: (a) The equilibrium bond length term (b) The angle bend term (c) The torsion term (d) The non-bonding terms: The atoms in molecule 1 and 2 are not connected to each other but interact via the van der Waals and Coulomb forces.

2.7 is given by

$$E = \sum_{bond} v(l) + \sum_{angle} v(\theta) + \sum_{torsion} v(\phi) + \sum_{non-bond} \qquad (2.42)$$

The exact functional form of equation (2.42) depends on the system under investigation or in general on the program being used. Equation (2.43) shows one of the simplest forms of equation (2.42).

$$E = \sum_{bond} \frac{k_r}{2}(r_i - r_{eq})^2 + \sum_{angle} \frac{k_\theta}{2}(\theta_i - \theta_{eq})^2 + \sum_{dihedral} \sum_{n} \frac{k_\phi}{2}[1 + \cos(n\phi - \gamma)] +$$

$$\sum_{i,j} 4\epsilon_{ij}\left[\left(\frac{\sigma_{ij}}{r_{ij}}\right)^{12} - \left(\frac{\sigma_{ij}}{r_{ij}}\right)^6\right] + \sum_{i,j} \frac{1}{4\pi\epsilon_0}\frac{q_i q_j}{r_{ij}} \quad (2.43)$$

r_{eq}/θ_{eq} is the equilibrium distance/angle, k_r, k_θ, k_ϕ are force constants and q_i denotes partial charges. n controls the periodicity in the torsion term while γ, which is a shifting parameter, shifts the curve along the rotation angle (ϕ) axis.

The bond and angle terms in equation (2.43) represent harmonic approximation and are treated as springs as illustrated in Fig. 2.7. This is tantamount to saying that all the bonding terms are dictated by a simple harmonic potential thereby restraining the covalent bond from breaking. Any perturbations away from the equilibrium values are counteracted by a restoring force that acts to bring the system back to equilibrium. Therefore, this simple force field does not allow for dissociation/bond break-up/chemical reaction. The magnitude of the restoring force is a function of both the force constants k_r, k_θ and the equilibrium values r_{eq}, θ_{eq}.

The three different kinds of force field are: "**All-atom**" force fields, which takes into account every atom in the system by providing parameters for each

an every type of atom, including hydrogen; the "**United-atom**" force fields, which basically couple together the hydrogen and carbon atoms. For example in methyl groups the carbon and hydrogen atoms are treated as one interaction kernel; "**Coarse-grained**" force fields sacrifice a lot of individualistic chemical information at the altar of augmented computational efficiency.

The simplest force field is the Lennard Jones potential[34] which is an effective pair potential used to capture the dispersive van der Waals interaction between two uncharged particles e.g. argon atoms. It is mathematically expressed as:

$$V(r) = 4\epsilon \left[\left(\frac{\sigma}{r} \right)^{12} - \left(\frac{\sigma}{r} \right)^{6} \right] \tag{2.44}$$

where ϵ is the depth of the potential well, σ is the equilibrium separation at which the inter-particle potential is minimum and r is the distance between the particles. The repulsive part of the potential is given by the $\frac{1}{r^{12}}$ term, which describes the short range repulsive potential due to the distortion of the electron clouds at small distances. The $\frac{1}{r^{6}}$ term describes the long-range attractive tail of the potential between two particles.

For most systems of practical interest, the pairwise Lennard Jones potential is very rudimentary. Its use is therefore limited to rare gases where the dominant forces are van der Waaals. Beyond the Lennard Jones potential, there are many force fields that have been developed depending on the complexity of the chemical bonding in the system under investigation. In general, force fields can be divided into non-reactive and reactive force fields. As the name suggests, non-reactive force fields do not allow for chemical reactions. The most popular applications for non-reactive force fields is in biological simulations such as protein folding. Some of the most widely used non-reactive force fields includes: GROMOS, GROMACS, CHARMM, CVFF, DLPOLY and AMBER. Reactive force fields, on the other hand, do allow for bond breaking and bond formation (chemical reaction). Some of the well known reactive force fields are: Brenner, Tersoff, embedded atom method (EAM), empirical valence bond (EVB), ReaxFF and AIREBO.

The embedded atom method (EAM) was developed for metallic systems by Daw and Baskes.[35,36] In formulating the EAM, Daw and Bakes considered each atom as an impurity embedded in a host matrix provided by the rest of the atoms. They therefore apportioned the internal energy into a density dependent term that accounts for the cohesion arising from the electronic cloud in which the ions are immersed and a pairwise term that contains the core repulsion

$$E_{tot} = \sum_{i=1}^{N} F_i(\phi, i) + \frac{1}{2} \sum_{j=1(j \neq i)}^{N} \phi_{ij}(r_{ij}) \tag{2.45}$$

where $\phi, i = \displaystyle\sum_{j=1(j\neq i)} \rho_j(r_{ij})$.

E_{tot} is the total energy of the system of N atoms, $F_i(\phi, i)$ is the embedding energy needed to place an atom i in the electron density ϕ, i due to all neighboring atoms and ϕ_{ij} is the pairwise interaction between atoms i and j as a function of their separation r_{ij}. An improvement of EAM is the modified embedded atom method (MEAM),[37] which takes into account the screening effect of the interatomic interactions and angular dependence. Other potentials with a similar setting as EAM includes: glue model,[38,39] effective medium theory,[40] Streitz-Mintmire,[41] Finnis-Sinclair[42] and Sutton-Chen[43] potentials. Although they have the same analytical form as the EAM they differ in the way ϕ and ρ are built.

For covalently bonded systems the Brenner-Tersoff potential is the most widely used. The pioneering work of Tersoff[44] was based on the concept of bond order of Abell.[45] In the bond order formalism, the strength of a bond between two atoms is assumed to be dependent on the local environment/coordination surrounding them. In his work, Tersoff expressed the total binding energy as a sum over individual bond energies comprised of a repulsive term and an attractive term. The attractive term was the product of the bond order and a pairwise bond integral. Further, the bond order was parameterized in such a way that it depended on the local chemical environment about the bond. The concept of covalent bonding was incorporated into the bond order by introducing angularities involving the nearest-neighbor bond angles. Brenner[46] later, in 1990, extended the Tersoff potential so as to counter the overbinding of radicals and improper treatment of conjugacy inherent in the original Tersoff model.

The Tersoff formalism can capture both the covalent and metallic bonding in the same set-up. In this formalism, the potential V_{ij}, which is the energy of the bond between two nearest neighbors i and j, is written as

$$E_b = \sum_i \sum_{j>i} f_c(r_{ij})[V_{ij}^R(r_{ij}) - \bar{B}_{ij}V_{ij}^A(r_{ij})] \qquad (2.46)$$

$V^R(r)$ and $V^A(r)$ are the repulsive and attractive parts of the pairwise interaction, with Morse-like terms:

$$V^R(r_{ij}) = \frac{D_{ij}}{S_{ij}-1}\exp[-\sqrt{2S_{ij}}\beta_{ij}(r_{ij}-R_{ij}^{(e)})] \qquad (2.47)$$

$$V^A(r_{ij}) = \frac{D_{ij}S_{ij}}{S_{ij}-1}\exp[-\sqrt{\frac{2}{S_{ij}}}\beta_{ij}(r_{ij}-R_{ij}^{(e)})] \qquad (2.48)$$

D_{ij} is the equilibrium 'dissociation' energy i.e. the depth of the potential energy function, r_{ij} is the bond length (distance between the two nuclei of the atoms

between which the bond acts), $R_{ij}^{(e)}$ is the equilibrium bond length, β_{ij} is determined by the groundstate oscillation frequency of the dimer and S_{ij} is a distance parameter and is usually adjusted to the slope of the Pauling plot. If $S_{ij} = 2$ then the pair terms reduce to the well known Morse potential. The magnitude of S shows the range of interactions. Higher values of S correspond to longer ranged interactions and vice versa.[47]

In equation (2.46) $\bar{B}_{ij}$ is the bond order parameter given by

$$\bar{B}_{ij} = \frac{B_{ij} + B_{ji}}{2} \tag{2.49}$$

The bond order B_{ij} which, represents many-body coupling between the bond ij and local environment of atoms i and j and is given by

$$B_{ij} = (1 + \zeta^n \alpha_{ij}^n)^{-\frac{1}{2n}} \tag{2.50}$$

Where α_{ij} is a coordination assigned to the bond i.e. it counts the number of other bonds to atom i besides the ij bond, and is defined as

$$\alpha_{ij} = \sum_{k(\neq i,j)} f_c(r_{ik}) \exp[\lambda_3^3 (r_{ij} - r_{ik})^3] g(\theta_{ijk}) \tag{2.51}$$

In other words the presence of other bonds ik involving atom i weakens the bond ij. An atom with many neighbors form weaker bonds than an atom with few neighbors. $f_c(r)$ and $g(\theta)$ are suitable functions while λ_3 is an adjustable parameter controlling the overall strength of the 3 body part.

2.8.1   Reactive force field (ReaxFF)

ReaxFF, which stands for "reactive force field", is a force field developed by Adri van Duin at the Materials and Process Simulation Center (in the group of William A. Goddard III) at the California Institute of Technology (Caltech) for use in molecular dynamics simulations involving chemical reactions. Initially developed for hydrocarbons,[48] ReaxFF has been successfully applied to study Si/SiO$_2$ interfaces,[49] NaH systems,[50] MgH$_2$ systems,[51] Al/α-Al$_2$O$_3$ systems[52] and nitramines.[53] A key feature in ReaxFF is using the bond-order formalism that allows for bond breaking and formation as per Tersoff,[54] Brenner[46] and environment dependent interatomic potential (EDIP)[55] formalism. Charge calculation are fitted using electronegativity equalization method (EEM),[56] which allows for polarizability and geometry dependent charge distribution. ReaxFF calculates non-bonded (van der Waals and Coulomb) interactions between all atoms (including 1-2 and 1-4 interactions) making it suitable for

systems in which there are covalent and ionic interactions. It is this last feature, coupled with the ability to create and annihilate bonds, that makes ReaxFF attractive for modeling $NaAlH_4$ (and other complex metal hydrides) in which there is an interplay of both polar and covalent interactions.

The total energy expression in ReaxFF is partitioned into several partial energy contributions as follows:

$$E_{sys} = E_{bond} + E_{over} + E_{under} + E_{val} + E_{pen}$$
$$+ E_{conj} + E_{lp} + E_{tors} + E_{vdWaals} + E_{Coulomb} \quad (2.52)$$

The meaning of the terms in equation (2.52) can be found in Ref.[57] The bond energy, E_{bond}, is determined from the bond order, which is defined as:

$$BO'_{ij} = BO^{\sigma}_{ij} + BO^{\pi}_{ij} + BO^{\pi\pi}_{ij} = \exp\left[p_{bo,1} \cdot \left(\frac{r_{ij}}{r_o^{\sigma}}\right)^{p_{bo,2}}\right] +$$
$$\exp\left[p_{bo,3} \cdot \left(\frac{r_{ij}}{r_o^{\pi}}\right)^{p_{bo,4}}\right] + \exp\left[p_{bo,5} \cdot \left(\frac{r_{ij}}{r_o^{\pi\pi}}\right)^{p_{bo,6}}\right] \quad (2.53)$$

where $p_{bo,i}$ is bond order and $r_o^k (k = \sigma, \pi$ or $\pi\pi)$ is the bond radius. In equation (2.53), ReaxFF assumes that the bond order, BO^{σ}_{ij}, between a pair of atoms can be directly obtained from the interatomic distance r_{ij}. The prime indicates that this is an uncorrected bond order. The bond order varies between 0 and 3 with $BO = 1$, $BO = 2$ and $BO = 3$ corresponding to single, double and triple bond respectively. It is important that all partial energy contributions tied to valence interactions disappear smoothly when any of the bonds making up the valence or torsion angles dissociates. As such all the covalent interactions are expressed in terms of the bond orders. Thus whenever any bond dissociates these terms (e.g. E_{tors} and E_{val}) disappear smoothly. Using equation (2.53) the bond energy is defined as follows:

$$E_{bond} = -D_e^{\sigma} \cdot BO^{\sigma}_{ij} \cdot \exp\left[p_{be1}(1 - (BO^{\sigma}_{ij})^{p_{be2}})\right] - D_e^{\pi} \cdot B0^{\pi}_{ij} - D_e^{\pi\pi} \cdot BO^{\pi\pi}_{ij}$$
$$(2.54)$$

where D_e^{σ} is the sigma bond dissociation energy and p_{be1}, p_{be2} are bond energies.

A more rigorous mathematical formalism of ReaxFF is given in Refs.[53,57] and in ReaxFF user's manual.

2.9 Molecular dynamics

Molecular dynamics (MD) is an atomistic simulation method where the time dependent evolution of particles are subject to simple force rules. In other

words, MD calculates the time dependent behavior of atomic/molecular systems. In molecular dynamics, the behavior of a molecular system under different conditions can be simulated by varying the temperature, pressure among other parameters.[58] The atomic positions and velocities are advanced using Newton's equations of motion.

The most fundamental form of equation used to solve classical equations of motion for a system of N particles is the Lagrange equation of motion.

$$\frac{d}{dt}\left(\frac{\partial L}{\partial \dot{q}_j}\right) - \frac{\partial L}{\partial q_j} \tag{2.55}$$

where the q_j are generalized coordinates and $\dot{q}_j$ their corresponding time derivatives. The momentum conjugate to the coordinates q_j is given by

$$P_j = \frac{\partial L}{\partial \dot{q}_j} \tag{2.56}$$

The Lagrangian L is defined as

$$L = T - V \tag{2.57}$$

T = kinetic energy and V = potential energy.

In MD simulations, the positions of the particles are advanced step-by-step using an integration algorithm. There are many integration algorithm in use today. The choice of an integration algorithm depends on the degree of accuracy of the problem at hand. Some of the integration algorithms are: Verlet algorithm, velocity Verlet algorithm,[59] Beeman algorithm,[60] Leapfrog algorithm and Gear predictor-corrector algorithm.[61] Details on how these algorithms work can be found in Ref.[62] In this work the velocity Verlet algorithm has been used and is discussed in the following section.

2.9.1   Verlet Algorithm

The most widely used algorithm for integrating equations of motion is the Verlet algorithm.[59] It uses positions and accelerations at time t and the positions from time t-dt to calculate new positions at time t+dt. The positions are advanced by:

$$\mathbf{r}(t + \delta t) = 2\mathbf{r}(t) - \mathbf{r}(t - \delta t) + \delta t^2 \mathbf{a}(t)........ \tag{2.58}$$

The velocities can be obtained by subtracting equations 2.59 and 2.60, which are obtained by a Taylor expansion about r(t).

$$\mathbf{r}(\text{t}+\delta\text{t}) = \mathbf{r}(\text{t}) + \delta\text{t}\mathbf{v}(\text{t}) + \frac{1}{2}\delta\text{t}^2\mathbf{a}(\text{t}) + ... \tag{2.59}$$

$$\mathbf{r}(\text{t}-\delta\text{t}) = \mathbf{r}(\text{t}) - \delta\text{t}\mathbf{v}(\text{t}) + \frac{1}{2}\delta\text{t}^2\mathbf{a}(\text{t}) - .... \tag{2.60}$$

The velocities are then post-computed as

$$\mathbf{v}(\text{t}) = \frac{\mathbf{r}(\text{t}+\delta\text{t} - \mathbf{r}(\text{t}-\delta\text{t})}{2\delta\text{t}} \tag{2.61}$$

A major drawback of Verlet is that the positions are correct to dt^4 while the velocities are correct to dt^2. It is also of moderate precision. The Verlet algorithm is time reversible and therefore absolutely stable. An improvement of the Verlet algorithm is the velocity Verlet algorithm[63] in which positions, velocities and accelerations at time $t+\Delta t$ are obtained from the same quantities at time t as follows:

$$r(t+\Delta t) = r(t) + v(t)\Delta t + (\frac{1}{2})a(t)\Delta t^2 \tag{2.62}$$

$$v(t+\frac{\Delta t}{2}) = v(t) + \frac{1}{2}a(t)\Delta t \tag{2.63}$$

$$a(t+\Delta t) = -\frac{1}{m}\nabla v(r(t)+\Delta t) \tag{2.64}$$

$$v(t+\Delta t) = v(t+\frac{\Delta t}{2}) + \frac{1}{2}a(t+\Delta t)\Delta t \tag{2.65}$$

The velocity Verlet algorithm has a good stability for a relatively large time step. It also requires little computer memory. When modeling large number of atoms these qualities are of paramount importance.

2.9.2   Time step

Choosing the right time step is important since it is directly related to how the Newton's equations of motion are integrated and ultimately the forces on the atoms. Ideally, a large time step will lead to faster calculation but the energy will fluctuate wildly with the possibility of the simulation being catastrophically unstable. Too large a time step results in the dynamics not correctly conserving the total energy of the system. On the other hand, too short a time step leads to computation being needlessly slow. Suffice it to say that a bad choice of a time step leads to integration errors, which will cause fluctuations and drift in the total energy.

A good initial guess for the time step, δt, is that it should be roughly an order of magnitude less that the Einstein period:

$$t_E = \frac{2\pi}{\omega_E} \tag{2.66}$$

with

$$\omega_E^2 = \frac{\langle f_i^2 \rangle}{m_i^2 \langle v_i^2 \rangle} = \frac{1}{3} \langle \Delta r_i^2 V \rangle \tag{2.67}$$

The general rule of thumb is,

$$\delta t = \frac{1}{10f} \tag{2.68}$$

where f is the highest mode frequency. In other words, the step size should be set in such a way that there are 10 discrete steps per period of the highest oscillation.

For example, if H - stretches are in the range of 3000 cm^{-1} then

$$f \approx 3000\text{cm}^{-1} \times (3 \times 10^{10}\text{cm/sec}) = 90 \times 10^{12}/\text{sec} \tag{2.69}$$

$$T = \frac{1}{f} = 0.011\text{ps} = 11\text{fs} \tag{2.70}$$

The time step is then 1 femto second (fs).

A brute force approach, within the Verlet algorithm, is to conduct several short runs, with each run starting from the same configuration and covering the same run time. The root mean square (RMS) energy fluctuations for each run is then calculated. The RMS energy fluctuations is expected to be proportional to δt^2 within the Verlet formalism. For more information on calibrating the time step see Ref.[62]

2.10   Statistical ensembles

Herein we discuss the various types of statistical ensembles. (An ensemble is a collection of particles!). The three common ensembles are: grandcanonical ensemble (μVT) in which the chemical potential, the volume of the container and the temperature are kept constant; canonical ensemble (NVT) and microcanonical ensemble (NVE). We discuss the latter two in the following section.

2.10.1 Microcanonical (NVE) ensemble

This is an adiabatic process with no heat exchange whereby the system is isolated from changes in number of particles (N), volume (V) and energy (E). There is an exchange of kinetic and potential energy such that the total energy is conserved. NVE simulation is like a classical analog of single point calculations in DFT whereby one is only interested in knowing the properties of a system. However, in experiments usually the temperature and/or pressure are kept constant and the other factors allowed to vary. In MD simulation these are called canonical and isothermal-isobaric (NPT) simulations, respectively. We now discuss the canonical ensemble.

2.10.2 Canonical (NVT) ensemble

This is a constant number of particles (N), volume (V) and temperature (T) ensemble. At the heart of NVT simulations are thermostats used to maintain the temperature. Some of the common thermostat used in NVT simulation are Berendsen thermostat,[64] Andersen thermostat, Nosé-Hoover thermostat, Langevin thermostat and Gaussian thermostat. The principles on how these thermostats work can be found in the literature.[62]

The temperature of the system can be determined from equipartition theorem:

$$\frac{3}{2}Nk_BT = \sum_i \frac{1}{2}mv_i^2 \qquad (2.71)$$

where k_B is the Boltzman constant ($k_B = 8.617343 \times 10^{-5}$ eV/K).

Therefore the temperature, T, is defined by the ensemble average of kinetic energies of all the particles. It is, however, not possible to keep the temperature constant during simulation since fluctuations are bound to occur. It can only be kept constant as an average. The fewer the number of particles the more the fluctuations in temperature. There are various types of thermostats designed to keep the temperature constant, see Ref.[62]

All the NVT simulations in this work have been done using Berendsen thermostat and therefore I shall limit the discussion of thermostats to it.

2.10.3   Berendsen Thermostat

The idea of Berendsen thermostat is to rescale the velocities so as to control
the average temperature. The Berendsen thermostat pushes a system towards
a desired temperature rather than enforcing it. The scaling factor is given by:

$$\gamma = \sqrt{1 + \frac{\Delta t}{\tau}\left(\frac{T_d}{T} - 1\right)} \qquad (2.72)$$

where Δt = time step, τ = relaxation time/damping constant, T_d = de-
sired/target temperature and T = temperature of the system.

τ determines the degree of rescaling of the velocities and also the coupling of
the system to a hypothetical heat bath. The coupling of the heat bath to the
system is defined by the ratio between Δt and τ. $\tau >>> \Delta t$ - weak coupling,
$\tau \approx \Delta t$-strong coupling. For $\tau = \Delta t$ - simple velocity scaling. Essentially τ
defines how long it takes for a system to reach the desired temperature after
which the thermodynamical averages can be extracted from the atomic motions.
The larger the τ the longer it takes to reach a desired temperature after an
instantaneous change of T_d. The velocity is rescaled as follows:

$$\underline{v}(t + \frac{1}{2}\Delta t) \leftarrow \left[\underline{v}(t - \frac{1}{2}\Delta t) + \Delta t \frac{f(t)}{m}\right]\gamma \qquad (2.73)$$

A shortcoming of Berendsen thermostat is that it does not strictly follow the
canonical ensemble, nonetheless the deviation is small.

References

[1] E. Fermi. *Z. Phys*, 48:73–79, 1928.

[2] L. H. Thomas. *Proc. Camb. Phil. Soc*, 23:542–548, 1927.

[3] P. Hohenberg and W. Kohn. *Phys. Rev.*, 136:864–871, November 1964.

[4] D. M. Ceperley and B. J. Alder. *Phys. Rev. Lett.*, 45:566–569, August 1980.

[5] R. O. Jones and O. Gunnarsson. *Rev. Mod. Phys.*, 61:689–746, July 1989.

[6] J. P. Perdew and A. Zunger. *Phys. Rev. B*, 23:5048–5079, May 1981.

[7] J. P. Perdew and Y. Wang. *Phys. Rev. B*, 46:12947–12954, November 1992.

[8] M. Körling and J. Häglund. *Phys. Rev. B*, 45:13293–13297, June 1992.

[9] C. Verdozzi, D. R. Jennison, P. A. Schultz, and M. P. Sears. *Phys. Rev. Lett.*, 82:799–802, January 1999.

[10] Y. Yourdshahyan, U. Engberg, L. Bengtsson, B. I. Lundqvist, and B. Hammer. *Phys. Rev. B*, 55:8721–8725, April 1997.

[11] A. D. Becke. *J. Chem. Phys.*, 98:5648–5652, April 1993.

[12] C. Lee, W. Yang, and R. G. Parr. *Phys. Rev. B*, 37:785–789, January 1988.

[13] A. D. Becke. *Phys. Rev. A*, 38:3098–3100, September 1988.

[14] S. H. Vosko, L. Wilk, and M. Nusair. *Can. J. of Phys.*, 58:1200–+, 1980.

[15] J. Muscat, A. Wander, and N. M. Harrison. *Chem. Phys. Lett.*, 342, 2001.

[16] G. Steinle-Neumann, R. E. Cohen, and L. Stixrude. Magnetism in iron as a function of pressure. *J. Phys. Cond. Matt.*, 16:1109–+, April 2004.

[17] G. Steinle-Neumann, L. Stixrude, and R. E. Cohen. *Phys. Rev. B*, 60:791–799, July 1999.

[18] G. Cort, R. D. Taylor, and J. O. Willis. *J. Appl. Phys.*, 53:2064–2065, March 1982.

[19] R. D. Taylor, G. Cort, and J. O. Willis. *J. Appl. Phys.*, 53:8199–8201, November 1982.

[20] R. D. Taylor, M. P. Pasternak, and R. Jeanloz. *J. Appl. Phys.*, 69:6126–6128, April 1991.

[21] R. S. Mulliken. *J. Chem. Phys.*, 23:1833–1840, October 1955.

[22] A. Szabo and N. S. Ostlund. *Modern Quantum Chemistry: Introduction to Advanced Electronic Structure Theory*, page 151. McGraw-Hill Publishing Company, first edition edition, 1982.

[23] M. D. Segall, R. Shah, C. J. Pickard, and M. C. Payne. *Phys. Rev. B*, 54: 16317–16320, December 1996.

[24] W. J. Mortier, S. K. Ghosh, and S. Shankar. *J. Ame. Chem. Soc.*, 108:4315, 1986.

[25] G. O. A. Janssens, B. G. Baekelandt, H. Toufar, Mortier W. J., and R. A. Schoonheydt. *J. Phys. Chem.*, 99:3251, 1995.

[26] A. Peles, J. A. Alford, Z. Ma, L. Yang, and M. Y. Chou. *Phys. Rev. B*, 70 (16):165105–+, October 2004.

[27] A. D. Becke and K. E. Edgecombe. *J. Chem. Phys.*, 92:5397–5403, 1990.

[28] B. Silvi and A. Savin. *Nature*, 371:683–686, October 1994.

[29] S. I. Simak, U. Häußermann, I. A. Abrikosov, O. Eriksson, J. M. Wills, S. Lidin, and B. Johansson. *Phys. Rev. Lett.*, 79:1333–1336, August 1997.

[30] F. D. Murnaghan. The compressibility of media under extreme pressures. In *Proceedings of the National Academy of Sciences*, volume 30, pages 244–247. Springer-Verlag, Berlin, Heidelberg, New York, 1944.

[31] F. Birch. *Phys. Rev.*, 71:809–824, 1947.

[32] S. J. Duclos, Y. K. Vohra, A. L. Ruoff, S. Filipek, and B. Baranowski. *Phys. Rev.*, 36:7664, 1987.

[33] B. R. S.. Gupta and V. Kumar. *Czech. J. Phys.*, 33:1101, 1983.

[34] J. E. Lennard-Jones. *Trans. Faraday Soc.*, 28:333, 1932.

[35] M. S. Daw and M. I. Baskes. *Phys. Rev. Lett.*, 50:1285–1288, April 1983.

[36] M. S. Daw and M. I. Baskes. *Phys. Rev. B*, 29:6443–6453, June 1984.

[37] M. I. Baskes. *Phys. Rev. B*, 46:2727–2742, August 1992.

[38] F. Ercolessi, Parrinello M., and Tosatti E. *Philos. Mag. A*, 58:213, 1988.

[39] F. Ercolessi and J. B. Adams. *Europhys. Lett.*, 26:583–588, June 1994.

[40] K. W. Jacobsen, J. K. Norskov, and M. J. Puska. *Phys. Rev. B*, 35:7423–7442, May 1987.

[41] F. H. Streitz and J. W. Mintmire. *Phys. Rev. B*, 50:11996–12003, October 1994.

[42] M. W. Finnis and J. E. Sinclair. *Philos. Mag. A*, 50:45–55, July 1984.

[43] A. P. Sutton and J. Chen. *Philos. Mag. Lett.*, 61:139, 1990.

[44] J. Tersoff. *Phys. Rev. B*, 37:6991–7000, April 1988.

[45] G. C. Abell. *Phys. Rev. B*, 31:6184–6196, May 1985.

[46] D. W. Brenner. *Phys. Rev. B*, 42:9458–9471, November 1990.

[47] K. Huang, F. Milstein, and J. A. Baldwin. *Phys. Rev. B*, 10:3635–3646, October 1974.

[48] A. Strachan, A. C. van Duin, D. Chakraborty, S. Dasgupta, and W. A. Goddard. *Phys. Rev. Lett.*, 91(9):098301–+, 2003.

[49] A. C. T. van Duin, A. Strachan, S. Stewman, Q. Zhang, X. Xu, and W. Goddard III. *J. Phys. Chem. A*, 107:3803, 2003.

[50] J. G. O. Ojwang, R. van Santen, G. J. Kramer, A. C. T. van Duin, and W. A. Goddard. *J. Chem. Phys.*, 128:4714–+, April 2008.

[51] Sam Cheung, Wei-Qiao Deng, A. C. T. van Duin, and W. Goddard III. *J. Phys. Chem. A*, 109:851–859, 2005.

[52] Q. Zhang, T. Çağın, A. C. T. van Duin, W. A. Goddard, Y. Qi, and L. G. Hector. *Phys. Rev. B*, 69(4):045423–+, 2004.

[53] A. C. T. van Duin, S. Dasgupta, F. Lorant, and W. A. Goddard III. *J. Phys. Chem. A*, 105:9396, 2001.

[54] J. Tersoff. *Phys. Rev. Lett.*, 61:2879, 1988.

[55] M. Z. Bazant and E. Kaxiras. *Phys. Rev. Lett.*, 77:4370–4373, 1996.

[56] W. J. Mortier, S. K. Ghosh, and S. J. Shankar. *J. Am. Chem. Soc.*, 120: 2641, 1998.

[57] A. C. T. van Duin, A. Strachan, S. Stewman, Q. Zhang, X. Xu, and W. Goddard III. *J. Phys. Chem. A*, 107:3803, 2003.

[58] D. Frenkel and B. Smit. *Understanding Molecular Simulation.* Academic Press, Inc., Orlando, FL, USA, 2001. ISBN 0122673514.

[59] L. Verlet. *Phys. Rev.*, 159:98–103, July 1967.

[60] D. Beeman. *J. Comp. Phys.*, 20:130–+, February 1976.

[61] C. W. Gear. *Numerical Initial Values Problems in Ordinary Differential Equations.* Prentice-Hall, Englewood Cliffs, NJ, 1971.

[62] M. P. Allen and D. J. Tildesley. *Computer Simulation of Liquids.* Oxford University Press, Oxford, 2004.

[63] W. C. Swope, H. C. Andersen, P. H. Berens, and K. R. Wilson. *J. Chem. Phys.*, 76:637–649, January 1982.

[64] H. J. C. Berendsen, J. P. M. Postma, W. F. van Gunsteren, A. Dinola, and J. R. Haak. *J. Chem. Phys.*, 81:3684–3690, October 1984.

Part II

Modeling Studies

Chapter 3

Reactive force field for Sodium Hydride

"Research is to see what everyone else has seen and to think what nobody else has thought"

ALBERT SZENT-GYORGI

Abstract

A reactive force field for NaH, ReaxFF$_{NaH}$, has been parameterized against a training set of density functional theory (DFT) derived data. Tests were conducted to ascertain that ReaxFF was properly parameterized. This was done by comparing DFT's heats of formation of small representative NaH clusters with that of ReaxFF$_{NaH}$. The results and trend of ReaxFF$_{NaH}$ were found to be consistent with DFT values. ReaxFF$_{NaH}$ was then used to study the dynamics of hydrogen desorption in NaH-particles. It was seen that ReaxFF$_{NaH}$ properly described the charge transfer during the abstraction process of molecular hydrogen from Na$_{48}$H$_{48}$ cluster. Results on heat of desorption versus cluster size showed that there exists a strong dependence of the heat of desorption on the particle size, which implies that nanostructuring enhances desorption process. To gain more insight into the structural transformations of NaH during thermal decomposition a heating run in a molecular dynamics simulation was performed. The runs exhibited a series of drops in potential energy, associated with cluster fragmentation and desorption of molecular hydrogen.

3.1   Introduction

In this chapter the details of parameterization procedure for a reactive force field for NaH (ReaxFF$_{NaH}$) are discussed. NaH is primarily an ionic compound that is mostly used as a powerful base in organic and inorganic fine chemical synthesis. In organic synthesis it is used to deprotonate weak Bronsted acids to give the corresponding sodium derivatives. NaH reacts violently with water, is highly flammable and corrosive. Pure NaH is a silvery to whitish powder. It is normally formed by direct reaction of sodium and hydrogen at temperatures above 350 °C (623 K). In crystalline form NaH adopts a B$_1$-phase (face centered cubic) structure (space group $Fm\bar{3}m$). However, at high pressures the rock salt structure (B_1) transforms to the cesium chloride structure (B_2). This pressure induced phase transformation has been observed in diamond-anvil-cell high-pressure experiments.[1,2] In B_1 phase all atoms are on high symmetry sites. Each Na$^+$ ion is surrounded by six H$^-$ ions in an octahedral coordination.

At elevated temperatures of 698 K[3] NaH undergoes thermal decomposition during which time hydrogen molecules are desorbed. This release temperature is lower than the melting point of NaH, 1073 K, but much higher than the melting point of sodium, 371 K. Theoretically, Ke and Tanaka found that the desorption of hydrogen from NaH takes place at 726 K.[3] The thermal desorption process of molecular hydrogen from NaH proceeds as follows:

$$\text{NaH} \rightarrow \text{Na} + \frac{1}{2}\text{H}_2 \tag{3.1}$$

In previous works, ReaxFF was shown to be able to accurately predict the dynamical and reactive processes in hydrocarbons,[4] silicon/silicon oxides,[5] aluminum/aluminum oxides[6] and nitramines.[7] In section 3.2 the details of the parameterizations of ReaxFF$_{NaH}$ is presented. To ascertain that ReaxFF$_{NaH}$ is properly parameterized a comparison between _ab initio_ heats of formation of small representative NaH clusters with ReaxFF$_{NaH}$ is done. The results and trend of the heats of formation computed using ReaxFF$_{NaH}$ are found to be consistent with _ab initio_ values.

Further validation includes comparing the equations of state of condensed phases of Na and NaH as calculated from _ab initio_ and ReaxFF$_{NaH}$. There is a good match between the two results, showing that ReaxFF$_{NaH}$ is correctly parameterized as per the _ab initio_ training set. ReaxFF$_{NaH}$ is then used to study the dynamics of hydrogen desorption in NaH-particles. It is found that ReaxFF$_{NaH}$ properly describes the charge transfer during the abstraction process of molecular hydrogen from a cluster of Na$_{48}$H$_{48}$. Results on heat of

desorption versus cluster size shows that there is a strong dependence on the heat of desorption on the particle size, which implies that nanostructuring enhances desorption process. To gain more insight into the structural transformations of NaH during thermal decomposition a heating run in a molecular dynamics simulation is performed. These runs show a series of drops in potential energy, associated with cluster fragmentation and desorption of molecular hydrogen. This is consistent with experimental evidence that NaH dissociates at its melting point into smaller fragments. At a later part of this chapter the dynamical details including charge transfer during the process of abstraction of surface molecular hydrogen in sodium hydride clusters using ReaxFF$_{NaH}$ is discussed.

This chapter is organized as follows: The first part deals with force field parameterizations, the second part focuses on the tests taken to ensure that the force field is well parameterized and the last part deals with molecular dynamics simulation using ReaxFF$_{NaH}$.

3.2   Force Field Parameterization

Parameterization of ReaxFF$_{NaH}$ was done in line with the methodology used to develop ReaxFF$_{MgH}$.[8] The Kohn-Sham formulation of the density functional theory (DFT) data used in fitting ReaxFF parameters were obtained from VASP.[9] VASP uses a projector augmented plane wave method.[10] The Kohn-Sham ground state is self consistently determined in an iteration matrix diagonalization scheme. The generalized gradient approximation (GGA) of Perdew and Wang[11–13] was used to describe the exchange correlation effects for a particular ionic configuration. For the NaH phases, Brillouin zone integrations were performed using $13 \times 13 \times 13$ k-points as per the Monkhorst-Pack grid procedure[14] whereas for sodium the following kpoints were used: fcc-Na ($11 \times 11 \times 11$), bcc-Na ($11 \times 11 \times 11$), hcp-Na ($11 \times 11 \times 11$) and sc-Na ($17 \times 17 \times 17$). With these kpoints a total-energy convergence of within 1 meV was achieved. The reference configurations for valence electrons used were Na($3s^1$) and H($1s^1$).

For all volumes of the structures considered, the structures were fully optimized using force as well as stress minimization. The ions involved were steadily relaxed towards equilibrium until the Hellman-Feynman forces were minimized to less than 0.01 meV/Å (1 eV = 23.06 kcal/mol) during all relaxation runs using a conjugate gradient algorithm. In all calculations a well converged plane wave cutoff of 600 eV was used. To determine the equations of state (EoS), for a fixed cell volume of each structure the cell shape and atomic coordinates were fully relaxed until the forces were less that 1 meV/Å per atom. The structure with the lowest energy was then determined by plotting a total energy versus cell-volume curves for all the structures considered. This was then fitted to a

Birch-Murnaghan equation of state (EoS).[15]

Since VASP is a plane waves code it cannot compute Mulliken population analysis. Mulliken population analysis is implemented in CRYSTAL06,[16] which uses a periodic localized basis set (LCAO) approach. Therefore to determine the partial charges of the atoms in the crystal the cell parameters of the optimized structure in VASP was used as input in single point calculations in CRYSTAL06. Mulliken population analysis was then performed on the atoms in the crystal to obtain the mulliken charges. In CRYSTAL06, an all electron calculation was performed. The radical factors in the all electron basis set are expressed as a linear combination of Gaussian Type Functions (GTF) of the electron-nucleus distance according to 8(s)511(sp)G and 5(s)11(sp)1(p)G contractions for Na and H respectively.[17] To ensure high numerical accuracy the truncation tolerance for the numerical evaluation of bielectronic integrals (both the coulomb and the HF exchange series) were set at 10^{-8}, 10^{-8}, 10^{-8}, 10^{-8} and 10^{-16}. The meaning of these parameters can be found in Ref.[17] All the units are in a.u. (1 a.u. = 625.51 kcal/mol). Sampling points for Brillouin zone integration were generated using the Monkhorst-Pack (MP) scheme.[14] The irreducible Brillouin zone (IBZ) was sampled using 14 k-points. The Gilat net[18] was also set at 14 k-points. The convergence criteria on the total energy was set at 10^{-7} a.u.

Parameterization of the ReaxFF energy expressions was done by fitting to a training set containing the DFT derived EoS of pure Na and NaH condensed phases, reaction energies and bond dissociation profiles on small finite clusters. Phase transformations/crystal modifications in both Na and NaH systems during desorption process was accounted for by adding the high pressure phases of Na and NaH in addition to the ground state phase to the DFT calculations. In the case of Na, four phases were considered: bcc-Na (8-coordinated), sc-Na (6-coordinated), fcc-Na (12-coordinated) and hcp-Na (12-coordinated). For NaH, the NaCl-type (B_1) and the high pressure (B_2) phases were considered.

The bond and atom parameters for the ReaxFF energy functions (Tabs. 3.1 and 3.2) were determined from Na-Na and Na-H bonds in small NaH clusters such as NaH, Na_2H_2, Na_3H_3 and Na_4H_4 and from the EoS and cohesive energies of sodium metal and NaH condensed phases. The symbols of the parameters in Tabs. 3.1, 3.2, 3.3 and 3.4 are shown in Refs.[5,7]

Tab. 3.1: Bond Energy and Bond Order Parameters, (D_e^σ is in kcal/mol).

Bond	D_e^σ	$P_{be,1}$	$P_{be,2}$	$P_{b0,1}$	$P_{b0,2}$
Na-Na	60.0	-0.3548	2.4578	-0.05	4.518
Na-H	87.7	-0.7276	1.1502	-0.20	4.818

The EEM parameters (EEM-hardness η, EEM-electronegativity χ and EEM-

Tab. 3.2: Atom Parameters

Atom	$p_{ov/un}$	λ_{11}	$p_{v,5}$	$p_{v,6}$
Na	-2.50	3.99	8.0	2.5791
H	-15.76	2.15	1.0	2.8793

shielding parameter γ), which were parameterized to fit Mulliken charge distributions of small representative structures (NaH, Na_2H_2, Na_3H_3 and Na_4H_4) obtained from DFT calculations are shown in Tab. 3.3. ReaxFF successfully reproduces charge transfer for all the clusters considered.

Tab. 3.3: Coulomb Parameters

Atom	η(kcal/mol)	χ(kcal/mol)	γ(Å)
Na	115.3	-8.1425	0.3669
H	149.9	96.5799	0.7358

For the valence angle parameters, two cases have been considered H-Na-Na and H-Na-H. The clusters are first fully optimized in DFT calculations. This is followed by doing single point calculations in which the valence angles are modified while the other parameters are fixed. Table 3.4 shows the optimized valence angle parameters. The first line reflects a normal H-Na-Na angle

Tab. 3.4: Valence Angle Parameters

Angle	$\Theta\Theta_{0,0}^{\circ}$	k_a	k_b	$p_{v,1}$	$p_{v,2}$	p_{pen}	$p_{v,4}$
H-Na-Na	131.67	2.0048	5.0	0	0.7765	0	1.76
H-Na-Na	180.00	-27.9700	29.33	0	1.0074	0	1.56

interaction, with an equilibrium angle of 131.67° and force constants of 2.0048 kcal and 5.0 kcal. The second line aims to de-stabilize the Na-H-Na configuration (with the H directly in between the Na-atoms). Without the second angle this configuration gets to be too stable.

3.2.1 Bond Dissociation and Binding Energies

The bond energy in the reactive potential was optimized using DFT derived values of bond dissociation profiles of small NaH clusters. Figure 3.1 shows the

bond dissociation curve of NaH. The dissociation curves were constructed from
the equilibrium geometry using single point calculations by changing the bond
length. For the DFT case both the singlet and triplet states were considered.
ReaxFF gives an equilibrium bond length of 1.91 Å whereas DFT gives a value
of 1.895 Å. Chen et al. computed a theoretical Na-H bond length of 1.913 Å at
the QCISD/6-311G** level of theory.[19]
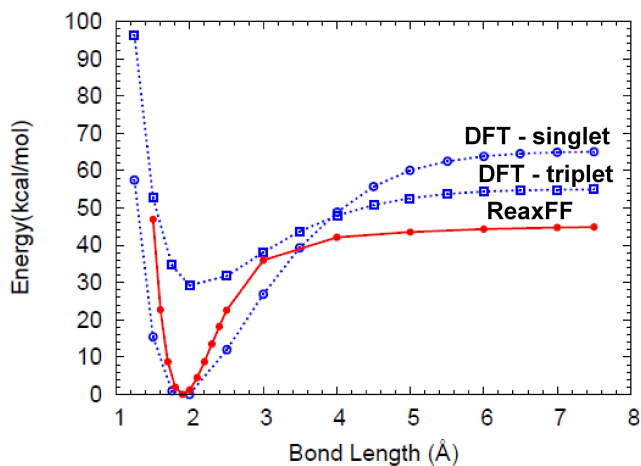
Fig. 3.1: Bond dissociation curves of small clusters of NaH as calculated by DFT and
ReaxFF. The energies were computed with reference to the equilibrium bond length's
energy. In the case of DFT the equilibrium energy of the singlet state was used as a
reference.

Another key test is on the adsorption energies on the Na surfaces. For (100)
hollow site DFT gives a value of 5.4 kcal/mol H_2 while ReaxFF gives 10.4
kcal/mol H_2 (see Fig. 3.2). For (100) bridge site DFT predicts the binding energy
to be 3.1 kcal/mol H_2 while ReaxFF predicts -1.7 kcal/mol H_2. For the (100)
top site DFT gives a binding energy of 57.4 kcal/mol H_2 while ReaxFF predicts
49.5 kcal/mol H_2. For (110) bridge site ReaxFF gives a binding energy of -1.2
kcal/mol H_2 compared to DFT value of 0.03 kcal/mol H_2. For (110) hollow site
ReaxFF gives a binding energy of 3.2 kcal/mol H_2, which is comparable to the
DFT value of 5.2 kcal/mol H_2.
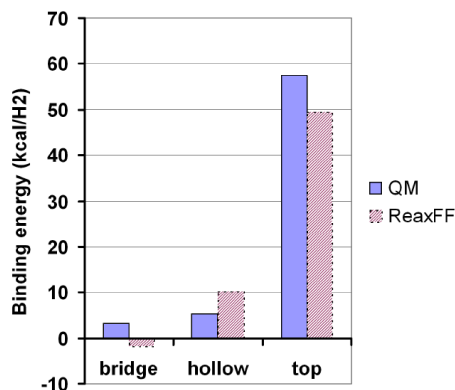
Fig. 3.2: Binding energies of dissociated H_2 on high symmetry sites on Na (100) surface.

3.2.2 Heats of Formation and binding energies

The possibility of a large cluster of NaH fragmenting into smaller clusters during heating runs was also considered by fitting into the training set the binding energies of NaH, Na_2H_2, Na_3H_3 and Na_4H_4 clusters. The binding energy is defined as:

$$BE = -[E(Na_nH_m) - E(Na_n) - mE(H_2)]/m \qquad (3.2)$$

where E(S) is the total energy of species S in the ground state. For molecular hydrogen, in DFT, E_{tot} = -156.87 kcal/mol. We used the total energy of molecular hydrogen because in ReaxFF the total energy is computed with reference to the isolated atomic species. Recall that all elements in their standard states (usually 101.325 kPa and 298 K) have a standard enthalpy of formation of zero since there is no change involved in their formation. Therefore, in ReaxFF, the total energy of isolated hydrogen atom is 0. The results are presented in Tab. 3.5. The DFT's binding energy of gas phase NaH from atomic

Tab. 3.5: Binding energies (in kcal/mol NaH) of small NaH clusters used in the training set.

Cluster	DFT	ReaxFF
NaH	28.5	6.9
Na_2H_2	0.8	-1.6
Na_3H_3	-6.3	-5.1
Na_4H_4	-8.5	-6.9

Na and molecular hydrogen is 28.51 kcal/mol, which is in good agreement with the literature value of 29.7 kcal/mol.[20] ReaxFF, on the other hand, gives a value of 6.91 kcal/mol. The table shows that there is good agreement on the value of binding energy between ReaxFF and DFT with increasing cluster size. For Na_4H_4 DFT gives a value of -8.5 kcal/mol NaH for the binding energy whereas ReaxFF gives a value of -6.9 kcal/mol NaH. This mismatch between DFT and ReaxFF values on the binding energy for a single NaH molecule is an artefact of ReaxFF. As the size of the cluster increases the values of ReaxFF closely parallels DFT values. For instance, for Na_3H_3 the binding energies are -6.3 kcal/mol NaH and -5.1 kcal/mol NaH as computed by DFT and ReaxFF respectively. The increase in binding energy with cluster size indicates the importance of ionicity (electrostatics) on chemical bonding in these systems.

Table 3.6 shows the bonding energies as computed by ReaxFF and DFT. For comparison the bonding energies computed in Ref.[21] are also shown.

Tab. 3.6: Bonding energies (in kcal/mol) of small NaH clusters used in the training set.

Cluster	DFT	ReaxFF	Ref.[21]
$NaH + NaH \rightarrow Na_2H_2$	-33.5	-45.9	-33.0
$NaH + Na_2H_2 \rightarrow Na_3H_3$	-38.8	-33.0	-37.0
$NaH + Na_3H_3 \rightarrow Na_4H_4$	-33.0	-33.9	-32.0

For the reaction $NaH + NaH \rightarrow Na_2H_2$, ReaxFF shows that Na_2H_2 is more stabilized with respect to the constituent NaH molecules by -45.9 kcal/mol whereas DFT gives a bonding energy of -33.5 kcal/mol (consistent with Ref.[21]) Thus ReaxFF value is approximately 11 kcal/mol higher than DFT value. For the two other cases there is a good match between the DFT values and ReaxFF values. The DFT values are consistent with those of Ref.[21] The values in Ref.[21] were calculated at the B3LYP level of theory with zero point energy corrections included.

For the condensed phase the experimental heat of formation of NaH is -13.49 kcal/mol NaH.[22] DFT gives a heat of formation value of -10.19 kcal/mol NaH while ReaxFF gives -11.60 kcal/mol NaH. Table 3.7 shows the interatomic distances and angles within the clusters as calculated by DFT, ReaxFF and from Ref.[19] For the atomic distances the ReaxFF values are consistent with those of DFT. For instance, from DFT computation the Na-H bond length in NaH cluster is 1.895 Å whereas ReaxFF gives 1.908 Å. For Na_4H_4 cluster DFT gives a Na-H bond length of 2.048 Å whereas ReaxFF gives 2.059 Å. For the angles, ReaxFF values approaches those of DFT as the size of the cluster increases. For instance from DFT calculation the Na-H-Na angle in Na_2H_2 is 82.27° whereas ReaxFF

Tab. 3.7: DFT and ReaxFF bond distances and bond angles of small NaH clusters. ReaxFF values are bracketed in bold while the values in square brackets are from Ref.,[19] which were computed at the MP2/6-311++G** level of theory.

Cluster	Distance(Å)	Angle(°)	
	d_{Na-H}	Na-H-Na	H-Na-H
NaH	1.895(**1.91**)[1.908]		
Na_2H_2	2.106(**2.075**)[2.121]	82.27(**107.58**)[84]	97.73(**72.43**)[96]
Na_3H_3	2.062(**2.074**)[2.079]	109.98(**124.35**)[112]	129.96(**115.68**)[128]
Na_4H_4	2.048(**2.069**)[2.059]	130.64(**131.86**)[127]	144.94(**138.30**)[144]

gives a value of 107.58°, a difference of 25.31°. In Na_3H_3 DFT computes the Na-H-Na to be 109.58° whereas ReaxFF gives 124.35°, a difference of 14.37°. In Na_4H_4 DFT gives the Na-H-Na angle to be 130.64° whereas ReaxFF gives 131.86°, a difference of 1.22°. Thus as the size of the cluster increases ReaxFF gives values that closely matches the DFT values. This is the reason why the values of binding energies of NaH clusters as computed by ReaxFF tends towards DFT values with increase in cluster size. It is worth noting that this artefact of ReaxFF is not a problem because the larger clusters are more relevant during the thermal decomposition of NaH. The very small clusters, being very unstable, are less likely to appear during the fragmentation of larger clusters of NaH.

3.2.3 Structural properties

The structural properties of NaH in the B_1-phase were computed by doing a fit to the total energy versus cell-volume data, as calculated by DFT and ReaxFF, using the Birch-Murnaghan equation of state.[15] The structural properties of NaH B_1-phase calculated using DFT and ReaxFF are given in Tab. 3.8. From the table, DFT gives a bulk modulus value of 23.7 GPa whereas ReaxFF gives 29.2 GPa. These values are consistent with the experimental bulk modulus of 19.4 ± 2.0 GPa[1] and theoretical values of 22.8 GPa[25] and 27 GPa.[23] For the B_1-phase the equilibrium lattice constant as computed by DFT is 4.82 Å while ReaxFF gives the lattice constant to be 4.78 Å. The experimental value of lattice constant is 4.91 Å (at 298 K).[1] For the B_2-phase, ReaxFF gives an equilibrium lattice constant of 2.993 Å, which agrees well with DFT value of 2.995 Å.

For both Na and NaH, the ability of ReaxFF to capture the relative stability of their condensed phases was tested against a number of Na and NaH crystal modifications. For each an every phase of Na-metal (fcc, hcp, sc and bcc) and NaH (B_1 and B_2 phases) considered in this work, the DFT energies were computed for a broad range of volumes, describing both expansion and

Tab. 3.8: Equilibrium lattice constant a(Å), bulk modulus B_0(GPa) and the pressure derivative of the bulk modulus B_0' for NaH in B_1-phase calculated using DFT and ReaxFF. Experimental values and theoretical calculations from other workers are also shown.

	a	B_0	B_0'	Temp
DFT (this work)	4.82	23.7	3.8	0
ReaxFF	4.78	29.2		0
Experiment (298 K)	4.91[a]	19.4 ± 0.2[a]	4.4 ± 0.5[a]	298
Theory	4.77[b]	27[b]	3.7[b]	0
	4.92[b]	20[b]	4.1[b]	0[c]
	4.89[d]	23.4[d]		0[c]
	4.74(4.87)[e]	27.2(24)[e]		0

[a] Reference.[1]
[b] Reference.[23]
[c] Zero point energy included.
[d] Reference.[3]
[e] Reference.[24]

compression. Figs. 3.3 and 3.4 compares the ReaxFF results against the DFT values. ReaxFF correctly describes the EoS for NaH phases and excellently estimates the relative phase stability of the two phases vis-á-vis the DFT predictions. DFT predicts that the B_1-phase is 7.24 kcal/mol more stable than the B_2-phase whereas ReaxFF gives a value of 5.83 kcal/mol.

Figure 3.4 shows that ReaxFF correctly describes the relative phase stabilities of 3 phases of sodium metal although it gives a rather flat curve for the volume expansion parts of the EoS. However, this will not cause a problem since the most relevant and physically interesting parts are the equilibrium volumes from which the relative phase stabilities are deduced. Moreover, all the metal phases dissociate smoothly to give the right dissociation energy (ReaxFF gives 21.61 kcal/mol for the atomization of bcc sodium metal, experiment gives 25.90 kcal/mol (at 25°C)[26] and DFT gives 28.5 kcal/mol). Figure 3.5 shows that ReaxFF produces the right dissociation curve at higher volumes for the bcc phase.

The energies in Figs. 3.4 and 3.5 were computed with respect to the bcc structure's equilibrium volume energy. DFT predicts that the bcc phase is more stable than the fcc, Al5 and sc phases by 0.34 kcal/mol, 0.64 kcal/mol and 3.76 kcal/mol respectively. ReaxFF, on the other hand, predicts that the bcc phase is more stable than the fcc, Al5 and sc phases by 0.32 kcal/mol, 0.54 kcal/mol and 1.65 kcal/mol respectively.
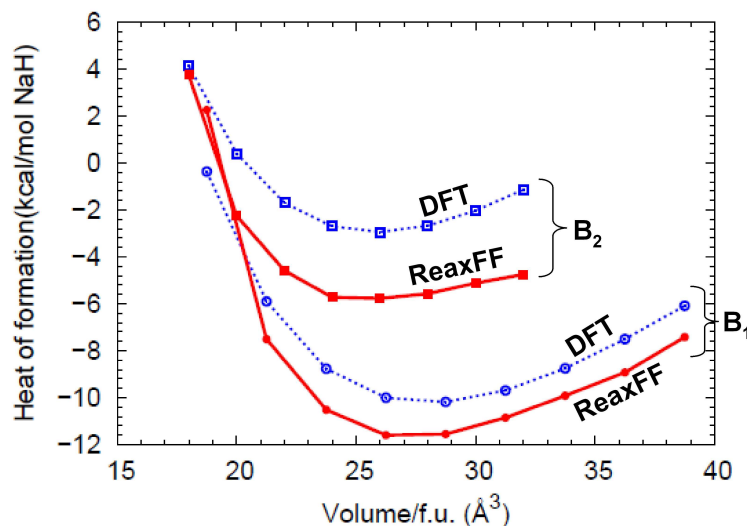
Fig. 3.3: Equations of state for the two phases (B_1-phase and B_2-phase) of NaH as computed using DFT and ReaxFF.

3.3 Abstraction of Hydrogen

ReaxFF was used to get a better insight on the nature of structural transformation during desorption of hydrogen. To do this, we simulated successive abstraction of surface molecular hydrogen from $Na_{48}H_{48}$ cluster. This is shown in Fig. 3.6. The process of abstraction is given by:

$$Na_{48}H_{n+2} \rightarrow Na_{48}H_n + H_2 \qquad (3.3)$$
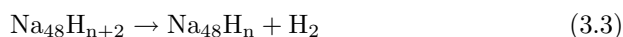
where n = 46 to 0. During the abstraction process, clusters were first minimized so as to find the nearest metastable conformation i.e. to relieve bad non-bonded contacts or to correct badly formed geometry. The minimized clusters were then equilibrated at 300 K for 50000 steps (using a time step of 0.25 fs). This was followed by annealing the equilibrated structures, at 300 K, to 0 K, after which molecular hydrogen abstraction was simulated by removing two hydrogen atoms from the 0 K configuration. This was done iteratively until all the H_2 atoms were removed. The entire process was repeated five times and the internal energy was then averaged.

There are two stages shown in Fig. 3.7, which shows that there is a non-linear trend in particle stability with respect to molecular hydrogen abstraction. During the abstraction process the surface hydrogen atoms are removed first
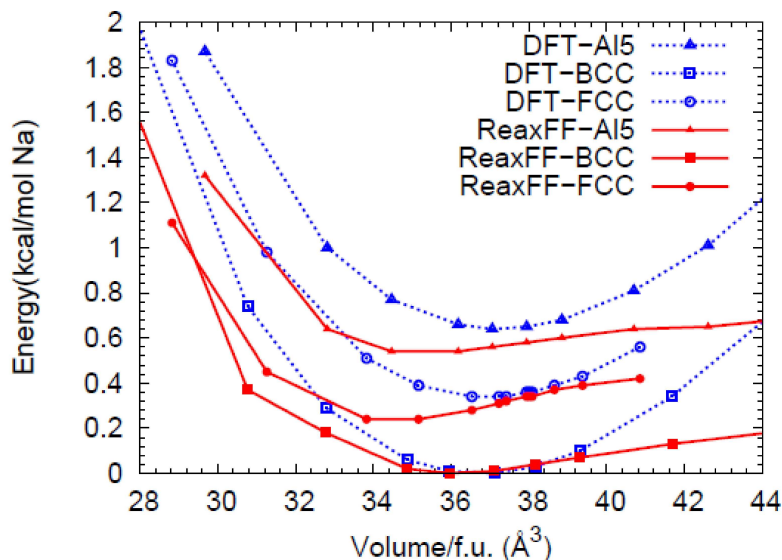
Fig. 3.4: Equations of state (compression and expansion) for three crystallographic phases of Na (Al5, bcc and fcc) as computed by DFT and ReaxFF.

since they have less number of neighbors and therefore lower stability. Upon hydrogen depletion, some of the bulk Na atoms comes to the surface to replace the depleted hydrogen atoms. In the initial structure, the surface hydrogen atoms mostly occupy the less stable two fold (bridge) sites. However, as more and more surface molecular hydrogen are abstracted the remaining hydrogen atoms adopt a subsurface conformation and they occupy three and four fold sites. With increasing depletion of hydrogen atoms, the sodium atoms in the bulk replaces the depleted hydrogen atoms. These remaining hydrogen atoms are more strongly bound in the system. This explains the trend in part (I) of Fig. 3.7. What is interesting about Fig. 3.7 is the change in the slope of the curve, (II), after slightly more than a half of the hydrogen atoms have been abstracted from the system. The reason for this change is that metallization dominates over ionization. This stage can be thought of as a situation in which hydrogen atoms are dissolved in Na metal matrix, with the metal retaining its metallic nature. The scattering in Fig. 3.7 is related to the rearrangement and cluster fragmentation during the abstraction process. Fig. 3.8 shows the desorption energy as a function of the number of H_2 molecules desorbed. The desorption energy is defined as

$$E^{desorb} = [E_{Na_{48}} + E_{\frac{n}{2}H_2}] - E_{Na_{48}H_n} \qquad (3.4)$$
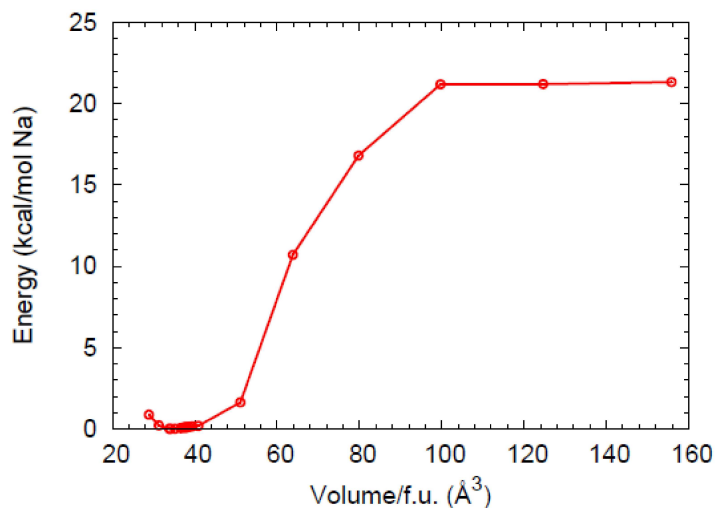
Fig. 3.5: The equation of state of the bcc phase of Na including volume expansions to the dissociation limit. In both cases the energies are calculated with respect to the equilibrium energy of the bcc-phase.
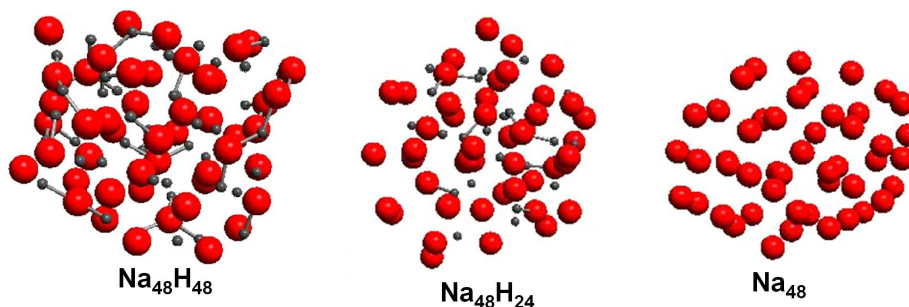
Fig. 3.6: Geometries of the annealed structures of$Na_{48}H_{48}$, $Na_{48}H_{24}$ and Na_{48}. The big balls represent sodium atoms.

where $n = 2, 4, 6, 8, ..., 48$.

From Fig. 3.8 one deduces that the energy of desorption for $Na_{48}H_{48}$ cluster on average is about 14 kcal/mol Na. This is interesting since it means that the molecular hydrogen desorption energy for a completely dehydrogenated $Na_{48}H_{48}$ cluster is more than the bulk desorption energy (11.6 kcal/mol NaH). One reason for this is the steric interactions arising from the hydrogen atoms in the bulk-
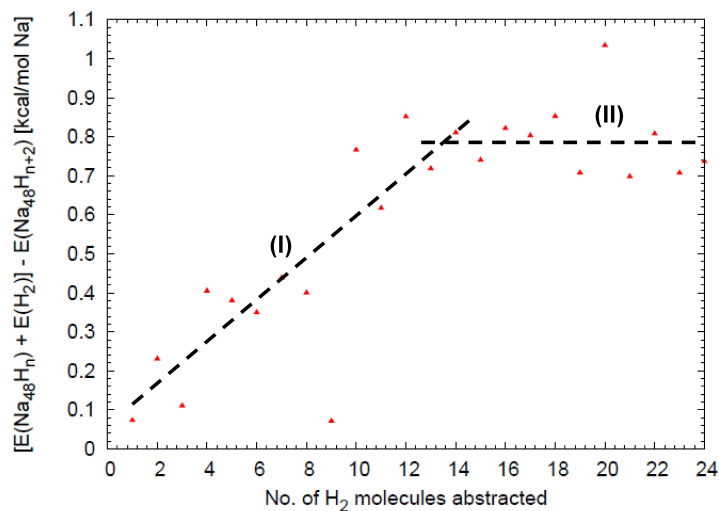
Fig. 3.7: Abstraction energy, $\Delta E = \{[E(Na_{48}H_n) + E(H_2)] - E(Na_{48}H_{n+2})\}$ as a function of the number of hydrogen molecules abstracted.

phase repulsing each other by means of Coulomb and three-body interactions. So an isolated H atom in a cluster may have higher abstraction energy.

The charge distribution plots for three different conformations during the abstraction runs are shown in Fig. 3.9. The hydrogen atoms are negatively charged. It can be seen in Fig. 3.9 ($Na_{48}H_{48}$) that the surface sodium atoms, which have fewer numbers of hydrogen atom neighbors, have low charges. The same applies to hydrogen atoms. As one moves from Fig. 3.9 ($Na_{48}H_{48}$) to Fig. 3.9 ($Na_{48}H_6$) the distribution of sodium charges tends towards the lower numbers. This illustrates the decrease in ionicity, which is dependent on number of neighbors, with increasing abstraction of surface molecular hydrogen.

3.3.1   Cluster size dependence effects (Nanostructuring)

An obvious choice for increasing the kinetics of hydrogen absorption and desorption is nanostructuring. In the nanoregime surface effects dominate over the bulk properties. Nanoclusters also offer a shorter diffusion distances for hydrogen thereby enhancing the diffusion-limited reaction rates. Figure 3.10 shows the dependence of the total desorption energy on the cluster size. The total desorption energy, which is the energy needed to desorb all the hydrogen
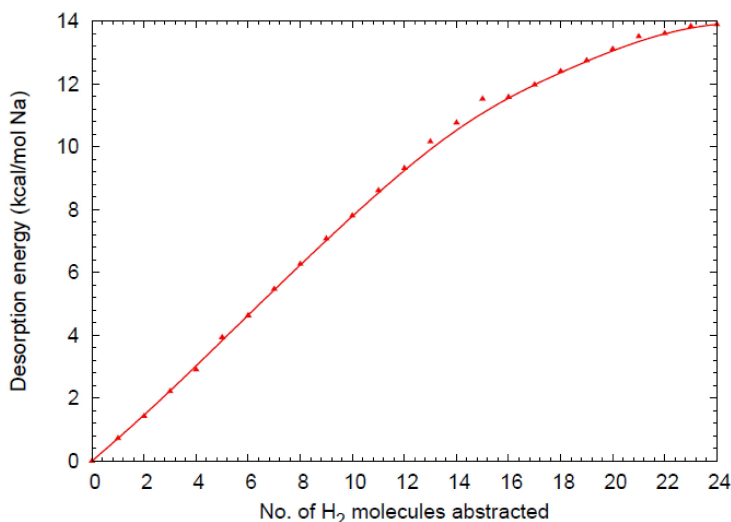
Fig. 3.8: Desorption energy, $E^{desorb} = [E_{Na_{48}} + E_{\frac{n}{2}H_2}] - E_{Na_{48}H_n}$, as a function of the number of hydrogen molecules abstracted from the system.

atoms from a given cluster is defined as:

$$\Delta H^{des} = E[nNa] + \frac{n}{2}E[H_2] - E[Na_nH_n] \qquad (3.5)$$

Also shown in the Fig. 3.10 are the Na_{400} cluster (about 3.3 nm) and Na_{32} clusters after desorption of all the hydrogen atoms. The figure shows that it easier to desorb all the hydrogen atoms from smaller clusters than from the larger clusters. The total desorption energy converges to a value of 15.5 kcal/mol NaH for clusters with more than 256 sodium atoms. This shows that the NaH clusters with less than 256 sodium atoms have different behavior from the relatively larger clusters. Decreasing cluster size leads to increase in surface/volume ratio, therefore for smaller clusters the average coordination number of surface atoms is reduced which implies lesser number of bonds. For small clusters surface effects are dominant leading to faster kinetics due to weakened bonds. In the case of larger clusters, once the surface molecular hydrogen have been abstracted it becomes increasingly difficult to abstract the remaining hydrogen atoms, which are strongly bound within the cluster. This approach makes the fundamental assumption that the cluster does not fragment during the desorption process otherwise the picture becomes quite complicated. There is no experimental evidence to backup our theoretical observations for the nanophase NaH.
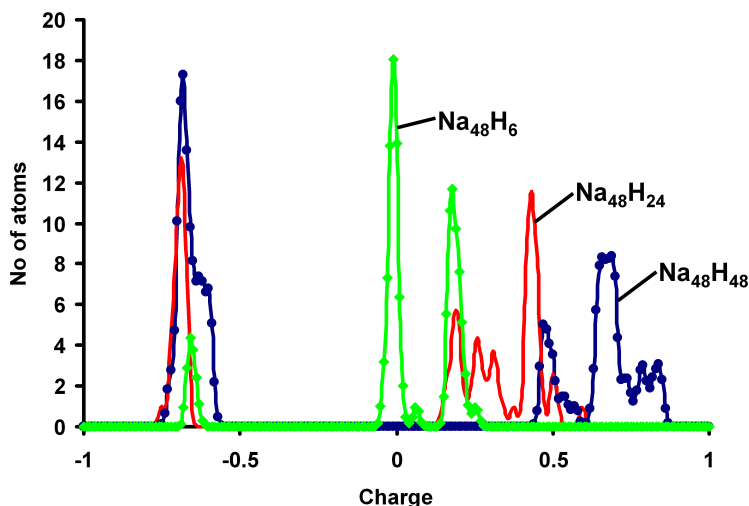
Fig. 3.9: The changes in charge distribution during abstraction of molecular hydrogen from $Na_{48}H_{48}$ cluster.

3.4 Molecular Dynamics Simulation

Desorption of hydrogen molecules during the heating up of a cluster of NaH was investigated. This was done by performing a NVT (constant number of particles, volume and temperature) simulation on a small cluster of NaH ($Na_{48}H_{48}$). The cluster was first minimized to find the nearest metastable state. After this it was equilibrated at 100 K for 5×10^4 steps. After equilibration, the cluster was then heated up from 100 K to 1200 K using Berendsen thermostat.[27] A velocity Verlet algorithm[28] with a time step of 0.25 femto seconds (fs) was used in all simulation runs. The heating rate was set at 0.0025 K/ps (2.5×10^9 K/s). In the heating up run, the temperature of the system was increased linearly by velocity scaling as follows:

$$T(t) = T_{100K} + \lambda t \qquad (3.6)$$

where λ is the heating rate. Figure 3.11 shows the time evolution of the potential energy (PE) during the heating up of $Na_{48}H_{48}$ from 100 K to 1200 K. It can be seen in the figure that at elevated temperatures there are drops in PE. These drops in PE can be attributed to the decomposition of the cluster and also to the desorption of molecular hydrogen. Since the heating rate is unphysically fast and temperatures involved are quite high the heated up cluster fragments into smaller conformations prior to the release of molecular hydrogen. These
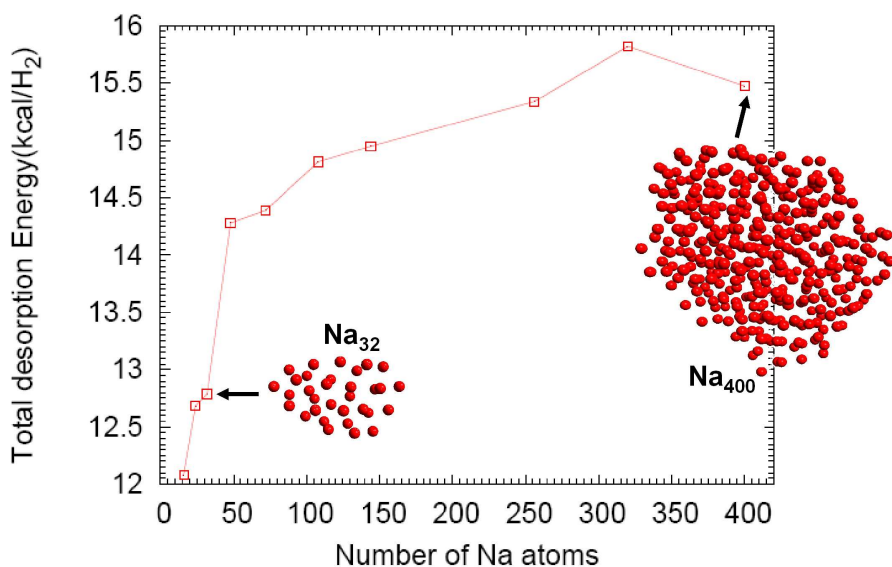
Fig. 3.10: Abstraction energy for all hydrogen atoms from different NaH clusters.

smaller clusters are stable entities (see Tab. 3.5). The fall in PE shows that the resultant structure is more stable than the immediate structure before it, i.e. before the release of molecular hydrogen or fragmentation of the cluster.

3.5 Diffusion Coefficient of Hydrogen

To explore the temperature dependence of diffusion constant of hydrogen atoms on the system, the hydrogen diffusion constant was computed by heating $Na_{320}H_{320}$ at a heating rate of 2.5×10^{10} K/s. The system was first heated up to the desired temperature in the range 300 K through 700 K and then equilibrated for 5×10^4 steps. This was then followed by an averaging run of 5×10^5 steps for each configuration and temperature condition in which diffusional analysis was performed. The diffusion coefficient is calculated from Einstein's relation:

$$D = \lim_{t \to \infty} \frac{\langle [\Delta r^2(t)] \rangle}{6t} \tag{3.7}$$
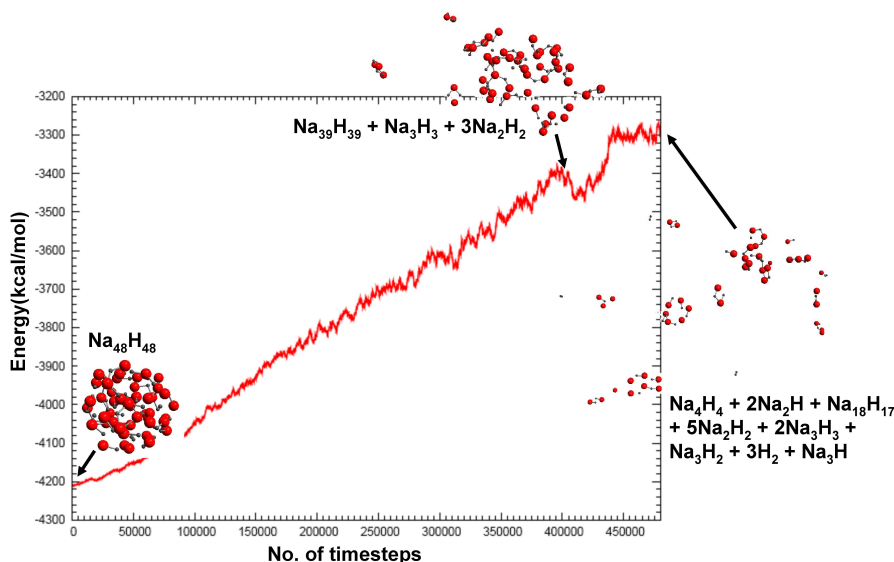
Fig. 3.11: Potential energy landscape during heating of $Na_{48}H_{48}$ cluster from 100 K to 1200 K.

where the mean square displacement (MSD) for each atomic species, a, is given by

$$\langle \Delta r^2(t) \rangle = \frac{1}{N_a} \sum_{i}^{N_a} [r_i(t) - r_i(t_0)]^2 \qquad (3.8)$$

with $t = t_0 + \Delta t$. The activation energy E_a for diffusion of hydrogen atoms within the cluster can be obtained from Arrhenius law

$$D = D_0 \exp \left(\frac{-E_a}{k_B T} \right) \qquad (3.9)$$

The temperature region considered in this particular computation is 300 K - 700 K since our focus is on the dynamics of the hydrogen atom during the heating process. Below 300 K there are only thermal vibrations of the atoms and above 750 K there is the possibility of desorption of hydrogen molecule. The MSD for 600 K and 700 K deviates from linearity, Fig. 3.12. The cause of this deviation is that beyond the 600 K there is partial fragmentation of the cluster into smaller subunits as shown in Fig. 3.13. This adds weight to statistical noise/errors in computation of MSD. If D is to be a constant then a plot of MSD versus time should be linear. For this reason only the linear parts of the MSD plots are considered in the computation of D. The parameters
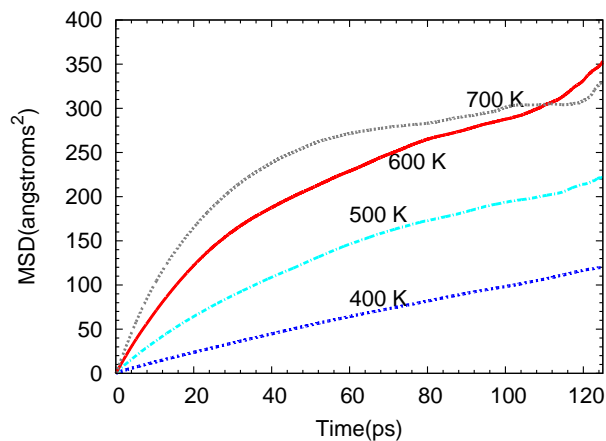
Fig. 3.12: Mean square displacement, $\langle \Delta r^2 \rangle$, for different temperatures for hydrogen. The simulation time corresponds to 125 ps, with a time step of 0.25fs.
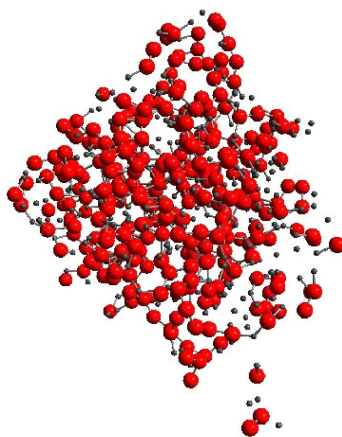
Fig. 3.13: Cluster fragmentation during the production run at 700 K.

in equation (3.9) can be determined from the temperature dependence of the diffusion constant. Figure 3.14(a) shows that the diffusion constant increases rapidly with increasing temperature but the trend changes slightly at the 650 K mark due to cluster fragmentation. Figure 3.14(b) shows that the diffusion constant of a hydrogen atom has an Arrhenius-type temperature dependence for the temperature range considered.
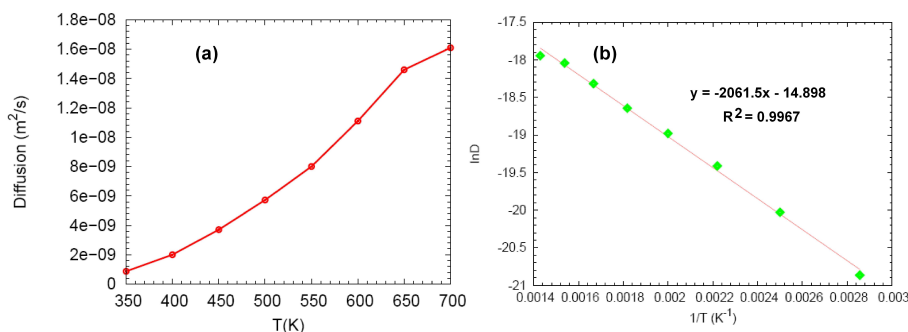
Fig. 3.14: (a) The temperature dependence of diffusion constant and (b) The 1/T dependence of lnD.

The activation energy for hydrogen diffusion, E_a, and the pre-exponential factor, D_0, were computed using a linear regression analysis of D as a function of 1/T, equation (3.9). The calculated pre-exponential is $D_0 = 3.39 \times 10^{-3} cm^2/s$, while the activation energy for hydrogen diffusion in NaH in the temperature range 350 K - 700 K is 4.1 kcal/mol. The energy cost for diffusion of hydrogen atoms is quite low due to the fact that this is predominantly an ionic system where electrostatic interactions play a major role. Heating the cluster to elevated temperatures disrupts the ionic lattice allowing the hydrogen/sodium atoms to easily diffuse within the cluster at low temperatures. The other reason is that the size of our cluster is small and surface effects might play a role in lowering the diffusional energy barrier of hydrogen within the system. It is difficult to apportion the diffusivity of hydrogen atoms in terms of those that diffuse on the surface and those that diffuse within the cluster since in the temperature range considered the highly mobile hydrogen species diffuses randomly within and on the surface of the cluster.

3.6 Conclusion

A reactive force field (ReaxFF$_{NaH}$) has been parameterized for Na and NaH systems by using DFT derived values for bond dissociation profiles, charge distribution, reaction energy data for small clusters and equations of state for Na and NaH condensed phases. ReaxFF$_{NaH}$ is built on the same formalism as previous ReaxFF descriptions.[4–8] It was found that ReaxFF$_{NaH}$ correctly reproduces the DFT data. For the atomization of bcc-Na metal ReaxFF$_{NaH}$ gives 21.61 kcal/mol, which is consistent with experimental value of 23.28 kcal/mol. DFT and ReaxFF binding energy studies on NaH clusters both show

that as the size of the cluster increases the binding energy converges towards the bulk heat of formation value of -11.60 kcal/mol (ReaxFF) or -10.19 kcal/mol (DFT). ReaxFF gives bulk modulus of 29.2 GPa. This compares quite well to the DFT and experimental values of 23.7 GPa and 19.4 ± 2.0 GPa, respectively.

During molecular dynamics simulations on hydrogen abstractions from a NaH cluster run it was observed that charge transfer is correctly described by $ReaxFF_{NaH}$. The reactive force field shows that there is charge transfer from Na and H atoms due to a phase transition from metallic hydride to solid solution. Furthermore, $ReaxFF_{NaH}$ predicts that desorption of hydrogen in smaller clusters is easier than in larger clusters since small particles are easily destabilized due to increase in surface area versus volume ratio. This indicates that nanostructuring enhances desorption of hydrogen. During a molecular dynamics heating up of NaH cluster, the system was seen to fragment at elevated temperatures, which is consistent with experimental evidence indicating that NaH decomposes at the melting point (698 K).[3,29]

References

[1] S. J. Duclos, Y. K. Vohra, A. L. Ruoff, S. Filipek, and B. Baranowski. *Phys. Rev. B*, 36:7664–7667, November 1987.

[2] H. D. Hochheimer, K. Strössner, W. Hönle, B. Baranowsky, and F. Filipek. *Z. Phys. Chem.*, 143:139, 1985.

[3] X. Ke and I. Tanaka. *Phys. Rev. B*, 71(2):024117–+, January 2005.

[4] A. Strachan, A. C. van Duin, D. Chakraborty, S. Dasgupta, and W. A. Goddard. *Phys. Rev. Lett.*, 91(9):098301–+, 2003.

[5] A. C. T. van Duin, A. Strachan, S. Stewman, Q. Zhang, X. Xu, and W. Goddard III. *J. Phys. Chem. A*, 107:3803, 2003.

[6] Q. Zhang, T. Çağın, A. C. T. van Duin, W. A. Goddard, Y. Qi, and L. G. Hector. *Phys. Rev. B*, 69(4):045423–+, 2004.

[7] A. C. T. van Duin, S. Dasgupta, F. Lorant, and W. Goddard III. *J. Phys. Chem. A*, 105:9396, 2001.

[8] Sam Cheung, Wei-Qiao Deng, A. C. T. van Duin, and W. Goddard III. *J. Phys. Chem. A*, 109:851–859, 2005.

[9] G. Kresse and J. Furthmüller. *Phys. Rev. B*, 54:11169–11186, 1996.

[10] P. E. Blöchl. *Phys. Rev. B*, 50:17953–17979, 1994.

[11] J. P. Perdew, J. A. Chevary, S. H. Vosko, K. A. Jackson, M. R. Pederson, D. J. Singh, and C. Fiolhais. *Phys. Rev. B*, 46:6671–6687, 1992.

[12] J. P. Perdew, K. Burke, and Y. Wang. *Phys. Rev. B*, 54:16533–16539, 1996.

[13] J. P. Perdew, K. Burke, and M. Ernzerhof. *Phys. Rev. Lett.*, 77:3865–3868, 1996.

[14] H. J. Monkhorst and J. D. Pack. *Phys. Rev. B*, 13:5188–5192, June 1976.

[15] F. Birch. *Phys. Rev.*, 71:809–824, 1947.

[16] R. Dovesi, M. Causá, R. Orlando, C. Roetti, and V. R. Saunders. *J. Chem. Phys.*, 92:7402–7411, 1990.

[17] *CRYSTAL2006 User's Manual, University of Torino*. 2006.

[18] G. Gilat and L. J. Raubenheimer. *Phys. Rev.*, 144:390–395, April 1966.

[19] Y. Chen, C. H. Huang, and W. Hu. *J. Phys. Chem. A*, 109:9627–9636, October 2005.

[20] M. W. Chase Jr., C. A. Davies, J. R. Downey Jr., D. J. Frurip, R. A. McDonald, and A. N. Syverud. JANAF Thermochemical Tables (Third Edition). *in J. Phys. Chem. Ref. Data,Suppl. 1*, 14:1, 1985.

[21] X. Wang and L. Andrews. *J. Phys. Chem. A*, 111:7098–7104, 2007.

[22] M. W. Chase. NIST-JANAF Themochemical Tables, fourth edition. *in J. Phys. Chem. Ref. Data, Monograph*, 9:1, 1998.

[23] J. L. Martins. *Phys. Rev. B*, 41:7883–7886, April 1990.

[24] G. D. Barrera, D. Colognesi, P. C. H. Mitchell, and A. J. Ramirez-Cuesta. *Chem. Phys.*, 317:119–129, October 2005.

[25] B. R. K. Gupta and V. Kumar. *Czech. J. Phys. B*, 33:1011, 1983.

[26] K. Barbalance. Periodic Table of Elements - Sodium. *http://EnvironmentalChemistry.com/yogi/periodic/Na.html*, 1995-2007.

[27] H. J. C. Berendsen, J. P. M. Postma, W. F. van Gunsteren, A. Dinola, and J. R. Haak. *J. Chem. Phys.*, 81:3684–3690, 1984.

[28] L. Verlet. *Phys. Rev.*, 159:98–103, July 1967.

[29] A. F. Hollemann and E. Wiberg. *in Lehrbuch der Anorgansichen Chemie*. Walter de Gruyter, Berlin, 1995.

Possible intermediate states in the thermal decomposition of NaAlH$_4$

> There's plenty of room at the bottom.
>
> RICHARD FEYNMAN

Abstract

Density functional theory (DFT) has been used to study the structural stability of possible intermediate alanate structures, Na$_5$Al$_3$H$_{14}$ and Na$_2$AlH$_5$, in the thermal decomposition of NaAlH$_4$. From theoretical calculations, Na$_5$Al$_3$H$_{14}$ is found to crystallize in the space group $P4/mnc$ with lattice constants $a = 6.769$ Å and $c = 10.289$ Å. It is shown that both Na$_5$Al$_3$H$_{14}$ and Na$_2$AlH$_5$ have the right thermodynamics and can fit in as intermediate states during the thermal decomposition process of NaAlH$_4$. The heat of formation of Na$_5$Al$_3$H$_{14}$ is -60 kJ/mol H$_2$, which is intermediate between that of NaAlH$_4$ (-51 kJ/mol H$_2$) and Na$_3$AlH$_6$ (-69.7 kJ/mol H$_2$). An alternative decomposition pathway based on Na$_2$AlH$_5$ has also been discussed. Frequency analysis showed that the least energetic structure of Na$_2$AlH$_5$ has imaginary frequencies, implying that it is unstable. The presence of soft phonon modes also shows that Na$_5$Al$_3$H$_{14}$ is mechanically metastable. These results are consistent with the notion they are intermediate states that lead to the formation of AlH$_3$. AlH$_3$ is believed to facilitate the mass transport of aluminum atoms during the thermal decomposition of NaAlH$_4$.

4.1 Introduction

Complex metal hydrides have generated much interest as candidates for hydrogen storage due to their relatively high weight percent of hydrogen and favorable thermodynamics like in the case of NaAlH$_4$.[1–10] The different phases that are formed during the thermal decomposition of NaAlH$_4$ have already been experimentally identified. However, the detailed transformation chemistry of the thermal decomposition of NaAlH$_4$ is not yet fully understood. Conventionally, based on experimental observations the putative desorption pathway is as follows:

$$\text{NaAlH}_4 \quad \rightleftharpoons \quad \frac{1}{3}\text{Na}_3\text{AlH}_6 + \frac{2}{3}\text{Al} + \text{H}_2 \qquad (4.1)$$

$$\text{Na}_3\text{AlH}_6 \quad \rightleftharpoons \quad 3\text{NaH} + \text{Al} + \frac{3}{2}\text{H}_2 \qquad (4.2)$$
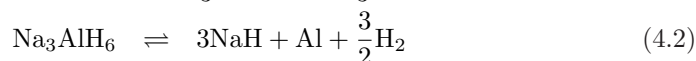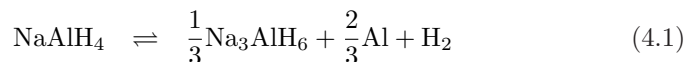
Although Na$_3$AlH$_6$ is an experimentally observable intermediate phase, there are speculations about the possible existence of other sub-intermediate phases since the above pathway (equations (4.1) and (4.2))[5] cannot explain how the long range mass transport of aluminum atoms during the thermal decomposition of NaAlH$_4$ is facilitated. It is now generally accepted that aluminum hydride might be an intermediate phase and play a key role in the mass transport of aluminum atoms.[5,11,12] Fu et al.[11] have shown, using inelastic neutron scattering (INS), that indeed AlH$_3$ species might be present during the decomposition of titanium-doped NaAlH$_4$. Gross et al.[5] did an in-situ X-ray diffraction study of the decomposition of NaAlH$_4$ and found that there were some unidentified intermediate phases, X$_1$ and X$_2$, during the process of decomposition. They were, however, not able to determine the crystal structure of these phases. In order to rationalize the fact that a surface catalyst influences a bulk transition they suggested that a better way to understand the thermal decomposition of NaAlH$_4$ is to reformulate the reaction:

$$\text{NaAlH}_4 \rightleftharpoons \frac{1}{3}\text{Na}_3\text{AlH}_6 + \frac{2}{3}\text{Al} + \text{H}_2 \rightleftharpoons \text{NaH} + \text{Al} + \frac{3}{2}\text{H}_2 \qquad (4.3)$$

into

$$3(\text{NaH})(\text{AlH}_3) \rightleftharpoons (\text{NaH})_3(\text{AlH}_3) + 2(\text{AlH}_3) \rightleftharpoons 3(\text{NaH}) + 3(\text{AlH}_3) \qquad (4.4)$$
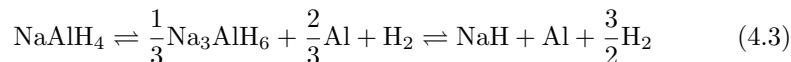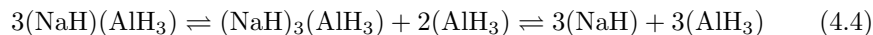
so that the phase transitions in equation (4.1) is caused by the molecular movements of AlH$_3$ and NaH species. The support for this model of Gross et al. is based on the fact that NaAlH$_4$ can be indirectly synthesized by mixing Na$_3$AlH$_6$[13] or NaH[14] with AlH$_3$ in Tetrahydrofuran. The mobile molecular AlH$_3$ (alane) species acts as the vessels through which the Al is transported in the system. The key question is how is AlH$_3$ formed? In an attempt to answer

this question, Walters and Scogin[15] proposed the following reaction pathway:

$$\mathrm{NaAlH_4} \rightleftharpoons \mathrm{NaH + AlH_3} \tag{4.5}$$

$$\mathrm{NaH + NaAlH_4} \rightleftharpoons \mathrm{[Na_2AlH_5]} \tag{4.6}$$

$$\mathrm{NaH + [Na_2AlH_5]} \rightleftharpoons \mathrm{Na_3AlH_6} \tag{4.7}$$

$$\mathrm{Na_3AlH_6} \rightleftharpoons \mathrm{3NaH + AlH_3} \tag{4.8}$$

$$\mathrm{AlH_3} \leftrightarrow \mathrm{Al + 3H} \tag{4.9}$$

$$\mathrm{2H} \leftrightarrow \mathrm{H_2} \tag{4.10}$$

In this reaction pathway, the initial concentration of NaH is limited to low level by the reactions in equation (4.7), which acts as a sink by consuming the NaH. The build up of NaH is enhanced in step (4.8). The metastable alane formed in step (4.8) quickly decomposes into Al and hydrogen atoms (which combine to form hydrogen molecules). In this way we can understand how Al is transported through the system. It is still unclear whether the $\mathrm{Na_2AlH_5}$ formed is an amorphous structure or has a well defined crystal structure. We discuss the likely structure of $\mathrm{Na_2AlH_5}$ at a later stage in this chapter. The most important thing is that this pathway nicely explains the mass transport of Al atom by using alane molecules as the mobile species. However, the most likely decomposition scenario of $\mathrm{Na_2AlH_5}$ is

$$\mathrm{2Na_2AlH_5 \rightleftharpoons NaAlH_4 + Na_3AlH_6} \tag{4.11}$$
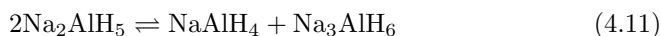
which is analogous to the disproportionation of $\mathrm{K_2ErF_5}$[16] as follows:

$$\mathrm{2K_2ErF_5 \rightleftharpoons KErF_4 + K_3ErF_6} \tag{4.12}$$

With this in mind, equation (4.11) calls for a re-examination of reactions (4.6) and (4.7) from a thermodynamics perspective.

A second and pragmatic approach to understanding the dynamical details of thermal decomposition of $\mathrm{NaAlH_4}$ is to look at the reactions involving $\mathrm{NaF\text{-}AlF_3}$ system, which is similar to the $\mathrm{NaH\text{-}AlH_3}$ system. It is worth noting that both α-$\mathrm{Na_3AlH_6}$ and α-$\mathrm{Na_3AlF_6}$ have similar crystal structure (monoclinic symmetry, space group $P2_1/n$) and undergo a pressure induced phase transformation to a cubic β-phase (space group $Fm\bar{3}m$), β-$\mathrm{Na_3AlH_6}$ and β-$\mathrm{Na_3AlF_6}$, respectively. Similarly, both α-$\mathrm{AlH_3}$ and α-$\mathrm{AlF_3}$[17] have a rhombohedral structure (space group $R\bar{3}c$) and both undergo a pressure induce phase transformation to a cubic phase (space group $Pm\bar{3}m$). In the sodium fluoride systems $\mathrm{NaF\text{-}AlF_3}$, NaF, $\mathrm{AlF_3}$, $\mathrm{Na_3AlF_6}$ and $\mathrm{Na_5Al_3F_{14}}$[18] exist as stable phases while $\mathrm{NaAlF_4}$ is metastable. In particular NaF, $\mathrm{Na_3AlF_6}$ and $\mathrm{Na_5Al_3F_{14}}$ occur in nature as villiamunite, cryolite and chiolite, respectively. Another important pointer to the similarity of the crystal structures of alanates and alarides (alumino-fluorides) is that both $\mathrm{K_2NaAlH_6}$[19] and $\mathrm{K_2NaAlF_6}$ (elpasolite) have cubic

symmetry (space group, $Fm\bar{3}m$). Of particular interest is the existence of Na$_5$Al$_3$F$_{14}$, which is yet to be explored in the NaH-AlH$_3$ system.

In this work we have examined the two possible pathways: Na$_2$AlH$_5$ and Na$_5$Al$_3$H$_{14}$. This chapter is divided as follows: Section 4.2 deals with the computational methodology deployed, section 4.3 dwells on results and discussion with emphasis on the possible crystal structures of Na$_5$Al$_3$H$_{14}$ and Na$_2$AlH$_5$, and decomposition pathways of NaAlH$_4$ using Na$_2$AlH$_5$ and Na$_5$Al$_3$H$_{14}$ as possible intermediate states. Section 4.4 gives a summary of what is discussed herein.

4.2   Computational methodology

Geometry optimizations of Na$_5$Al$_3$H$_{14}$ and Na$_2$AlH$_5$ were done using projector augmented[20] plane-wave implementation in VASP.[21] The Kohn-Sham ground-state is self-consistently determined and in the calculations the generalized gradient approximation of Perdew and Wang[22–24](GGA-PW91) was used to represent electronic-correlation effects for a particular ionic configuration. For all volumes considered the structures were fully optimized using force as well as stress minimization. The ions involved are steadily relaxed towards equilibrium until the Hellman-Feynman forces are minimized to less than 0.02 eV/Å (1 eV = 96.847 kJ/mol) with conjugate gradient algorithm during all relaxation runs. Once the optimized relaxed structure was found, a further local optimization was done by locally relaxing the structure until the Hellman-Feynman forces on the ions were less than 0.005 eV/Å using quasi-Newton algorithm. A convergence of 0.001 meV/atom was placed as a criterion on the self-consistent convergence of the total energy. In all calculations, a well converged plane wave cutoff of 600 eV was used. Brillouin zone integrations were performed using $4 \times 4 \times 4$ k-points for Na$_5$Al$_3$H$_{14}$ structures and $6 \times 6 \times 6$ k-points for Na$_2$AlH$_5$ structures as per the Monkhorst-Pack grid procedure.[25] The reference configurations for valence electrons used are H($1s^1$), Na($3s^1$) and Al($3s^23p^1$).

Two different symmetry constrained approaches were used to determine the equilibrium lattice parameters of the structures considered. In the first case, for a fixed cell volume of each structure the cell shape and atomic coordinates were fully optimized until the forces were less than 0.02 eV/Å per atom. The structure with the lowest energy was determined by plotting a total energy versus cell-volume curves for all the structures considered. The obtained energies were fitted to a Birch-Murnaghan equation of state[26] in order to get the equilibrium volume and minimum energy. The final structure was then determined by optimizing the lattice parameters and atomic positions at this equilibrium volume until the forces on the ions were less than 0.005 eV/Å per atom. In the second instance, all the three lattice parameters (cell volume, lattice constants

and atomic positions) were simultaneously relaxed with high accuracy.

To obtain the thermodynamic functions, and to check the mechanical stability for these crystals, the harmonic phonons were calculated using a direct *ab initio* force constant approach as implemented by Parlinski. [27] In this method, a specific atom is displaced to induce the forces on the surrounding atoms, which are calculated via the Hellmann-Feynman theorem (output from VASP code). The forces are then collected to construct the force-constant matrices. The harmonic phonons are obtained by diagonalizing the dynamical matrices. The internal energy of vibration (E_T) can be evaluated from the integral of phonon density of state (DOS) as follows:

$$E_T = \frac{1}{2} r \int_0^\infty \hbar \omega g(\omega) \coth \left(\frac{\hbar \omega}{2 k_B T} \right) d\omega \qquad (4.13)$$

where $g(\omega)$ is the phonon DOS, r is the number of degrees of freedom in the unit cell, $\hbar$ is the Planck constant, k_B is the Boltzmann constant, and T is temperature. Similar integrals can be applied to calculate the zero-point (ZP) energy, entropy ($S_{(T)}$) and free energy ($F_{(T)}$). [28] The temperature dependent vibrational entropy of the system, $S(T)$, is given by

$$S(T) = r k_B \int_0^\infty g(\omega) \left\{ \left(\frac{\hbar}{2 k_B T} \right) \left[\coth \left(\frac{\hbar}{2 k_B T} \right) - 1 \right] - \ln \left[1 - \exp \left(-\frac{\hbar \omega}{k_B T} \right) \right] \right\} d\omega \qquad (4.14)$$

To obtain Gibbs free energy for H_2 gas at elevated temperatures, the free energy at atmospheric pressure is calculated by combining calculated and measured data:

$$G_{(p_0 = 1 \text{atm}, T)}(H_2) = E_{elec}(H_2) + E_{zp}(H_2) + \triangle G_{(T)}(H_2) \qquad (4.15)$$

where $E_{elec}(H_2)$ is the electronic energy of a H_2 molecule obtained from the total-energy calculations, $E_{zp}(H_2)$ is the zero-point energy of a H_2 molecule obtained from the phonon calculations. $\triangle G_{(T)}(H_2)$ is Gibbs free energy with respect to that at 0 K, which can be obtained from the tabulated thermo-chemical data. [29]

4.3   Results and Discussion

4.3.1   Structure

The crystal structure of $Na_5Al_3H_{14}$ was explored by examining structures of the form $M'_5M_3F_{14}$ (where M$'$ is a monovalent atom and M is a trivalent atom). The structures fall into four space groups ($P4/mnc$, I4, $P2_1/n$ and $P4_22_12$). In general, the structures include $Na_5Al_3F_{14}$ ($P4/mnc$), $Na_5Cr_3F_{14}$ ($P2_1/n$), $Na_5Ga_3F_{14}$ ($P2_1/n$), $Na_5Fe_3F_{14}$ ($P2_1/n$) and its high tempera-

ture phase Na$_5$Fe$_3$F$_{14}$ ($P4_22_12$), Na$_5$W$_3$O$_9$F$_5$, Ca$_5$Te$_3$O$_{14}$, NaNd$_4$Sb$_3$O$_{14}$ and Na$_4$Lu(WNb$_2$)O$_9$F$_5$, which are all in the $P2_1/n$ space group. To the best of our knowledge, all structures of the form M$'_5$M$_3$F$_{14}$ should fall into one of these four space groups. This gives us the confidence that all the relevant space group geometric modifications of the structure have been taken into account. Among the phases considered, the $P4/mnc$ takes the lowest energy as presented in Fig. 4.1. Thus, using DFT, Na$_5$Al$_3$H$_{14}$ is expected to crystallize in the same space group as Na$_5$Al$_3$F$_{14}$.
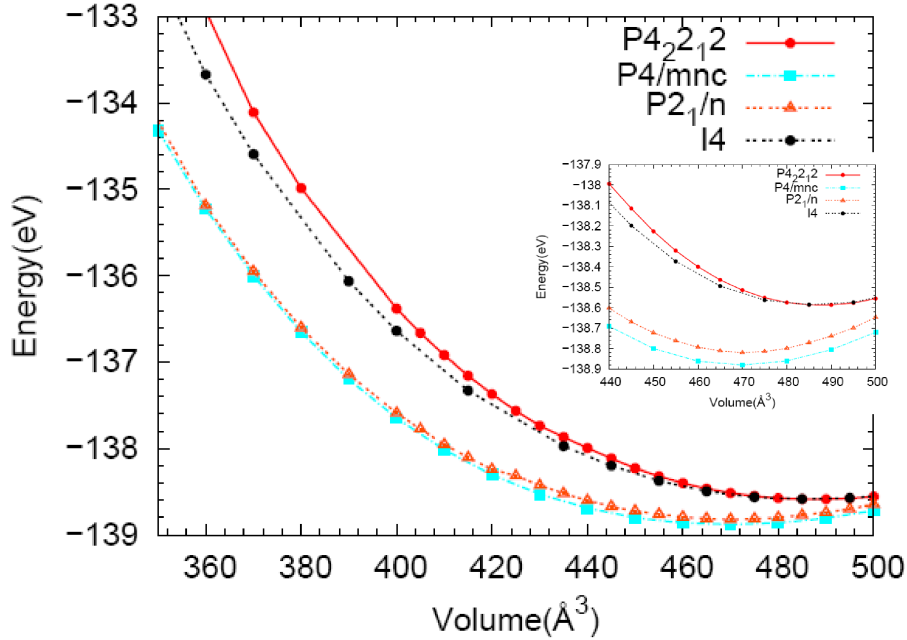
Fig. 4.1: The total energy E(eV) for different lattice volumes of Na$_5$Al$_3$H$_{14}$ in different structural modifications and inset is a closer look at the 450-500 region showing clear energetic difference between the $P4/mnc$ and $P2_1/n$ modifications.

The DFT calculated lattice parameters are $a = 6.769$ Å and $c = 10.289$ Å. A summary of the optimized internal coordinates is shown in Tab. 4.1 while the bond lengths and coordinations are shown in Tab. 4.2.

Figure 4.2 shows how the Na$_5$Al$_3$H$_{14}$ crystal looks like when viewed towards the (100) and (001) planes. The structure of Na$_5$Al$_3$H$_{14}$ can be thought of as a slightly distorted perovskite but that is where the similarity ends since the octahedrons in perovskite share corners infinitely in all three dimensions whereas

Tab. 4.1: Optimized internal coordinates of $Na_5Al_3H_{14}$.

Atom	site	symmetry	x	y	z
Na1	2b	4/m	0	0	0.5
Na2	8g	2	0.2851	0.7851	0.25
Al1	2a	4/m	0	0	0
Al2	4c	2/m	0	0.5	0
H1	4e	4	0	0	0.1694
H2	8h	m	0.7522	0.0731	0
H3	16i	1	0.3207	0.0420	0.6175

Tab. 4.2: The interatomic distances and coordination numbers of $Na_5Al_3H_{14}$.

Neighbors	Distance (Å)	Coordination
Na-Al (planar)	3.377	8
Na-Na	3.408	8
Al-Al	3.377	4
Na-H	2.221	8

the AlH_6's in this structure share corners infinitely in only two dimensions. Thus the structure forms layers of AlH_6's octahedra as illustrated in Fig. 4.2. There are two types of AlH_6 octahedra whose symmetries are different. These form shifted independent $[Al_3H_{14}]_n^{5n-}$ layers perpendicular to the c axis as shown in Fig. 4.3. Within the unit cell, a third of the octahedra share four corners and the remaining share only two. The sharing of *cis* two vertices of an octahedra can lead to either a zigzag chain or cyclic molecules. The doubly bridged and tetra-bridged octahedra form a linear chain due to sharing of *trans* vertices and at the same time are involved in a cyclic network of 8 octahedra due to sharing of *cis* vertices (see Fig. 4.3).

In the first $Al(1)H_6$ octahedron there are 4 bridging hydrogen atoms and in the second one, $Al(2)H_6$, there are two bridging hydrogen atoms, Fig. 4.3. The $Al(2)H_6$ octahedra is tilted by 45.69° away from the ideal octahedral structure in perovskite. The Al-H distances are as follows. For the first type, $Al(1)H_6$, $d_{Al_1-H}^{bridge} = 1.745$ Å and $d_{Al_1-H}^{terminal} = 1.746$ Å whereas for the second type, $Al(2)H_6$, $d_{Al_2-H}^{bridge} = 1.774$ Å and $d_{Al_2-H}^{terminal} = 1.737$ Å. Interestingly, in the case of $Al(1)H_6$ the two d_{Al-H} distances are almost equal whereas for $Al(2)H_6$ there is a clear difference. This difference emanates from differing crystalline field the two moieties are subjected to. For $Al(1)H_6$ the Al atom is completely shielded from direct interaction with Na atoms by the H anions while in the case of
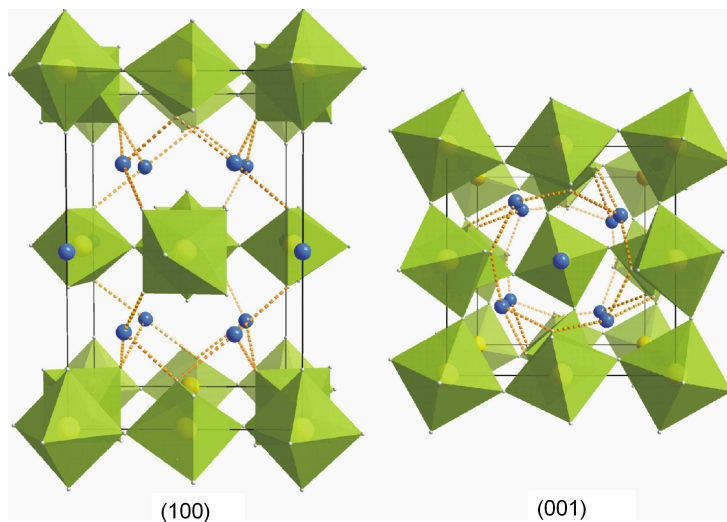
Fig. 4.2: Projections of the Na$_5$Al$_3$H$_{14}$ structure. Na atoms are represented by small spheres. The polyhedra represents the AlH$_6$ moiety.
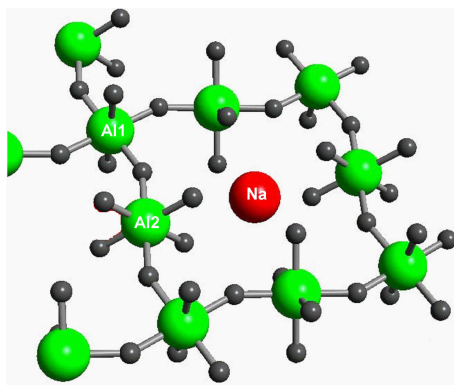
Fig. 4.3: The two types of AlH$_6$ octahedra, Al(1)H$_6$ and Al(2)H$_6$, in Na$_5$Al$_3$H$_{14}$ crystal structure.

Al(2)H$_6$ all the terminal H atoms are off planar and hence there is a subtle direct interaction between Na and Al. Within the layers some sodium cations occupy the cavities between the octahedra while the others are in the spaces between the octahedral layers. These two distinct sodium sites give rise to the following coordinations with respect to hydrogen atoms as nearest neighbors. Na(1) (axis

symmetry 4/m) is 8-fold coordinated whereas Na(2) (local symmetry 2) is 10 fold coordinated. For Na(1) all the Na(1)-H distances are 2.502 Å while for Na(2) the Na(2)-H distances vary from 2.221 Å to 3.528 Å. In comparison, in Na_3AlH_6, Na(1) is 6 fold coordinated and Na(2) is 8 fold coordinated. Further, in Na_3AlH_6 there are two d_{Al-H} distances of 1.783 Å and 1.773 Å respectively. In the case of α-AlH_3, $d_{Al-H} = 1.720$ Å. This suggests that the Al-H bonding in AlH_3 is stronger (i.e is subjected to a stronger crystalline field) than that in Na_3AlH_6 and $Na_5Al_3H_{14}$.

It appears that the $Al(2)H_6$ is a perfect octahedra with $\theta_{H-Al-H} = 90.0°$, where one H is a bridge atom and the other H is a terminal atom, whereas the $Al(1)H_6$ seems to be a distorted octahedra with $\theta_{H-Al-H} = 92.08°$. In comparison, the octahedra in α-AlH_3 and Na_3AlH_6 appear to be more distorted with $\theta_{H-Al-H} = 92.35°$ and $\theta_{H-Al-H} = 90.67°$ respectively. The $Na_5Al_3H_{14}$ structure can be best summed up as being made up of alternating layers of corner-sharing AlH_6^{3-} octahedra and distorted edge sharing $[NaH_6^{5-}]$ octahedra.

The crystal structure of Na_2AlH_5 was examined by exploring structures of the form $M_2''MF_5$ (where M'' is a monovalent atom and M is a trivalent atom). Among the structures considered include: K_2AlF_5 ($P4/mmm$), K_2ErF_5 ($Pc2_1n$), K_2FeF_5 ($Pbcn$), Rb_2CrF_5 ($Pnma$), Tl_2AlF_5 ($C2221$), $(NH_4)_2MnF_5$, K_2SmF_5,[30] and K_2FeF_5 ($Pbam$).
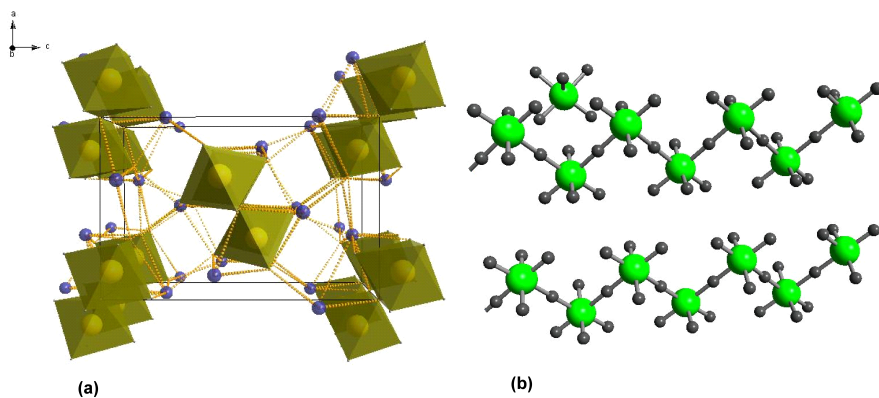
Fig. 4.4: (a) Projections of the Na_2AlH_5 structure. (b) The zigzag nature of the AlH_6 octahedra units in Na_2AlH_5 with the Na atoms removed.

Among these structures the K_2FeF_5-type (space group $Pbam$) has the lowest energy. However, a refined optimization followed by vibrational analysis at the Γ-point showed that the structure has soft phonon modes and therefore is unstable. The instability emanates from the frustrated rotation of the

AlH$_6$ octahedron. However, since we were able to identify only eight possible prototype structures, the results on the possible structures of Na$_2$AlH$_5$ are not conclusive. For the eight prototype structures of Na$_2$AlH$_5$ considered, the structure with the lowest energy (K$_2$FeF$_5$-type adopts a zigzag conformation of [AlH$_6$]$_n^{2n-}$ as illustrated in Fig. 4.4. In between the zigzag chains, the Na$^+$ ions provide the electrostatic stabilization of the lattice.

4.3.2 Heats of formation and reaction

The heat of formation ΔH_f from the VASP enthalpies of the constituent elements in their standard states were determined as per the definition:

$$\Delta H_f = H_{Solid} - \sum_a H^{isolated} \qquad (4.16)$$

a = different atoms constituting the solid.

Table 4.3 shows the values of the heats of formation of NaAlH$_4$, Na$_3$AlH$_6$, Na$_2$AlH$_5$ and Na$_5$Al$_3$H$_{14}$. The heat of formation of Na$_5$Al$_3$H$_{14}$ from its constituent elements falls in between that of NaAlH$_4$ and Na$_3$AlH$_6$. The heat of

Tab. 4.3: *Heats of formation for the various complex sodium alanates.*

Reactants	H$_f$(kJ/mol H$_2$)
Na + Al + 2H$_2$ → NaAlH$_4$	-51.0
5Na + 3Al + 7H$_2$ → Na$_5$Al$_3$H$_{14}$	-60.0
2Na + Al + $\frac{5}{2}$H$_2$ → Na$_2$AlH$_5$	-60.4
3Na + Al + 3H$_2$ → Na$_3$AlH$_6$	-69.7

formation of Na$_5$Al$_3$H$_{14}$ is similar to that of quasi stationary state of Na$_2$AlH$_5$ and falls in between that of NaAlH$_4$ and Na$_3$AlH$_6$, which implies that both are possible reaction intermediates in the thermal decomposition of NaAlH$_4$. The energetics of NaAlH$_4$ decomposition via the Na$_2$AlH$_5$ route are as follows:

$$NaAlH_4 \rightarrow NaH + AlH_3 \quad 36.7 \text{ kJ/mol AlH}_3 \qquad (4.17)$$

$$NaH + NaAlH_4 \rightarrow [Na_2AlH_5] \quad \text{-5 kJ/mol} \qquad (4.18)$$

$$NaH + [Na_2AlH_5] \rightarrow Na_3AlH_6 \quad \text{-14 kJ/mol} \qquad (4.19)$$

$$Na_3AlH_6 \rightarrow 3NaH + AlH_3 \quad 55 \text{ kJ/mol AlH}_3 \qquad (4.20)$$
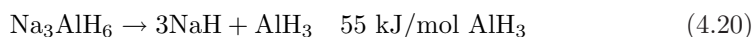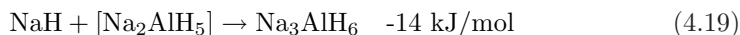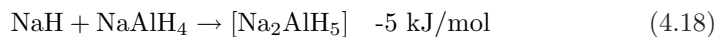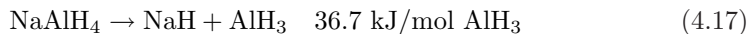
Figure 4.5 shows the overall energy cost involved in the Na$_2$AlH$_5$ pathway. It can be seen that Na$_3$AlH$_6$ has a local minima in this pathway while the position

Key:

a. $NaAlH_4$

b. $NaH + AlH_3$

c. Na_2AlH_5

d. Na_3AlH_6

e. $3NaH + AlH_3$
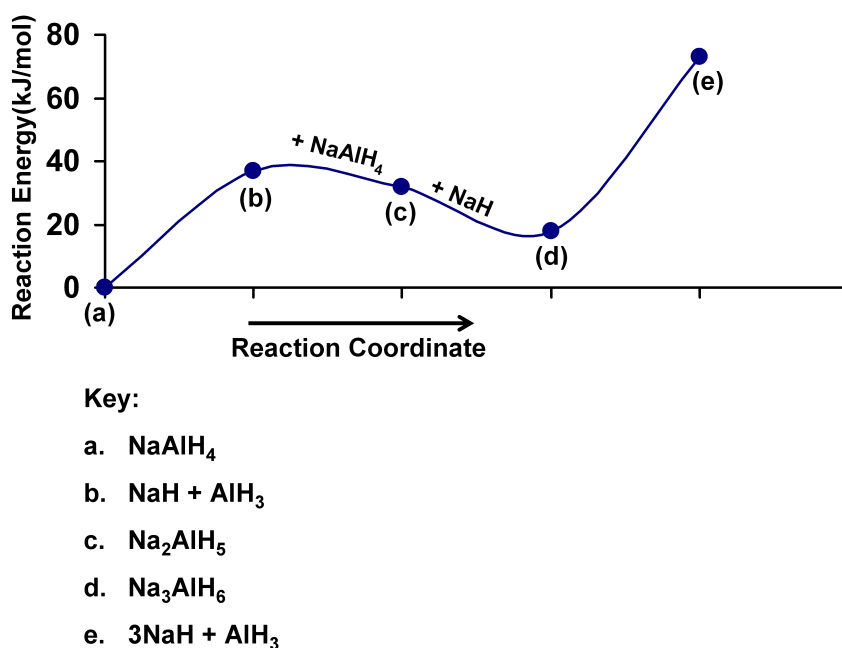
Fig. 4.5: The energetics of the Na_2AlH_5 pathway.

of Na_2AlH_5 is near a local maxima. This suggests that Na_2AlH_5 is a metastable intermediate and quickly reacts with NaH to form Na_3AlH_6 as was suggested in Ref.[15] This might explain why Na_2AlH_5 is not seen in experiments if indeed it is an intermediate phase during the thermal decomposition of $NaAlH_4$.

On the other hand, supposing that $Na_5Al_3H_{14}$ exists and is an intermediate in the decomposition pathway of $NaAlH_4$ then one route of forming AlH_3 is via the reaction

$$5NaAlH_4 \rightarrow Na_5Al_3H_{14} + 2AlH_3 \tag{4.21}$$

This is similar to the disproportionation of the metastable $NaAlF_4$ upon heating:

$$5NaAlF_4 \rightarrow Na_5Al_3F_{14} + 2AlF_3 \tag{4.22}$$

which takes place at the temperature range of 700-900 K.[31]

The $Na_5Al_3H_{14}$ then quickly disproportionates via two possible routes

$$Na_5Al_3H_{14} \rightarrow 5NaH + 3AlH_3 \tag{4.23}$$

or

$$Na_5Al_3H_{14} \rightarrow \frac{5}{3}Na_3AlH_6 + \frac{4}{3}AlH_3 \tag{4.24}$$
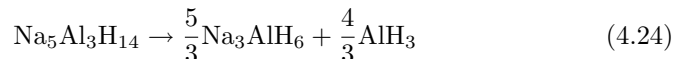
Considering the two possible pathways, it can be seen that route (4.23) is the back-reaction of the formation of $Na_5Al_3H_{14}$ from NaH and AlH_3 educts. Further, it does not account for the formation of the experimentally observed Na_3AlH_6 phase. In addition, in pathway (4.23) NaH is formed right at the onset of the decomposition reaction. This contradicts the experimental works of Gross et al.[5] in which it was shown that the $NaAlH_4$, Na_3AlH_6 and NaH are interdependent. This means that low concentrations of NaH have to be maintained during the thermal decomposition process until most of the $NaAlH_4$ is used up. Pathway (4.23) clearly violates this requirement, which leaves the reaction of equation (4.24) as the preferred pathway. The energy cost for disproportionation of $Na_5Al_3H_{14}$ into Na_3AlH_6 and AlH_3, reaction (4.24), is 27.6 kJ/mol AlH_3. We discuss this later.

With $Na_5Al_3H_{14}$ as the intermediate, the possible reaction pathway is as follows:

$$5NaAlH_4 \rightleftharpoons Na_5Al_3H_{14} + 2AlH_3 \tag{4.25}$$

$$Na_5Al_3H_{14} \rightleftharpoons \frac{5}{3}Na_3AlH_6 + \frac{4}{3}AlH_3 \tag{4.26}$$

$$Na_3AlH_6 \rightleftharpoons 3NaH + AlH_3 \tag{4.27}$$

$$AlH_3 \rightleftharpoons Al + \frac{3}{2}H_2 \tag{4.28}$$
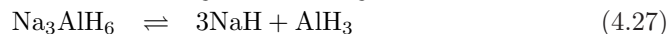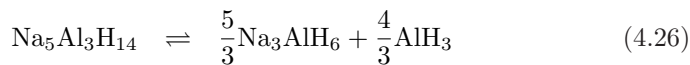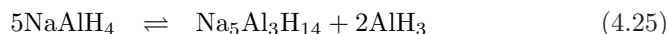
The heats of reaction of the process in equations (4.25) and (4.26) are given in Tab. 4.4. These energies are consistent with the trend in the thermal decomposition pathway of $NaAlH_4$.

Tab. 4.4: Heats of reaction for the various complex sodium alanates.

Reactants	H_r(kJ/mol AlH_3)
$5NaAlH_4 \rightarrow Na_5Al_3H_{14} + 2AlH_3$	23.9
$Na_5Al_3H_{14} \rightarrow 5NaH + 3AlH_3$	44.8
$Na_5Al_3H_{14} \rightarrow \frac{5}{3}Na_3AlH_6 + \frac{4}{3}AlH_3$	27.6
$Na_3AlH_6 \rightarrow 3NaH + AlH_3$	55.0

It is interesting to note that the heats of reaction of $NaAlH_4$ to form Na_3AlH_6

and that to form $Na_5Al_3H_{14}$ are very close.

$$5NaAlH_4 \quad \leftrightarrow \quad Na_5Al_3H_{14} + 2AlH_3 \quad 23.9 \quad kJ/mol \qquad (4.29)$$
$$3NaAlH_4 \quad \leftrightarrow \quad Na_3AlH_6 + 2AlH_3 \quad 25.4 \quad kJ/mol \qquad (4.30)$$

This suggests that these two processes are competitively similar. However, a better understanding of the two reactions entails computation of Gibbs free energy of formation (product minus reactant, ΔG). The Gibbs free energy is calculated as follows:

$$\begin{aligned} G \quad &= \quad U + pV - TS \qquad &(4.31) \\ &= \quad E_{elec} + E_T + pV - TS \qquad &(4.32) \end{aligned}$$

where E_{elec} is the electronic energy and E_T is the internal energy. In the case of solid-state materials the pV term contribution at atmospheric pressure is negligible e.g. for $NaAlH_4$ the value of this term at 300 K is $pV = 4.6 \times 10^{-5}$ eV. Therefore we can as well approximate G as

$$G = E_{elec} + E_T - TS \qquad (4.33)$$

The above thermodynamic functions are obtained by using the harmonic approximation.

Strictly speaking, the reactions (4.29) and (4.30) refer to molecular AlH_3, which decomposes into aluminum and hydrogen as shown in reaction (4.28). To calculate the Gibbs free energies for the two reactions we assume that AlH_3 dissociate into aluminum and hydrogen. Thus the two reactions can be rewritten as

$$NaAlH_4 \quad \rightarrow \quad \frac{1}{5}Na_5Al_3H_{14} + \frac{2}{5}Al + \frac{3}{5}H_2 \qquad (4.34)$$

$$NaAlH_4 \quad \rightarrow \quad \frac{1}{3}Na_3AlH_6 + \frac{2}{3}Al + H_2 \qquad (4.35)$$
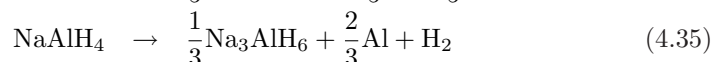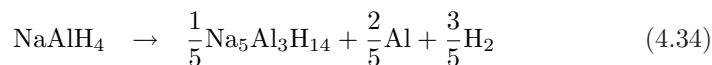
Figure 4.6 shows the calculated Gibbs free energy difference for reactions (4.34) and (4.35).

The figure shows that before the decomposition of $NaAlH_4$, the product of $(\frac{1}{5}Na_5Al_3H_{14} + \frac{2}{5}Al + \frac{3}{5}H_2)$ is more stable than that of $(\frac{1}{3}Na_3AlH_6 + \frac{2}{3}Al + H_2)$. Even more interesting, there is a coexistent point between these two reactions. This implies that reactions (4.34) and (4.35) can be switched. Hence, if we neglect the effect of soft modes (in $Na_5Al_3H_{14}$), then indeed $Na_5Al_3H_{14}$ may be considered as an intermediate state.

Figure 4.7 shows the entropy difference (product minus reactant) for the two
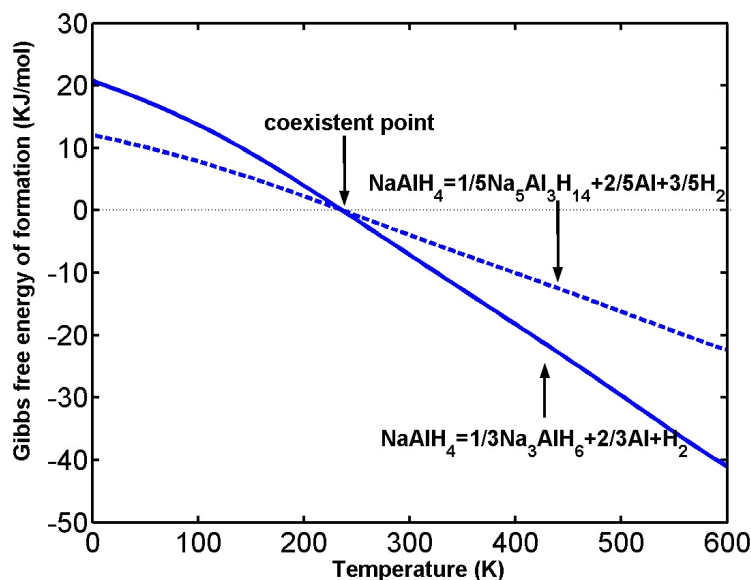
Fig.   4.6:   Calculated   Gibbs   free   energy   of   reactions
$NaAlH_4 \rightarrow \frac{1}{5}Na_5Al_3H_{14} + \frac{2}{5}Al + \frac{3}{5}H_2$ and $NaAlH_4 \rightarrow \frac{1}{3}Na_3AlH_6 + \frac{2}{3}Al + H_2$.
The reference energies are those of NaAlH$_4$ (denoted by the dotted lines).

reactions. The entropy differences are always positive. This shows that it is the
entropy contribution that is the driving force for reactions (4.34) and (4.35).
The entropy difference for reaction (4.35) increases at a faster rate than that for
reaction (4.34), which explains why as the temperature increases reaction (4.35)
becomes favored.

Na$_5$Al$_3$H$_{14}$ can be synthesized through ball milling of NaH and AlH$_3$ (amor-
phous). There are three possible structures that can result from this approach
as presented in Tab. 4.5 together with their reaction enthalpies.

Tab. 4.5: The reaction enthalpies for the formation of NaAlH$_4$, Na$_3$AlH$_6$ and
Na$_5$Al$_3$H$_{14}$ from NaH and AlH$_3$.

Reactants	H_r(kJ/mol AlH$_3$)
NaH + AlH$_3$ → NaAlH$_4$	-36.7
3NaH + AlH$_3$ → Na$_3$AlH$_6$	-55.1
5NaH + 3AlH$_3$ → Na$_5$Al$_3$H$_{14}$	-44.8
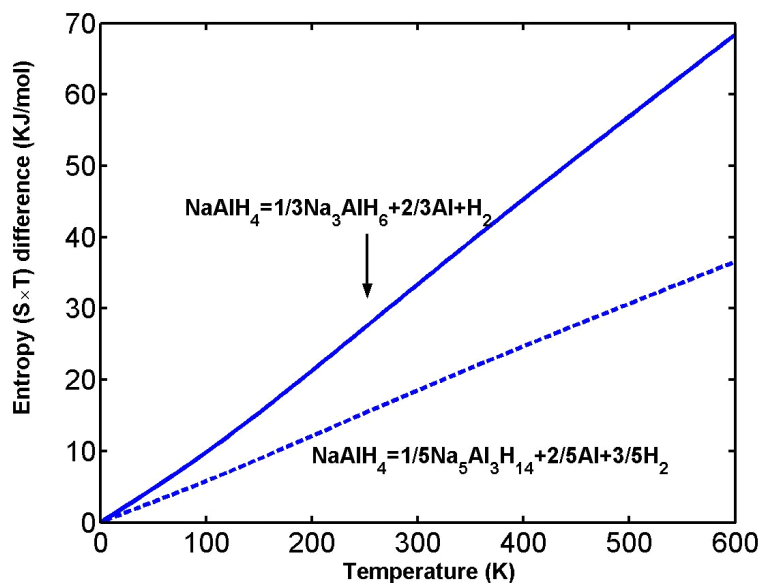
Fig. 4.7: Calculated entropy difference for the reactions $\text{NaAlH}_4 \rightarrow \frac{1}{5}\text{Na}_5\text{Al}_3\text{H}_{14} + \frac{2}{5}\text{Al} + \frac{3}{5}\text{H}_2$ and $\text{NaAlH}_4 \rightarrow \frac{1}{3}\text{Na}_3\text{AlH}_6 + \frac{2}{3}\text{Al} + \text{H}_2$.

It can be seen in Tab. 4.5 that the three routes have distinct morphological changes that entails bond breaking and formation. Therefore the end product ($\text{NaAlH}_4, \text{Na}_3\text{AlH}_6$ or $\text{Na}_5\text{Al}_3\text{H}_{14}$) might depend on the state/phase of AlH_3 used. AlH_3 is a covalent binary hydride, with polymeric $(\text{AlH}_3)_n$ forms. Although there are at least seven $(\alpha, \alpha', \beta, \gamma, \delta, \varepsilon, \zeta)$ known non-solvated phases of AlH_3 [32] but only the α, α', β and γ phases are well documented. In calculating the enthalpies of reaction in Tab. 4.5 we used the energy of β-AlH_3 polymorph, which was shown by Ke et al. [33] to be the most stable phase of AlH_3. One can deduce in Tab. 4.5 that the heat of formation of $\text{Na}_5\text{Al}_3\text{H}_{14}$ from the component hydrides, the process $5\text{NaH} + 3\text{AlH}_3 \rightarrow \text{Na}_5\text{Al}_3\text{H}_{14}$, is -44.8 kJ/mol AlH_3. This heat of formation falls between that leading to the formation of NaAlH_4 and Na_3AlH_6.

The state of AlH_3 in the thermal decompositions of NaAlH_4 should be molecular. However, in computing the enthalpies of reaction and formation throughout this work the formation enthalpy of crystalline AlH_3 was used for the sake of consistency with Tab. 4.4 and Tab. 4.5. Since the most important quantity here is the energy difference this should not affect the overall energy trend even if the enthalpy values of molecular AlH_3 were to be used.

4.4   Conclusion

A thermodynamics approach to understanding the reaction pathway of the thermal decomposition of NaAlH$_4$ has been undertaken. The ground state crystal structures of possible intermediates in this reaction pathway, Na$_2$AlH$_5$ and Na$_5$Al$_3$H$_{14}$, have been explored. Na$_5$Al$_3$H$_{14}$ is found to crystallize in the space group $P4/mnc$ with lattice constants $a = 6.769$ Å, $c = 10.289$ Å and $c/a = 1.52$. It can be thought of as being made up of a distorted and two dimensional perovskite like network of AlH$_6^{3-}$ and Na$^+$ units in which both linear and zigzag chains of [AlH$_6^{3-}$] octahedra exists. The structure is similar to that of Na$_5$Al$_3$F$_{14}$ with the F replaced by H. The decomposition mechanism proceeds as follows:

$$5\text{NaAlH}_4 \;\rightleftharpoons\; \text{Na}_5\text{Al}_3\text{H}_{14} + 2\text{AlH}_3 \; 23.9 \text{ kJ/mol AlH}_3 \tag{4.36}$$

$$\text{Na}_5\text{Al}_3\text{H}_{14} \;\rightleftharpoons\; \frac{5}{3}\text{Na}_3\text{AlH}_6 + \frac{4}{3}\text{AlH}_3 \; 27.6 \text{ kJ/mol} \quad \text{AlH}_3 \tag{4.37}$$

$$\text{Na}_3\text{AlH}_6 \;\rightleftharpoons\; 3\text{NaH} + \text{AlH}_3 \; 55 \text{ kJ/mol AlH}_3 \tag{4.38}$$

$$\text{AlH}_3 \;\rightleftharpoons\; \text{Al} + \frac{3}{2}\text{H}_2 \tag{4.39}$$
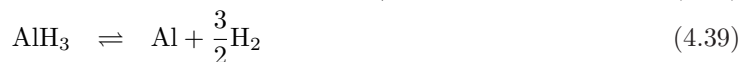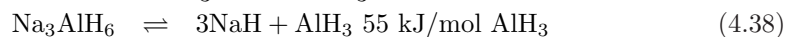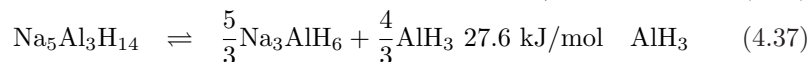
For the case whereby Na$_2$AlH$_5$ is an intermediate state the decomposition process is as follows:

$$\text{NaAlH}_4 \rightarrow \text{NaH} + \text{AlH}_3 \; 36.7 \text{ kJ/mol} \quad \text{AlH}_3 \tag{4.40}$$

$$\text{NaH} + \text{NaAlH}_4 \rightarrow [\text{Na}_2\text{AlH}_5] \; \text{-5 kJ/mol} \tag{4.41}$$

$$\text{NaH} + [\text{Na}_2\text{AlH}_5] \rightarrow \text{Na}_3\text{AlH}_6 \; \text{-14 kJ/mol} \tag{4.42}$$

$$\text{Na}_3\text{AlH}_6 \rightarrow 3\text{NaH} + \text{AlH}_3 \; 55 \text{ kJ/mol} \quad \text{AlH}_3 \tag{4.43}$$
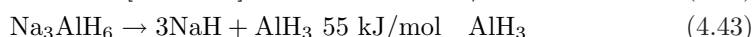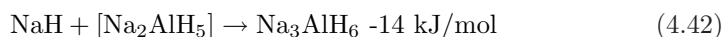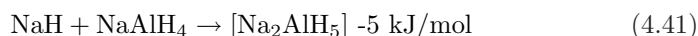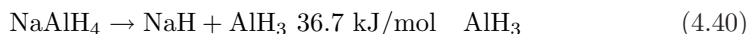
The lowest energy structure of Na$_2$AlH$_5$ considered was found to have negative frequencies during vibrational analysis and was therefore taken to be a quasi-stationary state. Based on the relative energies it can be argued that maybe Na$_2$AlH$_5$ is an intermediate state but is not observed because it is a quasi-stationary state. These results are consistent with the notion that AlH$_3$ is an intermediate state during the thermal decomposition process of NaAlH$_4$. The fact that neither Na$_2$AlH$_5$ nor Na$_5$Al$_3$H$_{14}$ are observed in experiments can be due to the fact that, if they occur during the thermal decomposition of NaAlH$_4$ then, they are quasi-stationary states. In particular, the inclusion of Na$_5$Al$_3$H$_{14}$ in the decomposition pathway of NaAlH$_4$ nicely illustrates how the lattice structure of NaAlH$_4$ is disrupted and the mobile alane (AlH$_3$) species are formed.

References

[1] B. Bogdanović and M. Schwickardi. *J. Alloys Compd.*, 253/254:1–9, May 1997.

[2] B. C. Hauback, H. W. Brinks, C. M. Jensen, K. Murphy, and A. J. Maeland. *J. Alloys Compd.*, 358:142–145, 2003.

[3] E. Rönnebro, D. Noreus, K. Kadir, A. Reiser, and Bogdanović B. *J. Alloys Compd.*, 299:101–106, 2000.

[4] V. Ozolins, E. H. Majzoub, and T. J. Udovic. *J. Alloys Compd.*, 375:1–10, 2004.

[5] J. K. Gross, S. Guthrie, S. Takara, and G. Thomas. *J. Alloys Compd.*, 297:270–281, 2000.

[6] J. Iniguez, T. Yildirim, T. J. Udovic, M. Sulic, and C. M. Jensen. *Phys. Rev. B*, 70(6):060101–+, 2004.

[7] A. Aguayo and D. J. Singh. *Phys. Rev. B*, 69(15):155103–+, April 2004.

[8] S. M. Opalka and D. L. Anton. *J. Alloys Compd.*, 356, 2003.

[9] A. Peles, J. A. Alford, Z. Ma, L. Yang, and M. Y. Chou. *Phys. Rev. B*, 70(16):165105–+, October 2004.

[10] E. H. Majzoub, K. F. McCarty, and V. Ozoliņš. *Phys. Rev. B*, 71(2):024118–+, January 2005.

[11] Q. J. Fu, A. J. Ramirez-Cuesta, and S. C. Tsang. *J. Phys. Chem. B*, 110:711–715, 2006.

[12] S. Chaudhuri and J. T. Muckerman. *J. Phys. Chem. B Lett.*, 109:6952–6957, 2005.

[13] Ashby E. C. and Kobetz P. *Inorg. Chem.*, 5:1615, 1966.

[14] Finholt A. E., Barbaras G. D., Barbaras G. K., Urry G., Wartik T., and Schlesinger H. I. *J. Inorg. Nucl. Chem.*, 1:317, 1955.

[15] R. T. Walters and J. H. Scogin. *J. Alloys Compd.*, 379:135, 2004.

[16] Podberezskaya N. V., Borisov S. V., Alekseev V. I., Tseitlin M. N., and Kurbanov Kh. M. *J. Struct. Chem.*, 23:158–160, 1982.

[17] R. Hoppe and D. Kissel. *J. Flourine Chem.*, 24:327–340, 1984.

[18] C. Jacoboni, A. Leble, and J. J. Rousseau. *J. Solid State Chem.*, 36:297–304, 1981.

[19] M. H. Sorby, H. W. Brinks, A. Fossdal, K. Thorshaug, and B. C. Hauback. *J. Alloys Compd.*, 415:284–287, 2006.

[20] P. E. Blöchl. *Phys. Rev. B*, 50:17953–17979, December 1994.

[21] G. Kresse and J. Furthmüller. *Phys. Rev. B*, 54:11169–11186, October 1996.

[22] J. P. Perdew, J. A. Chevary, S. H. Vosko, K. A. Jackson, M. R. Pederson, D. J. Singh, and C. Fiolhais. *Phys. Rev. B*, 46:6671–6687, September 1992.

[23] J. P. Perdew, K. Burke, and Y. Wang. *Phys. Rev. B*, 54:16533–16539, December 1996.

[24] J. P. Perdew, K. Burke, and M. Ernzerhof. *Phys. Rev. Lett.*, 77:3865–3868, October 1996.

[25] H. J. Monkhorst and J. D. Pack. *Phys. Rev. B*, 13:5188–5192, June 1976.

[26] F. Birch. *Phys. Rev.*, 71:809–824, 1947.

[27] K. Parlinski. *Software, PHONON*. Institute of Nuclear Physics, Crakow, 2005.

[28] A. A. Maradudin, E. W. Montroll, G. H. Weiss, and I. P. Ipatova. *Theory of lattice dynamics in the harmonic approximation in Solid State Physics Supplement*, volume 3. (Academic Press, New York), 1971.

[29] D. R. Stull and H. Prophet. *JANAF Thermodynamical Tables, 2nd ed.* U.S. National Bureau of Standards. Washington, DC, 1971.

[30] R. I. Bochkova, Y. N. Saf'yanov, É. A. Kuz'min, and N. V. Belov. *Sov. Phys. Doklady*, 18:575–+, March 1974.

[31] Bruno M., Herstad O., and Holm J. L. *J. Therm. Analys. Calor.*, 56:51–57, 1999.

[32] Jason Graetz and M. James Reilly. *J. Alloys Compd.*, 424:262–265, 2006.

[33] X. Ke, A. Kuwabara, and I. Tanaka. *Phys. Rev. B*, 71(18):184107–+, May 2005.

Chapter 5

Reactive force field for Aluminum

Abstract

Simulated annealing has been performed on aluminum clusters, Al_n, using
ReaxFF$_{Al}$, which is a force field that describes Al-Al interactions, to find
the stable isomers of the clusters. A plot of stability function versus versus
cluster size shows the existence of highly stable clusters (magic clusters). In
the quantification of the growth of cluster, it is seen that as the size of the
clusters increase there is preference for the coexistence of fcc/hcp orders at the
expense of simple icosahedral ordering although there is some contribution from
distorted icosahedral ordering. It is found that even for aluminum clusters with
512 atoms distorted icosahedral ordering exists. For clusters with $N \geq 256$
atoms FCC ordering dominates, which implies that at this point we are already
on the threshold of bulk like bonding.

5.1   Introduction

In this chapter we look at the parameterization of a reactive force field for aluminum. This development is in line with the fact that aluminum is one of the final products of the thermal decomposition of $NaAlH_4$. For this reason, parameterization of a force field for $NaAlH_4$ entails that the Al-Al interactions is also properly described. It is worth noting that there are a number of embedded atom method (EAM) potentials[1] and variable charge potentials (such as the Streitz-Mintmire potential[2]) designed for aluminum metal, which have been used for simulations with thousands of atoms. However, our eventual goal with this potential is to extend it to aluminium hydrides and finally, as mentioned before, to sodium aluminum hydride. While EAM is suitable for metals and Streitz-Mintmire is applicable to aluminium oxides, neither of these potentials have been parameterized for hydrides and it is unknown if EAM or Streitz-Mintmire would be accurate for the hydride systems. The higher degree of covalency in the hydrides may make extension of EAM and Streitz-Mintmire in this direction questionable. As such, while both EAM and Streitz-Mintmire would be valid for the aluminium metal, our eventual goal here requires a force field that can handle metals, covalent systems and variable charges, which points to the ReaxFF approach. Compared to earlier ReaxFF work for Al/Al_2O_3 systems (Zhang et al.[3]), we have significantly extended the training set, including not only bulk systems but also clusters, which is vital for the particular application presented in this chapter. Furthermore, we also modified the source of QM-data. In an earlier work[4] the SeqQuest-program (a Gaussian-based periodic DFT-method) was used. In this work we employed the VASP-program (Ref.[5]) to obtain the QM-data for the training set. The ReaxFF potential for the Al-metal uses the same set of potential functions as used by Zhang et al.[3]

That said, small aluminum clusters have been studied extensively with a view to getting a better understanding of atomic aggregates of aluminum, including the threshold of cluster-bulk interface[6,7] Previous works on aluminum clusters has addressed issues like magnetic properties,[8] static polarizabilities of Al_n clusters,[9] ionization thresholds and reactivities.[10] Other theoretical computations[11–16] have tackled issues to do with the energetically lowest structures of small aluminum clusters. Even for small clusters like Al_4, Al_5 and Al_7 there are still lingering uncertainties on the preferred configurations. The other point of interest is the existence of magic clusters (superatoms) of aluminum. Superatoms are clusters of atoms that exhibit some of the properties of elemental atoms. For instance, Al_7 and Al_{13} have been found to behave like superatoms. Al_7 behaves like an alkali since it has 21 valence electrons while Al_{13}, which has 39 valence electrons, behaves like a halogen. Studies have been conducted on the reactions of aluminum clusters with oxygen and it was observed that Al_7^+, Al_{13}^- and Al_{23}^- do not react with oxygen.[17] This

suggested that these clusters were stable entities due to their closed electronic shells with 20, 40, and 70 electrons for Al_7^+, Al_{13}^- and Al_{23}^-, respectively. These magic clusters should perhaps serve as the zone centers for crystal formation. Atoms agglomerate to form superatoms which then coalesce to form crystals. Using a glue potential,[18] Doye[19] investigated the stabilities of aluminum clusters upto Al_{190} and found a series of magic clusters starting from Al_{13}, Al_{19}, Al_{23},...,Al_{55},.... This elegant approach was purely based on geometrical structures of the aluminum clusters as in the higher the symmetry the more stable the structure.

Even more perplexing is the melting of smaller clusters. It is not always the case that small clusters have lower melting point than the bulk. It was found in the case of gallium and tin that the melting point of small clusters is higher than the bulk due to differing structures and stronger bonding in comparison to the bulk structures.[20–23] Such intrigues makes understanding the dynamics governing formation, magic numbers and melting of clusters an important key into unraveling how matter behaves in such small regimes. Clusters are the building blocks of bulk systems. Aluminum atoms must first agglomerate to form clusters. These clusters can then fuse together to form crystals. Studies of aluminum clusters will therefore shed some more light on the macroscopic evolution of the molecular phase to condensed matter realms with increase in the number of aluminum atoms.

In studying aluminum clusters a choice must be made between accuracy and computational efficiency. Traditionally, density functional theory (DFT) is the tool of choice for computational physicists/chemists especially in the condensed matter realm.[24] However, this is against a backdrop of enormous computational demands. For instance, optimization of Al_{19} cluster in a cubic cell of side 20 Å^3 at the Γ point using a plane waves cut-off of 600 eV (1 eV = 23.06 kcal/mol) in VASP on amd64 processors (with 8 nodes) took about 67 hours. In contrast, using a reactive force field (ReaxFF) this optimization was done in a fraction of a second. One must therefore take cognizance of the fact that a more robust approach is to use a force field without necessarily sacrificing accuracy at the altar of computational efficiency.

Our goal in this project was two fold: First, we wanted to show that ReaxFF, which has been successfully used to accurately predict the dynamical and reactive processes in hydrocarbons,[25] silicon/silicon oxides,[4] aluminum/aluminum oxides,[3] nitramines[26] and sodium hydride,[27] can also be used to predict the properties of metallic systems. Secondly, we wanted to have a better understanding on the nature of phase transition in the ordering of atoms as the size of the cluster increases. To achieve these goals, ReaxFF$_{Al}$ was used to study the energetics and conformations of small aluminum clusters, simulate melting and crystallization of larger clusters and study the local atomic ordering of clusters during crystallization. In particular we examined the transition

from icosahedral ordering to fcc ordering. We have used potential energy and heat capacity to characterize melting in the aluminum clusters. A Honeycutt-Andersen (HA) pair analysis[28] was used to discriminate between icosahedral and fcc ordering of aluminum clusters, starting with Al_{256} cluster and ending with Al_{3072} cluster.

This chapter is divided as follows: Section 5.2 deals with force field parametrization and simulation methods while section 5.3, which is the discussion section, focusses on the results for melting, crystallization and local atomic arrangements of aluminum clusters. The conclusion is detailed in section 5.4.

5.2 Computational methods

5.2.1 Force Field Parametrization and validation

$ReaxFF_{Al}$ has been parameterized in line with the methodology used to develop $ReaxFF_{NaH}$[27] and $ReaxFF_{MgH}$.[29] ReaxFF does not use fixed connectivity assignment between atoms but rather deploys the bond-order formalism, which allows for bond breaking and formation in line with the works of Tersoff[30] and Brenner.[31] The bond order is directly determined from the instantaneous interatomic distance r_{ij}, which are updated per every iteration. Implemented in ReaxFF is the electronegativity equalization method (EEM)[32] used to calculate the distribution of charges. Since charges are updated per every iteration it implies that the nonuniform distribution of charges in small clusters, which emanates from large variations in coordination of atoms and therefore large differences in charges in various parts of the cluster, is correctly treated.

The fitting data used in ReaxFF were obtained from high level quantum mechanical calculations using VASP, which implements a projector augmented plane waves (PAW) method approach.[33] For all calculations a plane waves cut-off of 600 eV was used. The Kohn-Sham ground state is self-consistently determined in an iteration matrix diagonalization scheme. The calculations used the generalized gradient approximation of Perdew and Wang[34–36] (GGA-PW91) to represent electronic-correlation effects for a particular ionic configuration. For cluster calculation a cubic supercell of side 20 Å (which ensured that interaction between clusters in adjacent cells is negligible) was used with the cluster/molecule placed at the center of the cell. The Brillouin zone was then sampled at the Γ point.

For the condensed phases, for all volumes of the structures considered, the structures were fully optimized using force as well as stress minimization. The ions involved are steadily relaxed towards equilibrium until the Hellman-

Feynman forces are minimized to less than 10^{-4} eV/Å with conjugate gradient algorithm during all relaxation runs. A convergence of 10^{-6} eV per atom was placed as a criterion on the self-consistent convergence of the total energy. Brillouin zone integrations were performed using the following kpoints: Al-fcc ($15 \times 15 \times 15$), Al-bcc ($19 \times 19 \times 19$), Al-hcp ($15 \times 15 \times 15$), Al-sc ($15 \times 15 \times 15$) and Al-diamond ($10 \times 10 \times 10$) as per the Monkhorst-Pack grid procedure.[37] The reference configuration for valence electrons used was Al($3s^2 3p^1$). In determining the equilibrium volume, for a fixed cell volume of each structure the cell shape and atomic coordinates were fully optimized until the forces were less that 10^{-4} eV/Å per atom. The structure with the lowest energy was determined by plotting a total energy versus cell-volume curves for all the structures considered. The obtained energies were fitted to a Birch-Murnaghan equation of state (EoS) (Ref.[38]) in order to get the equilibrium volume and minimum energy. The final structure was then determined by optimizing the lattice parameters and atomic positions at this equilibrium volume until the forces on the ions were less than 10^{-4} eV/Å per atom.

ReaxFF energy expressions were parameterized by fitting to a training set containing the DFT derived EoS of pure Al phases, reaction energies and bond dissociation profiles on small finite clusters. The bond and atom parameters for the ReaxFF energy functions (Tabs. 5.1 and 5.2) were determined from the equations of state and cohesive energies of Al-metal condensed phases. The symbols and meanings of the parameters in Tabs. 5.1, 5.2 and 5.3 are discussed in Refs.[4,26]

Tab. 5.1: Bond Energy and Bond Order Parameters. D_e^σ is in kcal/mol.

Bond	D_e^σ	$P_{be,1}$	$P_{be,2}$	$P_{b0,1}$	$P_{b0,2}$
Al-Al	34.1	0.4832	6.4631	-0.15	6.160

Tab. 5.2: Atom Parameters

Atom	$p_{ov/un}$	λ_{11}
Al	-23.18	4.50

Tab. 5.3: van der Waals Parameters and bond radius parameters

Atoms	r^σ(Å)	r_{vdW}(Å)	E_{vdW}(kcal/mol)	γ_{vdW}(Å)
Al-Al	2.1322	2.2966	5.364	3.104

5.2.2   Simulation, thermodynamic and structural analysis methods

The MD calculations were done using a velocity Verlet algorithm[39] to integrate Newton's equations of motion. The simulations were performed in the canonical ensemble, NVT (constant number of particles, volume and temperature). The time step used for all simulations was 1.0 fs, which led to stable dynamics trajectories. The original clusters were built up from geometries constructed from fcc blocks by removing the periodic boundary conditions. The clusters were then minimized to remove bad contact angles. After minimization the clusters were equilibrated at 300 K for 200000 time steps. This was followed by annealing to 0 K. The annealed structures were then heated up to desired temperatures in order to determine their global minima. Determining the global minima for clusters using simulated annealing is a delicate task since there are bound to be several "deep" local minima in the potential energy hypersurfaces. Merely equilibrating the structure at a particular temperature can lead to the system being trapped in a local minima. To circumvent this problem we used a slow heating rate, which enabled the system to have enough time to sample the various possible conformations in the phase space and wring itself out of the undesirable "deep" local minima. Careful analysis and tests showed that a heating rate of 2.5×10^9 K/s was capable of predicting the most stable isomers of small aluminum clusters while if a heating rate of 2.5×10^{10} K/s was used some of these isomers were missed during the simulated annealing process. For instance at a heating rate of 2.5×10^{10} K/s we could not capture the stable isomer of Al_{10} but when the heating rate was reduced to 2.5×10^9 K/s it was captured by the force field. Therefore it is important to use a well optimized heating rate so as to avoid being trapped in an energetically unfavorable "deep" local minima. For large clusters (N > 200 atoms) we had to use even a lower heating rate, 2.5×10^8 K/s, to capture the global minima. We shall return to this point in the discussion section.

The heat capacity was calculated by fitting smooth cubic splines to the average potential energy during the heating process. The heat capacity is the temperature derivative of the potential energy as follows:

$$C_p(T) = \frac{d(PE)}{dT} + \frac{3R}{2} \tag{5.1}$$

where R, $= 1.9872159$ cal $K^{-1}mol^{-1}$, is the molar gas constant. With this in mind, the melting point is defined as the temperature with the maximum apparent heat capacity, which is caused by a sharp increase in the mobility of atoms in the system. However, for clusters it becomes problematic to locate the exact melting point due to the pre-melting of the surface of the cluster. This leads to a temperature region in which both the liquid and solid phases coexist (dynamic coexistence melting). Since phase transformation in a material

is accompanied by an increase in vibrational motion, an alternative way of distinguishing the solid-liquid-like phase transition is to use Lindemann index, which measures the vibrational motion of atoms. The Lindemann concept[40] has it that melting occurs when the stretching curve gets unstable second derivatives. It can be taken to be a measure of dynamic disorder in a material. The Lindemann index is at times equated to the relative root-mean-square bond (rms) length fluctuations, which is expressed as:

$$\delta = \frac{2}{N(N-1)} \sum_{i,j(i\neq j)}^{N} \frac{\sqrt{\langle r_{ij}^2 \rangle_T - \langle r_{ij} \rangle_T^2}}{\langle r_{ij} \rangle_T} \tag{5.2}$$

where $\langle .. \rangle_T$ denotes the thermal average at temperature T and r_{ij} is the distance between atom i and j. During melting the Lindemann index is expected to increase abruptly by a factor of more than three. Usually in bulk materials δ < 0.1 indicates a solid phase. For clusters, due to surface effects, δ < 0.08 is an indication of a solid phase. An extensive analysis on the determination of heat capacity and rms bond length fluctuations for clusters is given in Ref.[41] Further insight into the structure of clusters has been done by analyzing the radial distribution function, g(r). The g(r) describes how the atoms are radially packed around each other and shows the structural ordering of the atoms in a system. The g(r) is linked to the experimentally observable structure factor, S(k), obtained in diffraction experiments.

To understand the phenomenon of icosahedral to fcc growth we studied the local atomic arrangements in four clusters of aluminum, viz Al_{256}, Al_{512}, Al_{1024} and Al_{3072}. The structures were first heated up to temperatures between 250 K and 2000 K and then annealed to 0 K at a rate of 2.5×10^9 K/s. HA pair analysis was then performed on the clusters during the annealing process in order to ascertain at which cluster size fcc ordering became more important with respect to icosahedral ordering. In HA pair analysis the local structure surrounding a pair of atoms (root pair) is classified using four indices (*klmn*) as follows:

1. The first index, *k*, is 1 when the atoms in the root pair are bonded, else it is 2.

2. The second index, *l*, is the number of near-neighbor atoms common to the root pairs.

3. The third index, *m*, is the number of nearest neighbor bonds between the shared neighbors.

4. The fourth index, *n*, is used to differentiate between cases in which the first three indices are the same but bond geometries differ like in the case of fcc and hcp.

The following holds in HA pair analysis prescription:

1. The 1421 pairs represents fcc ordering while the hcp ordering is represented by both 1421 and 1422 pairs.

2. The 1441 and 1661 pairs represents bcc ordering while the 1202, 1311, 1301, 1331 and 1321 represents rhombohedral ordering.

3. The 15's pairs (e.g. 1551 and 1541 pairs), 1321 and 2331 are indicative of rapidly quenched liquid or amorphous states and leads to simple icosahedral ordering. In particular, the 1551 pairs represent two neighboring atoms with five common neighbors that form a bonded pentagon. Thus the 1551 pairs, which are situated in a five fold symmetry environment, are characteristic of icosahedral ordering. The 143's pairs leads to distorted icosahedra (Ref. [42]), which can also be considered as $+72°$ disclinations. [43]

Since the interest here is to understand the underlying mechanism governing transition from icosahedral structure to fcc structure only the 1421, 1422, 1431 and 1551 pairs have been considered in this work. We take $R_{cut} = 3.0$ Å, which is just slightly larger than the DFT bulk value of aluminum-aluminum bond length (2.864 Å) and is the value of the first peak in $g(r)_{Al-Al}$. The HA pairs fraction are highly dependent on the value of R_{cut} and therefore it is not possible to make a quantitative comparison with other studies but a qualitative comparison holds.

5.3   Results and Discussion

5.3.1   Heats of Formation and geometry of clusters

The ability of ReaxFF to capture the relative stability of condensed phases of aluminum was tested against a number of Al crystal modifications. For each an every phase of Al-metal (fcc-Al, sc-Al, bcc-Al, hcp-Al and diamond-Al) considered in this work, the quantum energies were computed for a broad range of volume, describing both expansion and compression.

In Fig. 5.1 we see that ReaxFF correctly describes the relative phase stabilities of four phases of aluminum metal with respect to the quantum values. The hcp phase is not included since with ReaxFF the hcp and fcc phases get the same energy; the method does not have the multibody terms for metals that are needed to distinguish these phases. For the most stable fcc phase ReaxFF gives the equilibrium energy to be -78.97 kcal/mol per formula unit whereas
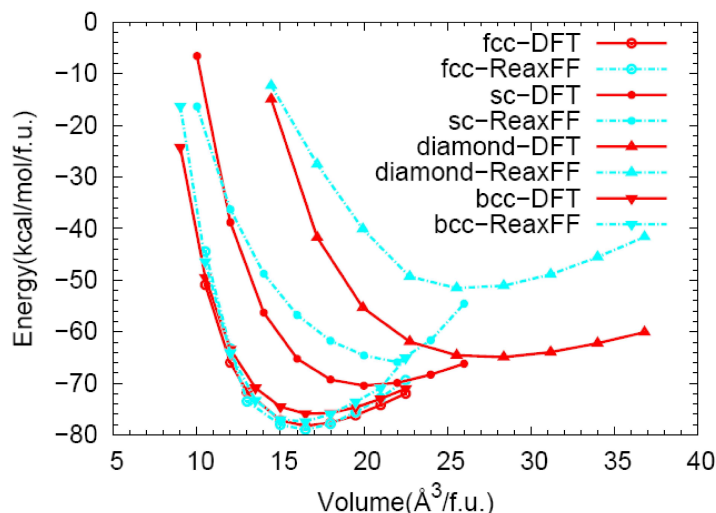
Fig. 5.1: Relative stability of the various phases of aluminum as computed by DFT and ReaxFF.

DFT gives -78.22 kcal/mol per formula unit. Thus ReaxFF value differs from DFT by 0.75 kcal/mol per formula unit. The experimental lattice parameter is 4.0494 Å while DFT gives 4.0498 Å and ReaxFF gives 4.250 Å.

Another important comparison is on surface energy, which gives a measure of the energy needed to cleave a surface. To obtain the surface energy a 5 layered 20 atoms slab with a vacuum layer equivalent to 5 layers was used. Brillouin zone was sampled using a well converged $9 \times 9 \times 1$ kpoints. The surface energy was then calculated by comparing the total energy of bulk and slab models as follows

$$E^{\text{surface}} = \frac{1}{2A}(E^{\text{slab}} - N \cdot E^{\text{bulk}}) \tag{5.3}$$

where E^{slab} is the energy of an N-layer slab, E^{bulk} is the bulk energy per formula unit and A is the bulk surface area. From ReaxFF the surface energy for Al(111) surface was computed to be 1.38×10^{-4} kcal/m^2, which is in good agreement with DFT value of 1.87×10^{-4} kcal/m^2.

The Al-Al bond energy in ReaxFF was optimized using DFT derived values of bond dissociation profile of Al$_2$ dimer and other small aluminum clusters. Figure 5.2 shows the bond dissociation curve of Al$_2$. The dissociation curves were constructed from the equilibrium geometry using single point calculations by changing the bond length. ReaxFF gives an equilibrium bond length of 2.6
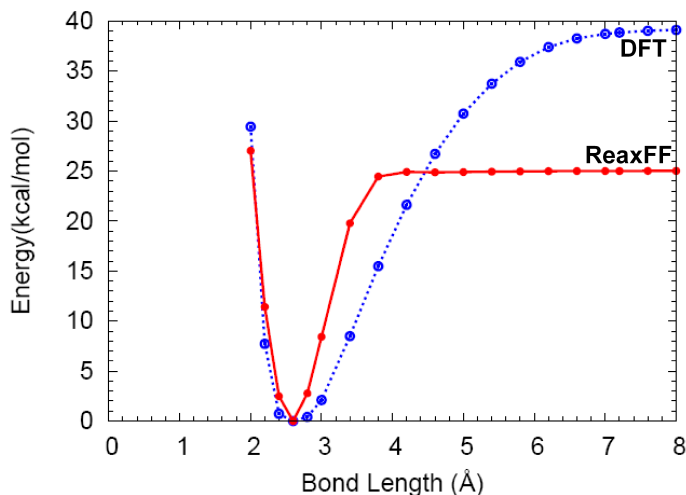
Fig. 5.2: Bond dissociation profile of Al_2 dimer as computed by DFT and ReaxFF. The energies were computed with reference to the equilibrium bond length's energy.

Å, which is the same as DFT value. These values are in good agreement with the experimental Al_2 dimer bond length of 2.47 Å.[44] Only the triplet values are shown because the singlet values are energetically unfavorable throughout the dissociation curve.

In computing the free energies of the aluminum clusters, spin polarization was taken into account. It was found that in most cases the electronic configuration that favored the lowest spin multiplicity was not necessarily the most stable. For instance, for Al_3 the spin doublet case was 2.07 kcal/mol more stable than the spin quartet and for Al_7 the doublet configuration was 24.8 kcal/mol more stable than the quartet arrangement. In the case of Al_2 the triplet state was found to be more stable than the singlet state by 7.76 kcal/mol while for Al_6 the triplet state was energetically more stable than the singlet state by 3.59 kcal/mol. For Al_4 the triplet state was more stable than the singlet state by 3.5 kcal/mol. For Al_{11} it was found that spin doublet state was more stable than the spin quartet state by 9.17 kcal/mol.

DFT calculation shows that the most stable form of Al_3 is an equilateral triangle in agreement with the work of Petterson et al.[6] For Al_4 the planar rhombus (D_{2h}) conformation is found to be more stable than the pyramidal form (C_{3v}), in agreement with Koutecky et al.[45] and Petterson et al. In the case of Al_5, Jug et al.[46] found the pyramidal form to be the most stable whereas Petterson et al. and Yang et al.[14] found the planar (C_{2v}) form to be more stable than

the pyramidal form. The DFT calculations for Al_5 are consistent with the works of Yang et al. In addition, Petterson et al. found that in the case of Al_6 the octahedron is the most stable form whereas Upton[7] found a distorted octahedron to be the most stable. Clearly, for Al clusters with more than 5 atoms three dimensional structures are favored since as the size of the clusters increases the number of nearest neighbors also increases but this cannot be achieved in a planar structure. For instance, the icosahedral arrangement of Al_{13} enables the atom in the middle of the structure to have 12 neighbors.

There are interesting differences between ReaxFF and DFT predictions as shown in Fig. 5.3. For Al_4 DFT favors the rhombus structure (Fig. 5.3(a)) in agreement
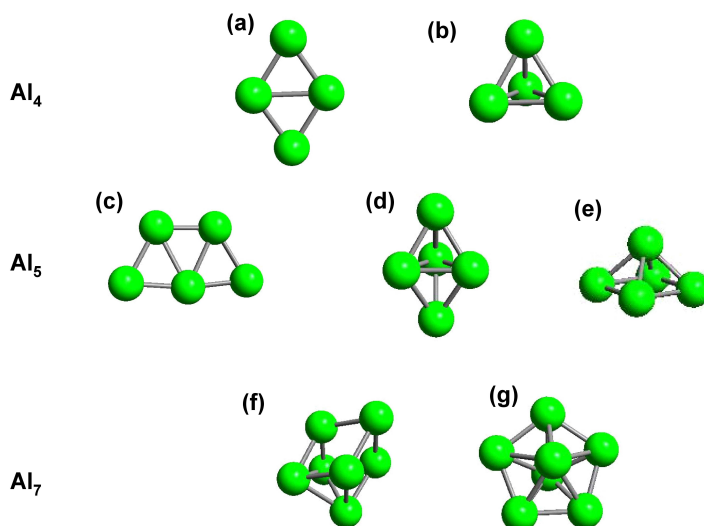
Fig. 5.3: Small representative isomers of Al_4, Al_5 and Al_7 clusters as predicted by DFT and ReaxFF. DFT predicts that structures **a**, **c** and **f** are the most stable configurations for Al_4, Al_5 and Al_7 respectively. ReaxFF, on the other hand, predicts that structures **b**, **d** and **g** are the most stable configurations for Al_4, Al_5 and Al_7 respectively.

with Pacchioni,[45] Bauschlicher and Pettersson[6,47] and Jones.[48] ReaxFF, on the other hand, finds a tetrahedron structure (Fig. 5.3(b)) to have the lowest energy. Upon heating the rhombus structure it immediately transforms into the tetrahedron isomer even at temperatures as low as 1 K. The tetrahedron structure was also found by Böyükata and Güvenç,[49] who used the embedded atom method (EAM),[1] to be the most stable isomer of Al_4. For Al_5 DFT favors the planar rhombus (C_{2v}) like structure (Fig. 5.3(c)) in agreement with Pettersson et al. but ReaxFF finds the trigonal bipyramidal (D_{3h}) isomer (Fig. 5.3(d)) to be the more stable (than the planar conformation by 56.2 kcal/mol)

in agreement with Böyükata and Güvenç. The trigonal bipyramidal structure is so stable such that even at 2000 K it is not distorted. It should be noted that from DFT computation the planar rhombus structure is 16.8 kcal/mol more stable than the trigonal bipyramidal structure. In DFT the trigonal bipyramidal isomer is found to optimize in the hexatet state. In the doublet configuration it transforms into a rhombus structure whereas in the quartet state it transforms into a square pyramidal structure (Fig. 5.3(e)). Another interesting finding is in the isomers of Al_7. DFT predicts that the capped trigonal antiprism (D_{3d}) (Fig. 5.3(f)) is the most stable isomer in agreement with the works of Jones[50] and Jug et al. However, Böyükata and Güvenç predicted that a pentagonal bipyramidal structure (Fig. 5.3(g)) was the most stable. In agreement with the latter, we found that the pentagonal bipyramidal structure was more stable than the capped trigonal antiprism by 2.3 kcal/mol. However, this energy difference is quite small. Interestingly, the pentagonal bipyramidal structure retained its shape when optimized in VASP in the hexatet but transformed to capped trigonal antiprism in the doublet and quartet states. This suggests that it is a higher excited isomer of Al_7. DFT predicts that the capped trigonal antiprism is more stable than the pentagonal bipyramidal structure by 44.9 kcal/mol.

The stability of the planar isomers of Al_4 and Al_5 over their 3 dimensional counterparts and of capped trigonal antiprism in the case of Al_7 is a quantum mechanical effect inherent in DFT due to exchange-correlation. If the overlap of the orbitals in not considered in DFT then the 3D isomers should be preferred. This explains the discrepancy between ReaxFF and DFT in the case of these clusters. From a force field point of view the stability of the pentagonal bipyramidal isomer of Al_7 over the capped trigonal antiprism is because the former is more symmetric than the latter. In the force field approach the higher the symmetry the more stable the structure. In the case of DFT/*ab initio*, on the other hand, orbital overlaps and exchange-correlation effects plays a crucial role in determining the stability of structures, which leads to isomers that are not necessarily highly symmetric being more stable.

In agreement with Ref.[49] both ReaxFF and DFT show that a capped pentagonal bipyramidal structure is the most stable isomer of Al_8. For $8 \leq n < 13$ clusters the pentagonal ring forms the backbone. Starting from Al_{11} onwards there is at least one internal atom coupled with bulk like coordination. Al_{12} has two pentagonal rings. The lowest energy structure can be thought of as being made from Al_{13} by removing an atom without changing the icosahedral symmetry. The most stable isomer of Al_{14} is formed by capping of one face of the icosahedral structure of Al_{13}. Al_{19} is made of two icosahedral structure fused together. Even at Al_{55} the icosahedral coordination is retained.

From the foregoing analysis, one might wonder that if in some cases ReaxFF gives results for small clusters that differ significantly from those of DFT why

then do the two agree for larger clusters? What is it about the size that gives rise to this? Can we be so confident about the force field in spite of the significant difference in prediction between ReaxFF and DFT for small clusters? We reiterate that ReaxFF results are in line with predictions of other potentials.[49,51,52] In the atomistic based-potential approach stability of structures are dictated by the number of bonds and symmetry. In DFT other effects such as Jahn Teller distortion and spin polarization play a role in determining the most stable configuration.[14,53] For instance in DFT and experiments Al_2 has two isomers but from a force field perspective Al_2 has only one conformation. In fact an extensive investigation of the isomers of Al_n upto n = 10 has been given by Jones.[48]

Table 5.4 shows the average interatomic distances for selected aluminum clusters as computed by DFT and ReaxFF in comparison to previous studies. Now, as

Tab. 5.4: Average interatomic distance, $d_{<nn>}$, (in Å) of small Al_x clusters used in the training set. c-s means the average distance from the atom in the center of the icosahedral to that on the surface.

Cluster	DFT	ReaxFF	Others
Al_2	2.636	2.585	2.51^1
Al_3	2.524	2.583	$2.51^1, 2.62^2$
Al_6	2.724	2.525	2.70^1
Al_{13}	2.814	2.842	
Al_{13}(c-s)	2.672	2.700	

^{1} Reference.[14]

^{2} Reference.[7]

mentioned earlier, determining the global minima for clusters using simulated annealing is a delicate task since there are bound to be several minima in the potential energy hypersurfaces. Therefore, it should be noted that using a slow heating rate is important since this enables the system to have enough time to sample the various possible conformations in phase space. Careful analysis and tests showed that a heating rate of 2.5×10^9 K/s was capable of predicting the most stable isomers of the well known isomers of small aluminum clusters while if a heating rate of 2.5×10^{10} K/s was used some of these isomers were missed during the simulated annealing process. For instance at a heating rate of 2.5 $\times 10^{10}$ K/s we could not capture the stable isomer of Al_{12}. When the heating rate was reduced to 2.5×10^9 K/s it was located by the force field. This is illustrated in Fig. 5.4. This shows that it is important to use a well optimized heating rate in order to avoid being trapped in an energetically unfavorable local minima. This point is also noted by Zhang et al. who concluded in their work on aluminum clusters with around 55 atoms that in the limit of long equilibration
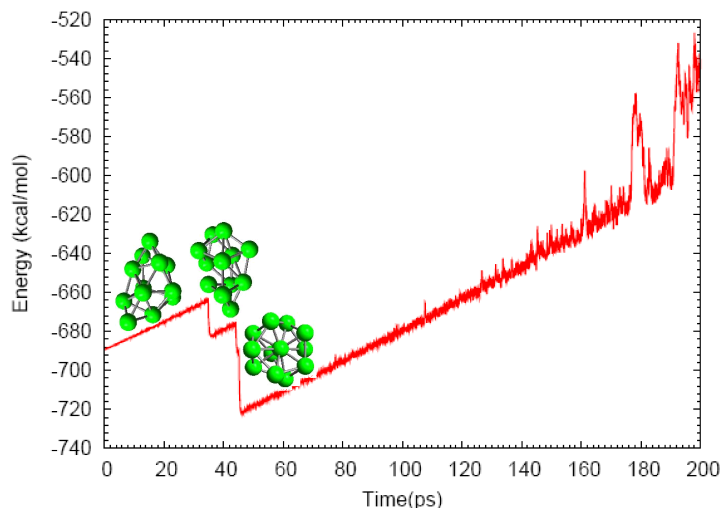
Fig. 5.4: Heating up of Al_{12} at a rate of 2.5×10^9 K/s. Various isomers of Al_{12} are captured at this heating rate.

time the system will anneal into the lowest energy structure prior to melting.[54]

Another important point is that the temperature at which the structure is equilibrated determines how soon the system locates its global minimum. As an example, the most stable form of Al_{13} cluster is an icosahedral (I_h) structure. To determine whether ReaxFF can reproduce this we took a distorted Al_{13} cluster and heated it up at various temperatures, viz: 500 K, 1000 K and 1500 K. Figure 5.5 shows the results of the simulation. At 500 K the system is trapped in a local minimum and the resulting structural modification is not the most stable. However, by equilibrating the cluster at an elevated temperature of 1000 K more phase space becomes accessible to the system and the icosahedral configuration is captured by the system. The system finds a global minimum at a much earlier time at a temperature of 1500 K as compared to 1000 K since more phase space is accessible to the system at earlier time at this temperature. Thus, an increase in temperature makes more phase space to be available to the system. At 500 K the icosahedral configuration is not accessible to the system within the timescale of the simulation.

To investigate the relationship between clusters and their relative stability, several aluminum clusters N $\leq$ 108 were cut from a periodic crystal. The clusters were then optimized using the force field optimization engine. To further reduce the bad contact angles the clusters were minimized using low temperature (1 K) MD simulation for 20000 steps (where one time step is 1 fs). This was then
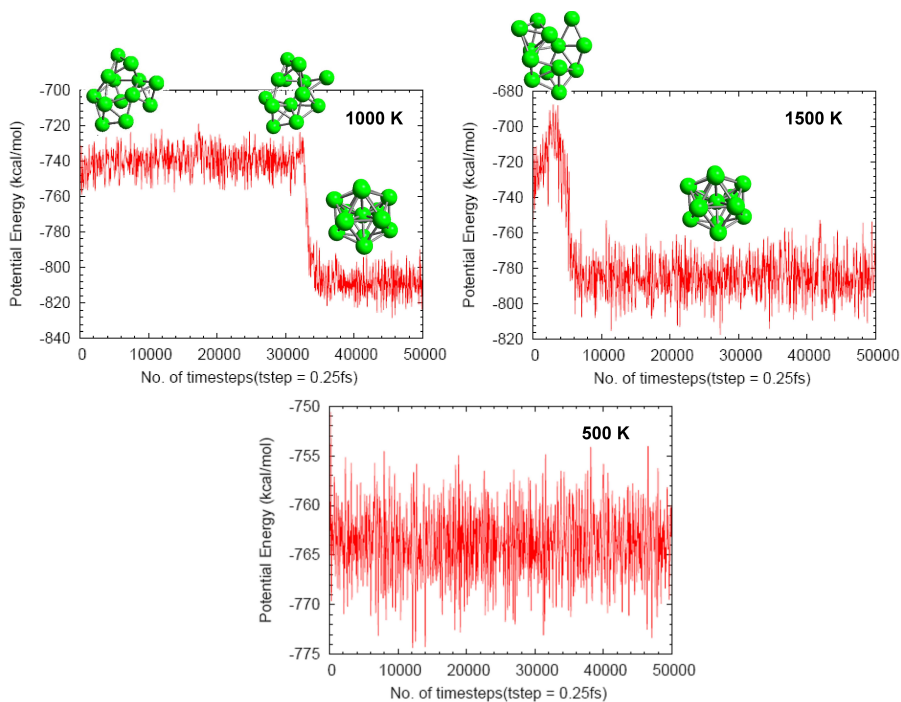
Fig. 5.5: Simulated tempering of Al$_{13}$ cluster. At 500 K the system is trapped in a local minimum and the resulting structural modification is not the most stable.

followed by an equilibration run at 300 K for 100000 time steps. After this, each of these clusters were heated upto 2000 K at a rate of 2.5×10^9 K/s for 800000 steps in a NVT simulation using Berendsen thermostat.[55] This was followed up by equilibration at this temperature for a further 200000 steps. The equilibrated structures were then slowly annealed to 0 K at a rate of 2.5×10^9 K/s. This process was repeated four times but each time at a different temperature, viz 300 K, 500 K, 600 K and 800 K. The internal energy values from the annealed geometries were then averaged. Figure 5.6 shows the second finite difference of the total energy (stability function) with respect to the cluster size N, which is defined as

$$S(N) = E_{tot}(N + 1) + E_{tot}(N - 1) - 2 * E_{tot}(N) \qquad (5.4)$$

The peaks in the figure indicates that the clusters are quite stable (magic clusters) while the minima correspond to the most unstable structures. We can see in Fig. 5.6 that Al$_{13}$, Al$_{19}$, Al$_{23}$ and Al$_{55}$ are magic clusters. The fact that the force field is able to capture these very stable clusters gives a further confidence
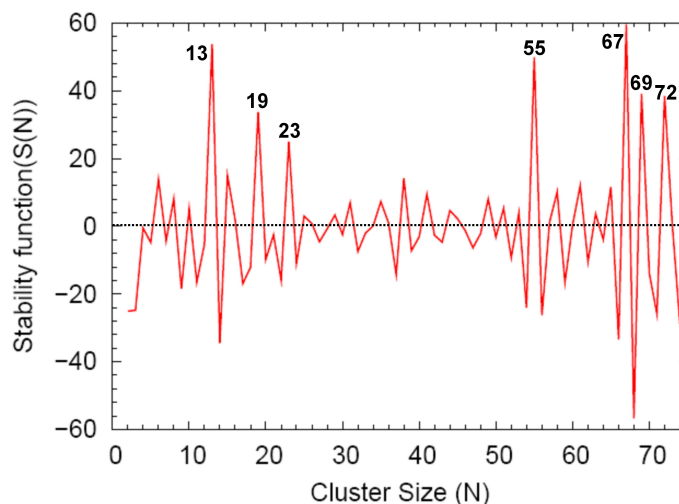
Fig. 5.6: Stability function as a function of cluster size. The peaks in the figure shows the most stable clusters based on geometric considerations. Positive values of stability function indicates that the cluster is stable.

in the suitability of ReaxFF_{Al} in modeling aluminum metal. Our predictions of magic clusters of aluminum is consistent with the work of Doye.[19] Doye predicts that Al_{44}, Al_{61}, Al_{67}, Al_{69} and Al_{72} are magic clusters. This is consistent with ReaxFF_{Al}'s prediction. One major area of disagreement with Doye is that he predicts Al_{48} to be a stable cluster whereas ReaxFF_{Al} predicts Al_{49} to be a stable structure. ReaxFF_{Al} prediction is consistent with the well known magic clusters.[56] The stability of these clusters from a geometrical approach has to do with their high symmetry in comparison to neighboring clusters along the stability energy surface. Joswig et al.,[51] using Sutton-Chen potential,[57] found the stable clusters to be those with n = 4,6,12,14,17,21,23,30,39,42,45,49 and 56 atoms whereas those with n = 5,11,13,15,22,28,33,36,41,44,46,51,53 and 55 were found to be particularly unstable. The authors, however, had some reservations on their results especially in view of the fact that Al_{13}, from *ab initio* computations, is a well known magic cluster. Figure 5.7 shows the annealed structures of Al_{13}, Al_{19}, Al_{23}, Al_{55}, Al_{67} and Al_{72}. Al_{13} has one atom in the middle whereas Al_{19} can be thought of as being made up of two Al_{13} clusters that have been fused together in such a way that that there is an atom at the center of each half of the fused cluster.

The overall binding energy for a cluster can be partitioned into bulk, surface,
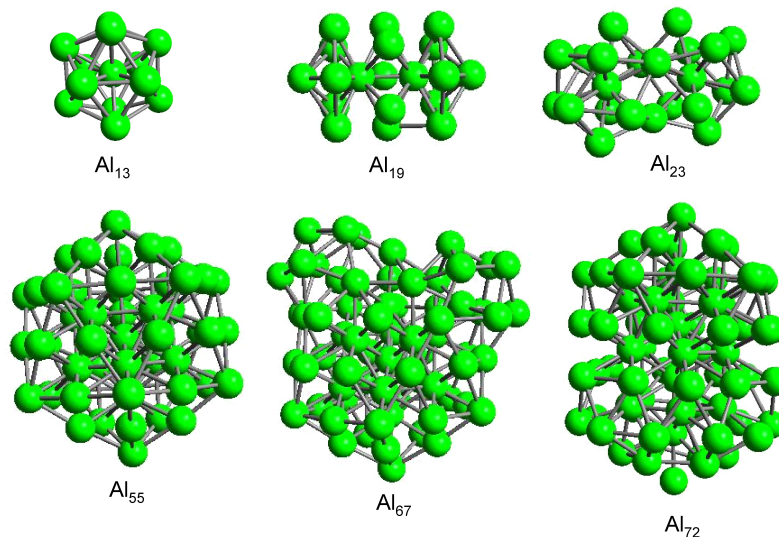
Fig. 5.7: Some of the magic clusters of aluminum: Al_{13}, Al_{19}, Al_{23}, Al_{55}, Al_{67} and Al_{72} predicted by ReaxFF.

edges and corners contribution as follows:

$$E_{coh} = E_{bulk} + a_{surf}N^{-\frac{1}{3}} + a_{edge}N^{-\frac{2}{3}} + a_{corner}N^{-1} \tag{5.5}$$

This approximation is valid provided that geometrical effects dominates and the electronic shell structures contributions are negligible. This is true especially for larger clusters whose stabilities are purely a function of structural configurations. Figure 5.8 shows a graph of binding energy as a function of $N^{-\frac{1}{3}}$. In general, the edges and corner contributions are negligible especially in the case of aluminum where the clusters tend to have a spherical shape. These two contributions might become important in the case of very small clusters.

By a linear regression analysis (in which we considered only clusters with $N \geq 20$) the bulk binding energy is estimated to be

$$E_{bulk} = 76.8 \quad kcal/mol \tag{5.6}$$

This is consistent with the experimental value of 77.48 kcal/mol[58] and that of Ahlrichs et al.[53] who found a value of 77.25 kcal/mol. One important thing is that the relationship in equation (5.5) should only be applied to clusters of comparable structure. If we only consider clusters for $N \geq 80$ then $E_{bulk} = 76.85$ kcal/mol, which is still close to that in equation (5.6). The domination of surface
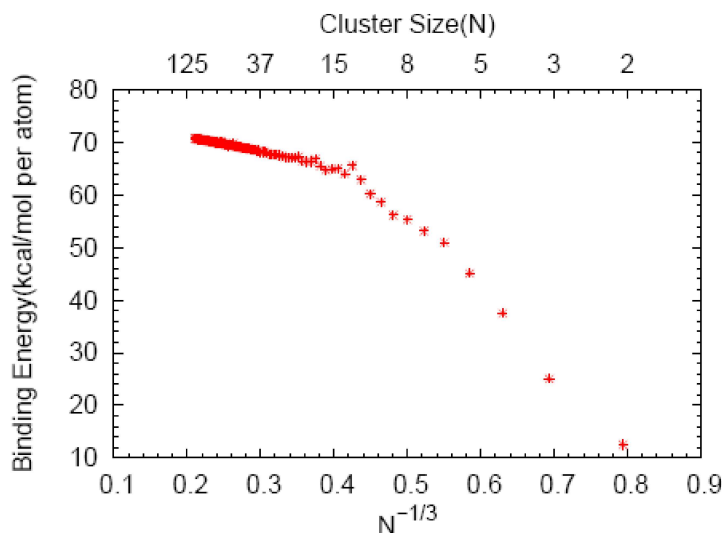
Fig. 5.8: Binding energy per atom for aluminum clusters with N = 2,3,4,5.....,108 as a function of cluster size (N).

energy contribution at low values of N can be seen from the fact that for $N \leq 13$ the value of $a_{surf,}$ term is -141.33 kcal/mol per $N^{-\frac{1}{3}}$. This term drops significantly to a value of -28.426 kcal/mol per $N^{-\frac{1}{3}}$ for $N \geq 20$. Thus surface energy contribution plays a dominant role for very small clusters.

5.3.2   Melting and icosahedra to fcc transition

Dynamic coexistence of solid and liquid phases for small clusters[59] makes it difficult to pinpoint with exactitude their melting points. In particular, for clusters there are fluctuations in potential energy with respect to temperature at the solid/liquid interface. This is due to pre-melting, which arises from surface effects. In the bulk scenario, melting is accompanied by an abrupt change in potential energy so that there is a clearly defined solid to liquid transition. In ideal experimental situation there is always some surface. Therefore to determine the bulk melting point we represented the Al(111) using the slab methodology. In this methodology a 5 layer slab of Al was generated by periodical repetition of a supercell geometry with a vacuum (equivalent to 5 layers) between any two successive aluminum metal slabs in the z direction. The dimensions of the Al(111) slab were (28.6 × 24.75) giving a total of 500 atoms. This suitably separated the slab from its periodic images. The system

was first equilibrated at 300 K and then heated up at a rate of 2.5×10^9 K/s. The results of the computation are shown in Fig. 5.9.
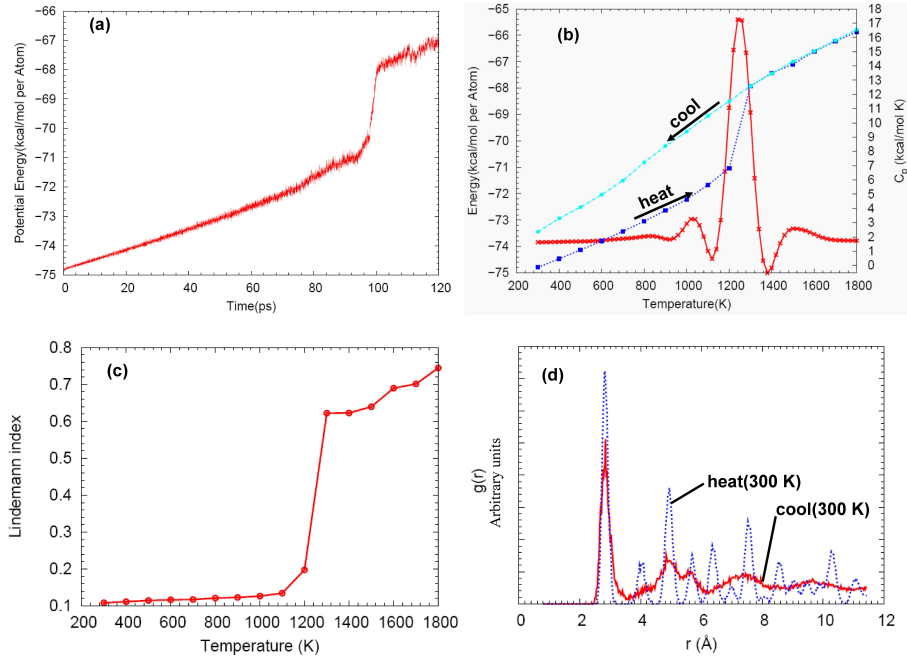
Fig. 5.9: (a) Variation of potential energy with time during the heating process of aluminum slab with 500 atoms. (b) Potential energy and heat capacity $C_p(T)$ for heating and cooling cycle of aluminum slab with 500 atoms. (c) Lindemann index for heating aluminum slab with 500 atoms. (d) The RDFs of the initial starting structure at 300 K and the cooled structure at 300 K. From the RDFs, the starting structure is crystalline but the cooled structure is in an amorphous state (indicated by a split in the second peak).

As can be seen in Figs. 5.9(a) and 5.9(b), the melting transition is accompanied by a rapid increase in energy. If we take the melting temperature to be the center on the peak in the heat capacity then we get a melting temperature of 1240 K. This is consistent with the Lindemann index criterion (Fig. 5.9(c)). In Fig. 5.9(b) the cooled structure is less stable than the starting structure. This means that the system undergoes a phase transformation into a less stable (amorphous) structure. Amorphosization occurs because the cooling rate is fast and as such the system does not have enough time for atomic rearrangement into a crystalline structure. This is why the energy of the cooled structure is higher than that of the starting structure. The RDFs of the starting and the

end (cooled) structures are shown in Fig. 5.9(d). An interesting observation on bulk melting is given by Lutsko et al.[60] They suggested the introduction of a factor between the simulated and the experimental melting points when periodic boundary conditions are imposed for bulk systems. The experimental melting point is taken to be 0.75-0.85 times its simulated counterpart. Strictly speaking, Lutsko's criteria applies to a superheating required to melt a perfect crystal in the 3D periodic simulations. Superheating in ideal, periodic simulations is related to the fact that only the homogeneous nucleation mechanism is available in the simulations. In a surface slab simulation, the surface induced melting mechanism is available, and for a properly equilibrated simulation, superheating should not be observed. Since we used a slab approach, Lutsko's criteria does not hold.

Unlike bulk situation, in clusters, due to surface effects, there are no abrupt change in the calorific curve, which normally is an indication of a phase transition from solid to liquid state. This presents a challenge in locating the exact melting point of clusters. Moreover, the phenomenon of dynamic coexistence melting implies that melting occurs over a range of temperature. A popular way to circumnavigate this problem is by equilibrating the clusters at various specific temperatures and then computing the thermodynamical and structural properties at each respective state. Figure 5.10 shows the potential energy scans for aluminum cluster with 1024 atoms.
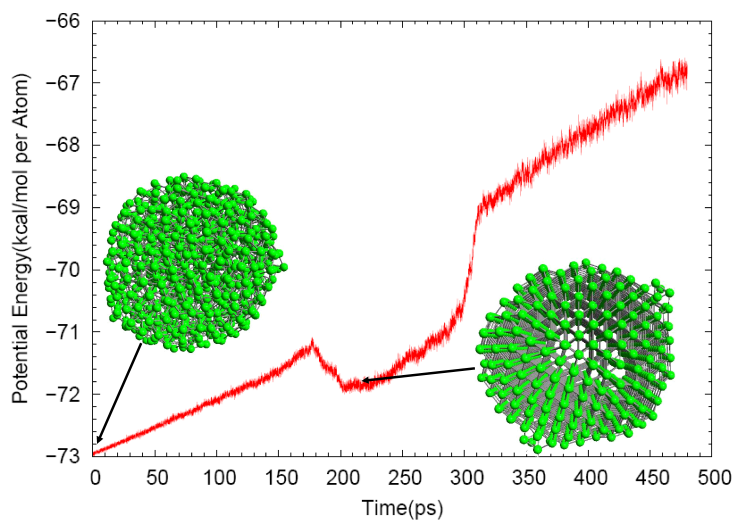
Fig. 5.10: Variation of potential energy with time during the heating process of aluminum cluster with 1024 atoms. The starting structure is amorphous. At about 170 ps (700 K) the system finds a more stable configuration, which is crystalline.

What is interesting in Fig. 5.10 is the fall in potential energy at about 170 ps, which is due to the system finding a more stable configuration. The annealed crystalline geometry of this stable configuration is also shown in the figure. We shall discuss the local ordering in this stable structure later. Figure 5.11 shows the variations in the heat capacity during the heating up process of aluminum cluster with 1024 atoms, i.e. the cluster in Fig. 5.10. The heat capacity heat
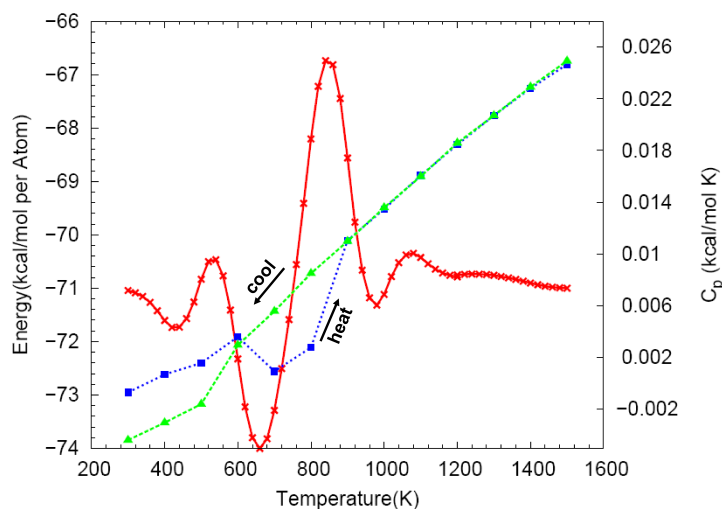
Fig. 5.11: Potential energy and heat capacity, $C_p(T)$, for heating-cooling cycle of aluminum cluster with 1024 atoms. When cooled the system goes to a crystalline state.

capacity has negative values. Since this was not a microcanonical simulation, the negative heat capacity implies that the system was initially in a metastable state but found a more stable configuration prior to melting. This led to a fall in potential energy and concomitantly gave rise to a negative heat capacity. At around 310 ps the potential energy of the system rises up rapidly due to melting. The calculated melting point for this representative configuration is 840 K. In the cooling stage the cluster finds a lower minimum than the starting structure. The geometry of this minimum is crystalline. This implies that the cooling rate was slow enough so that the atoms had enough time to diffuse into their equilibrated positions and crystallize. It can be seen in the figure that there is hysteresis between the heating and cooling graphs due to entropy-induced supercooling. These graphs intersects at 620 K and 900 K. The 620 K is the threshold temperature for the crystallization of the supercooled structure while the 900 K is very close to the melting point of the cluster.

Figure 5.12 shows the RDFs of the Al_{1024} cluster at 1500 K and 300 K (upon

cooling).
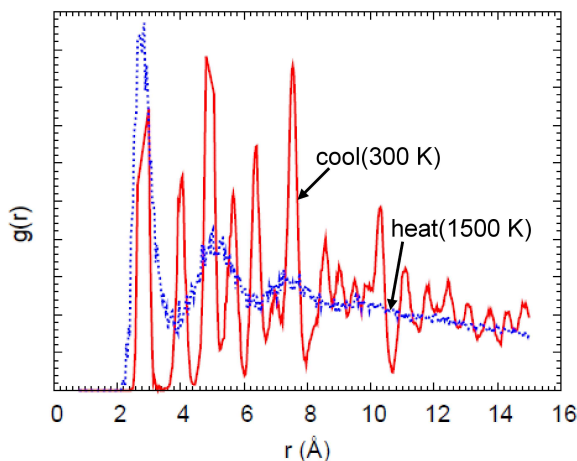
Fig. 5.12: The radial distribution functions of the heated and cooled conformations of aluminum cluster with 1024 atoms as shown in Fig. 5.10.

There is a very strong dependence of the melting point on the starting configuration. This is illustrated in Figs. 5.13 and 5.14, which show the calorific and heat capacity curves for the case whereby the annealed stable configuration in Fig. 5.13 is used as the starting structure in Fig. 5.14.

As illustrated in Fig. 5.13, in this instance there is no negative heat capacity although the starting configuration is amorphous. The annealed configuration in Fig. 5.13 was used as the starting configuration in Fig. 5.14.

Interestingly, although the cooling rate in Fig. 5.14 is the same as that in Fig. 5.13 the structure (in Fig. 5.14) goes to an amorphous configuration. Actually it is as if it goes back to the starting configuration in Fig. 5.13. The calculated melting points in Fig. 5.13 and Fig. 5.14 are 760 K and 960 K respectively. Note that both the starting structures in Fig. 5.10 and Fig. 5.13 anneal to the same crystalline state. This crystalline state is the starting structure in Fig. 5.14. The high melting point of Fig. 5.14 shows that this configuration is the most stable.

It should be reiterated that one must be very careful when talking about the melting point of clusters. Clusters can have many isomers and the system can be trapped in any one of these accessible configurations. Therefore, the ideal melting point of a cluster should be an average of all the accessible states.
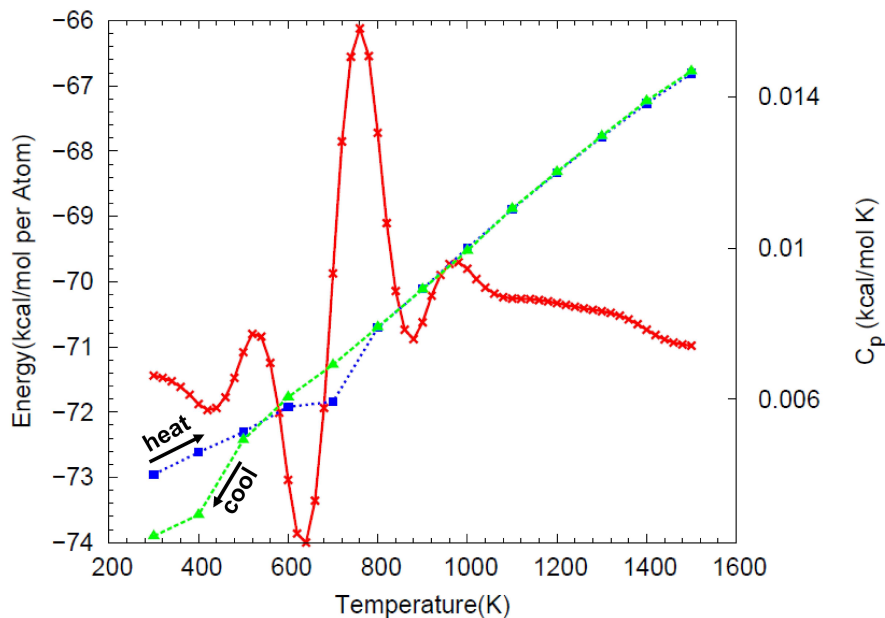
Fig. 5.13: The energy and heat capacity $C_p(T)$ for heating-cooling cycle of aluminum cluster with 1024 atoms starting with different configurations.

However, the theoretical melting points of clusters in the literature are those for the most stable configurations. Table 5.5 shows the melting point of Al_{256} and that of the bulk as computed by various potentials in Ref.[61] and ReaxFF. ReaxFF values were computed using a heating rate of 2.5×10^8 K/s. The bulk experimental value (933 K) is also given.

Tab. 5.5: Melting point of Al_{256} and bulk aluminum as computed by various potentials,[61] and ReaxFF. The given values for ReaxFF were those determined from a heating rate of 2.5×10^8 K/s.

| Method	Al_{256}	Bulk
Glue[62]	473	1244
EAM	448	1146
Streitz-Mintmire	448	1146
Sutton-Chen	400	529
Exp.		933
ReaxFF	800	1240
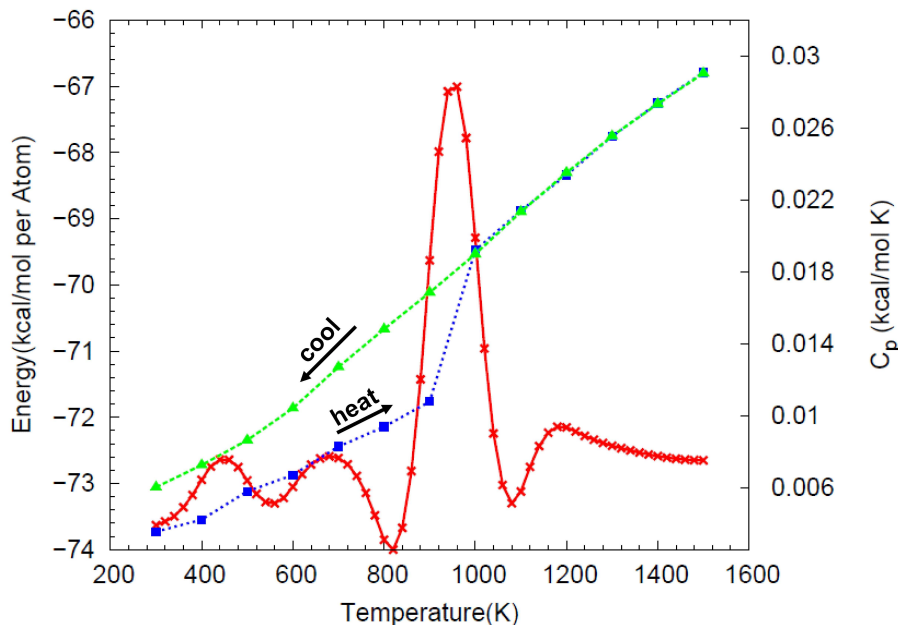
Fig. 5.14: The potential energy and heat capacity $C_p(T)$ for heating-cooling cycle of aluminum cluster with 1024 atoms starting with different configurations. In this particular run, the annealed configuration shown in Fig. 5.13 was used as the starting configuration.

It can be seen that ReaxFF gives a bulk melting point (1240 K) that is in excellent agreement with the glue potential[62] but higher than EAM[1] and Streitz-Mintmire[2] potentials by about 100 K. Using the glue, EAM, Streitz-Mintmire and Sutton-Chen[57] potentials, the melting point of Al_{256} was calculated to be 473 K, 448 K, 448 K and 400 K, respectively. ReaxFF, on the other hand, gives a melting point of 800 K. However, for clusters of this size there is dynamical coexistence melting and as such it is quite challenging to pinpoint the exact melting point. There are no experimental works to validate our results. However, Gary et al.[63] experimentally determined the melting points for Al_{49}^+ - Al_{63}^+ to be in the range of 450 K - 650 K. In the work of Neal et al.[64] they computed the melting point of aluminum clusters with 25 - 83 atoms to be in the range of 600 K - 700 K. These results are therefore consistent with the previous works. Figure 5.15 shows the heating curve for Al_{256}. The Al_{256} cluster was heated up from 0 K to 1250 K at a rate of 2.5×10^8 K/s.

In the figure, at around 600 ps there is a fall in the energy (region (a)), at about 200 K. This energy fall is due to the system finding an energetically lower
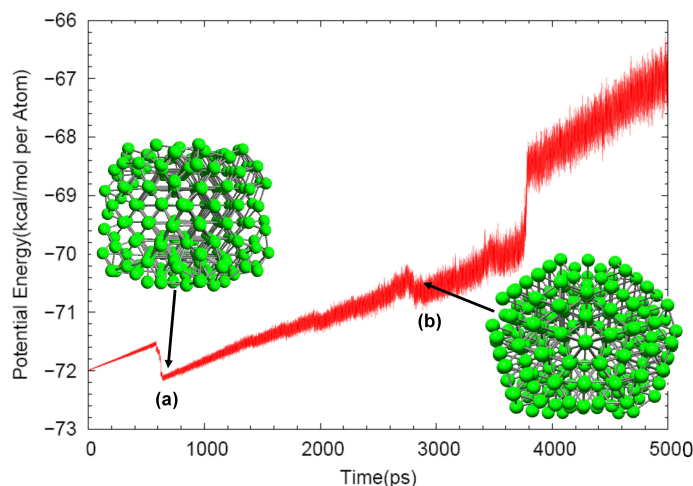
Fig. 5.15: Variation of energy with time during heating of Al_{256}. The temperature was ramped up at a rate of 2.5×10^8 K/s.

conformation in comparison to the starting structure. Upon further heating, the system again finds another lower minimum at approximately 2800 ps (region (b)), about 800 K. Shortly afterwards, at 3800 ps, the energy of the system rises up rapidly indicating that there is a transition from solid to liquid state. The geometries of the annealed structures of (a) and (b) are shown in Fig. 5.15. The two lower minimum structures (a and b) were annealed to 0 K at a rate of 2.5×10^8 K/s. From the energies of the annealed configurations, the structure at point (b) was found to be more stable than that at point (a) by 0.455 kcal/mol per atom. This is a huge energy difference. Figure 5.16 shows the radial distribution functions of structures at point (a), (b) and the starting structure (start) as illustrated in Fig. 5.15.

The presence of a double peak in the second shell of structure (start) shows that it is amorphous. Structures (a) and (b) are clearly crystalline. As noted earlier, the rate at which the structure is heated up determines whether it adequately samples the whole of the phase space and therefore finds global minimum or it is trapped in a local minima. At a faster heating rate of 2.5×10^9 K/s the two structures (a) and (b) in Fig. 5.15 were not seen. Structures (a) and (b) in Fig. 5.15 were first annealed to 300 K and then heated up at a rate of 2.5×10^8 K/s. During the heating process it was seen, from the potential energy versus time curves, that structure (a) found other more stable conformations but structure (b) did not. Therefore structure(b) should be very stable. Figure 5.17 shows the heating curve for structure (b).
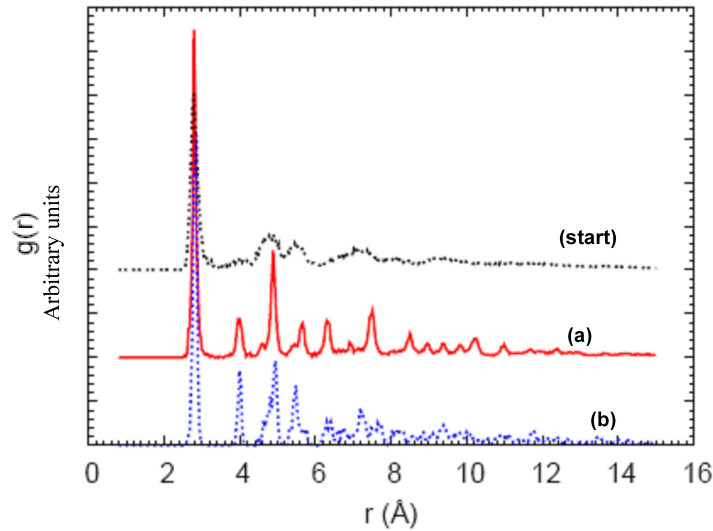
Fig. 5.16: Radial distribution functions of structures (a), (b) and starting structure(start).
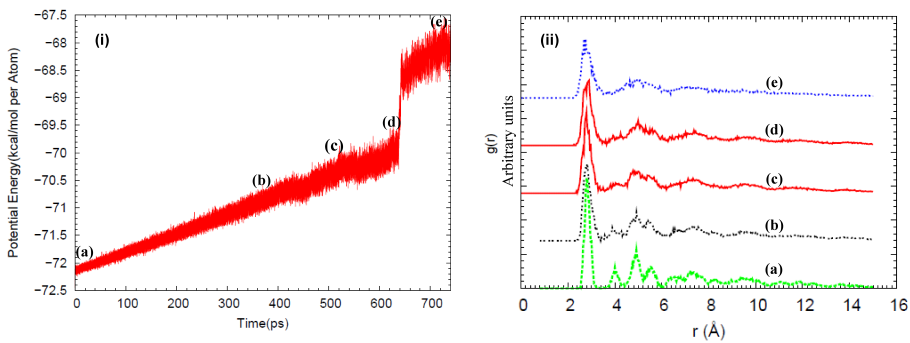
Fig. 5.17: (i) The heating curve, at a heating rate of 2.5 $\times 10^8$ K/s, for structure (b) in Figure 5.15(i). (ii) Radial distribution functions of structures (a), (b), (c), (d) and (e) formed during the heating process.

It is clear in Fig. 5.17(i) that there are no dips in potential energy arising as a consequence of the system finding other more stable conformations during the heating process. This indicates that indeed this structure might be the true minima. Figure 5.17(ii) shows the RDFs of various points in Fig. 5.17(i). While structure (b) shows some tendency towards amorphosization, structures (c) and

(d) exhibits liquid like characteristics. Melting in small clusters of this size can be understood as follows. At the onset of melting the system spends most of its time in the solid phase but it intermittently swings to the liquid phase. Gradually as the temperature increases the system oscillates between the solid and liquid states. Further rise in temperature leads to the system spending most of its time in the liquid phase although the solid phase is also present. What this tells us is that on melting a small system tries to avoid partially molten states by converting some of its kinetic energy into potential energy. As a result it keeps on oscillating between the solid and the liquid states as more and more energy is added to it. It is like the system is being driven towards liquid state by the addition of energy but it resists this force by converting some of its kinetic energy into potential energy thereby becoming colder and reverting back to the solid state.[65] Care must be taken though since we are dealing with a canonical ensemble. However, for small clusters there exist wide fluctuations of temperature due to the finite cluster size. The overall temperature might remain constant but there can be local drops in temperature within certain regions of the cluster in tandem with the lowering of the potential energy. Eventually at a critical temperature, T^{crit}, the system overcomes the transitional barrier to the pure liquid phase and spontaneously switches to the liquid state. This dynamic competition between the solid and liquid phases leads to a cluster size dependent semi-liquid region, which is schematically shown in Fig. 5.18. The smaller the
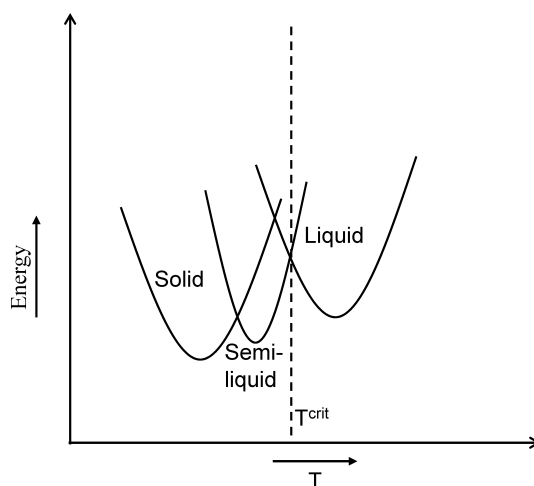
Fig. 5.18: Schematic representation of the structural evolution of a cluster with increase in temperature.

size of the cluster the larger the width of the semi-liquid region and vice-versa. A larger width implies that the system spends an appreciable amount of time in the liquid state before oscillating back to the solid state. In the bulk case the

semi-liquid phase does not exist.

One of the most fascinating issues when studying clusters is the threshold of bulk ordering as the size of the cluster increases. In order to understand the underlying nature of microscopic local atomic arrangement in structures (a) and (b) in Fig. 5.15(i) we performed a HA pair analysis on the two structures during the cooling process. The results are shown in Fig. 5.19. In the following, in all HA pairs analysis, quantities have been normalized such that the total number of pairs considered (1421, 1422, 1551 and 1431) is unity. Clearly, as can be seen
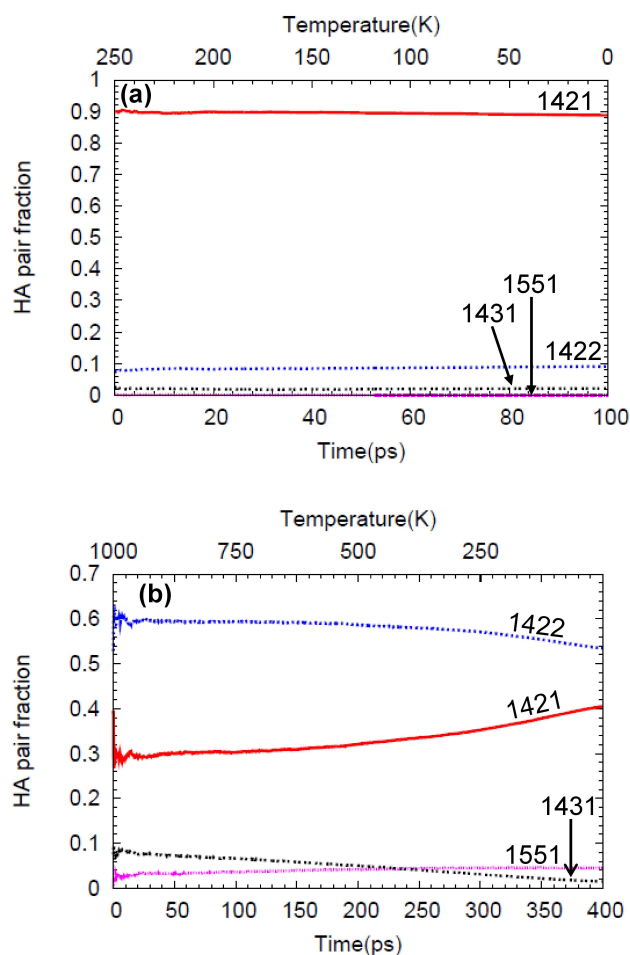
Fig. 5.19: The relative number of bonded pairs: 1421, 1422, 1551 and 1431 for the two conformations of Al_{256} clusters (a) and (b) as shown in figure 5.15(i).

in Fig. 5.19, in structure (a) the 1421 pairs, which are indicative of fcc ordering dominates. Contributions from 1422, 1431 and 1551 pairs are negligible. The 1421 and 1422 pairs remains fairly constant during the cooling process. This implies that the fcc ordering is an inherent structure and cooling the system merely freezes the atoms at their equilibrium positions. Structure (b), on the other hand, has appreciable contributions from both 1421 and 1422 pairs but the 1422 pairs are more dominant relative to the 1421 pairs. Therefore for a cluster of this size the most energetically favored geometry is the one with mixed hcp-fcc ordering.

Figure 5.20 shows the HA pair analysis for the Al_{1024} cluster whose annealed crystalline geometry is shown in Fig. 5.10(a). During the cooling process from
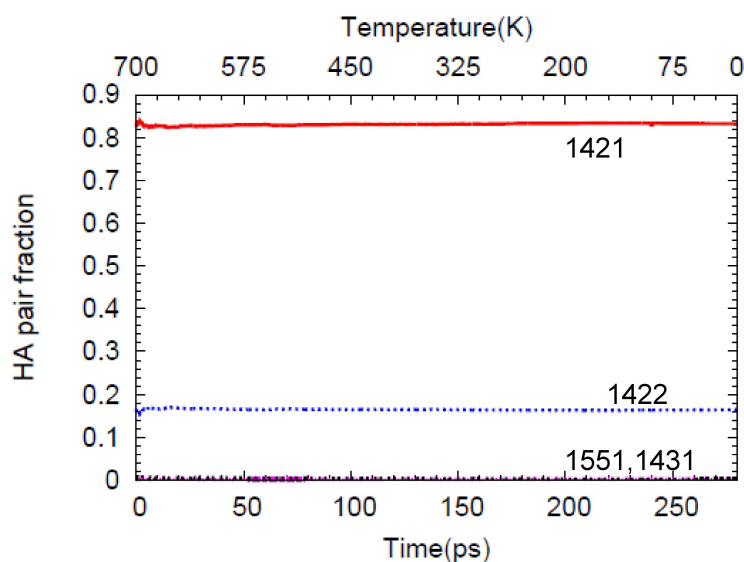
Fig. 5.20: Honeycutt-Andersen pairs for Al_{1024} during the cooling process from 700 K to 0 K.

700 K to 0 K the ratio of 1421 pairs to 1422 pairs remains quite high, $\approx$ 8:1. The 1551 and 1431 pairs are essentially 0 in this cluster throughout the cooling range. These high values of the 1421 pairs relative to the 1422 pairs throughout the whole of the cooling range shows that for a cluster of this size the dominant domains are fcc.

Figure 5.21 shows two different configurations of the Al_{3072} cluster. The amorphous configuration was the starting structure during the heating process. The crystalline configuration was a global minimum conformation located during

the heating process. This configuration was then slowly cooled to 0 K at a rate of 2.5×10^9 K/s. The RDF of the two structures is shown in Fig. 5.22 in which

Amorphous   Crystalline
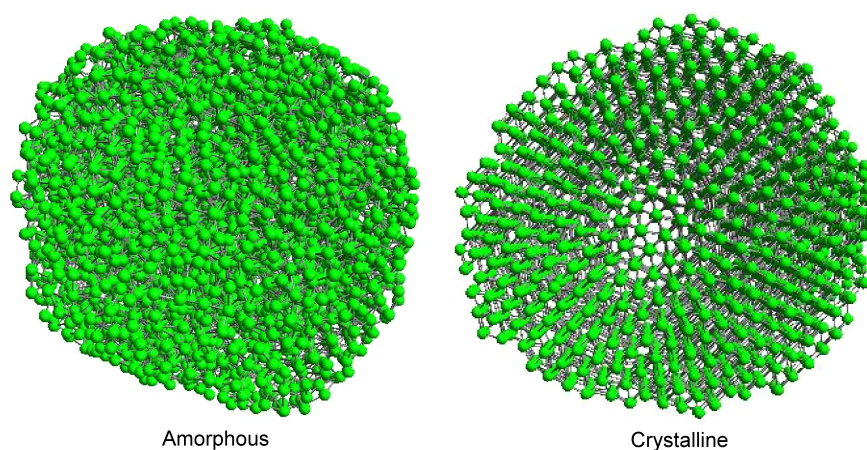
Fig. 5.21: Geometries of Al_{3072}. The amorphous configuration was the starting structure during the heating process. The crystalline configuration was a global minimum conformation located during the heating process.

a double peak on the second shell shows the amorphosization of the starting configuration. Although the end configuration is crystalline the periodicity is irregular. This suggests that the ordering is not purely fcc but perchance an admixture of fcc and hcp.

From the foregoing, a possible structural transformation scenario is icosahedral domains to hcp domains then to mixed HCP/FCC ordering and lastly to fcc domains for the clusters nearing bulk like properties. There is an obvious interplay between favorable energy and the geometry of the cluster. For clusters with N $\leq$ 55 icosahedral ordering is favored, for $256 \leq N < 1024$ mixed hcp-fcc ordering is favored while for N $\geq$ 1024 fcc ordering is favored. From the respective potential energies at 0 K the cohesive energies per atom for Al_{55}, Al_{108}, Al_{256}, Al_{512}, Al_{1024} and Al_{3072} clusters are as shown in Tab. 5.6. In Tab. 5.6 the cohesive energy for Al_{3072} cluster is -75.78 kcal/mol per atom, which is quite close to the bulk cohesive energy (76.8 kcal/mol per atom). This is why fcc ordering should dominate in this region.
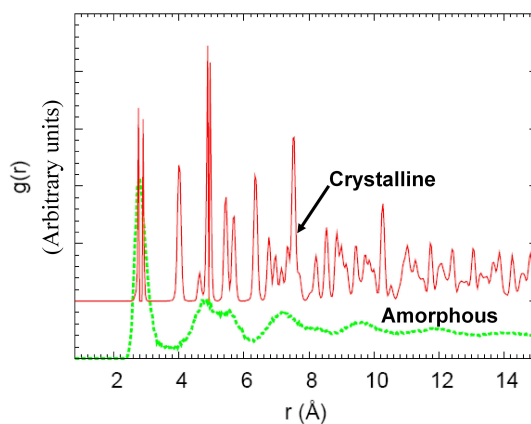
Fig. 5.22: Radial distribution function of the amorphous and crystalline states of Al_{3072} cluster.

Tab. 5.6: Cohesive energies (in kcal/mol per atom) for some aluminum clusters.

Cluster	E_{coh}
Al_{55}	-69.62
Al_{108}	-71.03
Al_{256}	-72.33
Al_{512}	-73.29
Al_{1024}	-73.85
Al_{3072}	-75.78

5.4 Conclusion

A parameterized force field has been trained for aluminum systems. A detailed study of the energetics and optimized structures for aluminum clusters in the range of 2-108 atoms has been presented. In DFT computation spin polarization was taken into account where it was seen that the lowest multiplicities were not necessarily the most stable. Apart from Al_4 and Al_5 in which DFT prefers planar orientation but ReaxFF favors three dimensional structures there is a general agreement between ReaxFF and DFT on the structures of aluminum clusters. The disparity between DFT and ReaxFF in these smaller clusters is due to quantum mechanical effect whereby orbital overlap plays an important part in determining the most stable structure. As the size of the clusters increases the geometrical effects plays a dominant role relative to electronic

shell contributions. Therefore for larger clusters there is a good agreement between DFT and ReaxFF predictions. The results for the energetics, structural configurations and magic numbers are in good agreement with both theoretical studies and experimental works. The bulk binding energy is computed to be 76.8 kcal/mol, which is consistent with the experimental value of 77.48 kcal/mol.[58] This gives confidence in the suitability of ReaxFF for studying and understanding the underlying dynamics in aluminum clusters.

In the quantification of the growth of cluster it is seen that as the size of the clusters increase there is preference for the coexistence of fcc/hcp orders at the expense of icosahedral ordering. It has been found that even for aluminum clusters with 512 atoms surface effects are dominant and distorted icosahedral orders exists. Although it is well known that it is not easy to get to the global minima of a structure by doing simulated annealing but an important aspect of this research was the realization that it is possible to capture the global minimum of a structure by heating up the system very slowly. A possible structural transformation scenario is icosahedral domains to hcp domains then to mixed hcp/fcc ordering and lastly to fcc domains for the clusters nearing bulk like properties. There is an obvious interplay between favorable energy and the geometry of the cluster. For clusters with $N \leq 55$ icosahedral ordering is favored, for $256 \leq N < 1024$ mixed hcp-fcc ordering is favored while for $N \geq 1024$ fcc ordering is favored.

References

[1] M. S. Daw and M. I. Baskes. *Phys. Rev. B*, 29:6443–6453, June 1984.

[2] F. H. Streitz and J. W. Mintmire. *Phys. Rev. B*, 50:11996–12003, October 1994.

[3] Q. Zhang, T. Çağın, A. C. T. van Duin, W. A. Goddard, Y. Qi, and L. G. Hector. *Phys. Rev. B*, 69(4):045423–+, 2004.

[4] A. C. T. van Duin, A. Strachan, S. Stewman, Q. Zhang, X. Xu, and W. Goddard III. *J. Phys. Chem. A*, 107:3803, 2003.

[5] G. Kresse and J. Furthmüller. *Phys. Rev. B*, 54:11169–11186, 1996.

[6] L. G. M. Pettersson, C. W. Bauschlicher, Jr., and T. Halicioglu. *J. Chem. Phys.*, 87:2205–2213, August 1987.

[7] T. H. Upton. *J. Chem. Phys.*, 86:7054–7064, June 1987.

[8] D. M. Cox, D. J. Trevor, R. L. Whetten, E. A. Rohlfing, and A. Kaldor. *J. Chem. Phys.*, 84:4651–4656, April 1986.

[9] W. A. de Heer, P. Milani, and A. Chtelain. *Phys. Rev. Lett.*, 63:2834–2836, December 1989.

[10] D. M. Cox, D. J. Trevor, R. L. Whetten, and A. Kaldor. *J. Phys. Chem.*, 92:421, 1988.

[11] J. Akola, M. Manninen, H. Häkkinen, U. Landman, X. Li, and L.-S. Wang. *Phys. Rev. B*, 62:13216–13228, November 2000.

[12] H.-P. Cheng, R. S. Berry, and R. L. Whetten. *Phys. Rev. B*, 43:10647–10653, May 1991.

[13] S. Debiaggi and A. Caro. *Phys. Rev. B*, 46:7322–7325, September 1992.

[14] S. H. Yang, D. A. Drabold, J. B. Adams, and A. Sachdev. *Phys. Rev. B*, 47: 1567–1576, January 1993.

[15] J. Akola, H. Häkkinen, and M. Manninen. *Phys. Rev. B*, 58:3601–3604, August 1998.

[16] J.-Y. Yi, D. J. Oh, and J. Bernholc. *Phys. Rev. Lett.*, 67:1594–1597, September 1991.

[17] R. E. Leuchtner, A. C. Harms, and A. W. Castleman, Jr. *J. Chem. Phys.*, 94:1093–1101, January 1991.

[18] F. Ercolessi, Parrinello M., and Tosatti E. *Philos. Mag. A*, 58:213, 1988.

[19] J. P. K. Doye. *J. Chem. Phys.*, 119:1136–1147, July 2003.

[20] K. Joshi, D. G. Kanhere, and S. A. Blundell. *Phys. Rev. B*, 67(23):235413–+, June 2003.

[21] Z.-Y. Lu, C.-Z. Wang, and K.-M. Ho. *Phys. Rev. B*, 61:2329–2334, January 2000.

[22] K. Joshi, D. G. Kanhere, and S. A. Blundell. *Phys. Rev. B*, 66(15):155329–+, October 2002.

[23] S. Chacko, K. Joshi, D. G. Kanhere, and S. A. Blundell. *Phys. Rev. Lett.*, 92(13):135506–+, April 2004.

[24] M. C. Payne, M. P. Teter, D. C. Allan, T. A. Arias, and J. D. Joannopoulos. *Rev. Mod. Phys.*, 64:1045–1097, October 1992.

[25] A. Strachan, A. C. van Duin, D. Chakraborty, S. Dasgupta, and W. A. Goddard. *Phys. Rev. Lett.*, 91(9):098301–+, 2003.

[26] A. C. T. van Duin, S. Dasgupta, F. Lorant, and W. Goddard III. *J. Phys. Chem. A*, 105:9396, 2001.

[27] J. G. O Ojwang, Rutger van Santen, Gert Jan Kramer, Adri C. T. van Duin, and William A. Goddard III. *J. Chem. Phys.*, 128:164714, May 2008.

[28] J. D. Honeycutt and H. C. Andersen. *J. Phys. Chem.*, 91:4950, August 1987.

[29] Sam Cheung, Wei-Qiao Deng, A. C. T. van Duin, and W. Goddard III. *J. Phys. Chem. A*, 109:851–859, 2005.

[30] J. Tersoff. *Phys. Rev. Lett.*, 61:2879, 1988.

[31] D. W. Brenner. *Phys. Rev. B*, 42:9458–9471, 1990.

[32] W. J. Mortier, S. K. Ghosh, and S. J. Shankar. *J. Am. Chem. Soc.*, 120: 2641, 1998.

[33] P. E. Blöchl. *Phys. Rev. B*, 50:17953–17979, 1994.

[34] J. P. Perdew, J. A. Chevary, S. H. Vosko, K. A. Jackson, M. R. Pederson, D. J. Singh, and C. Fiolhais. *Phys. Rev. B*, 46:6671–6687, 1992.

[35] J. P. Perdew, K. Burke, and Y. Wang. *Phys. Rev. B*, 54:16533–16539, 1996.

[36] J. P. Perdew, K. Burke, and M. Ernzerhof. *Phys. Rev. Lett.*, 77:3865–3868, 1996.

[37] H. J. Monkhorst and J. D. Pack. *Phys. Rev. B*, 13:5188–5192, June 1976.

[38] F. Birch. *Phys. Rev.*, 71:809–824, 1947.

[39] L. Verlet. *Phys. Rev.*, 159:98, 1967.

[40] F. A. Lindemann. *Z. Phys.*, 11:609, 1910.

[41] J. Jellinek and A. Goldberg. *J. Chem. Phys.*, 113:2570–2582, August 2000.

[42] W. K. Luo, H. W. Sheng, F. M. Alamgir, J. M. Bai, J. H. He, and E. Ma. *Phys. Rev. Lett.*, 92(14):145502–+, April 2004.

[43] D. R. Nelson. *Phys. Rev. Lett.*, 50:982–985, March 1983.

[44] Edited by D. R. Lide and E. Wiberg. *Handbook of Chemistry and Physics, 82nd ed.* CRC Press, New York, 2001.

[45] J. Koutecky, G. Pacchioni, G. H. Jeung, and E. C. Hass. *Surf. Sci.*, 156: 650–669, June 1985.

[46] K. Jug, H. Schluff, H. Kupka, and R. Iffert. *J. Comp. Chem.*, 9:803–809, 1988.

[47] C. W. Bauschlicher, Jr. and L. G. M. Pettersson. *J. Chem. Phys.*, 84:2226–2232, February 1986.

[48] R. O. Jones. *J. Chem. Phys.*, 99:1194–1206, July 1993.

[49] M. Böyükata and Z. B. Güvenç. *Braz. J. Phys.*, 36:720–724, September 2006.

[50] R. O. Jones. *Phys. Rev. Lett.*, 67:224–227, July 1991.

[51] J.-O. Joswig and M. Springborg. *Phys. Rev. B*, 68(8):085408–+, August 2003.

[52] L. Lloyd and R. Johnston. *Chem. Phys.*, 236:107–121, September 1998.

[53] Reinhart Ahlrichs and D. Simon Eliiot. *Phys. Chem. Chem. Phys.*, 1:13–21, 1999.

[54] W. Zhang, F. Zhang, and Z. Zhu. *Phys. Rev. B*, 74(3):033412–+, July 2006.

[55] H. J. C. Berendsen, J. P. M. Postma, W. F. van Gunsteren, A. Dinola, and J. R. Haak. *J. Chem. Phys.*, 81:3684–3690, 1984.

[56] I. A. Harris, R. S. Kidwell, and J. A. Northby. *Phys. Rev. Lett.*, 53(25): 2390–2393, Dec 1984.

[57] A. P. Sutton and J. Chen. *Philos. Mag. Lett.*, 61:139, 1990.

[58] M. F. Jarrod. *in clusters of Atoms and Molecules*, page 293. Ed. H. Haberland, Springer, Berlin, Heidelberg, 1992.

[59] S. Alavi and D. L. Thompson. *J. Phys. Chem. A*, 110:1518, 2006.

[60] J. F. Lutsko, D. Wolf, S. R. Phillpot, and S. Yip. *Phys. Rev. B*, 40:2841–2855, August 1989.

[61] P. Puri and V. Yang. *J. Phys. Chem. C*, 111:11776, 2007.

[62] F. Ercolessi and J. B. Adams. *Europhys. Lett.*, 26:583–588, June 1994.

[63] G. A. Breaux, C. M. Neal, B. Cao, and M. F. Jarrold. *Phys. Rev. Lett.*, 94 (17):173401–+, May 2005.

[64] C. M. Neal, A. K. Starace, and M. F. Jarrold. *Phys. Rev. B*, 76(5):054113–+, August 2007.

[65] H. Haberland. Melting of clusters. In C. Guet, P. Hobza, F. Spiegelman, and F. David, editors, *Atomic clusters and nanoparticles: Les Houches Session LXXIII 2-28 July 2000 (Les Houches - Ecole d'Ete de Physique Theorique)*, pages 31–55. Springer-Verlag, Berlin, Heidelberg, New York, 2001.

Parametrization and applications of a reactive force field for AlH$_3$

Abstract

A reactive force field, ReaxFF, for aluminum hydride has been developed based on density functional theory (DFT) derived data. ReaxFF$_{AlH_3}$ is used to study the dynamics governing hydrogen desorption in AlH$_3$. It has been postulated that essential to the thermal decomposition of NaAlH$_4$ is the formation of mobile alane species (AlH$_3$ molecules) that facilitates the mass transport of aluminum atoms. Using a reactive force field, which incorporates dynamic charge transfer between atoms, the behavior of alanes in the gas phase and on Al(111) surface has been studied. It was observed that in the gas phase there is a thermodynamically driven agglomeration of alane clusters into a large alanes complex. Molecular hydrogen was then desorbed from the complex. On Al(111) surface alanes oligomerize to form compound alanes. We also unambiguously identified a molecular hydrogen trapped in the AlH$_3$ matrix.

6.1   Introduction

One of the major challenges in the quest for hydrogen storage solutions is the development of solid-state hydrogen storage media for vehicles. The United States' Department of Energy (DoE) has set a minimum target of 6 wt.% H$_2$ for economically practical storage of hydrogen in a solid state material by the year 2010. AlH$_3$, which has about 10.1 wt.% of H$_2$ and a volumetric density of 0.148 kg H$_2$/l is quite attractive as a potential candidate for onboard hydrogen storage applications in proton exchange membrane (PEM) fuel cells. AlH$_3$ is a covalently bonded metastable binary hydride, with polymeric (AlH$_3$)$_n$ forms. There are at least 7 ($\alpha, \alpha', \beta, \gamma, \delta, \varepsilon$ and ζ) known non-solvated phases of AlH$_3$.[1,2] Experimentally, under ambient conditions, the most stable phase of AlH$_3$ is α-AlH$_3$, which has a trigonal/rhombohedral crystal structure (space group $R\bar{3}c$) with lattice parameters a = 4.449 Å and c = 11.804 Å.[3] The basic building unit of all the AlH$_3$ polymorphs is the AlH$_6$ octahedra and the α-AlH$_3$ polymorphic modification is the most densely packed. In 2005, Ke et al.,[4] using density functional theory (DFT) identified two structures of AlH$_3$ (cubic $Fd\bar{3}m$ and orthorhombic $Cmcm$), which were theoretically calculated to be more stable than α-AlH$_3$. In 2006, the Institute for Energy Technology (IFE) experimentally solved the structure of, orthorhombic, α'-AlH$_3$. In the same year, a joint collaboration of University of Hawaii (UH), IFE and Brookhaven National Laboratory (BNL) synthesized and solved the structures of cubic $Fd\bar{3}m$ (β-AlH$_3$) and tetragonal $Pnnm$ (γ-AlH$_3$) using organo-metallic methods.[5] All the three structures were found to be less stable than α-AlH$_3$ at temperatures over 300 K.

The metastable AlH$_3$ does not release hydrogen under normal conditions. Although all the known AlH$_3$ phases are thermodynamically unstable with an equilibrium decomposition pressure in the range of kbars at room temperature, they are usually metastable and hardly decompose rapidly at room temperature. The cause of this metastability is the encapsulation of the hydrogen in AlH$_3$ by a layer of Al$_2$O$_3$ that surrounds the surface of the AlH$_3$ particles. At atmospheric pressure and in the temperature range 330 K - 400 K, subject to its preparation history, the decomposition of AlH$_3$ occurs in a single step as follows:

$$\text{AlH}_3 \rightarrow \text{Al} + \frac{3}{2}\text{H}_2 \tag{6.1}$$

Thermodynamically, this reaction is not easily reversible. To rehydride Al back to AlH$_3$ hydrogen gas pressures of over 2.5 GPa are needed.[6,7] AlH$_3$ has a low decomposition enthalpy of about 1.82 kcal/mol H$_2$,[8] which is 20% that of NaAlH$_4$.[9] The decomposition rate of AlH$_3$ can be tuned through nanostructuring (particle size reduction).[5] However, the decomposition reaction

of AlH_3 is not reversible and therefore the desorbed hydrogen must be regenerated offboard. There are various ongoing research efforts to improve the sorption kinetics of AlH_3. Sandrock et al.[10,11] have shown that doping of AlH_3 with small amounts of alkali metal hydrides (LiH, NaH and KH) leads to accelerated H_2 desorption rates at low temperatures.

In this work we have parameterized a reactive force field ($ReaxFF_{AlH_3}$) for AlH_3, with the objective of describing the H_2 desorption process in AlH_3. ReaxFF has already been shown to be able to accurately predict the dynamical and reactive processes in hydrocarbons,[12] silicon/silicon oxides,[13] aluminum/aluminum oxides,[14,15] nitramines,[16] sodium hydride,[17] and magnesium hydride.[18] Herein, the details of the parameterizations of $ReaxFF_{AlH_3}$, the diffusion mechanism of hydrogen atoms and hydrogen molecules in AlH_3, the abstraction process of surface molecular H_2 in AlH_3 cluster, the possibility of phase transition between different polymorphic modifications during the heating process and the role of alane clusters in the transportation of Al atoms are examined. In addition, interestingly, this paper shows that small alane molecules have to first of all agglomerate before desorption of molecular hydrogen can occur. This is very important in understanding the mass transport of aluminum atoms during the thermal decomposition of $NaAlH_4$.[19–21]

This paper is organized as follows: Section 6.2 deals with force field parameterizations and the tests taken to ensure that the force field is well parameterized, section 6.3 deals with the dynamics of hydrogen desoprtion in aluminum hydride clusters and the behavior of alanes on Al(111) surface, section 6.4 focusses on the abstraction process of molecular hydrogen from a cluster of AlH_3, section 6.5 is devoted to the issue of trapped molecular hydrogen in the channels of a cluster of AlH_3. We conclude in section 6.6.

6.2 Force Field Parameterizations

$ReaxFF_{AlH_3}$ has been parameterized in the same way as $ReaxFF_{NaH}$[17] and $ReaxFF_{MgH}$.[18] The force field does not use fixed connectivity assignment between atoms but rather the bond-order formalism, which allows for bonds to be created and broken up in line with the works of Tersoff[22] and Brenner.[23] ReaxFF calculates non-bonded (van der Waals and Coulomb) interactions between all atoms (including 1-2, 1-3 and 1-4 interactions) making it suitable for systems which have polar-covalent interactions. Implemented in ReaxFF are polarizable charges that are calculated using electronegativity equalization method (EEM)[24] and which provides a geometry dependent charge distribution.

The fitting data used in ReaxFF were obtained from DFT using using the efficient and accurate total-energy package, VASP (Vienna ab initio simulation

package).[25] VASP implements a projector augmented[26] plane-waves approach. In determining the relaxed geometries of the structures considered in this work a plane waves cut-off of 600 eV (1 eV = 23.06 kcal/mol) was used. A convergence of 10^{-6} eV/atom was placed as a criterion on the self-consistent convergence of the total energy. The ions involved are steadily relaxed towards equilibrium until the Hellman-Feynman forces are minimized to less than 0.02 eV/Å using conjugate gradient algorithm during all relaxation runs. A further local optimization was done on the already relaxed structure using quasi-Newton algorithm until the Hellman-Feynman forces on the ions were less than 0.005 eV/Å. To represent electronic-correlation effects for a particular ionic configuration, the calculations used the generalized gradient approximation of Perdew and Wang[27–29] (GGA-PW91). For cluster calculations, a cubic supercell of side 20 Å was used and the Brillouin zone was sampled at the Γ point. For all the AlH$_3$ condensed phases, Brillouin zone integrations were performed using $4 \times 4 \times 4$ k-points as per the Monkhorst-Pack grid scheme.[30] The reference configurations for valence electrons used were Al($3s^2 3p^1$) and H($1s^1$).

To parameterize ReaxFF energy expressions, a fitting was done to a training set containing the DFT derived equations of state (EoS) of pure Al and AlH$_3$ condensed phases, reaction energies and bond dissociation profiles on small finite clusters. The bond and atom parameters for ReaxFF energy functions (Tabs. 6.1 and 6.2) were determined from Al-Al and Al-H bonds in small AlH$_3$ clusters such as AlH$_3$, Al$_2$H$_6$, Al$_3$H$_9$, Al$_4$H$_{12}$, Al$_5$H$_{15}$, Al$_6$H$_{18}$, Al$_7$H$_{21}$ and Al$_8$H$_{24}$ and from the equations of state and cohesive energies of Al-metal and AlH$_3$ condensed phases. The symbols of the parameters in Tab. 6.1, 6.2, 6.3 and 6.4 are shown in Refs.[13,16]

Tab. 6.1: Bond Energy and Bond Order Parameters. D$_e^\sigma$ is in kcal/mol.

Bond	D$_e^\sigma$	$P_{be,1}$	$P_{be,2}$	$P_{b0,1}$	$P_{b0,2}$
Al-H	93.4	-0.6599	8.7138	-0.08	6.978

Tab. 6.2: Atom Parameters ($p_{ov/un}$ is in kcal/mol)

Atom	$p_{ov/un}$	λ_{11}	p$_{v,5}$	p$_{v,6}$
Al	-23.18	2.53	8.0	2.5791
H	-15.76	2.15	1.0	2.8793

Table 6.3 shows the EEM parameters (EEM-hardness η, EEM-electronegativity χ and EEM-shielding parameter γ). These parameters were optimized to fit Mulliken charge distributions of small representative structures (AlH$_3$, Al$_2$H$_6$, Al$_3$H$_9$ and Al$_4$H$_{12}$) obtained from DFT calculations. ReaxFF successfully

reproduces charge transfer for all the clusters considered. The partial charges fitted into the training set were obtained by performing a Mulliken charge distribution analysis in an all electron calculation in CRYSTAL06.[31,32] CRYSTAL06 implements a localized basis set (LCAO) approach. The radical factors in the all electron basis set are expressed as a linear combination of Gaussian Type Functions (GTF) of the electron-nucleus distance according to 85(s)11(sp)G and 5(s)11(sp)1(p)G contractions for Al and H respectively.[32] To ensure high numerical accuracy the truncation tolerance for the numerical evaluation of bielectronic integrals (both the coulomb and the HF exchange series) were set at 10^{-8}, 10^{-8}, 10^{-8}, 10^{-8} and 10^{-16}.[32] All the units are in a.u. (1 a.u. = 627.51 kcal/mol).

Tab. 6.3: Coulomb Parameters

Atom	η(kcal/mol)	χ(kcal/mol)	γ(Å)
Al	4.9	1.8921	0.6191
H	6.5	4.1882	0.7358

Table 6.4 shows the optimized valence angle parameters for H-Al-Al and H-Al-H angles. To obtain these quantities, the clusters are first fully optimized in DFT calculations. This is followed by doing single point calculations in which the valence angles are modified while other parameters are fixed.

Tab. 6.4: Valence Angle Parameters

Angle	$\Theta\Theta_{0,0}$	k_a	k_b	$p_{v,1}$	$p_{v,2}$	p_{pen}	$p_{v,4}$
H-Al-Al	66.95	39.1233	0.1935	0	1.0	0	3.00
H-Al-Al	180.00	-26.6261	5.3467	0	1.0	0	0.80
H-Al-H	70.85	3.4517	8.8153	0	2.9	0	1.75
Al-H-Al	0.00[a]	36.0088	0.0603	0	2.3	0	1.75

[a] The value leads to an equilibrium angle of 180-0 = 180° for the single bond Al-H-Al valence angle.

The first line reflects a normal H-Al-Al angle interaction, with an equilibrium angle of 113.05° and force constants of 39.1233 kcal and 0.1935 kcal. The valence angle with a negative force constant (H-Al-Al), -26.6261 kcal, aims to destabilize the case where the hydrogen atom is exactly in between the Al-atoms (i.e. H-Al-Al angle is zero degrees). This is effectively an inverted angle function, with a maximum at H-Al-Al equals zero degrees and falling off to zero for different values of this angle.

6.2.1   Bond Dissociation, Angle bending and Binding Energies

Figure 6.1(a) shows the bond dissociation curve of AlH$_3$ while Fig. 6.1(b) shows the angle bending-energy curve of the AlH$_3$ molecule used to optimize the valence angle parameter of ReaxFF$_{AlH_3}$. These DFT curves were used to optimize the bond energy in the reactive potential. The dissociation curves were constructed from the equilibrium geometry through single point calculations by changing the bond length. ReaxFF gives an equilibrium bond length of 1.6 Å, which is in excellent agreement with DFT value of 1.59 Å. The energies were computed with reference to the equilibrium bond length's energy. To optimize
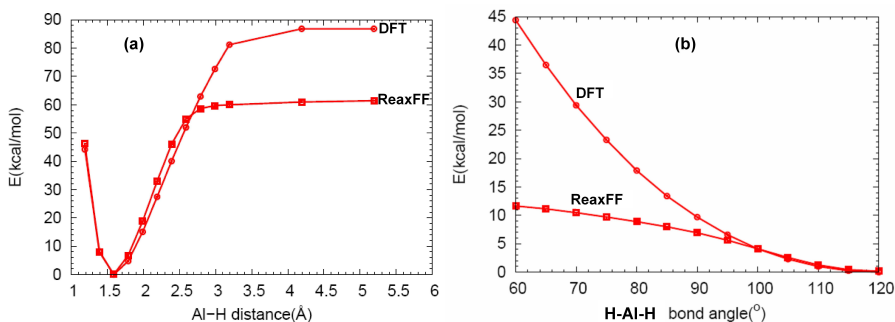
Fig. 6.1: (a) Bond dissociation profile of AlH$_3$. ReaxFF gives an equilibrium bond length of 1.6 Å. This is in excellent agreement with DFT value of 1.59 Å. (b) H-Al-H angle bend in AlH$_3$ molecule. The energies are computed with reference to the equilibrium angle energy.

the valence angle parameter the geometry of the AlH$_3$ molecule was minimized for various fixed values, viz 120°, 115°, 110°,...., 65°, 60°. ReaxFF predicts that the H-Al-H equilibrium angle is 120°. This is in excellent agreement with DFT. For smaller angles, DFT gives larger energy barriers than ReaxFF due to electron-electron repulsion inherent in the former. For instance, at 60° the AlH$_3$ is destabilized by 44.4 kcal/mol in DFT whereas ReaxFF, which does not care about electrons, gives a destabilization energy of 11.66 kcal/mol.

Table 6.5 shows the DFT values versus ReaxFF values of adsorption energies of hydrogen on Al(111) surface. The adsorption energy, E$_{ads}$, is defined as $E_{ads} = [E_{(S/H)} - E_S - nE_{(H)}]/n$, where E$_{(S/H)}$ is the total energy of hydrogen-adsorbed aluminum slab, E$_S$ is the total energy of aluminum slab, E$_H$ is the total energy of hydrogen atom (-25.79 kcal/mol) and n stands for the number of adsorbed hydrogen atoms. To calculate E$_H$, two hydrogen atoms were placed 12 Å apart in a cubic box of side 20 Å. The Brillouin zone was sampled at the gamma point. The total energy of the hydrogen atom was then taken as half the

calculated total energy. In the context of this definition, $E_{ads} < 0$ corresponds to exothermic adsorption. The Al surface was modeled by a repeated slab of five layers, giving a slab thickness of 9.6 Å. A vacuum equivalent to a slab with 5 layers of aluminum atoms was imposed in the z-direction to separate the slab from its periodic images. H is adsorbed on one side of the slab only. The top two layers plus the H atom are relaxed while the bottom three layers are fixed at their bulk positions. The Brillouin zone was sampled using a well converged $9 \times 9 \times 1$ k-points.

ReaxFF gives decent adsorption energies in comparison to DFT predictions (Tab. 6.5). From DFT calculations, atomic hydrogen preferably adsorbs on the fcc site. This is consistent with the work of Stumpf,[33] who showed that H preferably adsorbs on the fcc site with an exothermic adsorption energy of -45.58 to -45.89 kcal/mol (depending on the coverage). This value can be slightly higher or lower depending on the exchange-correlation functional (LDA, PBE or PW91) used. In agreement with Stumpf, we calculated the fcc adsorption energy to be -47.63 kcal/mol. From ReaxFF, the adsorption energies for bridge, hcp and top sites are -47.37 kcal/mol, -44.80 kcal/mol and -45.87 kcal/mol, respectively.

Tab. 6.5: Adsorption energies of hydrogen atoms on the high symmetry sites on Al(111) surface. The energies are in kcal/mol per H.

Site	DFT	ReaxFF
hcp	-44.80	-47.80
fcc	-47.63	-49.24
top	-45.87	-47.14
bridge	-47.37	-48.93

For Al(111) hcp site DFT gives a value of -44.8 kcal/mol per H while ReaxFF gives -47.8 kcal/mol. For Al(111) fcc site DFT predicts the adsorption energy to be -47.63 kcal/mol while ReaxFF gives -49.24 kcal/mol. For the Al(111) top site ReaxFF predicts the adsorption energy to be -47.14 kcal/mol, which is in good agreement with DFT value of -45.87 kcal/mol. The DFT calculated energy barrier for H hopping from the bridge to the fcc site is 2.07 kcal/mol. ReaxFF gives a migration energy barrier of 2.7 kcal/mol, which is in excellent agreement with DFT value. These values are in good agreement with those of Hjelmberg who determined the diffusion energy barrier of H from the bridge to 3-fold site to be in the range of 2.3 - 4.6 kcal/mol.[34]

That said, there is an increasing interest in studying small clusters of aluminum hydride since nanostructuring might be the key to hydrogen storage in AlH$_3$ system. During the thermal decomposition process of large systems of aluminum

hydride it is possible that the release of hydrogen and subsequent formation of aluminum clusters occurs in tandem with cluster fragmentation.[17] Herein, we make a comparison between DFT's binding energies and ReaxFF binding energies for AlH$_3$, Al$_2$H$_6$, Al$_3$H$_9$, Al$_4$H$_{12}$ and Al$_5$H$_{15}$ clusters. These small clusters are shown in Fig. 6.2.
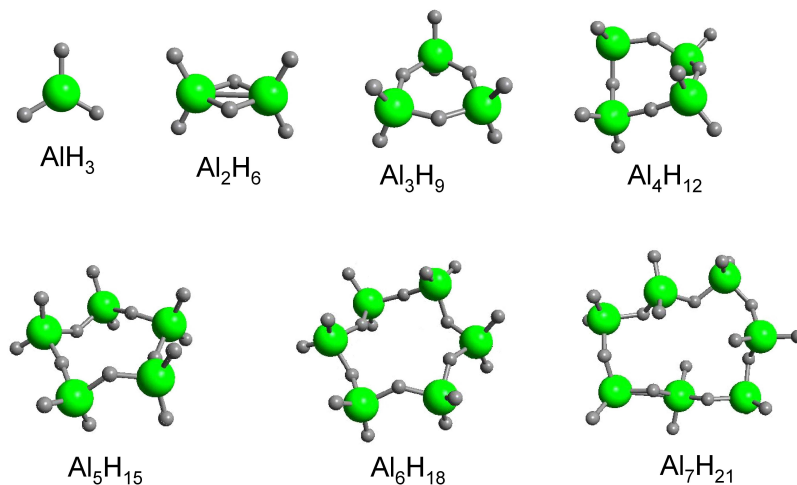
Fig. 6.2: Small representative [AlH$_3$]$_n$, n = 1-7, clusters used in the training set of ReaxFF.

Kawamura et al.[35] have given an extensive study on small AlH$_3$ clusters and have shown that the energetics are very close for singly bridged cyclic, doubly bridged cyclic and linear clusters. In general, the singly bridged structures are more favored over the doubly bridged structures. However, Kawamura et al. also found out that in some instances, due to exchange-correlation effects, the doubly bridged structures are preferred to singly bridged structures. In ReaxFF computations, it was seen that for Al$_n$H$_{3n}$ (n $\geq$ 4) the doubly bridged structures are preferred while the singly bridged structures are unstable. This can be understood from the fact that the more the inter-connectivity of the Al-H bonds the stronger the bonding. Doubly bridged structures have more bonds and therefore bound to be more stable than singly bridged structures. Table 6.6 shows the binding energies of various (AlH$_3$)$_n$ clusters considered in this work. Here, the binding energy is defined as:

$$\mathrm{BE} = -[\mathrm{E(Al_nH_{2m})} - \mathrm{E(Al_{fcc})} - \mathrm{mE(H_2)}]/\mathrm{m} \tag{6.2}$$

where E(P) is the total energy of particle P in the ground state. For molecular hydrogen, in DFT, E$_{tot}$ = -156.87 kcal/mol. The total energy of molecular hydrogen was used because in ReaxFF the total energy is computed with

reference to the isolated atomic species. It can be seen in the table that

Tab. 6.6: Binding energies, BE, (in kcal/mol H_2) of small AlH_3 clusters used in the training set.

Cluster	DFT	ReaxFF
AlH_3	30.77	32.51
Al_2H_6	22.60	28.66
Al_3H_9	29.72	30.13
Al_4H_{12}	39.33	34.50
Al_5H_{15}	42.88	38.80

there is a slow decrease in binding energy per hydrogen of these clusters with increasing cluster size. This is contrary to the expectation that the binding energy per hydrogen should increase concomitantly with increase in cluster size. The decrease in the binding energy can be attributed to the fact that as the cluster size increases so does the free energy of pure aluminum clusters, which raises the cost of fragmenting the aluminum clusters to accommodate hydrogen atoms. The DFT values are consistent with the works of Kawamura et al. However, Kawamura et al. used the total energy of atomic hydrogen instead of that of molecular hydrogen. Therefore, in Tab. 6.7 we make a comparison between DFT values and Kawamura et al.'s[35] work using the total energy of atomic hydrogen, E_{tot} = -25.79 kcal/mol. There is an excellent match between

Tab. 6.7: Comparison between DFT and Kawamura et al.'s binding energies, BE, (in kcal/mol H) of small AlH_3 clusters.

Cluster	DFT	Ref.[35]
AlH_3	68.79	67.50
Al_2H_6	70.01	70.29
Al_3H_9	64.98	65.19
Al_4H_{12}	63.53	62.70
Al_5H_{15}	61.52	60.65
Al_6H_{18}	60.21	59.22
Al_7H_{21}	58.60	57.63
Al_8H_{24}	58.50	58.60

our calculated DFT values and those from Kawamura et al.'s work, which was done at the LCAO+GGA level of theory.

In the condensed state, for each an every phase of AlH_3 (α, α', β and γ) polymorphic modifications considered in this work, the DFT energies

were computed for a broad range of volume describing both expansion and compression. Figure 6.3 shows the crystal structure of the four polymorphs of AlH$_3$ ($\alpha, \alpha', \beta, \gamma$) considered in this work. All the AlH$_3$ polymorphs are made
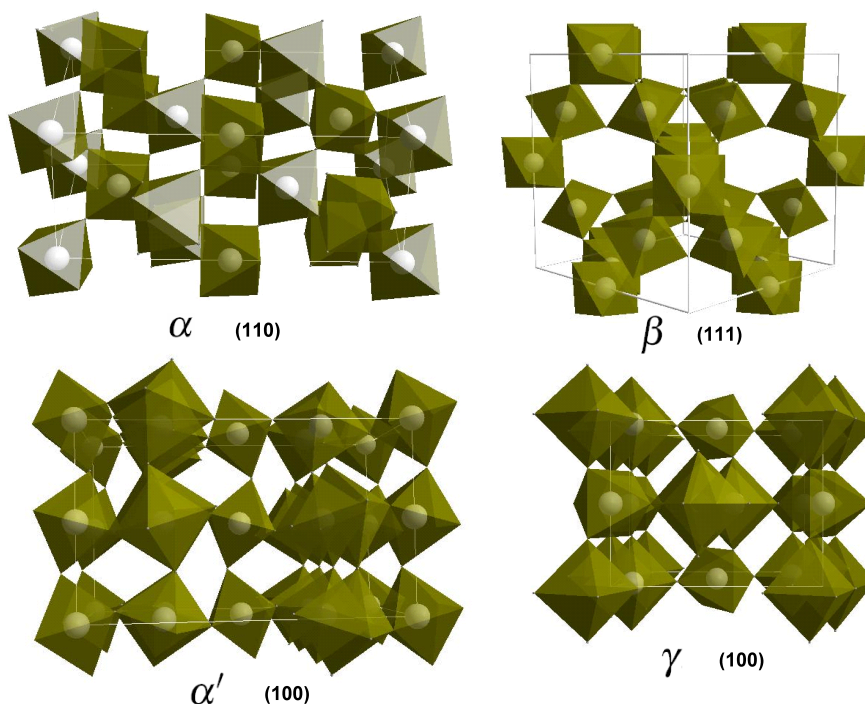
Fig. 6.3: The various polymorphic modifications of AlH$_3$ illustrated by the connection of the AlH$_6$ octahedra and channels through the polymorphs.

up of three dimensional networks of AlH$_6$ units. α-AlH$_3$ crystallizes in the trigonal $R\bar{3}c$ space group, β-AlH$_3$ crystallizes in the cubic $Fd\bar{3}m$ space group, α'-AlH$_3$ crystallizes in the $Cmcm$ space group and γ-AlH$_3$ crystallizes in the orthorhombic $Pnnm$ space group.

The crystal structure of α-AlH$_3$ is made up of a three dimensional network of corner sharing tilted AlH$_6$ octahedra. In α-AlH$_3$ the Al-H bond length is 1.72 Å and the Al-H-Al angle is 142.39°. The shortest H-H distance is 2.44 Å, which is found within the octahedra. The Al-Al bond length is 3.26 Å. β-AlH$_3$ has large empty channels in between the AlH$_6$ octahedra units as illustrated in Fig. 6.4. In the case of β-AlH$_3$ the octahedra are close to regular with H-Al-H angles varying between 87.62° and 92.52°. The Al-H-Al angle is 137.2° while the Al-H bond length is 1.72 Å. The shortest H-H distance is 2.38 Å, which is also
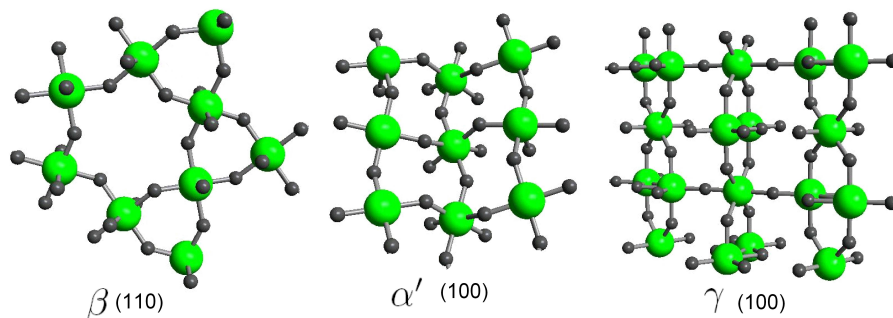
Fig. 6.4: The AlH$_6$ octahedra in three of the four polymorphic modifications of AlH$_3$.

found within the octahedra. The Al-Al bond length is 3.21 Å. In α'-AlH$_3$ the Al-H bond length is 1.72 Å and the Al-H-Al angle is 139.47°. The shortest H-H distance is 2.43 Å, which is found within the octahedra. The Al-Al bond length is 3.23 Å. γ-AlH$_3$, which is built up of AlH$_6$ octahedra similar to the other three AlH$_3$ phases, has doubly bridged Al-2H-Al bonds with edge sharing AlH$_6$ octahedra units. However, this is where the similarity ends as can be seen in Fig. 6.4. γ-AlH$_3$ is built up of AlH$_6$ octahedra, similar to the other three AlH$_3$ phases. γ-AlH$_3$ has double bridged Al-2H-Al bonds with edge sharing AlH$_6$ octahedra units as illustrated in Fig. 6.5. There are two different H bridges in
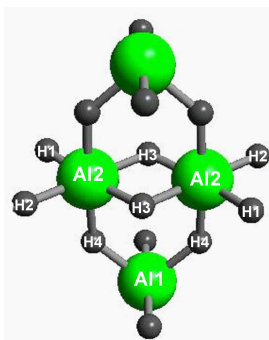
Fig. 6.5: The interconnections of the two types of octahedra in γ-AlH$_3$.

γ-AlH$_3$ in which two kinds of AlH$_6$ share edges and vertices. The Al-H bond lengths within the two octahedra are not the same, see Tab. 6.8.

The issue of the relative stability of AlH$_3$ polymorphic modifications is quite interesting. Experimentally, α-AlH$_3$ is the most stable polymorph for

Tab. 6.8: Calculated interatomic distances(Å) and bond angles(°) for γ-AlH$_3$

Atoms	Distances	Atoms	Angles
Al2-H1	1.689	Al1-H4-Al2	134.77
Al2-H2	1.707	Al2-H3-Al2	97.60
Al2-H3	1.731	H3-Al2-H4	88.39
Al2-H4	1.728	H2-Al2-H3	179.21
Al2-Al2	2.632		

temperatures greater than or equal to 300 K.[3] Theoretically, Ke et al.,[4] using DFT, found β-AlH$_3$ polymorphic modification of AlH$_3$ to be the structure with the lowest energy. It is possible that at 0 K the β-phase is indeed more stable than the α-phase as found by Ke et al., especially with the zero point energy (ZPE) contribution taken into account. On the other hand, the relative energy differences between these two phase is in the order of 1 kcal/mol. It might be difficult for DFT to resolve this small energy difference. We found that indeed the cubic β-AlH$_3$ has the lowest energy. However, this result seems to be an artefact of the pseudopotential used. For the PAW pseudopotentials the β-AlH$_3$ phase has the lowest energy whereas for ultrasoft (US) pseudopotential α'-AlH$_3$ phase has the lowest energy, see Tab. 6.9. In both cases, however, the relative energy differences between α, α' and β phases is less than 1 kcal/mol. This implies that it should be possible for these phases to transform into one another at certain temperatures and pressures. In particular, since the β phase has more open channels, it can transform to the α phase during the desorption of molecular hydrogen but only if the α phase is more stable. We did not include the ZPE corrections. In the work of Ke et al., ZPE corrections were included.

Figure 6.6 shows the EoS for the $R\bar{3}c$ (α-AlH$_3$), $Fd\bar{3}m$ (β-AlH$_3$), $Pnnm$ (γ-AlH$_3$) and $Cmcm$ (α'-AlH$_3$) phases of AlH$_3$. ReaxFF correctly describes the EoS of the four phases of AlH$_3$ and excellently estimates their relative phase stability vis-á-vis the DFT's predictions. For instance, DFT (PAW) predicts that β-AlH$_3$ is more stable than γ-AlH$_3$ by 0.76 kcal/mol H$_2$ whereas ReaxFF gives a value of 0.02 kcal/mol H$_2$. The experimental heat of formation, for the condensed phase, of AlH$_3$ range from -2.37 $\pm$ 0.1 kcal/mol H$_2$[2] to -2.72 $\pm$ 0.2 kcal/mol H$_2$[8] while the calculated values are in the range of -1.66 kcal/mol H$_2$[36] to -2.95 kcal/mol H$_2$.[4] For α-AlH$_3$ phase, both DFT and ReaxFF give bulk values that are consistent with the calculated values, with DFT giving a value of -2.36 kcal/mol H$_2$ and ReaxFF giving -3.01 kcal/mol H$_2$. These values were calculated by comparing to Al(fcc) at its most stable volume and 1.5 H$_2$ (gas).
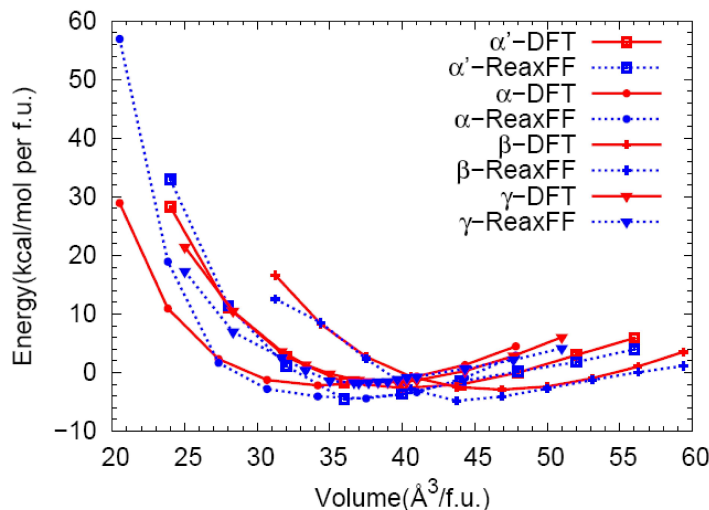
Fig. 6.6: Equations of state for AlH$_3$ phases (DFT values are drawn using straight lines while those for ReaxFF are drawn using dotted lines).

Tab. 6.9: Relative stability of three AlH$_3$ phases with respect to the $R\bar{3}c$ phase using the PAW and ultrasoft pseudopotentials (US-PP) and ReaxFF. The units are in kcal/mol.

Phase	PAW	US-PP	ReaxFF
$R\bar{3}c$	0	0	0
$Fd\bar{3}m$	-0.76	-0.76	-0.02
$Cmcm$	-0.39	-1.04	+0.38
$Pnnm$	+0.53	+0.51	+2.56

6.2.2 Phase transformation during heating

During the thermal desorption process there might be phase transformations/crystal modifications or conformational changes in both Al and AlH$_3$ systems. Graetz et al.[2] showed that transitions between α, β and γ phases are exothermic and likely to occur spontaneously even at room temperature. Further, Grove et al.[37] showed that in the case of deuterated Al, there is a phase transformation of both β-AlD$_3$ and γ-AlD$_3$ to α-AlD$_3$ starting at 353 K and 363 K, respectively. This is illustrated in Figs. 6.7(a) and 6.7(b).

(a)

(b)
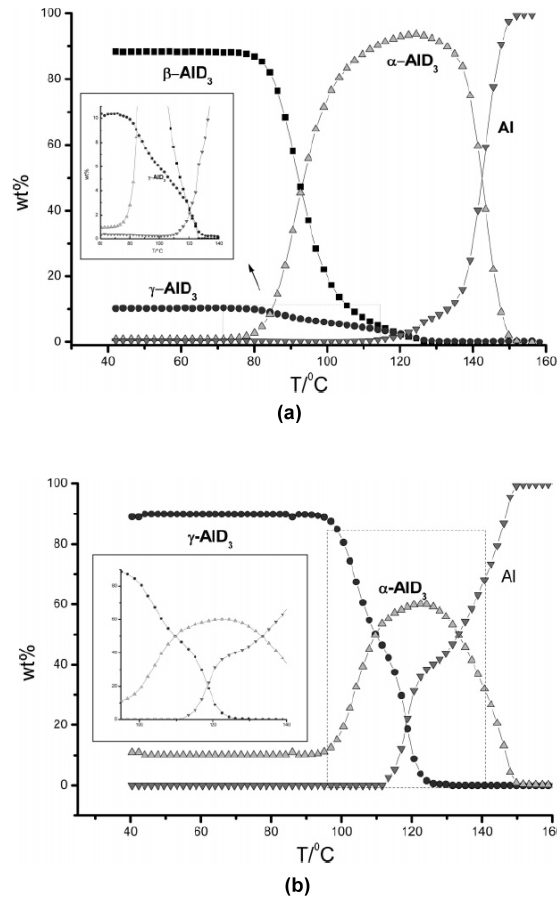
Fig. 6.7: (a) The relative amount of β-AlD$_3$ (black squares), α-AlD$_3$ (light gray triangles), γ-AlD$_3$ (dark gray circles) and Al (inverted gray circles) calculated from *in situ* synchrotron powder X-ray diffraction (SR-PXD) measurements of the β sample plotted against temperature. The γ phase is present as impurity. (b) Relative amount of γ-AlD$_3$ (dark gray circles), α-AlD$_3$ (light gray circles) and Al (inverted gray circles) plotted against temperature. (Reproduced from Ref. [37] with permission.)

Figure 6.7(a) shows the thermal decomposition of β-AlD$_3$ (The heating rate is 1 K/min). From 40°C to 80°C nothing happens. At about 80°C the fraction of α-AlD$_3$ in the sample starts to increase while that of β-AlD$_3$ decreases. At around 120°C there is a build up of Al as α-AlD$_3$ decomposes into Al and D$_2$. At 150°C all the α-AlD$_3$ has been used up leaving only Al in the heated sample. The transformation of β-AlD$_3$ is as follows:

Figure 6.7(b) is analogous to Fig. 6.7(a) but with β-AlD$_3$ replaced by γ-AlD$_3$. The transformation of γ-AlD$_3$ is a bit more complicated. At 90°C it transforms to α-AlD$_3$, which the decomposes to D$_2$ at around 130°C. It can also be seen in Fig. 6.7(b) that at 110°C the quantity γ-AlD$_3$ rapidly decreases while that of aluminum increases. This suggests that at this temperature γ-AlD$_3$ directly decomposes to aluminum and hydrogen without going through the α-AlD$_3$ phase.

Maehlen et al.[38] observed a phase transformation of γ-AlH$_3$ to α-AlH$_3$ during the decomposition process of the former. There have been claims that such transitions are expected and in fact are indicative that the system transforms to a less stable structure. However, it should be noted that the formation of the various polymorphs of AlH$_3$ depends on their preparation history. Secondly, a clear sign that the resulting structure is more stable than the starting structure is to do the reverse process i.e. reduce the temperature to 0 K. If indeed the structure is more stable it should not transform back to the starting (β) phase. It is important to emphasize that the α-AlH$_3$ is considered stable for temperatures $\geq$ 300 K. Therefore, it is possible that for temperatures below 300 K the β phase can be more stable than the α phase.

Since ReaxFF was parameterized using DFT values it has it that the β phase is the most stable phase. To reflect the experimental observations on relative stabilities of the four aluminum hydride phases (especially the experimentally observed phase transition of β to α-phase during heating process) we modified the force field so as to make the α-phase the most stable. In Graetz et al.'s work the heats of formation of the three polymorphic modifications are as follows: α-AlH$_3$ (2.366 kcal/mol H$_2$), β-AlH$_3$ (1.912 kcal/mol H$_2$) and γ-AlH$_3$ (1.617 kcal/mol H$_2$). We modified ReaxFF by these values so as to reflect the experimental results. Figure 6.8 shows the equations of state of the three polymorphic modifications using the modified ReaxFF$_{AlH_3}$.

For the modified force field, the heats of formation of the three polymorphic modifications are as follows: α-AlH$_3$ (3.10 kcal/mol H$_2$), β-AlH$_3$ (2.75 kcal/mol H$_2$) and γ-AlH$_3$ (2.46 kcal/mol H$_2$). These values are in good agreement with the experimental values of Graetz et al.[2]

6.3   Dynamics of hydrogen desorption

An important part of force field parametrization is to get the right reaction dynamics during the thermal decomposition of a cluster (or bulk) of aluminum hydride. Therefore, to ascertain that the force field reproduces the right thermal decomposition dynamics, we heated up a representative aluminum hydride
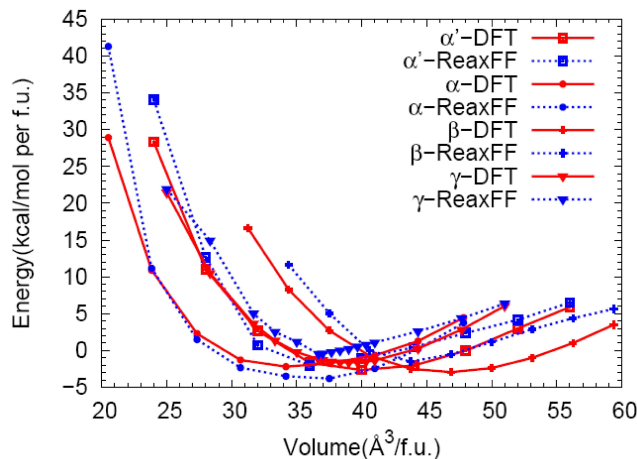
Fig. 6.8: Modified force field in which the α-phase is more stable than the β and α' phases.

cluster (Al_2H_6). Al_2H_6 decomposes endothermically as follows:

$$Al_2H_6 \rightarrow Al_2H_4 + H_2 \quad \Delta H_r = 22.95 \quad \text{kcal/mol} \tag{6.3}$$
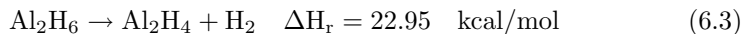
The transition state and the minimum energy path (MEP) for the process in equation (6.3) was calculated in VASP (DFT) using NEB.[39] This is shown in Fig. 6.9(i). In the NEB simulation it was ascertained that both end points were stable manifolds by performing frequency analysis. To get an accurate identification of the saddle point the climbing image flag was turned on.[40] This has the effect of driving up to the saddle point the image with the highest energy. This permits an accurate determination of the transition state. To compute the activation energy barrier, the image at the top of the MEP was further locally optimized in VASP using quasi-Newton algorithm. The barrier was calculated to be 51 kcal/mol. In general, the dissociation process is endothermic but since the transition state is at a higher energy than the end point then a fall in potential energy during the stage where molecular hydrogen is released is expected, which indicates that this portion of the reaction is an exothermic process. This is also reflected in Fig. 6.9(ii), which shows the energy profile during a molecular dynamics (MD) simulation of a heating run of Al_2H_6 at 2.5×10^8 K/s. In the MD simulation, velocity Verlet algorithm was used and the temperature was increased linearly by velocity scaling. The dynamics of hydrogen desorption in the two instances are similar. In Fig. 6.9(ii) there is a slight rise in energy at about 600 ps. This energy rise occurs due to the

Fig. 6.9: (i) Dissociation profile of Al_2H_6 as calculated by DFT using nudged elastic band method. (ii) The energy profile during a molecular dynamics (MD) simulation of a heating run of Al_2H_6. The temperature was ramped up at a rate of 2.5 $\times 10^8$ K/s.
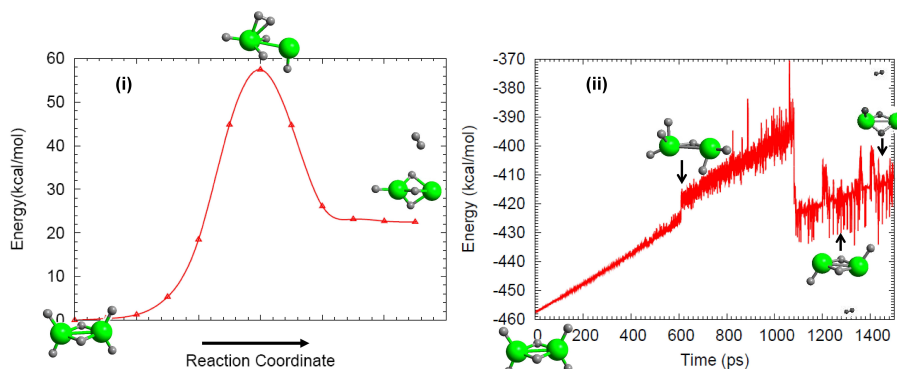
distortion of the Al_2H_6 structure. Also shown in Fig. 6.9(ii), after fragmentation of Al_2H_6 into Al_2H_4 and H_2, are the various geometrical modifications of the resultant Al_2H_4 during the heating process. The most important point to note in Fig. 6.9(ii) is that like in DFT, the desorption of molecular hydrogen in MD simulation is accompanied by a fall in the potential energy just after the transition state. This gives confidence that the force field reproduces the right desorption dynamics in comparison to DFT.

Table 6.10 shows the approximate temperature at which molecular hydrogen was desorbed (cluster dissociation) from various Al_nH_{3n} clusters. These temperatures are an approximation. In reality, the true fragmentation/desorption temperatures might be much lower, subject to long equilibration times, which is beyond the timescale of our simulation. The most important thing to note here is the decrease in fragmentation/desorption temperature with increase in the size of clusters.

In all the simulation runs, a heating rate of 2.5 $\times 10^8$ K/s was used because at a heating rate of 2.5 $\times 10^9$ K/s molecular AlH_3 (alane) remained intact throughout the heating range. There are a number of factors that contribute to the temperature at which molecular hydrogen is desorbed from the cluster. First, the length of equilibration. For instance, molecular hydrogen was only desorbed from Al_3H_9 after equilibrating at this temperature (1700 K) for 3500 ps (3.5 ns). When the cluster was heated up from 1 K to 2000 K at a rate of 2.5 $\times 10^8$ K/s it fragmented into AlH_3 and Al_2H_6 without molecular hydrogen being desorbed. Secondly, as mentioned in the foregoing, during the heating process these clusters fragment into smaller clusters (which re-agglomerate) prior to

Tab. 6.10: The temperature at which molecular hydrogen is released from Al$_n$H$_{3n}$ cluster. As the size of the cluster increases the temperature at which molecular hydrogen is released from the cluster also decreases.

Cluster	Temp. (K)
AlH$_3$	2100
Al$_2$H$_6$	1900
Al$_3$H$_9$	1700
Al$_4$H$_{12}$	1400
Al$_5$H$_{15}$	1200

desorption of molecular hydrogen. This fragmentation and re-agglomeration process occurs throughout the heating range, once the temperature of the cluster has been elevated (roughly at temperatures greater than 700 K, in the timescale of our simulation). We term this phenomenon as dynamic fragmentation-agglomeration. The reason for fragmentation is that at elevated temperatures the system is already at the threshold where it can fragment into smaller clusters. However, the fragments are less stable. As a result of they again agglomerate so as to attain greater stability. The agglomeration process is exothermic and is therefore accompanied by a local rise in temperature. This local rise in temperature facilitates the dissociation of Al-H bonds resulting in the desorption of molecular hydrogen. The calculated energy costs for fragmentation of Al$_4$H$_{12}$ into smaller clusters are summarized in Tab. 6.11. Al$_4$H$_{12}$ fragmented into smaller clusters during the heating process as follows: First, it fragmented into Al$_3$H$_9$ + AlH$_3$. This was then followed by re-agglomeration back to Al$_4$H$_{12}$. The re-agglomerated Al$_4$H$_{12}$ then re-fragmented into Al$_3$H$_9$ + AlH$_3$. This was then followed by re-agglomeration and a further fragmentation into Al$_2$H$_6$, Al$_2$H$_4$ and H$_2$.

Tab. 6.11: The heat of fragmentation of Al$_4$H$_{12}$ into various clusters during thermal heating of the cluster. The DFT values were computed using VASP at the PW91 level of theory. The energies are in kcal/mol.

Starting	Products	DFT(PW91)	ReaxFF
Al$_4$H$_{12}$ $\rightarrow$	Al$_4$H$_{10}$ + H$_2$	20.92	18.77
	Al$_3$H$_9$ + AlH$_3$	21.16	29.15
	Al$_2$H$_6$ + Al$_2$H$_4$ + H$_2$	28.82	32.61
	Al$_2$H$_4$ + 2AlH$_3$ + H$_2$	67.75	66.93

As shown in Tab. 6.11, Al$_4$H$_{12}$ can fragment into Al$_3$H$_9$ and AlH$_3$ at an energy

cost of 21.16 kcal/mol (DFT). This is quite close to the dissociation reaction $Al_4H_{12} \rightarrow Al_4H_{10} + H_2$, which costs 20.92 kcal/mol. Therefore, it is possible that during the heating up process a given cluster of (Al_nH_{3n}) can fragment into smaller clusters prior to desorption of molecular hydrogen once the temperature required to facilitate fragmentation has been reached.

The DFT calculated activation barrier of AlH_3 fragmentation (i.e. $AlH_3 \rightarrow Al + H_2$) in the gas phase is 96.94 kcal/mol and that for Al_2H_6 decomposition (i.e $Al_2H_6 \rightarrow Al_2H_4 + H_2$) is 51 kcal/mol. By comparison the experimental activation energy for hydrogen desorption in α-AlH_3 is 23.22 kcal/mol H_2.[41] The activation energy barrier for fragmentation of alane is almost four times that for desorption of molecular hydrogen from bulk AlH_3. This large difference cannot be due to computational inaccuracies. This implies that the fragmentation temperature of alane is much higher than the temperature of desorption of hydrogen from bulk AlH_3. For instance, in the timescale of our simulation, we find that molecular hydrogen dissociates from Al_2H_6 at about 1900 K. For bulk AlH_3, in the timescale of our simulation, molecular hydrogen desorbs at 700 K. This is clearly much less than the dissociation temperature of alane. From this comparison, it is clear that alane dissociates at a relatively higher temperature in comparison to bigger clusters. It follows therefore that if alanes were to be the facilitators of mass transport of aluminum atoms during the thermal decomposition of $NaAlH_4$ (as suggested in Refs.[20,21]) there must be a different mechanism by which they can release molecular hydrogen at lower temperature. One mechanism is that alanes undergo oligomerization. We discuss this issue in the following section.

6.3.1   Gas phase behavior of alanes

Figure 6.10(a) shows the dimerization of two AlH_3 molecules while Fig. 6.10(b) shows the agglomeration of two Al_2H_6 molecules resulting in the formation of a doubly bridged Al_4H_{12} molecule. The NVT (constant number of particles, constant volume and constant temperature) simulation was done at 300 K using Berendsen thermostat[42] for 30 ps. The molecules were placed in a cube of side 20 Å. The dimerization of AlH_3 molecules is in agreement with the well known fact that as the size of AlH_3 clusters increases so does its stability with respect to the individual AlH_3 species. Higher alanes can be easily formed from smaller alanes since the agglomerated alanes are more stable than the individual alanes species.[35] The theoretical formation energy of Al_2H_6 molecule from two alane molecules as computed by DFT and ReaxFF are -19.47 kcal/mol AlH_3 and -18.2 kcal/mol AlH_3 respectively. The DFT value is consistent with the previous works in Refs.[43–46] From Fig. 6.10(a), the dimerization energy for alanes is approximately -19 kcal/mol per AlH_3. This is consistent with the calculated value in Tab. 6.12. Table 6.12 shows the energy of agglomeration of various
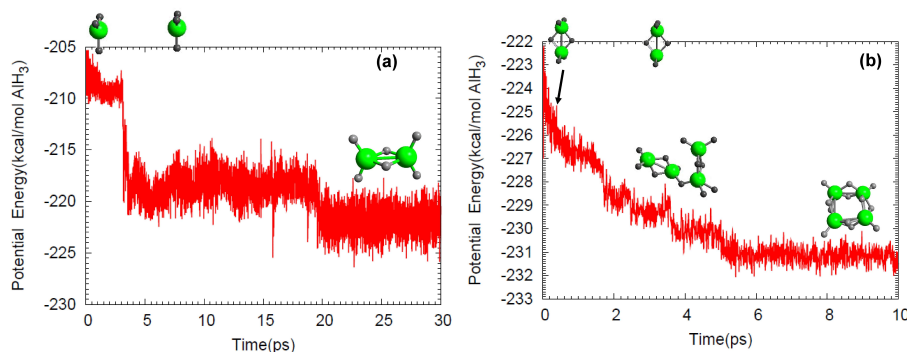
Fig. 6.10: Illustrations of the atomic configurations and energy profiles for (a) Alane dimerization reaction (b) Agglomeration of Al$_2$H$_6$ molecules.

small clusters of Al$_n$H$_{3n}$ series as calculated using DFT and ReaxFF. ReaxFF values are consistent with DFT values and that the agglomeration process is exothermic.

Tab. 6.12: The energy of agglomeration (per AlH$_3$) of various small clusters of the Al$_n$H$_{3n}$ series as calculated using DFT and ReaxFF.

Cluster	DFT	ReaxFF
2AlH$_3$ → Al$_2$H$_6$	-19.47	-18.17
3AlH$_3$ → Al$_3$H$_9$	-20.86	-22.46
4AlH$_3$ → Al$_4$H$_{12}$	-20.94	-23.88
5AlH$_3$ → Al$_5$H$_{15}$	-22.19	-24.74
6AlH$_3$ → Al$_6$H$_{18}$	-20.90	-25.27

To study the correlation between agglomeration and desorption of molecular hydrogen, we did a MD simulation using twenty Al$_2$H$_6$ molecules. We used Al$_2$H$_6$ molecules because Al$_2$H$_6$ molecule is more stable relative to two alanes (AlH$_3$ molecules). The molecules were placed at least 10 Å apart in a cubic box of side 80 Å. The system was first minimized to find the nearest metastable state. After minimization, the system's temperature was ramped up to 1000 K. This was then followed by a NVT MD equilibration period, using Berendsen thermostat. The temperature of 1000 K was chosen because we wanted to observe the desorption of molecular hydrogen during the agglomeration process. As will be shown later, even in the temperature range of 300 K - 800 K agglomeration still takes place but molecular hydrogen is not desorbed. In the equilibration process, at 0 ps, the following molecules/clusters exists in the

system: Al_8H_{24}, two Al_6H_{18}, two Al_4H_{12} and six Al_2H_6. This is so because during the minimization and temperature ramping up process some of the Al_2H_6 molecules agglomerated. As illustrated in Fig. 6.11, at the end of the simulation there are two molecular hydrogen desorbed from the agglomerated cluster.
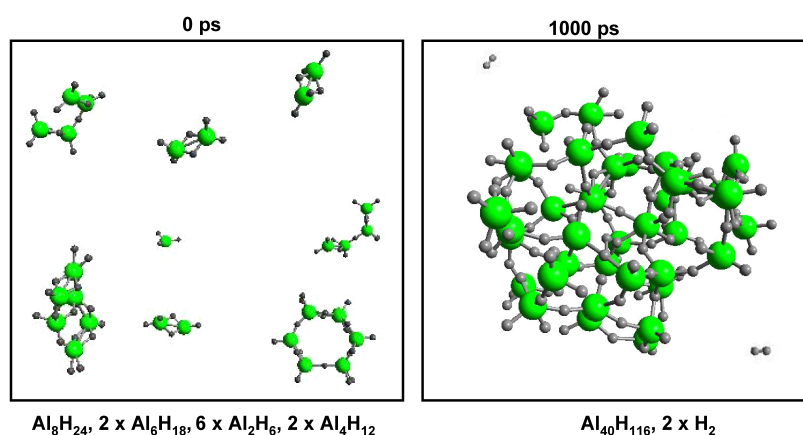

0 ps   **1000 ps**

Al_8H_{24}, 2 x Al_6H_{18}, 6 x Al_2H_6, 2 x Al_4H_{12}   **$Al_{40}H_{116}$, 2 x H_2**

Fig. 6.11: Snapshots of the Al_2H_6 clusters at the (a) beginning and (b) end of the simulation.

A number of factors contribute to desorption of molecular hydrogen. Firstly, the agglomeration process is exothermic. Although, globally, the temperature is kept constant by a thermostat there is a local rise in temperature due to exothermic nature of the agglomeration process. This local rise in temperature facilitates the instantaneous dissociation of the Al-H bond. Therefore, it becomes easy to desorb molecular hydrogen at this temperature (1000 K). Secondly, the growth of the cluster leads to the existence of many surface atoms, which are weakly bonded to aluminum atoms. Bigger clusters provide more facile paths for hydrogen desorption as they can make Al-Al metal bonds to compensate for the loss of Al-H bonds. Although the local rise in temperature during the agglomeration process might play a role in hydrogen desorption, in the long term limit, large cluster size effect is the major contributor to desorption of molecular hydrogen.

In Fig. 6.11 the snapshot at 0 ps shows the initial clusters after being heated up to 1000 K. Already at this stage some A_2H_6 molecules have agglomerated. Notice the ring like conformation of Al_6H_{18} in Fig. 6.11. At 260.9375 ps the cluster present in the system is $Al_{40}H_{120}$, implying that all the small clusters have agglomerated into one cluster. At 261 ps the cluster undergoes partial fragmentation leading to the formation of $Al_{39}H_{117}$ and AlH_3. This partial fragmentation and re-agglomeration goes back and forth throughout the

simulation period. The first molecular hydrogen is desorbed at 267.875 ps, leading to the formation of the following clusters/molecules: Al$_{39}$H$_{114}$, AlH$_4$ and H$_2$. Actually, the AlH$_4$ moiety is quite unstable and is immediately re-absorbed back by the bigger cluster. At 286.25 ps we have the following clusters/molecules: Al$_7$H$_{23}$, Al$_{33}$H$_{95}$ and H$_2$. At the end of the simulation (1000 ps) the clusters/molecules present in the system are Al$_{40}$H$_{116}$ and two molecular hydrogen. What is quite interesting is that in the end structure (at 1000 ps) there is a central aluminum atom which has six neighboring hydrogen atoms. This is illustrated in Fig. 6.11(b). The central aluminum atom is in a pentagonal ring of aluminum atoms, which resembles the coordination of aluminum in β-AlH$_3$.

In a different simulation run, in which the temperature of the system was kept fixed at 800 K, the Al$_2$H$_6$ molecules agglomerated into Al$_{40}$H$_{120}$ cluster during the 500 ps simulation run. However, at this temperature no molecular hydrogen was desorbed. Further tests (simulations) showed that in the temperature range 300 K to 800 K the Al$_2$H$_6$ clusters agglomerated into one cluster (Al$_{40}$H$_{120}$). However, in these cases no molecular hydrogen was desorbed from the cluster. Figure 6.12(a) shows the agglomerated structure while the pair distribution function for the annealed (to 0 K) agglomerated cluster is illustrated in Fig. 6.12(b).

(a)   **(b)**
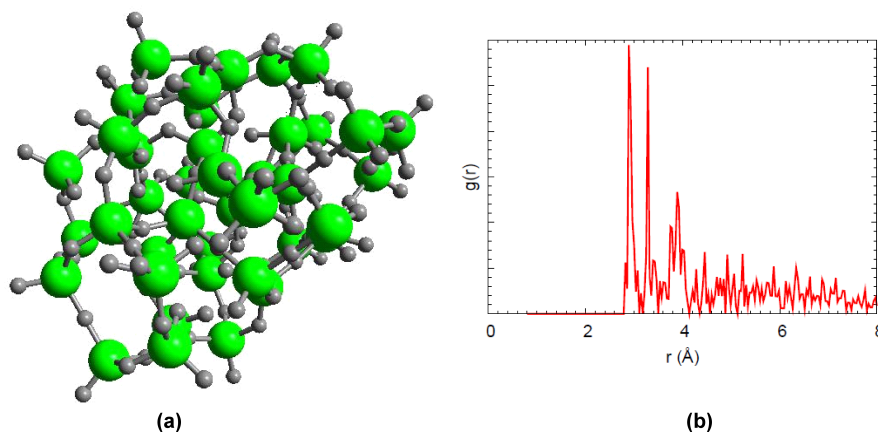
Fig. 6.12: (a) The completely agglomerated Al$_2$H$_6$ clusters at a temperature of 800 K. No molecular hydrogen was desorbed at this temperature. (b) The Al-Al pair distribution function of the cooled agglomerated Al$_2$H$_6$ clusters. The agglomerate was annealed to 0 K at a rate of 2.5 $\times 10^9$ K/s.

The figure shows that the radial distribution function has a slightly broad delta peaks. This suggests that the cluster is in a quasi-crystalline state. The quasi-

crystalline state can be explained by the fact that the aluminum and hydrogen atoms are somehow arranged in a semi-periodic pattern. The average Al-Al distance is approximately 3.0 Å. This value compares quite well to the DFT calculated Al-Al bond length in β-AlH$_3$ (3.2 Å). However, this structure does not have the local coordination of any of the condensed phases of AlH$_3$. There are some central Al atoms that are five coordinated in hydrogen while the rest have four hydrogen neighbors. The changes in charge redistribution as a result of agglomeration (i.e. plots of the clusters at the beginning of the simulation and that of the agglomerated cluster at the end of the simulation run) are shown in Fig. 6.13. The figure shows that at the end of the simulation run (500 ps),
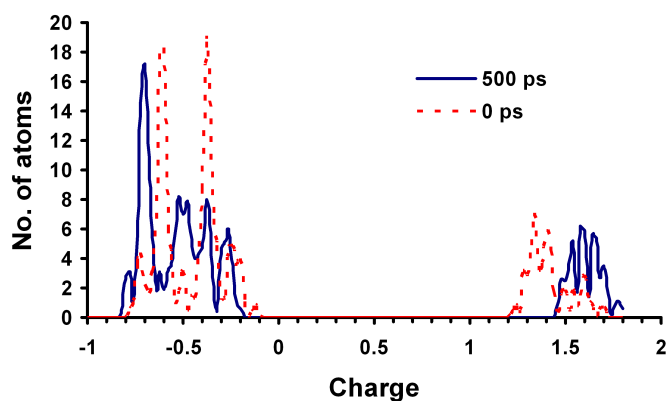

Fig. 6.13: The charge distribution plots of the alane clusters (0 ps) at the beginning of the simulation and (500 ps) that of the agglomerated cluster at the end of the simulation run

there is an upward shift on the charge on aluminum atoms as compared to at the beginning of the simulation. Therefore there is a substantial charge transfer from aluminum atoms to hydrogen atoms during the agglomeration process. The distribution of charge on aluminum atoms is also less than the nominal charge of aluminum, implying that the bonding between Al and hydrogen is covalent. Although there is an increase in the negative charge on hydrogen atoms a considerable number still have charges in the range -0.1 to -0.5. These are the surface hydrogen atoms as illustrated in Fig. 6.12.

In the light of these results, one might wonder if the same scenario (agglomeration) is mirrored in the condensed phase. In other words, how do clusters of AlH$_3$ behave on the surface of aluminum? Several experimental studies based on deposition of atomic hydrogen on aluminum surface have been conducted by various groups.[47–53] In some of these studies it was found that alanes were formed and then oligomerized. The oligomerization process was dependent on

surface coverage, surface morphology and temperature. In their study, Go et al.[50] observed that on the vicinity of steps the alanes oligomerized into long strings. Hara et al.[51] showed, using thermal desorption spectroscopy (TDS), that AlH_4, AlH_3, AlH and AlH_2 species were desorbed from 0.5 ML H/Al(111) surface at 330 K, which was heated at a rate of 10 K/s. In their study, Hara and coworkers dosed atomic hydrogen on Al(111) surface and noted that all of adsorbed species desorbs at around 340 K as aluminum hydrides such as AlH_3 or Al_2H_6. However, this happened at a ramping rate above 10 K/s. At low heating rates, and at 340 K, only molecular hydrogen is desorbed. This suggests that the adsorbed species are unstable and continuously undergo disproportionation to aluminum and molecular hydrogen.[51,54] In the experimental work of Herley et al.[52] they mentioned the formation of "small clusters of agglomerated lumps on reacted surface" during the thermal decomposition of AlH_3. Using energy dispersive (EDAX) spectroscopy scans they detected aluminum as the only metal present in the aggregate. One possibility is that the aggregate formed was aluminum oxide. However, this seems remote since aluminum oxide should have passivated the surface yet the decomposition process at 150°C was accelerated by the presence of the aggregates. The other possibility is that these clusters were purely made up of aluminum atoms. However, the formation of more aluminum should have led to a slow rate segment as discussed in Ref.[55] Based on our present results, we suggest that these aggregates might have been alane clusters. Chaudhuri et al.[53] showed, using experimental fourier transform infrared (FTIR) spectroscopy data, the coexistence of several adsorbed species on Al(111) surface. The relative concentration of these species was shown to be dependent on the roughness of the surface, surface coverage and the temperature.

6.3.2   Alanes interaction on Al surface

In this section we discuss a number of theoretical models that were carried out in order to shed more light on these experimental findings, especially the work of Go et al.[50] There are three issues we set out to address/clarify: (a) the details of the formation of alanes due to the reaction between atomic hydrogen and Al(111) surface, (b) the ordering and dynamical behavior of the formed alanes on Al(111) surface, (c) the corrugation and reconstruction of the Al(111) surface after the formation and re-arrangement of the alanes. In the theoretical simulation, in all cases unless stated otherwise, a (10×10) unit cell with dimensions (28.6×24.75) was used. The slab was made up of 5 layers. Each layer had 100 atoms giving a total of 500 atoms. A vacuum equivalent to 20 layers was used in the z direction, which more than suitably separated the slab system from its periodic images. The system was first minimized and then equilibrated at 300 K for 50000 time steps. In the first simulation, the temperature of the entire system was kept constant at 300 K. The atomic configurations of the adsorbed alanes

on the Al(111) surface are shown in Fig. 6.14. This snapshot of the atomic configurations was taken after 500 ps of simulation run.
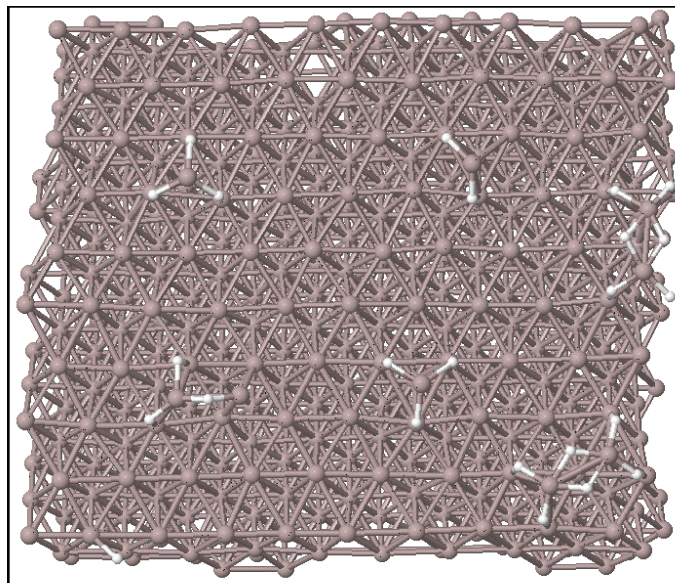

Fig. 6.14: Snapshots of one AlH$_2$, one H atom, three AlH$_3$ and two Al$_2$H$_6$ clusters chemisorbed on the Al(111) surface. The AlH$_2$ and H are products of the fragmentation of one of the AlH$_3$ molecule during the chemisorption process. Both the aluminum slab and the clusters were kept at a temperature of 300 K throughout the simulation process.

At a temperature of 300 K the alanes are essentially immobilized on the Al(111) surface. They vibrate about their mean position but cannot diffuse because they are strongly chemisorbed on the substrate. The bond length between the aluminum atom in the AlH$_3$ adparticle and that of the Al(111) surface is in the range of 2.6 Å to 2.8 Å. This is less than the Al-Al bond length in bulk aluminum (2.864 Å). This means that the adparticle (aluminum hydride) is chemisorbed on the Al(111) surface. Notice in Fig. 6.14 that there is one AlH$_2$ and a H atom also adsorbed on the surface. The AlH$_2$ and H are products of the fragmentation of one of the AlH$_3$ molecule during the chemisorption process.

In order to study the mobility of the adparticles we conducted a different simulation run. The initial atomic configuration was the same as that in Fig. 6.14. After minimization, the temperature of the system was divided into two zones. The temperature of the system was quickly ramped up to 800 K and kept constant for 125 ps. One reason for ramping up the temperature to 800 K was to try and see if we could observe desorption of molecular hydrogen during the

production stage. This is based on the work of Go et al. [50] who noted that there was a loss of smaller alanes to higher alanes and to desorption at temperatures above 360 K. The other reason was to accelerate the diffusion process of atomic hydrogen and the aluminum hydride complex on the metal surface. Figure 6.15 is a snapshot of the simulation run after 500 ps.
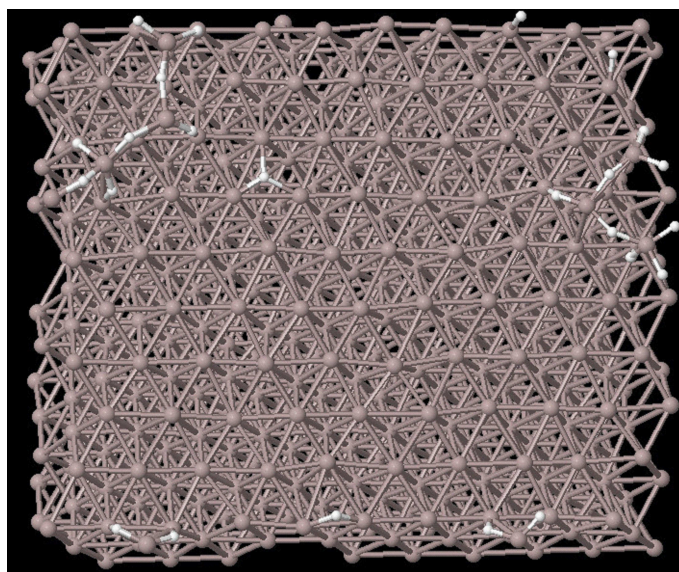

Fig. 6.15: Oligomerization of smaller alanes into a large alanes at 800 K on Al(111) surface.

The most important finding is that the alanes oligomerized as illustrated in Fig. 6.15. In trying to understand the figure one should take into consideration the presence of periodic boundaries. One conspicuous difference between Fig. 6.14 and Fig. 6.15 is that the initial Al$_2$H$_6$ configuration (Fig. 6.14) is either completely distorted or fragments into smaller Al-H clusters and atomic hydrogen (Fig. 6.15). At the beginning of the simulation (Fig. 6.14) we had one AlH$_2$, one H atom, three AlH$_3$ and two Al$_2$H$_6$ clusters. At the end of the simulation (Fig. 6.15) most of these alanes have oligomerized. There are also three hydrogen atoms and an alane molecule diffusing on the surface. It could be that in the limit of long equilibration times the hydrogen atoms and the remaining alane will also agglomerate with the oligomer. The formation of strings is consistent with the experimental work of Go et al. where string-like conformations in the vicinity of steps was seen. The oligomerization of alanes on Al(111) surface explains why there is a lack of coverage dependance of atomic hydrogen adsorption on Al(111) surface. [49] On the Al(111) surface, larger chemisorbed alane, starting with Al$_2$H$_6$, diffuse by reptation i.e. snake

like motion. The diffusion mechanism of AlH_3 is quite complex. Since the AlH_3 is chemisorbed on the surface it is quite difficult for it to diffuse by shearing. The preferred mode of diffusion is leapfrog and summersault. In the leapfrog diffusion one of the diffusing atoms moves atop the AlH_3 molecule before settling in a different location. In the summersault scenario the AlH_3 slightly spins around its axis before the three H atoms settle in different locations but they are all still bonded to the same aluminum atom. The diffusion mechanism of AlH_2 is quite interesting. It seems as if it diffuses in a manner similar to someone rowing a boat. The aluminum atom moves forward and simultaneously the two hydrogen atoms move backwards. In the next movement, as the two hydrogen atoms move forward the aluminum atom moves backwards. The AlH_2 particle can also spin around its axis with the two hydrogen atoms acting as wings. The preferred diffusion process of atomic hydrogen is to hop between the bridge and the 3-fold hollow sites. The calculated activation energy for hopping diffusion on the flat Al(111) surface, from ReaxFF, is 2.7 kcal/mol.

In experiments, usually atomic hydrogen is deposited on aluminum surface.[49,51,52] Complementary scanning tunneling microscopy (STM) and surface infrared (IR) measurements show that H reacts strongly with Al(111), producing a variety of new alane (aluminum hydride) surface species.[50] Fig. 6.16 is an illustration of what happens when atomic hydrogen impinges on Al(111) surface. The figure shows that when atomic hydrogen are deposited on Al(111) surface they extract aluminum atoms from the surface, forming alanes. The formed alanes then oligomerize.
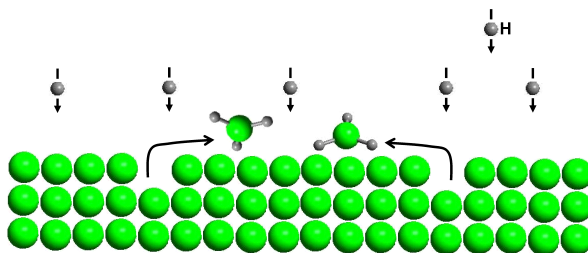
Fig. 6.16: Schematic representation of the deposition of atomic hydrogen on Al(111) surface. The hydrogen atoms etch aluminum atoms from the surface leading to the formation of alanes.

In order to investigate the etching of aluminum from the surface, the formation and subsequent dynamics of alanes on Al(111) surface, we used Go et al.'s work as a benchmark for modeling the interaction of atomic hydrogen with Al(111) surface. To do this, we placed atomic hydrogen (adatoms) on the top site of Al(111) surface. In this initial configuration, the hydrogen atoms were bonded

terminally to aluminum atoms and inclined to the surface normal. If we define
the surface coverage as the ratio of actual surface coverage of adsorbed species
to that of saturation coverage (of surface atoms) then we have a monolayer
coverage (1 ML). In reality, this coverage was reduced to 0.92 ML because
upon minimization four molecular hydrogen were desorbed from the surface.
Given that we are not interested in the interaction of molecular hydrogen with
the Al surface, these desorbed molecular hydrogen were removed from the
system. Figure 6.17 shows the configuration of the atoms immediately after
minimization. The figure shows that the hydrogen atoms maximize their co-
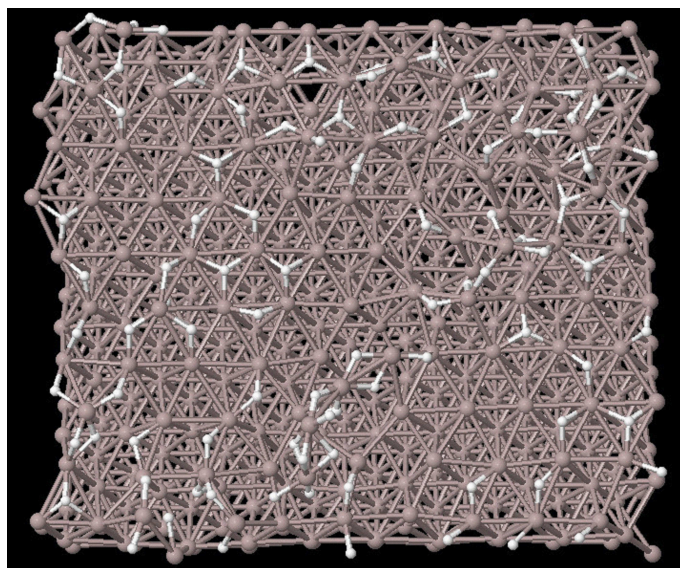
Fig. 6.17: (Top view) Adsorption of atomic hydrogen on Al(111) surface. The picture
shows the adsorbent-adsorbate configuration, just after minimization.

ordination by hopping from the top site and adsorbing on the 3-fold hollow
sites, specifically fcc sites. The hydrogen atoms that remain bonded to the top
site are tilted instead of being inclined to the surface normal. Interestingly,
even at the minimization stage some hydrogen atoms extracts aluminium atoms
from the surface forming alane oligomers (aluminum hydride complex) as can
be seen in Fig. 6.17. We observed that hydrogen atoms extracts aluminum
atoms directly on impinging the surface regardless of whether there is a vacancy
or not. The notion of direct extraction of aluminum atoms from the terraces
by impinging atomic hydrogen was also noted by Go et al.[50] The etching and
chemisorption of the hydrogen atoms during the minimization process results in
the formation of aluminum vacancies and as a consequence the corrugation of Al
surface. Since defects are sites of high reactivity some hydrogen atoms diffuse

to these sites during the equilibration process. This results in the formation of more aluminum hydride complexes. The formation of aluminum hydride complex results in significant adsorbate induced reconstruction, which is driven by the strong adsorbate-substrate interaction.

Like in the previous simulations, the temperature of the system was quickly ramped up and held at 800 K. The equilibration process leads to rapid evolution of the population of alanes as the adsorbed hydrogen atoms etch aluminum atoms to form alanes. At this high temperature there is significant thermal harvesting of alanes. The alanes then oligomerize and cluster together leading to the formation of what we can term as aluminum hydride complex islands. This is illustrated in Fig. 6.18. The figure shows a top view of the structure
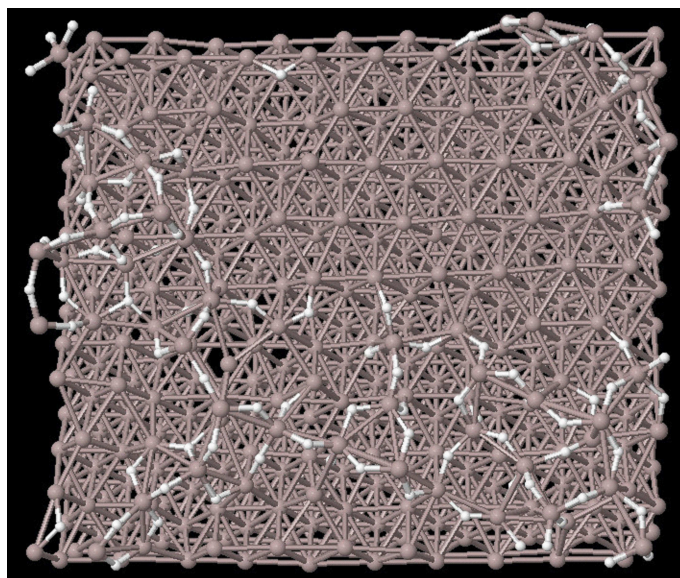
Fig. 6.18: (Top view) Oligomerization of the alanes to form an aluminum-hydride mound. This simulation run was done at 800 K.

at the end of the simulation run (125 ps). What the figure shows is that at the middle of the aluminum surface we have an almost perfect (111) ordering instead of being corrugated or having atomic vacancies as one would expect. This surface is then almost surrounded by an alanes mound. This is quite interesting because in the initial set-up, after energy minimization, the surface was highly corrugated due to the formation of aluminum hydride and the etching of aluminum atom from the Al(111) surface by atomic hydrogen. This means that there must be some sort of re-ordering of the Al surface leading to the creation of a perfect (111) surface. We can attribute this restructuring to two

factors: (a) there is a thermally activated vacancy migration. These vacancies then aggregate near the step edge. (b) Some aluminum atoms from aluminum hydrides are captured back by some of the vacancies. The vacancy is then sealed (self-repaired) using these atoms. This is explained in the next section. Fig. 6.19 is an illustration of the charge transfer distribution after minimization and at the end of the simulation run.
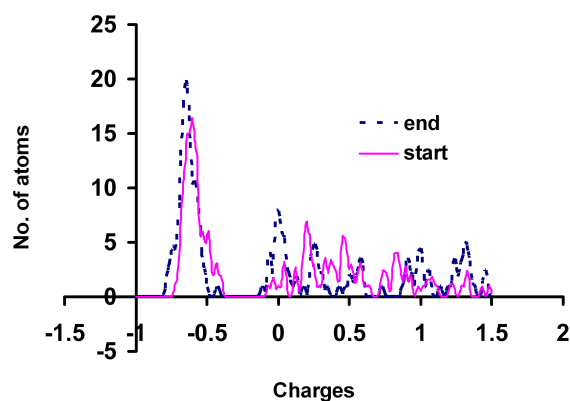
Fig. 6.19: Charge distributions of the aluminum atoms on the top layer of the slab plus the adsorbed hydrogen atoms, after minimization and at the end of the equilibration run.

The figure shows the charge distributions of the aluminum atoms on the top layer of the slab plus the adsorbed hydrogen atoms, after minimization and at the end of the equilibration run. It can be seen in the figure that at the end of the simulation there is a significant increase on the number of aluminum atom with charge of approximately 0. At the same time there is also an increase in the number of aluminum atoms with charges between +1 and +1.5. We can interpret this observation as follows. As a result of reconstruction some of the aluminum atoms are reabsorbed back onto the aluminum surface. These are the aluminum atoms whose charge tends towards 0 as illustrated in Fig. 6.19. The aluminum atoms whose charge increase to the higher numbers belong to the alane oligomers. Notice in Fig. 6.19 that there is also a significant increase of charges of hydrogen atoms due to oligomerization and formation of the aluminum hydride mound.

6.3.3   Trapping of atomic hydrogen by an aluminum vacancy

To get an insight on the effects of defects on diffusion and agglomeration process of alanes, aluminum vacancies were created around an alane. It was observed that the alane that was surrounded by defective sites dissociated into H and AlH_2. As the AlH_2 flipped over the vacant site the Al atom in AlH_2 was captured by a defective site leaving the two atomic hydrogen to diffuse on the surface. In other words, the Al surface compensates for the defect by capturing an aluminum atom from alane and then self repair itself. This self reparation perhaps can explain why the aluminum surface in Fig. 6.18 looks smooth. In their work, Go and coworkers noted that it is possible that mobile atomic vacancies created during hydrogen adsorption may capture surface alanes and immobilize them on the substrate. However, from our simulations, it seems that mobile atomic vacancies should fragment alane and use the aluminum in alane for self repair. Larger alanes, however, can be captured and immobilized by the atomic vacancies. This leads to a reconstruction of the vacant site and eventual fragmentation of the trapped large alane. In our simulation we saw that atomic hydrogen can be trapped at the bridge site if there are aluminum vacancies on either side of the bridge. This is schematically illustrated in Fig. 6.20. It is well
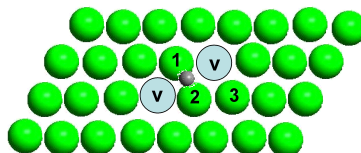
Fig. 6.20: Schematic representation of a hydrogen atom trapped at the bridge site due to existence of vacancies on either side of the bridge.

known that the facile path for atomic hydrogen diffusion on Al(111) surface is between the bridge and hollow sites. For the hydrogen atom to diffuse to the hollow site it must pass through the bridge site and vice versa. Therefore, creation of vacancies on either side of the bridge site leaves the hydrogen atom trapped at the bridge site. It cannot diffuse over the top due to the high energy barrier involved. It therefore remains trapped at the bridge site. However, it might be possible that at elevated temperatures the hydrogen atom can either garner enough energy to flip over the top or jump to the adjacent bridge site.

One very interesting observation was the formation of Al_{vac}-H pair (vac = vacancy). As noted earlier, the facile path for hydrogen diffusion is between bridge and hollow sites. What happens if there is a vacant site on only one side of the bridge site? A priori, we might think that the atomic hydrogen should be able to diffuse away since there is a hollow site on one side of the

bridge. Interestingly, we observed a H-atom diffusing (hopping between bridge and hollow sites) towards and being trapped by a vacant site due to the localised minima of this site on the potential energy surface. This is schematically illustrated in Fig. 6.21.
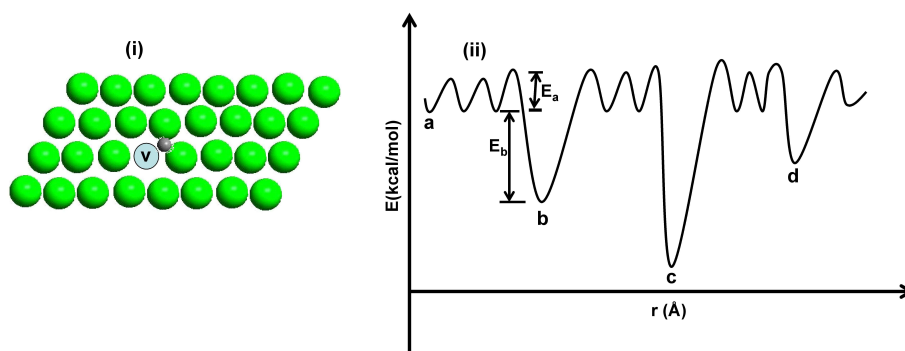

Fig. 6.21: (i) A hydrogen atom trapped at the bridge site due to localised minimum on the potential energy surface of this site as shown in (ii)b. E$_a$ is the migration energy barrier, E$_b$ is the binding energy of the vacancy.

Figure 6.21(ii) shows the various minima in the potential energy surface. (**a**) represents the chemisorption potential energy well on the flat Al(111) surface. Once chemisorbed, the atomic hydrogen hops between the bridge and hollow sites. In the course of the diffusion there is a finite probability that it can fall into the potential well of the vacant site (represented by **b** in Fig. 6.21(ii)). The vacancy desorption energy, which is the energy needed by the hydrogen atom to wring itself out of the vacancy potential energy well is given by E$_d$ = E$_b$ + E$_a$. There are also other minima like the step edge, given by (**c**) in Fig. 6.21(ii). It must be that these trapped atomic hydrogen are what were observed by Go and coworkers. What was actually very interesting in this simulation is that we observed the Al$_{vac}$-H pair diffusing as one entity. This is akin to the electron-hole concept in semiconductors.

6.3.4   Diffusion of Aluminum

In a different simulation run, two Al atoms were placed apart and simulated at 800 K. The two atoms were observed to dimerize on the Al(111) surface. The agglomeration of Al atoms was also seen in the case whereby five Al atoms were placed apart from each other on Al(111) surface. The temperature was kept at 800 K for 625 ps. It was observed that the Al atoms agglomerated

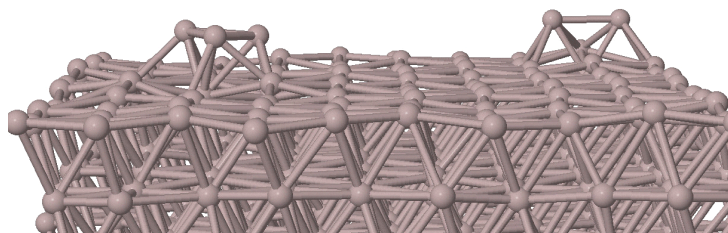into a dimer and a trimer. This is illustrated in Fig. 6.22. It was noticed

Fig. 6.22: The agglomeration of five aluminum atoms on Al(111) surface. The aluminum atoms agglomerate into a dimer and a trimer on the Al(111) surface. These clusters are strongly chemisorbed on the surface and cannot diffuse any further.

that, once formed, the dimer and the trimer were strongly chemisorbed on the surface and did not diffuse any further. We can infer from this observation that although aluminum atom is also mobile on Al(111) surface once two or three Al atoms agglomerate they are strongly chemisorbed on the surface owing to the strong metallic cohesion between the atoms in the cluster and the surface. They therefore cannot diffuse any further. The presence of hydrogen therefore enhances the mobility of the massive aluminum atoms. This implies that the long range mass transport of Al atoms must be facilitated by alanes.

6.4 Abstraction of molecular hydrogen

An important question in hydrogen storage is knowing the nature of structural transformation that takes place during the desorption process of hydrogen. In order to get a better insight of structural transformation during the desorption of hydrogen, we simulated successive abstraction of surface molecular hydrogen from a representative aluminum hydride nanoparticle ($Al_{28}H_{84}$ cluster). This is illustrated in Fig. 6.23. The abstraction process of surface molecular hydrogen is given by:

$$Al_{28}H_n \rightarrow Al_{28}H_{n-2} + H_2 \tag{6.4}$$
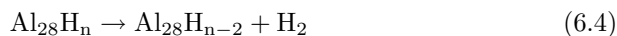
where n = 84 to 0. The desorption energy is defined as

$$E^{desorb} = [E_{Al_{28}H_{84-n}} + E_{\frac{n}{2}H_2}] - E_{Al_{28}H_{84}} \tag{6.5}$$

where $n = 2, 4, 6, 8, ..., 48, 50, 52, ..., 84$.

Systematically, in the abstraction process, clusters were first minimized and then annealed to 0 K using molecular dynamics (MD) simulation to find the nearest

metastable conformation. After minimization, the temperature was ramped up to between 600 K - 900 K at a rate of 2.5×10^{10} K/s. This was then followed by a NVT (constant number of particles, constant volume and constant temperature) equilibration period of 300000 steps at this temperature (600 K - 900 K) using Berendsen thermostat.[42] In all cases, a time step of 0.25 fs was used. After the equilibration run, the clusters were annealed to 0 K at a rate of 2.5×10^{9} K/s. After this, molecular hydrogen was abstracted by removing two hydrogen atoms from the configuration at 0 K. This was done iteratively until all the hydrogen atoms were abstracted. The entire process was repeated several times, each time starting out with $Al_{28}H_{84}$ but with a different geometrical arrangement. Only the energies of the most stable conformations that gave rise to the nearly smooth curve shown in Fig. 6.23 were considered.

Figure 6.23 shows the trend in particle stability as a function of hydrogen unloading. The negative values of the heat of formation show that at the initial stages the forward decomposition reaction in equation (6.4) is thermodynamically favored. During the abstraction process, the exothermicity of the desorption process decreases with increasing abstraction of molecular hydrogen. When almost a half of the hydrogen atoms have been abstracted, the process becomes endothermic.

The observation can be understood as follows. Region (I) shows the high rate segment when desorption of molecular hydrogen is very favorable while region (II) is the slow rate segment when desorption of molecular hydrogen systematically becomes unfavorable. The cluster size dependence of the desorption process is related to the local coordination of aluminum atoms with hydrogen. Therefore, the higher the concentration of hydrogen the more favored the decomposition of AlH_3. Large aluminum clusters can be understood to have a bulk like decomposition as follows:

$$(AlH_3)_2 \rightarrow (AlH)(AlH_3) + H_2 \tag{6.6}$$
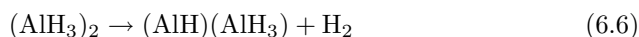
The reaction in equation (6.6) should be interpreted as follows. The AlH_3 unit from which the hydrogen is abstracted is embedded in other AlH_3 units. There is a saturation of AlH_3 species in the cluster such that each AlH_3 species is surrounded by other AlH_3 species. This provides facile paths for hydrogen desorption as they can make Al-Al metal bonds to compensate for the loss of H-Al bonds. The critical point in Fig. 6.23 is the point at which there is a transition from exothermicity to endothermicity. In other words, the abstraction of hydrogen start to become unfavorable since the system is stabilized. We can understand the stable region as follows. There are fewer hydrogen atoms in comparison to aluminum atoms. This implies that the AlH_3 units are dispersed within the system and not embedded in other AlH_3 units. Therefore, the abstraction process essentially behaves like dissociation of AlH_3, $AlH_3 \rightarrow AlH + H_2$, which is energetically unfavorable.
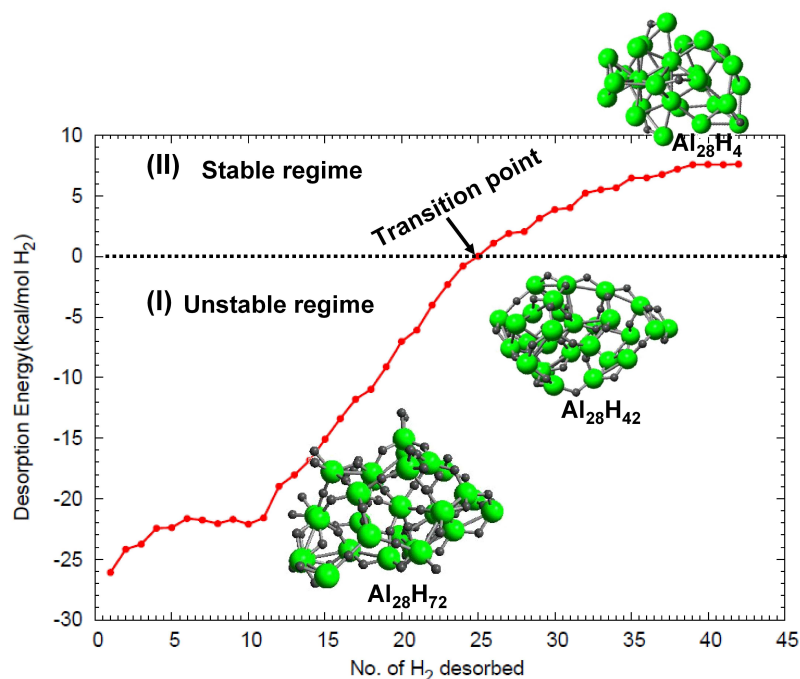
Fig. 6.23: Desorption energy, E^{desorb}, as a function of number of H_2 molecules abstracted from the system. The reference energy, shown by the dotted line, is the energy for $Al_{28}H_{84}$.

Intuitively, one is bound to think that as more and more surface hydrogen atoms are abstracted the remaining hydrogen atoms should become subsurface and be strongly bound to the aluminum atoms (see Ref.[17]). However, this is not the case. As more and more surface hydrogen atoms are abstracted the bulk hydrogen atoms come to the surface. In fact, for $Al_{28}H_{84}$ the bulk aluminum atoms are octahedrally coordinated to hydrogen atoms (the average bond lengths are: $d_{Al-H} = 1.64$ Å and $d_{Al-Al} = 3.342$ Å) while for $Al_{28}H_{42}$ the bulk aluminum atoms are tetrahedrally coordinated to hydrogen atoms (average bond lengths: $d_{Al-H} = 1.65$ Å and $d_{Al-Al} = 2.843$ Å). In the case of $Al_{28}H_4$ the bulk aluminum atoms have no nearest hydrogen neighbors, instead they are icosahedrally coordinated to neighboring aluminum atoms. The average Al-Al bond length in this case is 2.75 Å. Notice that d_{Al-H} remains almost constant throughout the abstraction process whereas d_{Al-Al} decreases towards the aluminum bulk value. The decrease in d_{Al-Al} with increasing abstraction of molecular hydrogen implies that there is a transition towards metallization.

On the other hand, the almost constant value of d$_{Al-H}$ shows that the Al-H bond length is independent of the chemical environment for a given system (in this case binary aluminum hydride). The observations detailed herein shows that aluminum atoms prefer to form bond with each other rather than with hydrogen. Hydrogen atoms prefer to stay on the surface rather than subsurface sites and since the surface hydrogen atoms prefer to mostly occupy the less stable two fold (bridge) sites it becomes easy to desorb them. On the Al(111) surface hydrogen prefer to occupy the 3-coordinated hollow (fcc and hcp) sites. The fact that hydrogen atoms prefer to occupy the bridge sites in clusters of this size shows that the surface has a corrugated morphology. The behavior of aluminum hydride cluster is therefore very different from that of NaH.[17] It is also markedly different from that of MgH$_2$. Wagemans[56] showed that the hydrogen atoms in hydrogen depleted magnesium hydride prefer to cluster together instead of being evenly distributed. Using ReaxFF, Cheung et al.[18] showed that there are no surface hydrogen atoms for hydrogen depleted Mg$_{20}$H$_x$ (x = 2, 4,6) systems. We find a different behavior for hydrogen atoms in aluminum hydride systems. In a hydrogen depleted aluminum hydride cluster, the hydrogen atoms are randomly scattered over the aluminum rich surface. This can be seen in Fig. 6.24, which shows the geometries of the annealed clusters of Al$_{28}$H$_{84}$, Al$_{28}$H$_{72}$, Al$_{28}$H$_{42}$ and Al$_{28}$H$_4$.

The dynamics taking place within the structure during the systematic abstraction of molecular hydrogen can be understood better by examining charge transfer. To investigate the changes in charge transfer due depletion of hydrogen atom, charge distribution plots were made for Al$_{28}$H$_{84}$, Al$_{28}$H$_{42}$ and Al$_{28}$H$_4$ clusters during the abstraction runs. This is illustrated in Fig. 6.25. As illustrated in Fig. 6.25, in Al$_{28}$H$_{84}$ there is a broad distribution of charges on both aluminum and hydrogen. This is because there are many subsurface and surface hydrogen atoms. The low charges are associated with surface atoms, which have less number of neighbors. As one moves from Al$_{28}$H$_{84}$ to Al$_{28}$H$_4$ the distribution of charges of aluminum atoms tends towards the lower numbers and concomitantly there is an increase in the negative charge on hydrogen atoms. This is reflected in the charge distribution on Al$_{28}$H$_{42}$ as illustrated in Fig. 6.25. However, we see in Fig. 6.25 that the charges located at the hydrogen atoms in Al$_{28}$H$_4$ actually decrease. We can understand this disparity as follows. Since charge distribution is a function of the number of nearest neighbors, this shows that with increasing abstraction of hydrogen there is a decrease in the number of nearest neighbors of opposite charge for both aluminum and hydrogen. The four hydrogen atoms are not subsurface but rather occupy surface sites where they are lowly coordinated to aluminum neighbors. Therefore, they have less number of aluminum atoms neighbors. This makes them to have low negative charges. In the case of aluminum, at this point the aluminum atoms have formed metallic bonds since the number of hydrogen in the system is negligible. In other words the system tends towards metallization. In Al$_{28}$H$_4$ there are three aluminum atoms that have icosahedral coordination. These aluminum atoms,
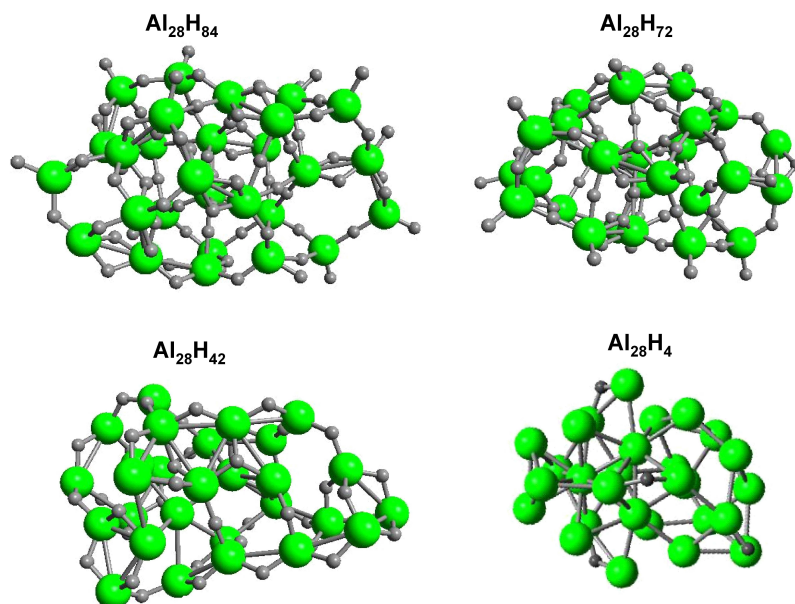
Fig. 6.24: Geometries of the annealed clusters of $Al_{28}H_{84}$, $Al_{28}H_{72}$, $Al_{28}H_{42}$ and $Al_{28}H_4$. In the hydrogen deficient $Al_{28}H_4$ cluster the hydrogen atoms prefer to occupy surface sites rather than bulk.

therefore, have a bulk coordination. This suggests that once almost half the hydrogen atoms have been removed the hydrogen deficient aluminum hydride tends towards metallization.

6.5 Molecular hydrogen trapped in aluminum hydride solid

For many years now, there have been discussions on the possibility of molecular hydrogen being trapped in the channels of potential hydrogen storage materials such as $NaAlH_4$ and AlH_3.[57–60] The issue of hydrogen molecules being trapped in cages or channels of hydrogen storage media will present the next technological challenges with a view to fully harnessing the storage capabilities of these systems. Trapped molecular hydrogen implies that not all the desorbed hydrogen diffuses out during the thermal decomposition process of the potential hydrogen storage materials. This reduces the efficiency of these materials. How to channel out these trapped hydrogen molecules from the

Fig. 6.25: Charge distribution plots showing the transfer of charge during abstraction process of molecular hydrogen from Al$_{28}$H$_{84}$ cluster. The hydrogen atoms are negatively charged.

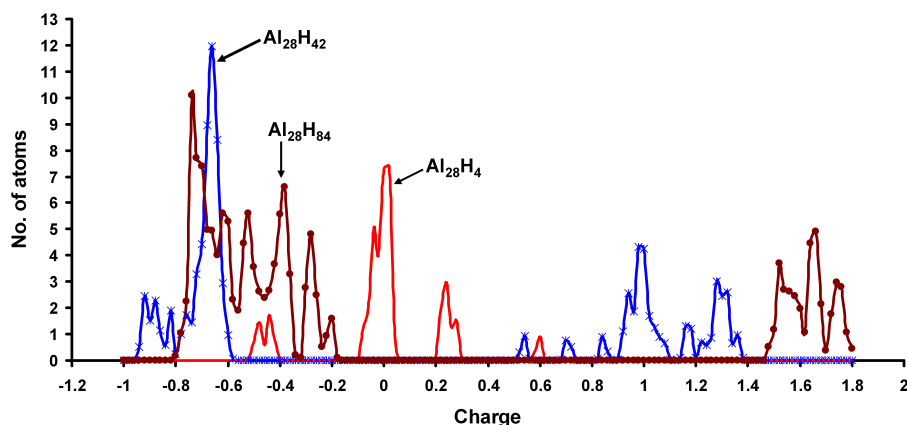system during the desorption process is clearly a non-trivial task. Using nuclear magnetic resonance (NMR) spectra, Herberg et al. deduced that there were molecular hydrogen trapped in small cages in the interstitial sites of NaAlH$_4$.[61] Recent experimental work, using proton NMR, by Senadheera et al. showed that molecular hydrogen can be trapped in solid matrix of AlH$_3$ during the thermal decomposition of AlH$_3$.[62] To simulate this possibility a cluster of AlH$_3$, consisting of 472 atoms, was heated up. The cluster was built up from a supercell of β-AlH$_3$ by removing the periodic boundary conditions. β-AlH$_3$ has very open channels compared to the α-phase. The resultant cluster was first minimized then equilibrated at 300 K. The equilibrated cluster was then heated to 800 K, at a heating rate of 2.5×10^{-9} K/s. This temperature (800 K) was maintained for 120 ps. Figure 6.26 shows a hydrogen molecule, indicated by an arrow, trapped in the channels of the cluster.

There is dispersive van der Waals interaction between the trapped molecule and the walls of the cages. The trapped molecular hydrogen easily diffuses along the channels into different cages of the cluster. It was noticed that after sometime the molecule escaped. At a faster heating rate the molecular hydrogen escaped at a much earlier time due to the collapse of some cages of the cluster. Even at a constant temperature of 500 K the molecular hydrogen escaped after sometime although at this temperature it took much longer time to escape.

These results therefore presents an unambiguous identification that molecular hydrogen can be trapped in AlH$_3$ matrix and for that matter other hydrogen
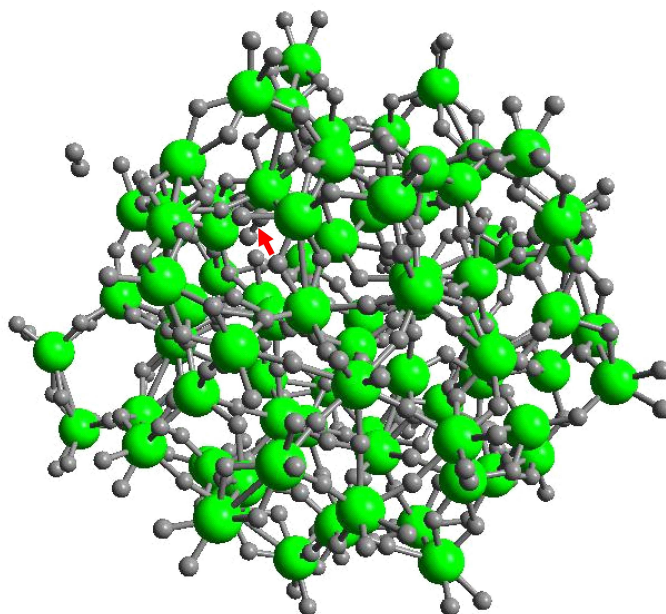
Fig. 6.26: The arrow shows a hydrogen molecule trapped in AlH$_3$ channel.

storage materials. We should re-emphasize that our cluster consisted of only 472 atoms (with an approximate width of 1.6 nm). In experiments, usually after ball milling, the size of the particles vary from 150 nm - 200 nm. Such a particle can contain as much as hundreds of thousands of atoms. This implies that several hundreds or even thousands of molecular hydrogen can be trapped in cages or interstitial sites within the solid matrix during its thermal decomposition.

6.6   Conclusion

Based on DFT derived values for bond dissociation profiles, charge distribution, reaction energy data for small clusters and equations of state for Al and AlH$_3$ condensed phases a reactive force field, (ReaxFF$_{AlH_3}$), has been parameterized for AlH$_3$ systems. ReaxFF$_{AlH_3}$ is built on the same formalism as previous ReaxFF descriptions.[17,18] We find that ReaxFF$_{AlH_3}$ correctly reproduces there DFT data. For the experimentally stable α-AlH$_3$ phase ReaxFF gives a heat of formation of -3.1 kcal/mol H$_2$, which compares excellently with DFT value of -2.36 kcal/mol H$_2$. The experimental heat of formation ranges from -2.37 $\pm$ 0.1

kcal/mol H_2[2] to -2.72 $\pm$ 0.2 kcal/mol H_2.[8]

In the gas phase, there is a thermodynamically driven agglomeration of AlH₃ molecules due to the tendency of the system towards attaining a lower free energy configurations. On Al(111) surface the alane molecules also oligomerize. At the stepped surfaces the molecules oligomerize into long strings. Taking into account the formation and oligomerization of alanes, the dehydrogenation mechanism of NaAlH₄ should proceed as follows:

$$\text{NaAlH}_4 \rightleftharpoons \frac{1}{3}\text{Na}_3\text{AlH}_6 + \underbrace{\frac{2}{3}\text{AlH}_3}_{\text{(oligomers)}} \rightleftharpoons \frac{1}{3}\text{Na}_3\text{AlH}_6 + \frac{2}{3}\text{Al} + \text{H}_2 \qquad (6.7)$$

$$\text{Na}_3\text{AlH}_6 \rightleftharpoons 3\text{NaH} + \underbrace{\text{AlH}_3}_{\text{(oligomers)}} \rightleftharpoons 3\text{NaH} + \text{Al} + \frac{3}{2}\text{H}_2 \qquad (6.8)$$
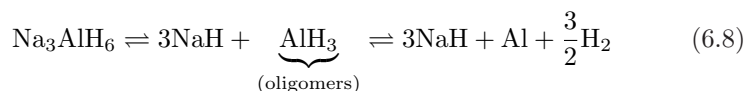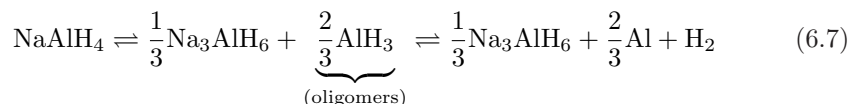
In the initial stages the dominant factor contributing to desorption of hydrogen is the local rise in temperature during the agglomeration process, which weakens/dissociates the Al-H bond. However, as the size of the agglomerated cluster increases the large cluster size effect starts to play a decisive role in desorption of hydrogen. The other contributing factor, to a smaller extent, is the inter-cluster attraction, which weakens the Al-H bond leading to desorption of molecular hydrogen in a nearby cluster as the clusters move towards each other. Presence of defects such as stepped surfaces accelerates the formation of alane oligomers. These simulation results, especially the oligomerization process, are qualitatively consistent with the experimental work of Go et al.,[50] who noted that heating of alanes at 360 K led to "loss of both mobile and smaller alanes to higher alanes and to desorption". They showed that small alane clusters do agglomerate to form large clusters but added that experimental limitations might hinder the observation of the resultant compound aluminum hydride clusters.

In the abstraction process of molecular hydrogen it was seen that with increasing abstraction the remaining hydrogen atoms prefer to occupy surface sites rather than sub-surface sites. This behavior is quite different from that of NaH[17] and MgH₂[18,56] clusters in which with increasing abstraction of molecular hydrogen the remaining hydrogen atoms prefer sub-surface sites. In the gas phase, there is a thermodynamically driven agglomeration of alane molecules. In the process of agglomeration molecular hydrogen is desorbed from the oligomer. Using the method of molecular dynamics, based on ReaxFF, we have unambiguously identified a molecular hydrogen trapped in the AlH₃ matrix.

References

[1] F. M. Brower, N. E. Matzek, P. F. Reigler, H. W. Rinn, C. B. Roberts, D. L. Schmidt, J. A. Snover, and K. Terada. *J. Am. Chem. Soc.*, 98:2450–2453, 1976.

[2] Jason Graetz and James J. Reilly. *J. Alloys Compd.*, 424:262–265, 2006.

[3] J. W. Turley and H. W. Rinn. *Inorg. Chem.*, 8:18, 1968.

[4] Xuezhi Ke, Akihide Kuwabara, and Isao Tanaka. *Phys. Rev. B*, 71:184107–+, 2005.

[5] Jason Graetz and James J. Reilly. *J. Phys. Chem. B*, 109(47):22181–22185, 2005.

[6] M. Baranowski, B. Tkacz. *Z. Phys. Chem. NF*, 135:27, 1983.

[7] S. K. Konovalov and B. M. Bulychev. *Inorg. Chem.*, 34:172, 1995.

[8] G. C. Sinke, L. C. Walker, F. L. Oetting, and D. R. Stull. *J. Chem. Phys.*, 47:2759–2761, October 1967.

[9] B. Bogdanović and G. Sandrock. *MRS Bull.*, 27:712, 2002.

[10] G. Sandrock, J. Reilly, J. Graetz, W.-M. Zhou, J. Johnson, and J. Wegrzyn. *Appl. Phys. A*, 80:687–690, February 2005.

[11] G. Sandrock, J. Reilly, J. Graetz, W.-M. Zhou, J. Johnson, and J. Wegrzyn. *J. Alloys Compd.*, 421:185–189, 2006.

[12] A. Strachan, A. C. van Duin, D. Chakraborty, S. Dasgupta, and W. A. Goddard. *Phys. Rev. Lett.*, 91(9):098301–+, 2003.

[13] A. C. T. van Duin, A. Strachan, S. Stewman, Q. Zhang, X. Xu, and W. Goddard III. *J. Phys. Chem. A*, 107:3803, 2003.

[14] Q. Zhang, T. Çağın, A. C. T. van Duin, W. A. Goddard, Y. Qi, and L. G. Hector. *Phys. Rev. B*, 69(4):045423–+, 2004.

[15] J. G. O. Ojwang', R. van Santen, G. J. Kramer, A. C. T. van Duin, and W. A. Goddard. *J. Chem. Phys.*, 129(24):244506–+, 2008.

[16] A. C. T. van Duin, S. Dasgupta, F. Lorant, and W. Goddard III. *J. Phys. Chem. A*, 105:9396, 2001.

[17] J. G. O. Ojwang, R. van Santen, G. J. Kramer, A. C. T. van Duin, and W. A. Goddard. *J. Chem. Phys.*, 128:4714–+, April 2008.

[18] Sam Cheung, W. Deng, A. C. T. van Duin, and W. A. Goddard III. *J. Phys. Chem. A*, 109:851–859, 2005.

[19] J. K. Gross, S. Guthrie, S. Takara, and G. Thomas. *J. Alloys Compd.*, 297:270–281, 2000.

[20] J. G. O. Ojwang, R. van Santen, G. J. Kramer, and X. Ke. *J. Solid State Chem.*, 181:3037–3043, 2008.

[21] R. T. Walters and J. H. Scogin. *J. Alloys Compd.*, 379:135, 2004.

[22] J. Tersoff. *Phys. Rev.*, 61:2879, 1988.

[23] D. W. Brenner. *Phys. Rev. B*, 42:9458–9471, 1990.

[24] W. J. Mortier, S. K. Ghosh, and S. J. Shankar. *J. Am. Chem. Soc.*, 120:2641, 1998.

[25] G. Kresse and J. Furthmüller. *Phys. Rev. B*, 54:11169–11186, 1996.

[26] P. E. Blöchl. *Phys. Rev. B*, 50:17953–17979, 1994.

[27] J. P. Perdew, J. A. Chevary, S. H. Vosko, K. A. Jackson, M. R. Pederson, D. J. Singh, and C. Fiolhais. *Phys. Rev. B*, 46:6671–6687, 1992.

[28] J. P. Perdew, K. Burke, and Y. Wang. *Phys. Rev. B*, 54:16533–16539, 1996.

[29] J. P. Perdew, K. Burke, and M. Ernzerhof. *Phys. Rev. Lett.*, 77:3865–3868, 1996.

[30] H. J. Monkhorst and J. D. Pack. *Phys. Rev. B*, 13:5188–5192, June 1976.

[31] R. Dovesi, M. Causá, R. Orlando, C. Roetti, and V. R. Saunders. *J. Chem. Phys.*, 92:7402–7411, 1990.

[32] R. Dovesi, V. R. Saunders, C. Roetti, R. Orlando, C. M. Zicovich-Wilson, F. Pascale, B. Civalleri1, K. Doll, N. M. Harrison, I. J. Bush, Ph. DŠArco, and M. M. Llunell. *CRYSTAL06 User's Manual, University of Torino*, 2008.

[33] R. Stumpf. *Phys. Rev. Lett.*, 78:4454–4457, June 1997.

[34] H. Hjelmberg. *Surf. Sci.*, 81:539–561, March 1979.

[35] Hiroaki Kawamura, Vijay Kumar, Qiang Sun, and Kawazoe Yoshiyuki. *Phys. Rev. A*, 67:063205–1 – 063205–8, 2003.

[36] C. Wolverton, V. Ozoliņš, and M. Asta. *Phys. Rev. B*, 69(14):144109–+, April 2004.

[37] H. Grove, M. H. Sørby, H. W. Brinks, and B. C. Hauback. *J. Phys. Chem. C*, 111:16693–16699, 2007.

[38] J. P. Maehlen, V. A. Yartys, R. V. Denys, M. Fichtner, Ch. Frommenc, B. M. Bulychev, P. Pattison, H. Emerich, Y. E. Filinchuk, and D. Chernyshov. *J. Alloys Compd.*, 446, 2007.

[39] G. Henkelman and H. Jónsson. *J. Chem. Phys.*, 113:9978–9985, December 2000.

[40] G. Henkelman, B. P. Uberuaga, and H. Jónsson. *J. Chem. Phys.*, 113:9901–9904, December 2000.

[41] X. Tang, B. Laube, D. Anton, S.-J. Hwang, and R. Bowman. *APS Meeting Abstracts*, pages 39008–+, March 2007.

[42] H. J. C. Berendsen, J. P. M. Postma, W. F. van Gunsteren, A. Dinola, and J. R. Haak. *J. Chem. Phys.*, 81:3684–3690, 1984.

[43] K. Lammertsma and J. Leszczy'nski. *J. Phys. Chem.*, 94:2806–2809, 1990.

[44] X. Wang, A. Lester, S. Tam, M. E. DeRose, and M. E. Fajardo. *J. Am. Chem. Soc.*, 125:9218–9228, 2003.

[45] M. Shen and H. F. Schaefer, III. *J. Chem. Phys.*, 96:2868–2876, February 1992.

[46] B. K. Rao, P. Jena, S. Burkart, G. Ganteför, and G. Seifert. *Phys. Rev. Lett.*, 86:692–695, January 2001.

[47] J. Paul. *Phys. Rev. B*, 37:6164–6174, April 1988.

[48] A. Winkler, C. Resch, and K. D. Rendulic. *J. Chem. Phys.*, 95:7682–7688, November 1991.

[49] H. Kondoh, M. Hara, K. Domen, and H. Nozoye. *Surf. Sci.*, 287:74–78, May 1993.

[50] E. Go, K. Thuermer, and J. E. Reutt-Robey. *Surf. Sci.*, 437:377–385, September 1999.

[51] M. Hara, K. Domen, T. Onishi, H. Nozoye, C. Nishihara, Y. Kaise, , and H. Shindo. *Surf. Sci.*, 242:459–463, 1991.

[52] P. J. Herley, S O. Christofferson, and J. A. Todd. *J. Solid State Chem.*, 35: 391, 1980.

[53] S. Chaudhuri, S. Rangan, J. Veyan, J. T. Muckerman, and Y. J. Chabal. *J. Am. Chem. Soc.*, 130:10576–10587, 2008.

[54] A. Winkler, G. Poigainer, and K. D. Rendulic. *Surf. Sci.*, 251:886–890, 1991.

[55] I. M. K Ismail and T. Hawkins. *Thermochi. Acta*, 439:32–43, 2005.

[56] R. W. P. Wagemans. *Magnesium for hydrogen storage: from micrometer to nanometer*. PhD thesis, Universiteit Utrecht, Sept. 2006.

[57] G. Majer, E. Stanik, L. E. Valiente Banuet, F. Grinberg, O. Kircher, and M. Fichtner. *J. Alloys Compd.*, 404-406:738–742, 2005.

[58] O. J. Zogal, M. Punkkinen, E. E. Ylinen, and B. Stalinski. *J. Phys.: Condens. Matt.*, 2:1941–1944, February 1990.

[59] V. P. Tarasov, S. I. Bakum, and S. F. Kuznetsova. *Russ. J. Inorg. Chem.*, 42:694–701, 1997.

[60] V. P. Tarasov and G. A. Kirakosyan. *Russ. J. Inorg. Chem.*, 42:1223–1227, 1997.

[61] J. L. Herberg, R. S. Maxwell, and E. H. Majzoub. *J. Alloys Compd.*, 417: 39–44, 2006.

[62] L. Senadheera, E. M. Carl, T. M. Ivancic, M S. Conradi, R. C. Bowman Jr, S. J. Hwang, and T. J. Udovic. *J. Alloys Compd.*, 463:1–5, 2008.
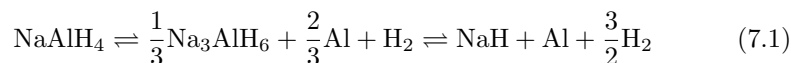
Summary

The main goal of this research work was to have an atomic-scale understanding of the microscopic mechanisms involved in the thermal decomposition process of $NaAlH_4$. Key questions that we set out to answer were: (i) what are the exact phase transformation associated with the thermal decomposition of $NaAlH_4$ and ultimately desorption of hydrogen?, and (ii) what mechanism facilitates the long range mass transport of aluminum atoms? Since the chemistry of the decomposition process is very complex, we divided the problem into three subsets as follows:
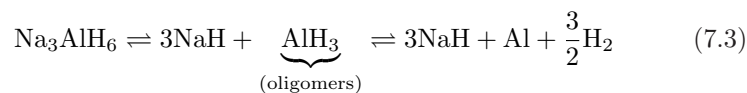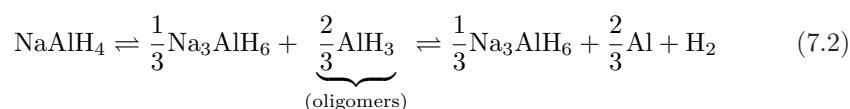
1. A study of the thermodynamics and possible intermediate structures during the thermal decomposition of $NaAlH_4$ (4). The issue of intermediate pathways is important. The conventional and experimentally observed intermediate phase in the thermal decomposition of $NaAlH_4$ is Na_3AlH_6. However, this pathway does not explain the mass transport of aluminum atoms. Using Na_2AlH_5 and $Na_5Al_3H_{14}$ as possible intermediate phases in the decomposition profile of $NaAlH_4$ it is shown that alanes are formed. The alanes facilitate the mass transport of aluminum atoms.

2. Parameterization of a force field for NaH, $ReaxFF_{NaH}$, to study the decomposition dynamics of NaH (chapter 3). The parameterized force field is used to study the dynamics of hydrogen desorption in NaH clusters. During the abstraction process of molecular hydrogen from a cluster of NaH it is seen that charge transfer is correctly described by $ReaxFF_{NaH}$. To get a better understanding of the structural transformations of NaH during thermal decomposition a heating run in a molecular dynamics simulation is performed. The runs exhibits a series of drops in potential energy, associated with cluster fragmentation and desorption of molecular hydrogen. This is found to be consistent with experimental works.

3. Parameterization of a reactive force field for aluminum (chapter 5) and aluminum hydride (chapter 6) to study the thermal decomposition dynamics of AlH_3. Using $ReaxFF_{AlH_3}$, the mechanism of mass transfer of aluminum atoms with alanes (AlH_3 molecules) as facilitators is explored. Alane is very stable to decomposition and for this reason it cannot desorb molecular hydrogen under the experimental temperatures. Interestingly during a molecular dynamics heating run, alanes are seen to agglomerate and once the agglomerated cluster reaches a particular size it desorbs molecular hydrogen at relatively lower temperatures. This suggests that alanes can facilitate the mass transport of aluminum atoms. They do this by oligomerizing. Molecular hydrogen is then desorbed from the agglomerated cluster leading to the formation of aluminum clusters and ultimately bulk aluminum. Even on aluminum surface alanes oligomerize into larger clusters. The oligomerization of alanes on aluminum surfaces is consistent with the experimental work of Chabal et al.[1] and Go et al.[2] In their study, Go et al. observed that on the vicinity of steps the alanes arrange themselves into long strings after oligomerization.

Based on these results we have been able to propose a decomposition mechanism for $NaAlH_4$. To do this, we need to recast the conventional decomposition pathway into a form that takes into account the formation and subsequent oligomerization of alanes. The conventional decomposition process is as follows,

$$NaAlH_4 \rightleftharpoons \frac{1}{3}Na_3AlH_6 + \frac{2}{3}Al + H_2 \rightleftharpoons NaH + Al + \frac{3}{2}H_2 \qquad (7.1)$$

One way to recast equation (7.1) is as follows:

$$NaAlH_4 \rightleftharpoons \frac{1}{3}Na_3AlH_6 + \underbrace{\frac{2}{3}AlH_3}_{\text{(oligomers)}} \rightleftharpoons \frac{1}{3}Na_3AlH_6 + \frac{2}{3}Al + H_2 \qquad (7.2)$$

$$Na_3AlH_6 \rightleftharpoons 3NaH + \underbrace{AlH_3}_{\text{(oligomers)}} \rightleftharpoons 3NaH + Al + \frac{3}{2}H_2 \qquad (7.3)$$

We can infer from equations (7.2) and (7.3) that not only are AlH_3 formed during the decomposition process of $NaAlH_4$ but they also oligomerize. The oligomers agglomerate further and in the process molecular hydrogen is desorbed from the system. In trying to understand the formation of AlH_3 we cannot limit ourselves to just one pathway. There might be other possible pathways during the thermal decomposition of $NaAlH_4$. There are two pathways that have been

proposed, which take into account the formation of alanes. One such pathway was proposed by Walters and Scogin[3] and the other was proposed by Ojwang et al.[4] The thermodynamics associated with these pathways is discussed in chapter 4.

A schematic diagram showing the possible thermal decomposition process of $NaAlH_4$ is illustrated in Fig. 7.1. What Fig. 7.1 shows is this. When heated, $NaAlH_4$ decomposes into a metastable intermediate state plus alanes. Since the intermediate state is quasi-stationary it is shown as a fuzzy region in Fig. 7.1. The intermediate state decomposes further leading to the formation of more alanes. Once formed, the alanes migrate and oligomerize. After oligomerization or in the process of oligomerization molecular hydrogen is desorbed from the oligomer, leaving behind aluminum atoms. These aluminum atoms then agglomerate into aluminum clusters and ultimately into aluminum metal.
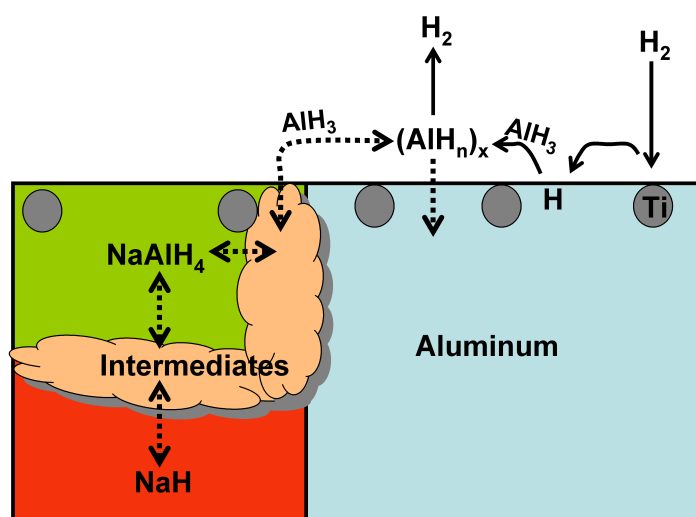
Fig. 7.1: Proposed desorption/absorption mechanism of $NaAlH_4$.

The reverse reaction is more complicated. First of all we need to understand the role of titanium in this. Bogdanovic showed that the dehydrogenation of $NaAlH_4$ occurs at a lower temperature and also become reversible when doped with Ti.[5] On the theoretical front, Iniguez and Yildrim, using first-principles, showed that it is energetically favorable for Ti to stay on the surface of $NaAlH_4$ rather than in the bulk of the material.[6] Experimentally, the addition of Ti dopants to $NaAlH_4$ does not affect its bulk lattice parameters. This again suggests that the Ti dopants stay on the surface of $NaAlH_4$.[7] Marashdeh et

al. suggested a zipper model in which Ti moves into the subsurface region of the structure, replacing Na in the process.[8] The Ti then works its way into the structure effectively unzipping it. Titanium therefore plays a role in dissociating molecular hydrogen on aluminum surface.

What Fig. 7.1 shows, in the reverse reaction, is the following: first molecular hydrogen, under the right pressure and temperature conditions, is physisorbed on the surface of aluminum. The Ti,which are located on Al surface, catalyzes the dissociation of the molecular hydrogen. Ti dissociates the hydrogen molecules since it has d-orbitals of the right symmetry. It does this by backdonating electrons to the antibonding orbitals of hydrogen molecule. As it strikes the Al surface, the atomic hydrogen abstracts Al atoms from the surface to form aluminum hydride. Presence of defects on the surface should accelerate the abstraction of Al and formation of alanes. Once formed, the alanes oligomerize and are mass transported to the NaH zone where they jump into and react with NaH. This solid state reaction and ordering leads to the formation of $NaAlH_4$.

References

[1] S. Chaudhuri, S. Rangan, J. Veyan, J. T. Muckerman, and Y. J. Chabal. *J. Am. Chem. Soc.*, 130:10576–10587, 2008.

[2] E. Go, K. Thuermer, and J. E. Reutt-Robey. *Surf. Sci.*, 437:377–385, September 1999.

[3] R. T. Walters and J. H. Scogin. *J. Alloys Compd.*, 379:135, 2004.

[4] J. G. O. Ojwang, R. van Santen, G. J. Kramer, and X. Ke. *J. Solid State Chem.*, 181:3037–3043, 2008.

[5] B. Bogdanović and M. Schwickardi. *J. Alloys Compd.*, 253/254:1–9, May 1997.

[6] J. Iniguez and Yildirim. *Appl. Phys. Lett.*, 86:103109, 2005.

[7] V. Ozolins, E. H. Majzoub, and T. J. Udovic. *J. Alloys Compd.*, 375:1–10, 2004.

[8] A. Marashdeh, R. Olsen, O. Løvvik, and G. Kroes. *J. Phys. Chem. C*, 111: 8206–8213, 2007.

List of publications

[1] J. G. O. Ojwang, S. Chaudhuri, Y. Y. Chabal, G. J. Kramer, R. van Santen, A. C. T. van Duin, and W. A. Goddard III. An infrared absorption spectroscopy and theoretical modeling of dependence of sorption dynamics of aluminum hydride on particle size. *(in preparation)*, 2009.

[2] J. G. O. Ojwang, R. van Santen, G. J. Kramer, S. Chaudhuri, A. C. T. van Duin, and W. A. Goddard III. Parametrization of a force field for aluminum hydride: A combined experimental and density functional theory approach. *(in preparation)*, 2009.

[3] J. G. O. Ojwang, R. van Santen, G. J. Kramer, and X. Ke. Structural stability and electronic structure of $Na_3Li_3Al_2H_{12}$. *(Submitted to J. Alloys Compds.)*, 2009.

[4] J. G. O. Ojwang, R. van Santen, G. J. Kramer, A. C. T. van Duin, and W. A. Goddard III. Predictions on melting, crystallization and local atomic arrangements of aluminum clusters using a reactive force field. *J. Chem. Phys.*, 129:244506, 2008.

[5] J. G. O. Ojwang, R. van Santen, G. J. Kramer, and X. Ke. An ab initio study of possible pathways in the thermal decomposition of sodium alanate. *J. Solid State Chem.*, 181:3037, 2008.

[6] J. G. O. Ojwang, R. van Santen, G. J. Kramer, A. C. T. van Duin, and W. A. Goddard III. Modeling the sorption dynamics of sodium hydride using a reactive force field. In *AIP Conference Proceedings: SELECTED PAPERS FROM ICNAAM-2007 AND ICCMSE-2007*, volume 768, page 236, 2008.

[7] J. G. O. Ojwang, R. van Santen, G. J. Kramer, A. C. T. van Duin, and W. A. Goddard III. Modeling the sorption dynamics of sodium hydride using a reactive force field. *J. Chem. Phys.*, 128:4714–+, 2008.

[8] O. Scholten, J. G. O. Ojwang, and S. Tamenaga. Dibaryon resonance and two-photon bremsstrahlung in pp scattering. *Phys. Rev. C*, 71:034005–+, 2005.

[9] J. G. O. Ojwang and O. Scholten. Effects of a dibaryon on two-photon bremsstrahlung in pp scattering. In *AIP Conference Proceedings:FEW-BODY PROBLEMS IN PHYSICS: The 19th European Conference on Few-Body Problems in Physics.*, volume 768, page 236, 2005.

Acknowledgements

I have been very privileged to work under two incredible supervisors: Rutger van Santen and Gert Jan Kramer. To Gert Jan, thank you for accepting me as your PhD student and having faith in me during the initial teething stages of my research work. To Rutger, it has been nothing short of thrilling to work with you. I am still awed by your in-depth knowledge on many issues in science and I feel privileged to have had a chance to learn so much from you. I look forward to continuing our collaboration in the hydrogen sphere as well as other areas of mutual interests.

Secondly, I am very grateful to the members of my thesis committee (Geert Jan Kroes, Peter Notten, Adri C.T. van Duin, Bert Hintzen and Andreas Zuttel) for taking their time to review my thesis and for offering critical analysis and suggestions on the same.

My days in Groningen as a master's student are quite memorable. I had the privilege of being tutored by great lecturers who increased my passion for research. In particular, I thank my master's thesis supervisor, Olaf Scholten, for his constant support. Olaf, you are without a doubt one of the best teachers I have ever had in my life. It was an incredible experience to work under your tutelage as a research student. I still vividly remember how you simplified the concepts of eigenvectors and eigenvalues so I could grasp them. I believe that with the new accelerator at CERN the dibaryons will hopefully be observed. I also wish to thank my former lecturers at Groningen Mees de Roo, Eric Bergshoeff,Herbert LÄohner, Paul van Loosdrecht, and Frank van Steenwijk (MSc physics course manager). It was a wonderful to interact with all of you as your student. Although my brief romance with quantum computation led to boredom, I did enjoy the lectures of and brief communications with Hans De Raedt. Thank you Hans.

My stay in Eindhoven would not have been easy without the superb help of Elize and Marion. Elize, I really appreciate the extra mile you went to make me feel very comfortable during my initial days in SKA. I also wish to thank all my colleagues in the theory group, viz Evgeny, Bouke, Thuat, Sharan, Ionel, Chrétien, Pieter vG, Willy, Chrétien and Cristina. Chrétien, you taught me what "chmod u+x" means. This simple command has formed the backbone of my research work. Cristina, it was a real pleasure discussing with you issues within and outside academic confines. Willy, thank you for your superb assistance with making various scripts to run my jobs. To Christian Müller, thank you for giving me a ride every now and then and for stimulating discussions on astronomy. I wish to express my gratitude to Evgeny for the light-hearted moments and, most importantly, for designing the cover of my thesis. Ionel, thank you for the bread-making lessons. Tonek, I appreciate the fact that I had a chance to be a tutor in your chemical bonding course. I also thank Joost, who gave me my first lessons in Linux, although four years down I still cannot wean myself off Windows.

Outside the office corridors and in my social circle, I enjoyed the friendship of Jimmy, Pina, Seith, Katunzi, Kakuba, Chris, Arthur, Yeneneh, Eva, among others. You all made my days in Eindhoven enjoyable. It was always fun to hang out with you. Eva, your sense of humor is indeed weird and always made my day!

In April 2006 I had the opportunity to visit William Goddard's group at the California Institute of Technology (Caltech), or the Material Process and Simulations Centre (MSC) as it is called. It was the start of what is turning out to be a long-term collaboration. I am deeply grateful to Adri van Duin and William Goddard III (Bill as he is fondly called). Adri, the last time I checked my "inbox" and "sent" folders, I realized that we have exchanged more than 1,500 emails. And the number is growing. You are one of the most meticulous and busiest people I have known, and in spite of your schedule, you still find time to address burning issues related to our collaboration. It has been a pleasure to work with you. I look forward to our continued collaboration as we preach and spread the reactive force field gospel according to ReaxFF. Bill, you are a towering colossus of knowledge, and conversations with you, be it on the academic front or on "simple life," have always been thrilling. No one says "Sounds good" better than you! Thank you for inviting me to participate in the very stimulating annual MSC research conferences.

My research work entailed extensive collaboration and consultation across the globe: Among the people I have had the pleasure to collaborate or discuss issues/questions pertaining to hydrogen storage with include: Geert Jan Kroes (Leiden), Roar Olsen (Norway), Ali Marashdeh (Delft), Terry Francombe (Sweden), Ke Xuezhi (China), Karl Gross, Andreas Zuttel (ETH), Jason Graetz (Brookhaven), Ole Martin Lovvik (Norway), Zhu Ma (Gatech), Ronald Stumpf

(Sandia), Yves Chabal (Texas), Santanu Chaudhuri (Washington), Saman Alavi (Canada), and Bill Lester (Berkeley). To Paul Vermulen and Suleiman Ertl (Twente), thank you for the wonderful time in Iceland. Dear Ke, it has been fun collaborating with you, and I look forward to further collaborations in future. I also wish to thank Dr. Alexander Hofmann for helping me understand the CRYSTAL03 code during the initial stages of my research work. To Harold Stokes, although I did not really use your program, Isotropy, I thank you for your assistance in teaching me how to use the software. My thanks to Jorge Iniguez for providing me with useful data on Ti-doped NaAlH4. To Bill and Rochelle Lester, my wife and I look forward to meeting you again.

Many thanks to my former lecturers at JKUAT, notably Ndeda, Korowe, Mwose, and to the many wonderful lecturers and laboratory technicians who were always there when I needed them most. To Ndeda, what can I say, from my lecturer you have become a true friend. To Chege, thank you for your superb assistance during my stay in JKUAT. To Professor Thairu, you were always hospitable to me whenever I visited JKUAT, long after my student days, thank you so much. To Tatsuo Hoshi and Sadanori Taguchi (the then JICA permanent representatives in JKUAT), thank you. It was Taguchi who encouraged me to consider pursuing physics further. To Mbuthia (in-charge of printery at JKUAT), thank you for the tidbits on printing and your help in shaping and setting up CampusView. To Davies Araka, thanks for your support with CampusView. To Professor Genga (of UoN), thank you. To Mrs. Onditi, you were like a mother to me during my student days at JKUAT. You truly have a golden heart. Thank you!

To the students and teachers of Chebisaas Boys High school during 1999-2002 (in particular Mr. Kinyua, with whom I had the pleasure to work, Mrs. Wainaina, Mr. Wanyonyi, Mrs. Nandi, Mr. Oduor, Mrs. Musau, Mr. Kibet, Mrs. Barasa, Mr. Keter, Mrs. Miano, among others). I wish to thank you all for the memorable times I had while in Chebisaas. It was definitely a delight to be part of Chebisaas community. Many thanks to a man who unfortunately will never have the chance to see this thesis, the late principal of Chebisaas High School, Thomas K. Musau. Mus, as we all fondly called him, gave us all without asking for anything in return except excellence. I would also like to thank my teachers at Sawagongo High School, in particular Mr. Opiyo, Mr. Bwaringa, Mr. Obiero and Mr. Odindo.

It is difficult to express my gratitude to my parents, John and Martha, for their never-ending love and support, which has kept me going all these years. To my siblings, Evans, Leonard, Rose, Hellen and Dick, I love you guys. To Richard, I am so proud of you. To my wonderful in-laws: MGD, Aspil, Don, Gina and Tessy, thank you all! To Mr. Rachier, you are a dear friend indeed. I am grateful for your endless support over the years. To Alex and Winnie Wainaina, thank you so much! To Jumba, thanks mate. To my cousins Alfred and Hellen

and the late Lorraine, thanks for your moral support and friendship. To my uncle Gordon, thanks for the tidbits about living in the Netherlands. There are many more relatives whom I have not mentioned by name, but I say thanks to all of you.

Last but by every means first is the person who gave me unwavering support every step of the way in spite of the transatlantic distance, my lovely wife, Madona. Mado, life without you will be pointless, just like a broken pencil. "Osiep chunya," you take my breath away!

About the author

J.G.O. Ojwang was born in Garissa (Kenya) but hails from Siaya (Kenya). He studied physics at the Jomo Kenyatta University of Agriculture and Technology (JKUAT), where he graduated with honors from the Faculty of Science in April 1998. In August 2004 he received his MSc. (Physics and Astronomy) degree, *cum laude*, from the Rijksuniversiteit Groningen, Netherlands. His masters research thesis, "*Dibaryon Resonance and two photon bremsstrahlung in pp-scattering*", was supervised by Olaf Scholten (at the Kernfysisch Versneller Instituut). In August 2004 he started his doctorate studies in the group of Rutger van Santen, co-supervised by Gert Jan Kramer at Eindhoven University of Technology. The aim of the project was to get an atomistic-scale understanding of the microscopic mechanisms involved in the thermal decomposition process of sodium aluminum hydride, a potential hydrogen storage material. The project was carried out in collaboration with William A. Goddard III (Caltech) and Adri C. T. van Duin (Penn State). Since June 2006 he is a guest researcher at the Materials and Process Simulation Center (Goddard's group) in Caltech. During the course of this research work, in 2007, he won a best lecture award (2nd place) at the 21st "Darmstadt" Molecular Modeling Workshop, Erlangen, Germany and in 2008 he was one of the finalists in the Young Researcher Prize "Summer School on Modern Concepts for Creating and Analyzing Surfaces and Nanoscale Materials, Costa Brava, Spain". He is a Peer Reviewer for Journal of Solid State Chemistry, Nanotechnology and Journal of Physics: Condensed Matter.